Experimental Investigation of the Shear Resistance of Circular Concrete-Filled Steel Tubes (CFTs) Subjected to Transverse Loading

Todd R. Maki

A thesis

submitted in partial fulfillment of the

requirements for the degree of

Master of Science in Civil Engineering

University of Washington

2015

Committee:

Charles W. Roeder

Dawn E. Lehman

Jeffrey W. Berman

Program Authorized to Offer Degree:

Civil and Environmental Engineering

University of Washington

Abstract

Experimental Investigation of the Shear Resistance of Circular Concrete-Filled Steel Tubes (CFTs) Subjected to Transverse Loading

Todd R. Maki

Co-Chairs of the Supervisory Committee:
Charles W. Roeder
Dawn E. Lehman
Civil and Environmental Engineering

Concrete-filled steel tubes (CFTs) and reinforced concrete-filled steel tubes (RCFTs) are used throughout the world in building and transportation structures. While the axial and flexural properties of CFTs have been well-researched, little research has been performed on their shear strength and behavior. Currently accepted methods for calculating their shear capacity significantly underestimate the effectiveness of the composite section, potentially increasing undesirable conservatism and cost.

The purpose of this research was to investigate the shear resistance and deformation of CFT and RCFT members subjected to large shear stresses, and to develop an improved, more accurate method for their prediction. To do so, an experimental study of large-scale CFTs subjected to transverse shear load was undertaken, and high-resolution finite element models will be employed to extend the experimental results. The experimental and analytical results will then be combined to recommend office-ready design expressions for shear resistance, stiffness, and deformation capacity.

TABLE OF CONTENTS

LIST OF FIGURES

LIST OF TABLES

ACKNOWLEDGEMENTS

This research was funded by the Washington State Department of Transportation. Mr. Bijan Khaleghi and his team provided advice and support throughout.

I would like to thank Charles Roeder and Dawn Lehman for the opportunity to work on this project and to study with them. Their experience and knowledge has been invaluable.

I would also like to thank all those who lent a helping hand or two to complete this portion of the project: Vince Chaijaroen for his time and dedication to the lab; Ashley Heid for her collaboration and tireless work in the lab; Max Stephens for returning to the lab many times after he thought he was finished; Nate Clemen, Anthony Gasca, Marisa Gelms, Becky Gilbertson, and Truc Thai for their help during specimen preparation, instrumentation, and testing. The project would not have been completed without them.

Most importantly I'd like to thank my wife, Beth, for her support, understanding, help, and counsel.

Chapter 1. INTRODUCTION

1.1 CONCRETE-FILLED STEEL TUBES

Concrete-filled steel tubes have been used extensively throughout the world in building and transportation structures as columns, beams, braces, truss elements, and foundation components. CFTs combine steel and concrete to create efficient and economical composite structural members. They utilize the high strength and ductility of steel and the ability concrete has to efficiently carry compressive loads. The concrete restrains local buckling of the steel tube while the steel tube acts as reinforcement—both longitudinal and transverse—and provides needed confinement for the concrete. The steel tube also acts as the concrete form during construction, thus eliminating the need to erect and remove formwork. The combination of the intrinsic strengths of the constituent materials provides CFT members with high stiffness, strength, and inelastic deformation capacity. Reinforced concrete-filled steel tubes (RCFTs) are not as commonly employed, but can be found when other structural components are connected to CFTs or when an increase in strength is required due to geometric limitations, among other conditions. While CFTs can be constructed with either rectangular or circular steel tubes, research (Roeder et al. 2009) has shown that circular CFTs offer better confinement of the concrete and better bond stress between the concrete and steel, increasing the effective composite action in the member. This thesis will focus on circular CFTs and their behavior.

The axial and flexural properties of CFTs have been well researched and reported in the literature but little research has been performed on their shear strength and behavior. The *Specification for Structural Steel Buildings* by the American Institute of Steel Construction (AISC 2010) provides three methods for calculating the shear capacity of CFT members. The

Washington Department of Transportation (WSDOT 2012), in a design memorandum addressing the use of concrete-filled steel tubes and reinforced concrete-filled steel tubes in bridge foundations, recommends using a design expression that sums the shear capacities of the individual steel and concrete components without accounting for any interaction. All four methods neglect the composite behavior and are likely to significantly underestimate the shear capacity of the composite section, potentially increasing undesirable conservatism and cost. Other specifications have either similar design recommendations or none at all.

Current research on the shear resistance of CFTs, although limited in quantity, has been focused primarily in Japan and China, where CFTs are used more frequently in construction than in the United States. With more research and awareness of their benefits, CFTs are gaining more widespread acceptance in the U.S., especially in transportation structures constructed in high seismic regions on the west coast. Their stiffness, strength, durability, toughness, and rapid constructability make them attractive alternatives to traditional reinforced concrete bridge piers and deep foundation systems. It is important to understand the shear strength and deformation behavior of CFTs to provide more economical and reliable designs.

One potential area for increased efficiency in design is in the use of CFT and RCFT members in pile and drilled shaft foundations. Recent research (Lehman and Roeder 2012) has detailed many advantages to their use. Deep foundations are often used in areas with poor soils, such as river beds, to mitigate the risks of liquefaction and lateral spreading. Large, extremely localized transverse forces can be exerted on the pile or drilled shaft if these phenomena occur in thin soil layers due to their short effective length through those layers (McGann 2013). Current design provisions underestimate the available capacity of CFT or RCFT foundations, thus requiring a design that is larger and costlier than necessary.

1.2 Research Objectives

The primary purpose of this research is to investigate the shear resistance and deformation of CFT and RCFT members subjected to large shear stresses, and to develop an improved, more accurate method for their prediction. The research program includes the following steps:

- a thorough study and evaluation of prior research work
- an experimental study of large-scale CFTs subjected to transverse shear load
- the use of high-resolution finite element models to extend the experimental results
- combination of the experimental and analytical results to develop office-ready design expressions for shear resistance, stiffness, and deformation capacity

It is expected that many factors will affect the shear behavior of circular CFTs and that the design expressions may ultimately depend on many of them. Some potential influences are material strength, geometry, axial load, bond stress, and interaction with applied bending moment.

This report will focus on the first two tasks: 1) a review of prior experimentation and its applicability to the current program and 2) the design and implementation of the experimental program. Potential design expressions will be evaluated herein but recommendations will not be made until after a more thorough analysis is performed with the finite element models that will be validated by the experimental results.

1.3 Report Overview

This thesis summarizes the research undertaken to determine the shear resistance and deformation behavior of CFT and RCFT member subjected to transverse loading. It comprises

six chapters covering previous research, the experimental program, the observed results, analysis and interpretation, and evaluation of design expressions.

Chapter 2 reviews the prior research on the shear strength of circular CFTs and stated conclusions. It also briefly summarizes available shear design expressions.

Chapter 3 discusses the study parameters, test matrix, and material properties as well as expected moment and shear capacities of the specimens. The design of the test apparatus, the specimen instrumentation, and specimen construction are also covered.

Chapter 4 reports the observed response of each specimen and associated damaged states for the concrete and steel components.

Chapter 5 discusses failure modes, the parameter study series results, and trends in behavior. Two shear design expressions are formulated and evaluated with the test results.

Chapter 6 includes a summary of the experimental results, observations, recommendation for future study of shear in concrete-filled steel tubes.

Chapter 2. LITERATURE REVIEW AND CURRENT DESIGN PROVISIONS

2.1 CURRENT DESIGN PROVISIONS

The flexural and axial strengths, as well as the P-M interaction, of circular CFTs have been relatively well-studied, but there is no consensus on design expressions. Moon et al. (2012) and Roeder et al. (2010) have covered many available design expressions that will not be treated here. There has been very little study of the shear behavior of CFTs and RCFTs, and the available shear design expressions lack refinement. They do not take advantage of the benefits that composite behavior provides to both the steel and concrete constituents of CFTs nor do they provide for any increase in shear resistance due to the presence of longitudinal reinforcement. AISC (2010) and WSDOT (2012) provide design expressions that will be reviewed herein. The American Concrete Institute (ACI 2014) does not explicitly address the shear resistance of composite compression members but refers to the AISC *Specification (2010)* for shear resistance of concrete-steel composite flexural members.

2.1.1 *AISC Shear Strength*

The AISC *Specification* (2010) permits three methods for calculating the shear strength of CFT and RCFT members. The first, shown in Equations 2.1, relies only upon the available shear strength of the steel tube, neglecting any contribution by the concrete fill. The second method, shown in Equations 2.2, utilizes the shear strength of the concrete and any internal shear reinforcement, ignoring the steel tube. The third method, shown in Equations 2.3, is a hybrid of the first two, utilizing the shear strength of the steel tube and the contribution from any transverse reinforcement that is in the concrete fill.

2.1.1.1 AISC Method 1

$$V_{n\,(AISC\_1)} = V_s \tag{2.1a}$$

where $V_s = 0.6f_y(0.5A_s)$ (2.1b)

2.1.1.2 AISC Method 2

$$V_{n\,(AISC\_2)} = V_c + V_{sr} \tag{2.2a}$$

where $V_c = 2\sqrt{f_c'}A_c$ (2.2b)

$$V_{sr} = \frac{A_y f_y D}{s} \tag{2.2c}$$

2.1.1.3 AISC Method 3

$$V_{n\,(AISC\_3)} = V_s + V_{sr} \tag{2.3a}$$

where $V_s = 0.6f_y(0.5A_s)$ (2.3b)

$$V_{sr} = \frac{A_y f_y D}{s} \tag{2.3c}$$

2.1.2 *WSDOT Shear Strength*

The WSDOT shear design expression combines the respective strengths of the concrete fill and the steel tube but neglects the positive effects the concrete fill and the steel tube have on each other. Equations 2.4 show the WSDOT design expression for CFT and RCFT members.

$$V_{n\,(WSDOT)} = V_s + 0.5V_c \tag{2.4a}$$

where $V_s = 0.6f_y(0.5A_s)$ (2.4b)

$$V_c = 0.0316\beta\sqrt{f'_c}A_c \; if \; P_u \; is \; compressive \tag{2.4c}$$

and *f'c* is in ksi and □ = 2.

2.1.3 *Axial and Flexural Strength*

The axial and flexural capacities of CFTs and RCFTs will not be presented in detail here. The reader is referred to papers by Moon et al. (2012) and Roeder et al. (2010), as well as to design standards from AISC (2010) and ACI (2014), among others, for a more complete understanding. Both flexural and axial strength, however, played key roles in this experimental program; several of the tests were flexurally-controlled and one of them had an axial load applied. The guidelines from the WSDOT design memorandum (2012) will be covered briefly. They are similar in nature to the design provisions mentioned above as they are drawn from them with some minor modifications.

The plastic stress distribution method (PSDM) is used to calculate the flexural and axial strength of circular CFTs and RCFTs. The general stress distribution is shown in Figure 2.1a. The PSDM assumes that, due to axial and/or flexural loading, the concrete fill has reached a compressive stress of $0.95f'_c$ for circular sections and that the steel tube and longitudinal reinforcement (if present) have reached the yield stress, f_y, in either tension or compression. Figure 2.1b shows the full P-M interaction curve that can be developed. The WSDOT memorandum (2012) and the AISC *Specification* (2010), upon which the WSDOT provisions are partially based, provide a full discussion of local and global stability effects.

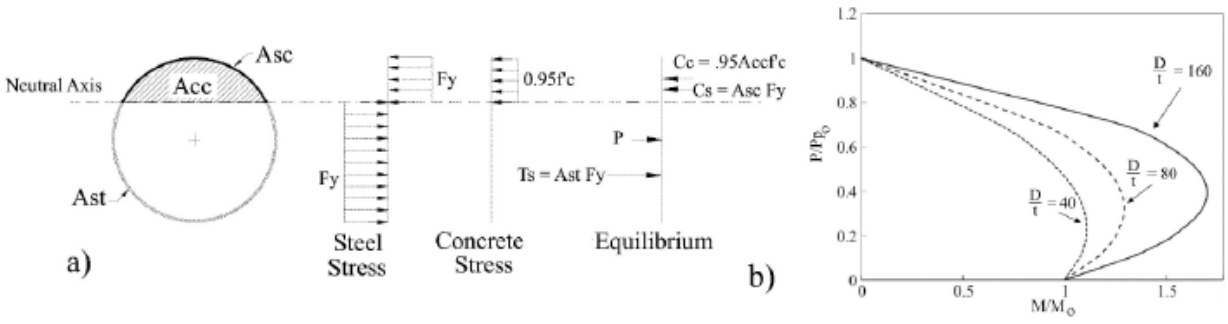

a) Stress diagram b) P-M interaction curve

Figure 2.1: Plastic stress distribution after WSDOT (2012)

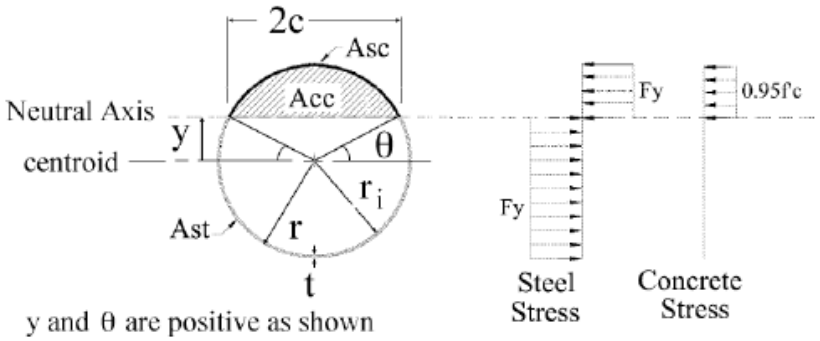

Figure 2.2: Geometry diagram for use with CFT PSDM for flexure after WSDOT(2012)

Equations 2.5 define a closed-form solution for the PSDM based on the geometry shown in Figure 2.2.

$$r_m = r - \frac{t}{2} \tag{2.5a}$$

$$\theta = \sin^{-1}\left(\frac{y}{r_m}\right) \tag{2.5b}$$

$$c = r_i \cos\theta \tag{2.5c}$$

$$P = F_y t r_m\{(\pi - 2\theta) - (\pi + 2\theta)\} + \frac{1}{2}0.95f'_c\{(\pi - 2\theta)r_i^2 - 2yc\} \tag{2.5d}$$

$$M_{p,PSDM} = 0.95f'_c c\left\{\left(r_i^2 - y^2\right) - \frac{c^2}{3}\right\} + 4F_y t c\frac{r_m^2}{r_i} \tag{2.5e}$$

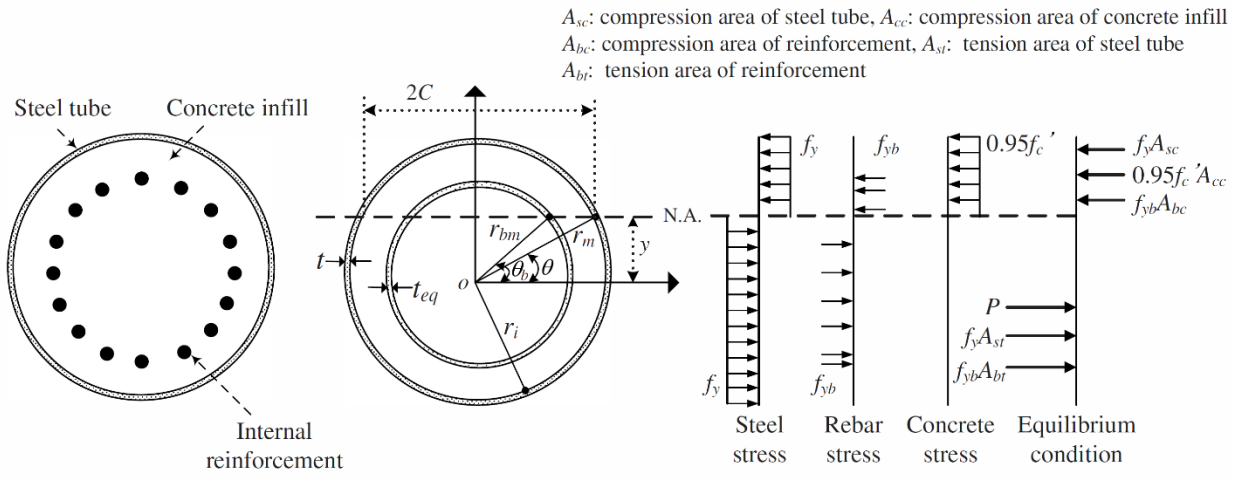

Figure 2.3: Geometry diagram for use with RCFT PSDM after Moon et al. (2012)

A similar closed-form solution has been derived for RCFTs and is outlined in Equations 2.6, with accompanying geometry shown in Figure 2.3. For simplicity, the reinforcing bars are treated as if they were another steel tube.

$$r_m = r - \frac{t}{2} \tag{2.6a}$$

$$\theta_s = \sin^{-1}\left(\frac{y}{r_m}\right) \quad \text{and} \quad \theta_b = \sin^{-1}\left(\frac{y}{r_b}\right) \tag{2.6b}$$

$$c = r_i \cos\theta_s \quad \text{and} \quad c_b = r_b \cos\theta_b \tag{2.6c}$$

$$t_b = \frac{nA_b}{2\pi r_b} \tag{2.6d}$$

$$P = F_y t r_m\{(\pi - 2\theta_s) - (\pi + 2\theta_s)\} + \frac{1}{2}0.95f'_c\{(\pi - 2\theta_s)r_i^2 - 2yc\} + t_b r_b\{F_{yb}(\pi - 2\theta_b) - (F_{yb} - 0.95f'_c)(\pi + 2\theta_b)\} \tag{2.6e}$$

$$M_{PSDM} = 0.95f'_c c\left\{(r_i^2 - y^2) - \frac{c^2}{3}\right\} + 4F_y tc\frac{r_m^2}{r_i} + 4F_{yb}t_b c_b r_b \tag{2.6f}$$

In both Equations 2.5 and Equations 2.6, P is the axial force and is positive in compression. M and y are also positive as shown, and y—the distance from the centroid to the neutral axis, *N.A.*—ranges from minus r_i to plus r_i. The axial force-moment interaction curve is developed by calculating P and M pairs for each neutral axis location, y, and normalizing by P_0 and M_0, the axial force corresponding to zero moment and the bending moment corresponding to no axial force, respectively. Note that if there is no internal reinforcement present, Equations 2.6 give the same result as Equations 2.5.

2.1.4 *Compressive Strength*

The available compressive strength of short, compact CFTs and RCFTs is given by Equation 2.7.

$$P_0 = A_s F_y + A_{sr} F_{yr} + 0.95A_c f'_c \tag{2.7}$$

2.2 PREVIOUS RESEARCH RESULTS

Few research programs have been performed to investigate the shear resistance of circular, concrete-filled steel tubes. This section reviews the results and conclusions of four experimental programs that employed small-scale CFTs. For axially loaded specimens, the axial load ratio, P/P_0, is reported with P_0 calculated by Equation 2.7. While the results of the WSDOT shear expression are presented for each specimen, only a brief statistical analysis of the AISC shear expressions is presented at the end of the chapter.

2.2.1 *Qian, Cui, and Fang (2007)*

Qian et al. (2007) performed thirty-five tests of circular CFTs to investigate their shear strength. The tests used a three-point bending setup with monotonic loading, as shown in Figure 2.4. The test parameters included shear span to depth ratio, concrete strength, axial force ratio, and tube wall thickness. All the specimens had an outer diameter of 194 mm (7.64 in.) and were outfitted with end-caps, thus severely limiting the potential for differential slip between the concrete fill and the steel tube. Fifteen of the specimens were tested with no axial load. The shear span to depth ratios included in the program varied from 0.1 to 1.0.

The authors reported that twenty-seven specimens failed in shear, three failed in flexure-shear, and five failed in flexure. For specimens with no axial load, shear span to depth ratio had

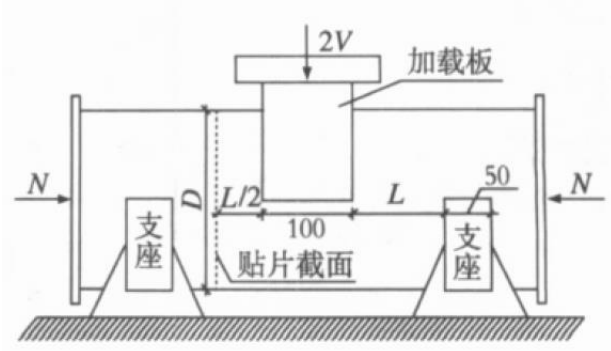

Figure 2.4: Diagram of test rig for Qian et al.

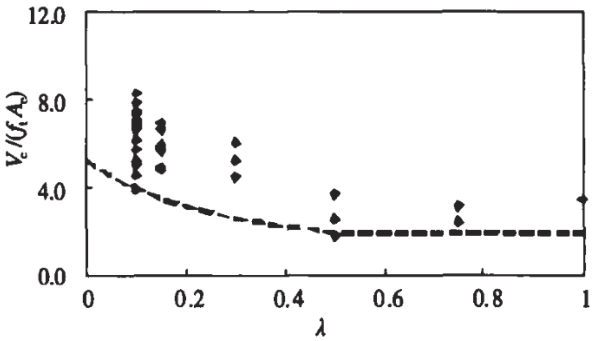

Figure 2.5: Dependence of V_c on a/D for Qian

the largest effect on failure mode; when $a/D \leq 0.3$, the CFT failed in shear; when $a/D = 0.5$, the CFT failed in flexure-shear interaction; and when $a/D \geq 0.75$, the CFT failed in flexure. When axial load was present, specimens with $a/D = 0.75$ also failed in flexure-shear interaction. Table 2.1 shows the specimen properties and the test results of the reported shear failures.

Qian et al. concluded the following:

- CFTs that fail in shear have a large deformation capacity.
- For a/D ratios less than 0.5 the concrete shear strength is dependent upon the shear span to depth ratios, as shown in Figure 2.5.
- The shear strength of the CFT increases with increasing axial load.

Table 2.1: Results for Qian et al.

Specimen	***a* (in)**	***a/D***	***t* (in)**	***D/t***	f_{ym} **(ksi)**	f'_{cm} **(ksi)**	P/P_0	V_{exp} **(kip)**	$V_{n\ (WSDOT)}$ **(kip)**	$V_{exp} / V_{n\ (WSDOT)}$
Q1	0.76	0.100	0.217	35.3	47.9	5.87		286	76	3.78
Q2	0.76	0.100	0.295	25.9	61.2	5.87		289	128	2.26
Q7	1.15	0.150	0.217	35.3	47.9	5.87		439	76	5.81
Q8	1.15	0.150	0.295	25.9	61.2	5.87		458	128	3.58
Q9	0.76	0.100	0.217	35.3	47.9	8.06		501	76	6.57
Q10	0.76	0.100	0.295	25.9	61.2	8.06		283	129	2.20
Q15	1.15	0.150	0.217	35.3	47.9	8.06	0	230	76	3.02
Q16	1.15	0.150	0.295	25.9	61.2	8.06		225	129	1.75
Q17	2.29	0.300	0.295	25.9	61.2	8.06		395	129	3.07
Q28	0.76	0.100	0.217	35.3	47.9	9.79		326	77	4.26
Q29	0.76	0.100	0.295	25.9	61.2	9.79		398	129	3.09
Q34	1.15	0.150	0.217	35.3	47.9	9.79		289	77	3.78
Q35	1.15	0.150	0.295	25.9	61.2	9.79		220	129	1.71
Q3	0.76	0.100	0.217	35.3	47.9	5.87	0.431	281	76	3.72
Q4	0.76	0.100	0.295	25.9	61.2	5.87	0.463	375	128	2.93
Q5	0.76	0.100	0.217	35.3	47.9	5.87	0.719	378	76	5.00
Q6	0.76	0.100	0.295	25.9	61.2	5.87	0.772	409	128	3.20
Q11	0.76	0.100	0.217	35.3	47.9	8.06	0.414	272	76	3.57
Q12	0.76	0.100	0.295	25.9	61.2	8.06	0.446	277	129	2.15
Q13	0.76	0.100	0.217	35.3	47.9	8.06	0.689	336	76	4.41
Q14	0.76	0.100	0.295	25.9	61.2	8.06	0.297	263	129	2.05
Q18	2.29	0.300	0.295	25.9	61.2	8.06	0.446	387	129	3.01
Q19	2.29	0.300	0.217	35.3	47.9	8.06	0.689	391	76	5.13
Q30	0.76	0.100	0.217	35.3	47.9	9.79	0.403	376	77	4.92
Q31	0.76	0.100	0.295	25.9	61.2	9.79	0.435	271	129	2.10
Q32	0.76	0.100	0.217	35.3	47.9	9.79	0.672	226	77	2.95
Q33	0.76	0.100	0.295	25.9	61.2	9.79	0.290	291	129	2.26

2.2.2 *Xu, Haixiao, and Chengkui (2009)*

Xu et al. (2009) investigated the shear behavior of self-stressing circular concrete-filled steel tubes (SSCFTs). They reported test results on thirty-five specimens with diameters ranging from 140 mm (5.5 in.) to 165.5 mm (6.5 in.). Twenty-seven of the specimens were SSCFTs and the remaining eight were standard CFTs. The SSCFTs were filled with an expansive concrete used to counteract the negative effects of concrete shrinkage on the composite behavior of CFTs (i.e. reduced bond capacity) and to investigate potential performance increase resulting from the radial pre-stressing of the section. The CFTs used a conventional concrete. The primary test parameters were the self-stressing and the shear span to depth ratio. The specimens were subjected to a three-point bending test with monotonic loading, as shown in Figure 2.7.

The authors reported thirty-one shear failures and four flexural failures. Only seven of the shear failures contained conventional concrete. Table 2.2 summarizes the specimen properties and the test results of the reported shear failures. None of the specimens were axially loaded.

All but five of the specimens tested had end-caps. Notable differences were observed in the ultimate shear strength and plastic deformation of specimens with and without end-caps. Figure 2.7 shows force-displacement plots of Specimen Sc-2 (Xu12 in the table), with end-caps, and Specimen Uc-2 (Xu25 in the table), without end-caps. Other variable parameters were consistent, and both specimens used expansive concrete.

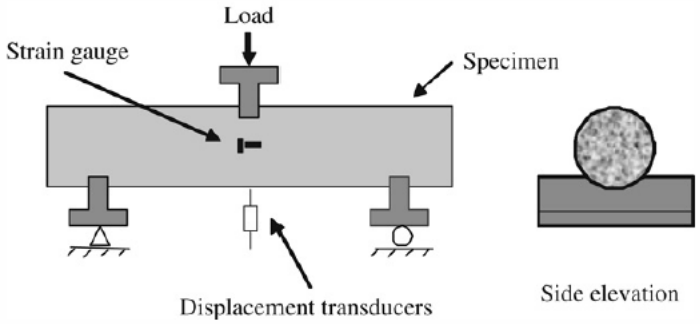

Figure 2.6: Diagram of test rig for Xu et al.

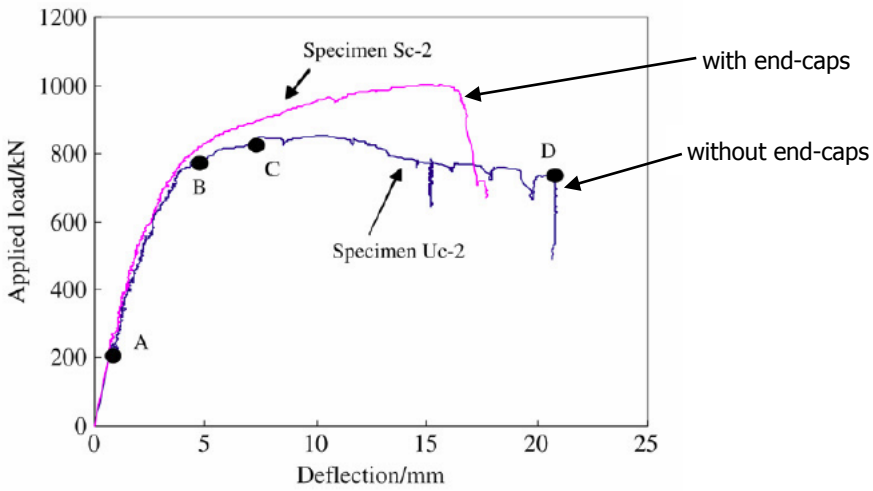

Figure 2.7: Effect of end-caps for Xu et al.

Eight of the specimens used conventional concrete. The CFT specimens had lower ultimate shear capacity and higher ultimate deformation when compared to the SSCFT specimens. Figure 2.8a shows the force-displacement plots two specimens with end-caps: Specimen Sb-2 (Xu7 in the table), with expansive concrete, and Specimen So-2 (Xu17 in the table), with conventional concrete. Figure 2.8b shows the force-displacement plots two specimens without end-caps: Specimen Ub-2 (Xu22 in the table), with expansive concrete, and Specimen Uo-2 (Xu27 in the table), with conventional concrete.

Xu et al. concluded the following:

- CFTs with $a/D < 0.5$ fail in shear.
- CFTs with $0.5 \leq a/D \leq 1.0$ fail in flexure.
- All other test parameters being equal, CFTs with expansive concrete fill have higher shear capacity than CFTs with conventional concrete fill.
- The shear capacity of CFTs with short a/D ratios varies with a/D.
- Relative slip between the concrete core and the steel tube decreases shear capacity.

Table 2.2: Results for Xu et al.

Specimen	a (in)	a/D	t (in)	D/t	f_{ym} (ksi)	f'_{cm} (ksi)	Radial Stress (ksi)	end-cap	V_{exp} (kip)	$V_{n\ (WSDOT)}$ (kip)	V_{exp} / $V_{n\ (WSDOT)}$
Xu16	0.55	0.1	0.145	38	52.8	4.88	0	Yes	40	93	2.31
Xu17	1.1	0.2	0.145	38	52.8	4.88		Yes	40	83	2.07
Xu18	1.65	0.3	0.145	38	52.8	4.88		Yes	40	80	1.99
Xu19	2.76	0.5	0.145	38	52.8	4.88		Yes	40	68	1.70
Xu26	0.55	0.1	0.145	38	52.8	4.88		No	40	88	2.20
Xu27	1.1	0.2	0.145	38	52.8	4.88		No	40	79	1.96
Xu28	1.65	0.3	0.145	38	52.8	4.88		No	40	75	1.87
Xu1	0.55	0.1	0.145	38	52.8	5.19	0.81	Yes	40	104	2.58
Xu2	1.1	0.2	0.145	38	52.8	5.19	0.81	Yes	40	97	2.42
Xu3	1.65	0.3	0.145	38	52.8	5.19	0.81	Yes	40	89	2.22
Xu4	2.76	0.5	0.145	38	52.8	5.19	0.81	Yes	40	69	1.71
Xu6	0.55	0.1	0.145	38	52.8	4.94	0.88	Yes	40	109	2.71
Xu7	1.1	0.2	0.145	38	52.8	4.94	0.88	Yes	40	91	2.25
Xu8	1.65	0.3	0.145	38	52.8	4.94	0.88	Yes	40	84	2.09
Xu9	2.76	0.5	0.145	38	52.8	4.94	0.88	Yes	40	76	1.88
Xu11	0.55	0.1	0.145	38	52.8	5.76	0.99	Yes	40	109	2.71
Xu12	1.1	0.2	0.145	38	52.8	5.76	0.99	Yes	40	100	2.48
Xu13	1.65	0.3	0.145	38	52.8	5.76	0.99	Yes	40	94	2.32
Xu14	2.76	0.5	0.145	38	52.8	5.76	0.99	Yes	40	69	1.72
Xu21	0.55	0.1	0.145	38	52.8	4.94	0.68	No	40	100	2.49
Xu22	1.1	0.2	0.145	38	52.8	4.94	0.68	No	40	88	2.18
Xu23	1.65	0.3	0.145	38	52.8	4.94	0.68	No	40	82	2.05
Xu24	0.55	0.1	0.145	38	52.8	5.76	0.84	No	40	110	2.73
Xu25	1.1	0.2	0.145	38	52.8	5.76	0.84	No	40	92	2.29
Xu29	0.65	0.1	0.117	56	52.8	5.19	0.68	Yes	39	107	2.71
Xu30	1.3	0.2	0.117	56	53.8	5.19	0.68	Yes	40	99	2.48
Xu31	1.95	0.3	0.117	56	53.8	5.19	0.68	Yes	40	91	2.26
Xu32	3.26	0.5	0.117	56	53.8	5.19	0.68	Yes	40	78	1.94
Xu33	0.65	0.1	0.117	56	53.8	5.76	0.75	Yes	40	111	2.77
Xu34	1.3	0.2	0.117	56	53.8	5.76	0.75	Yes	40	94	2.35
Xu35	1.95	0.3	0.117	56	53.8	5.76	0.75	Yes	40	88	2.18

Note: The radial stress is normal to the concrete surface and positive outwards.

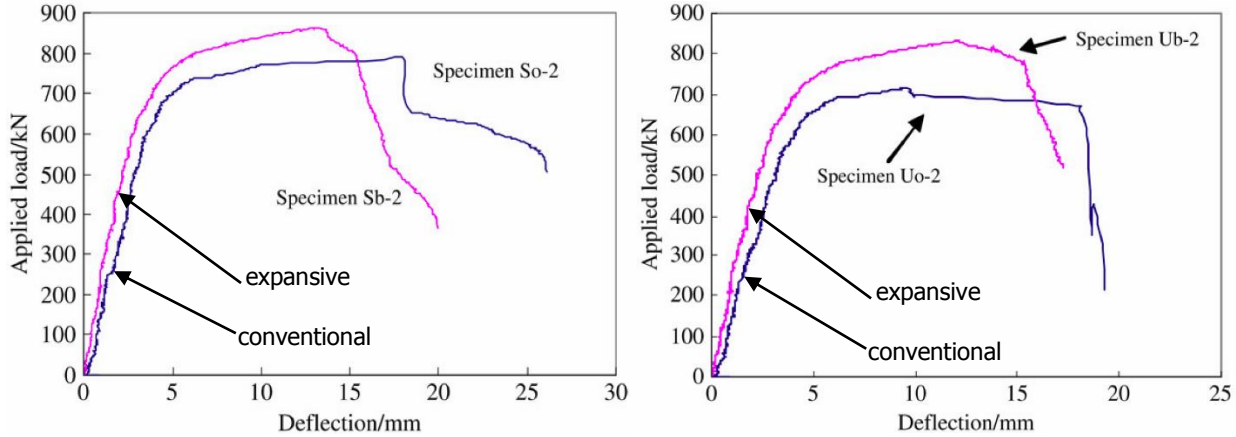

a) with end-caps b) without end-caps

Figure 2.8: Effect of concrete type for Xu et al.

2.2.3 *Xiao, Cai, Chen, and Xu (2012)*

Xiao et al. (2012) investigated the shear capacity, ductility, and damage modes of fifty-eight CFT specimens. The test parameters included tube wall thickness, shear span to depth ratio, concrete strength, and axial compression ratio. The tube diameters ranged from 160 mm (6.3 in.) to 166 mm (6.5 in). They employed a three-point bending rig and monotonically applied loading, as seen in Figure 2.9. Twenty-five specimens had no axial load.

All specimens and were outfitted with welded end-caps. The welds connecting the end-caps to the tubes failed prematurely on three test specimens allowing differential movement between the concrete fill and the steel tube. They are X25, X26, and X27 in the results table and exhibited less ultimate shear strength than comparable specimens with no weld failure. The welds on the remaining test specimens were strengthened to preclude such a failure. Figure 2.10 shows the force-displacement plots for specimens X27 and X28.

The authors reported fifty-one shear failures, three weld failures, two flexure failures and two flexure-shear failures. Table 2.3 summarizes the specimen properties and the test results of the reported shear failures. Flexural failures were indicated by a steel rupture in the tension zone and a uniform pattern of dense, transverse cracks in the concrete fill, both occurring in the middle of the span. Shear failures exhibited large shear deformations between the load and

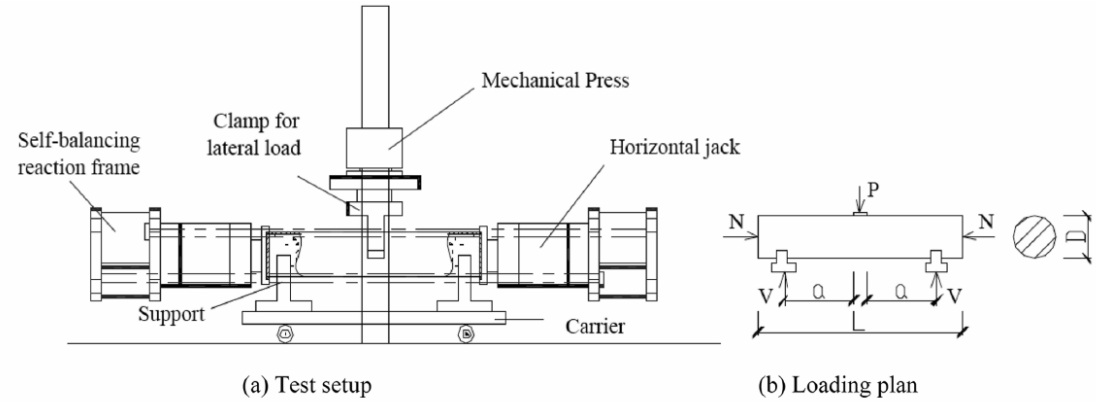

Figure 2.9: Diagram of test rig for Xiao et al.

Table 2.3: Results for Xiao et al.

Specimen	a (in)	a/D	t (in)	D/t	f_{ym} (ksi)	f'_{cm} (ksi)	P/P_0	V_{exp} (kip)	$V_{n\ (WSDOT)}$ (kip)	V_{exp} / $V_{n\ (WSDOT)}$
X1	2.52	0.40	0.217	29.1	54.7	3.76		221	70	3.17
X2	2.52	0.40	0.217	29.1	54.7	4.70		211	70	3.03
X3	2.52	0.40	0.217	29.1	54.7	4.28		209	70	3.00
X4	2.61	0.40	0.173	37.7	50.0	3.76		169	54	3.13
X5	2.61	0.40	0.173	37.7	50.0	4.70		174	54	3.22
X6	2.61	0.40	0.173	37.7	50.0	4.28		168	54	3.11
X7	2.6	0.40	0.118	55.0	59.2	3.76		115	44	2.61
X8	2.6	0.40	0.118	55.0	59.2	4.70		123	44	2.79
X9	2.6	0.40	0.118	55.0	59.2	4.28		118	44	2.68
X25	0.88	0.14	0.217	29.1	54.7	3.76		170	70	2.44
X26	0.88	0.14	0.217	29.1	54.7	4.70	0	174	70	2.49
X27	0.88	0.14	0.217	29.1	54.7	4.28		170	70	2.43
X28	0.88	0.14	0.217	29.1	54.7	4.28		289	70	4.15
X29	0.91	0.14	0.173	37.7	50.0	4.28		225	54	4.18
X30	0.91	0.14	0.118	55.0	59.2	4.28		155	44	3.53
X31	0.91	0.14	0.173	37.7	50.0	3.76		220	54	4.09
X32	0.91	0.14	0.173	37.7	50.0	4.70		220	54	4.07
X33	0.91	0.14	0.173	37.7	50.0	4.28		212	54	3.93
X34	0.91	0.14	0.118	55.0	59.2	3.76		154	44	3.51
X35	0.91	0.14	0.118	55.0	59.2	4.70		157	44	3.55
X36	0.91	0.14	0.118	55.0	59.2	4.28		169	44	3.85
X10	2.52	0.40	0.173	29.1	54.7	3.76	0.31	228	70	3.28
X11	2.52	0.40	0.118	29.1	54.7	4.70	0.30	218	70	3.12
X12	2.52	0.40	0.118	29.1	54.7	4.28	0.30	230	70	3.30
X13	2.61	0.40	0.118	37.7	50.0	3.76	0.30	195	54	3.62
X14	2.61	0.40	0.217	37.7	50.0	4.70	0.29	183	54	3.38
X15	2.61	0.40	0.217	37.7	50.0	4.28	0.29	190	54	3.52
X16	2.6	0.40	0.173	55.0	59.2	3.76	0.30	141	44	3.22
X17	2.6	0.40	0.173	55.0	59.2	4.70	0.28	133	44	3.01
X18	2.6	0.40	0.118	55.0	59.2	4.28	0.28	133	44	3.02
X19	2.52	0.40	0.118	29.1	54.7	3.76	0.62	198	70	2.85
X20	2.52	0.14	0.217	29.1	54.7	4.70	0.60	234	70	3.35
X21	2.61	0.14	0.217	37.7	50.0	3.76	0.61	184	54	3.42
X22	2.61	0.14	0.217	37.7	50.0	4.70	0.58	204	54	3.78
X23	2.6	0.14	0.173	55.0	59.2	3.76	0.60	144	44	3.29
X24	2.6	0.14	0.173	55.0	59.2	4.70	0.56	153	44	3.46
X37	0.88	0.14	0.173	29.1	54.7	3.76	0.31	327	70	4.71
X38	0.88	0.14	0.118	29.1	54.7	4.70	0.30	328	70	4.71
X39	0.88	0.14	0.118	29.1	54.7	4.28	0.30	337	70	4.84
X40	0.91	0.14	0.118	37.7	50.0	3.76	0.30	280	54	5.20
X41	0.91	0.14	0.217	37.7	50.0	4.70	0.29	284	54	5.26
X42	0.91	0.14	0.217	37.7	50.0	4.28	0.29	281	54	5.20
X43	0.91	0.14	0.217	55.0	59.2	3.76	0.30	216	44	4.91
X44	0.91	0.14	0.173	55.0	59.2	4.70	0.28	205	44	4.65
X45	0.91	0.14	0.173	55.0	59.2	4.28	0.28	214	44	4.87
X46	0.88	0.14	0.173	29.1	54.7	3.76	0.62	336	70	4.84
X47	0.88	0.14	0.118	29.1	54.7	4.70	0.60	405	70	5.80
X48	0.88	0.14	0.118	29.1	54.7	4.28	0.60	384	70	5.52
X49	0.91	0.14	0.118	37.7	50.0	3.76	0.61	333	54	6.19
X50	0.91	0.14	0.173	37.7	50.0	4.70	0.58	323	54	5.97
X51	0.91	0.14	0.173	37.7	50.0	4.28	0.58	233	54	4.31
X52	0.91	0.14	0.118	55.0	59.2	3.76	0.60	240	44	5.47
X53	0.91	0.14	0.118	55.0	59.2	4.70	0.56	222	44	5.03
X54	0.91	0.14	0.118	55.0	59.2	4.28	0.56	233	44	5.30

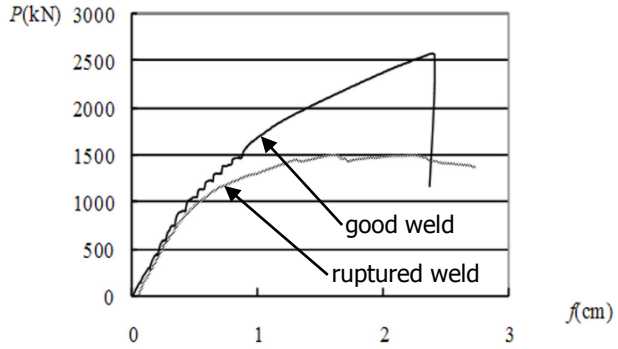

Figure 2.10: Effect of ruptured end-cap weld for Xiao et al.

supports points and the steel tube sheared open at a support. If the steel tube tore at a support, the concrete fill flowed out in powder form, having been crushed. If the steel tube did not tear, the concrete fill contained thin, irregular cracks. For shear failures with a/D = 0.14, the concrete exhibited a direct shear failure. For shear failures with a/D = 0.40, the concrete exhibited diagonal compression failure.

Xiao et al. concluded the following:

- CFTs with small *a/D* ratios, e.g. less than 0.5, fail in shear.
- CFTs with a small *a/D* ratio greater than or equal to 0.5 fail in flexure or flexure-shear.
- The shear capacity of CFTs with small *a/D* ratios varies with *a/D*.
- The shear strength of CFTs increases with increasing axial load.

2.2.4 *Nakahara and Tokuda (2012)*

Nakahara and Tokuda (2012) tested five CFTs subjected to shear loading to investigate their shear capacity and deformation behavior. The steel tubes all had a diameter of either 165 mm (6.5 in.) or 166 mm (6.5 in.) and the shear span to depth ratio was 0.5 for all specimens. They only varied concrete strength and axial load ratio in their experimental program. A double-curvature apparatus was employed as seen in Figure 2.11 and a cyclic shear load was applied. All specimens had end-caps.

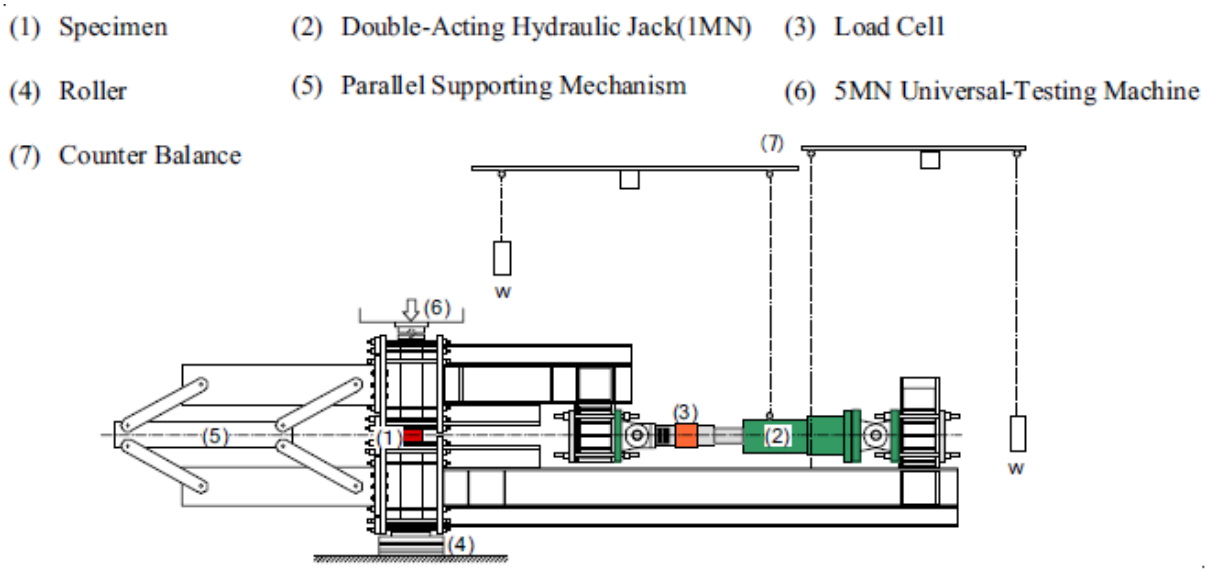

Figure 2.11: Diagram of test rig for Nakahara and Tokuda

The authors reported that all specimens failed in shear. The CFTs without axial load showed a stable but mildly pinched hysteretic response. The tube steel did not tear in any of the tests and they do not discuss the state of the concrete fill at the end of each test. Each CFT was tested until the drift equal 0.04 radians. Table 2.5 summarizes the properties and test results of each of the CFT specimens.

Nakahara and Tokuda concluded the following:

- All specimens failed in shear before flexural yielding occurred.
- The shear strength of the CFTs increased after shear yielding of the steel tube occurred, achieving maximum shear strength at a drift of 0.02 radians followed by stable deterioration until the tests were ended.
- The hysteresis properties of the short CFTs were sufficient to be used as damping devices in seismic regions.
- Low axial load ratios ($P/P_0 \leq 0.4$) increased the shear strength of the CFT. Higher axial load ratios decreased the available shear strength.

Table 2.4: Results for Nakahara and Tokuda

Specimen	a (in)	a/D	t (in)	D/t	f_{ym} (ksi)	f'_{cm} (ksi)	P/P_0	V_{exp} (kip)	$V_{n\ (WSDOT)}$ (kip)	V_{exp} / $V_{n\ (WSDOT)}$
N1	3.27	0.5	0.193	34	77.5	9.34	0	154	92	1.67
N2	3.27	0.5	0.193	34	77.5	9.34	0.3	158	92	1.77
N3	3.25	0.5	0.197	33	78.6	7.03	0.1	152	94	1.65
N4	3.25	0.5	0.197	33	78.6	7.03	0.2	155	94	1.69
N5	3.25	0.5	0.197	33	78.6	7.03	0.4	144	94	1.57

2.3 Comparison of Shear Provisions Using Previous Research Results

The experimental shear for each of the reported shear failures without axial load or expansive concrete was compared to the current shear design expressions, and a brief analysis was provided to assess their validity. The shear resistance was calculated per the current expressions for each of the thirty-nine specimens. The experimental shears were normalized by those capacities, and the results are summarized in Tables 2.5, 2.6, and 2.7. The current design expressions are extremely conservative. AISC Method 3 without shear reinforcement is the same as Method 1.

Table 2.5: Results for WSDOT without axial load or expansive concrete

Research Program	V_{exp} / $V_{n\ (WSDOT)}$						
	# of tests	Mean	Median	Min	Max	Std. Dev.	C.O.V.
Qian et al.	13	3.42	3.09	1.71	6.57	1.27	0.37
Xu et al.	7	2.01	1.99	1.70	2.31	0.21	0.10
Xiao et al.	18	3.42	3.37	2.61	4.18	0.52	0.15
Nakahara and Tokuda	1	1.67	1.67	1.67	1.67	N/A	N/A
All Specimens	39	3.28	3.07	1.53	6.57	1.21	0.37

Table 2.6: Results for AISC Method 1 without axial load or expansive concrete

Research Program	V_{exp} / $V_{n\ (AISC\_1)}$						
	# of tests	Mean	Median	Min	Max	Std. Dev.	C.O.V.
Qian et al.	13	3.60	3.19	1.76	6.91	1.55	0.43
Xu et al.	7	2.09	2.11	1.76	2.40	0.27	0.13
Xiao et al.	18	3.56	3.51	2.73	4.34	0.54	0.15
Nakahara and Tokuda	1	1.73	1.73	1.73	1.73	N/A	N/A
All Specimens	39	3.37	3.24	1.76	6.91	1.11	0.33

Table 2.7: Results for AISC Method 2 without axial load or expansive concrete

Research Program	V_{exp} / $V_{n\ (AISC\_2)}$						
	# of tests	Mean	Median	Min	Max	Std. Dev.	C.O.V.
Qian et al.	13	48.2	45.7	28.0	76.6	13.6	0.29
Xu et al.	7	27.1	27.2	22.8	31.1	3.42	0.13
Xiao et al.	18	43.3	40.1	27.1	71.2	11.6	0.27
Nakahara and Tokuda	1	26.8	26.8	26.8	26.8	N/A	N/A
All Specimens	39	42.9	39.8	22.8	76.6	14.0	0.33

Chapter 3. EXPERIMENTAL PROGRAM

The purpose of the experimental program was to investigate the available shear strength and deformation characteristics of concrete-filled steel tubes (CFTs) and reinforced concrete-filled steel tubes (RCFTs), and to assess the impact of various parameters on the strength and deformation behavior. The parameters to be studied were:

- the shear span to depth ratio (*a/D*)
- the length of the tube extending beyond the support, or tail length (L_T)
- the presence of internal reinforcement (ρ_{int})
- the condition of the interface between the steel tube and the concrete fill
- the axial load ratio (P/P_0)
- the concrete strength
- the tube-diameter-to-wall-thickness ratio (D/t)
- the steel strength to concrete strength ratio

3.1 EXPERIMENTAL TEST APPARATUS

Several apparatus configurations were analyzed in the *Abaqus* finite element analysis program to determine how to efficiently and accurately test the shear resistance of the circular CFTs. Possible configurations included a double curvature rig, a three-point bending rig, and a four-point bending rig. Previous research had used small-scale CFTs, ranging from 4 in. to 8 in. in diameter, and either three-point bending (Qian et al. 2007; Xiao et al. 2012; Xu et al. 2009) or a double curvature setup (Nakahara and Tokuda 2012). Due to the desire to use large-scale CFTs, a double curvature rig was unrealistic given the high strengths and stiffnesses required to impose the moment and shear demands on the CFTs. While there are many similiarities between the

three- and four-point bending configurations, the four-point bending scheme was chosen for the following reasons:

- The pure bending moment region at the center span would allow for clearer distinction between flexural and flexure-shear failures.
- The maximum shear demand during testing was expected to reach 800 – 900 kips, resulting in high bearing forces at the support and load cradles and requiring a large thickness for the cradles. The single load cradle in the three-point configuration would have been unreasonably large and disturbed the load region more than required.
- Any flexural buckling was expected to occur within the pure bending moment region, thus allowing the concrete to remain confined by the steel in the shear spans; this only affected the specimens that failed due to flexure-shear interaction or flexure.

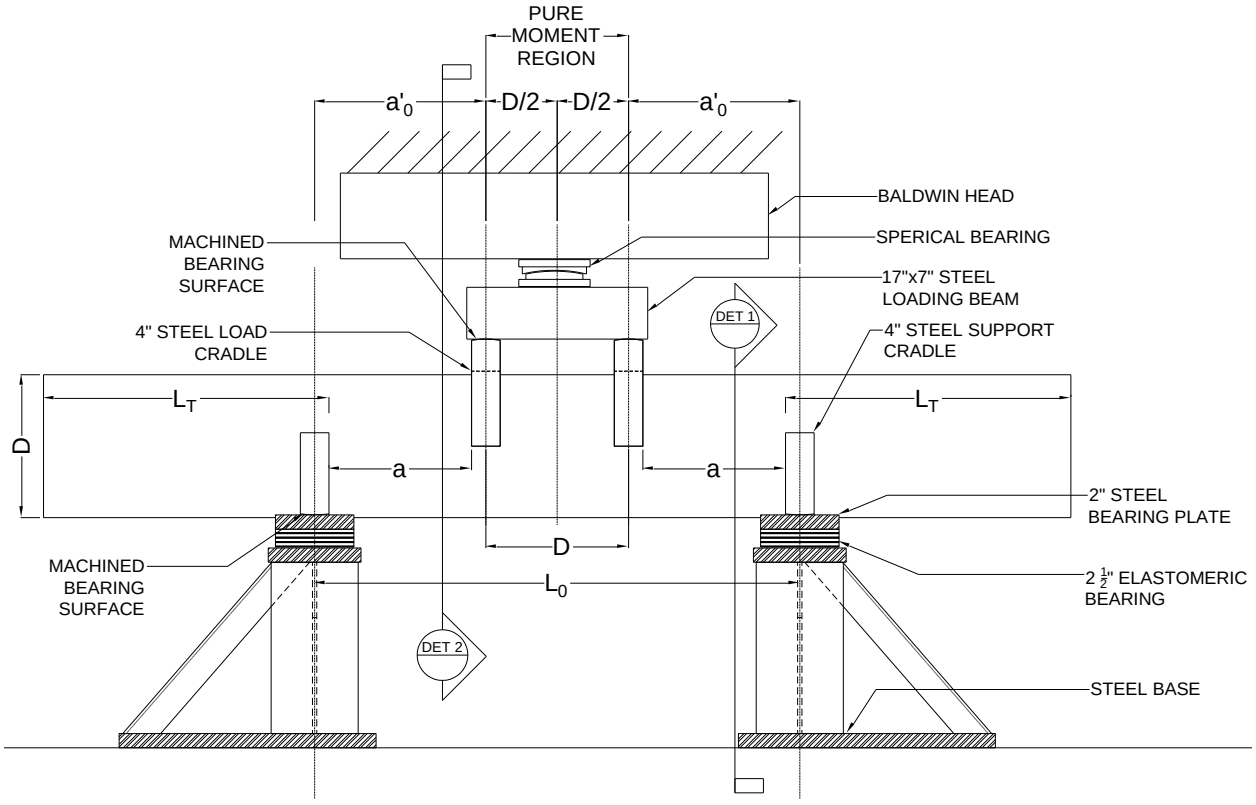

Figure 3.1: Experimental apparatus schematic

Figures 3.1, 3.2, and 3.3 show the test apparatus. The variables in the figures are defined as follows:

- a is the shear span
- a'_0 is the initial center-to-center distance from support cradle to load cradle and is used as the distance between the load resultant force and the support resultant force for equilibrium
- D is the outer diameter of the steel tube
- L_0 is the initial center-to-center span from support to support
- L_T is the tail length

While the actual shear capacity of circular CFTs and RCFTs is not well known, Bishop (2009) found that the mean flexural capacity from several CFT research programs was 123% of the plastic moment calculated by the plastic stress distribution method, $M_{p,PSDM}$. The apparatus was thus designed to accommodate $V_{pr,\,M_{p,PSDM}}$, the shear force corresponding to the development of 125% of $M_{p,PSDM}$ for most of the specimens. It was expected that some of the specimens—those that failed in flexure—would reach this shear force while the other specimens would fail in shear before reaching $V_{pr,\,M_{p,PSDM}}$,. The maximum probable applied force in the experimental program was expected to be on the order of 1,800 kips. The magnitude of the load necessitated the use of the 2.4 million pound Baldwin hydraulic test machine in the structures laboratory at the University of Washington.

The preliminary *Abaqus* analyses showed significant deformations throughout each specimen. All specimens showed substantial rotations at the load and support cradles. The flexure and flexure-shear specimens showed large longitudinal strains at the bottom of the tube

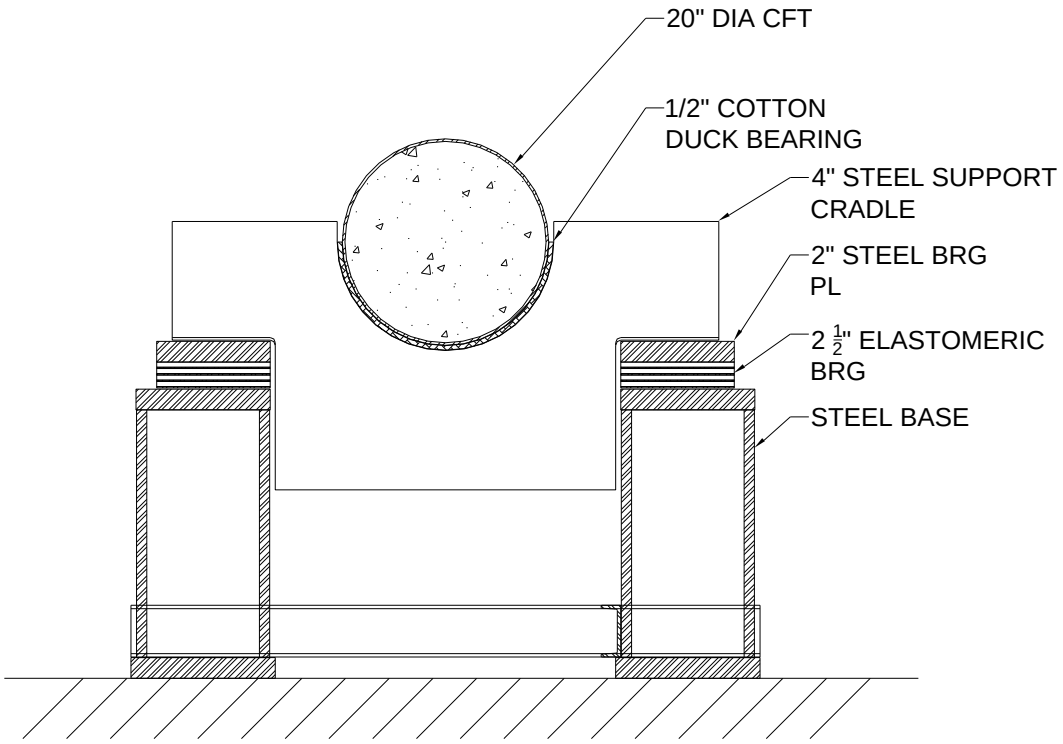

Figure 3.2: Apparatus detail 1

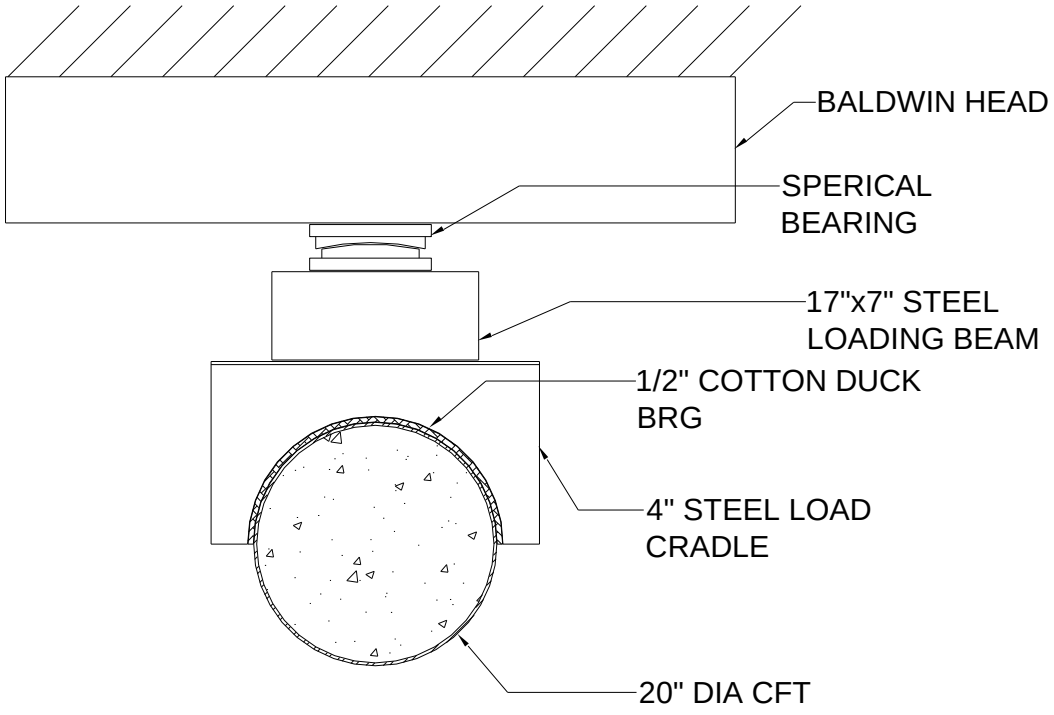

Figure 3.3: Apparatus detail 2

and flexural buckling in the pure moment region. In many cases, planes did not remain plane and perpendicular to the neutral axis.

The longitudinal strains along the bottom of the tube predicted a maximum longitudinal displacement of the support cradles of 3 – 4 in. at each end of the tube. The straining could result in a longitudinal extension of the bottom part of the specimen of 6 – 8 in. The extension, in turn, could exert significant horizontal forces on the apparatus or cause high restraint forces to be applied to the specimens. Elastomeric bearings were employed to allow the longitudinal extension without providing additional horizontal restraint. Force-deflection plots of the elastomeric bearing are included in Appendix H.

The localized bearing stresses were anticipated to be quite high for some of the specimens, due to both the available bearing area and the expected rotation of the CFTs at the load and support cradles. It was also desired to reduce the cutting effect produced by the sharp edge of the cradles and the hihg local shearing stresses. To mitigate some of these local effects of the boundary conditions, a radius was cut on the bearing surfaces of the cradles so they would rotate to remain perpendicular to the CFTs. Cotton duck bearing pads were also used between the CFTs and the cradles to smooth the bearing stresses and allow some differential rotation if needed.

Figure 3.4 shows the test apparatus before testing Specimen 4. Figure 3.5 shows the elastomertic bearing displacement near the end of the test for Specimen 8. Appendix B shows detailed drawings and images of the test setup.

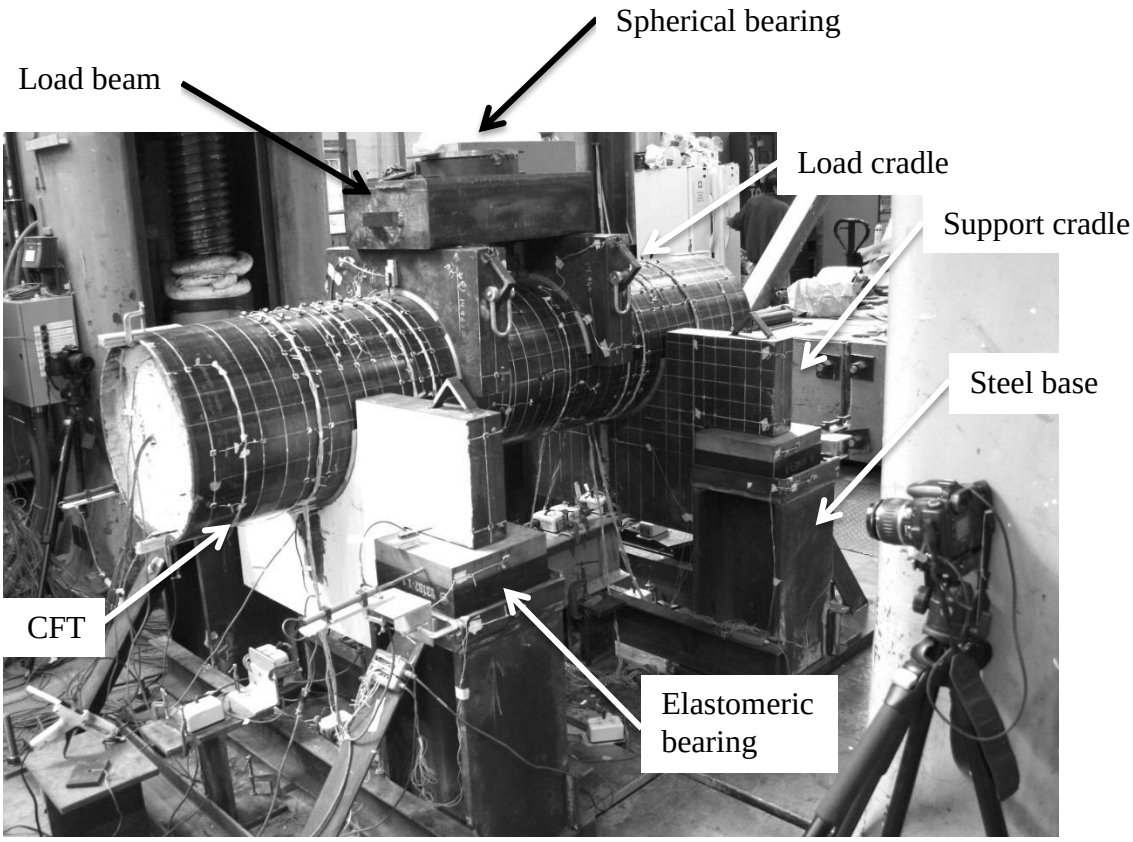

Figure 3.4: Test apparatus

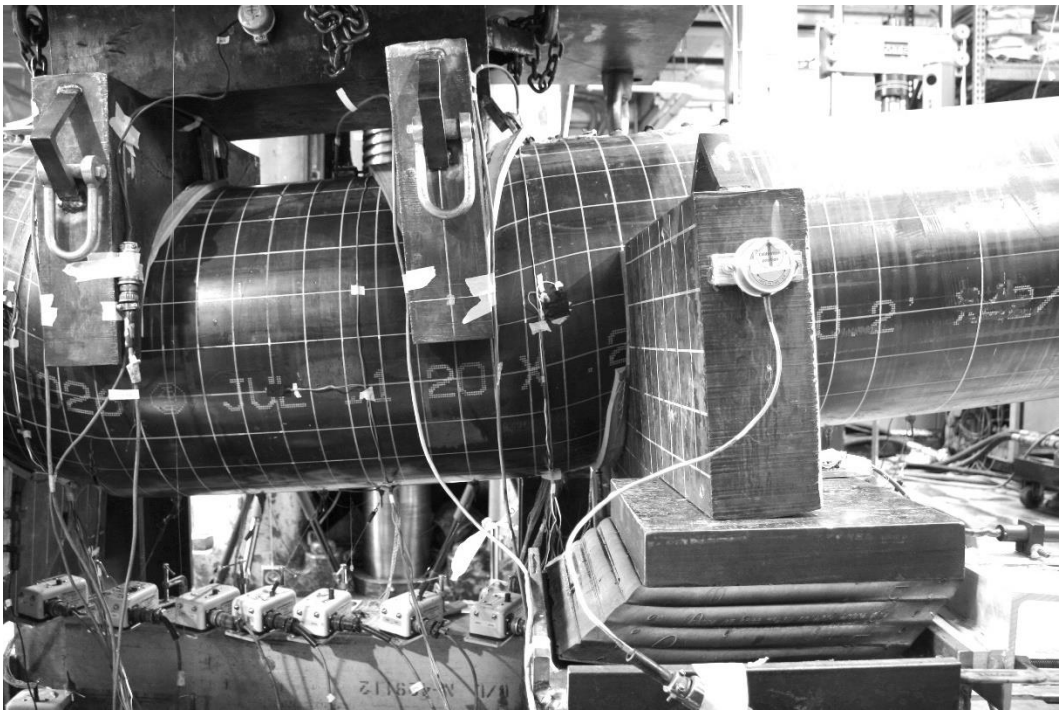

Figure 3.5: Typical elastomeric bearing displacement

3.2 TEST MATRIX

The test parameters were varied to create different series in order to study their effects on CFT behavior. The parameters and potential effects on CFT behavior are discussed in this section. The different series are tabulated in Section 5.2 where the results are discussed. Twenty two specimens were chosen for the program and are detailed in the test matrix in Table 3.1 and arranged by shear span to depth ratio. The moment capacities, $M_{p,PSDM}$, of each specimen based on nominal and measured material strengths are found in Table 3.3 accompanied by $V_{pr,\ M_{p,PSDM}}$ – the shear force required to reach 125% of $M_{p,PSDM}$. Table 3.4 compares the expected maximum shear force with the calculated shear capacity per the WSDOT design expression. All specimens

Table 3.1: Test matrix

Specimen	D (in)	t (in)	a (in)	D/t	*a/D*	f_y (ksi)	f'_c (ksi)	P/P0	LT	ρint	Interface
1	20	0.25	20.0	80	1.0	42	6.0	0%	2D	0%	Clean
22	20	0.25	20.0	80	1.0	70	10.0	0%	4D	0%	Spiral
2	20	0.25	10.0	80	0.5	42	6.0	0%	2D	0%	Clean
3	20	0.25	10.0	80	0.5	42	6.0	0%	D/2	0%	Clean
4	20	0.25	10.0	80	0.5	42	6.0	0%	D	0%	Clean
5	20	0.25	10.0	80	0.5	42	6.0	0%	2D	0%	Muddy
6	20	0.25	10.0	80	0.5	70	6.0	0%	2D	0%	Spiral
9	20	0.25	10.0	80	0.5	42	6.0	0%	2D	0%	Greased
12	20	0.25	10.0	80	0.5	42	6.0	0%	2D	1.13%	Clean
17	20	0.25	10.0	80	0.5	42	12.0	0%	2D	0%	Clean
18	20	0.375	10.0	53.3	0.5	42	12.0	0%	2D	0%	Clean
19	20	0.375	10.0	53.3	0.5	42	12.0	0%	2D	1.07%	Clean
7	20	0.25	7.5	80	0.375	42	6.0	0%	2D	1.04%	Clean
8	20	0.25	7.5	80	0.375	42	6.0	0%	2D	2.01%	Clean
10	**20**	**0.25**	**7.5**	**80**	**0.375**	**42**	**6.0**	**0%**	**2D**	**0%**	**Clean**
11	20	0.25	7.5	80	0.375	42	6.0	0%	D/2	0%	Clean
13	20	0.25	7.5	80	0.375	42	6.0	8.5%	D/2	0%	Clean
16	20	0.25	7.5	80	0.375	42	12.0	0%	2D	0%	Clean
21	20	0.25	7.5	80	0.375	42	0	0%	2D	0%	Clean
14	20	0.25	5.0	80	0.25	42	12.0	0%	2D	0%	Clean
15	20	0.25	5.0	80	0.25	42	12.0	0%	D/2	0%	Clean
20	20	0.25	5.0	80	0.25	42	2.5	0%	2D	0%	Clean

Notes: 1) Specimen 10 was the baseline test. While not all specimens will be compared to it, test parameters that vary from those of specimen 10 are highlighted.
2) All specimens used straight-seam steel tubes unless noted otherwise.
3) All tube steel conformed to both API 5L X42 and ASTM A53B, except Specimens 6 and 22 which conformed to ASTM A1011 HSLAS Gr 70 C1/C2.

are expected to fail in shear before they reach their full plastic moment capacity according to the WSDOT expressions.

3.2.1 *Shear Span to Depth Ratio*

Previous research has shown that shear spans need to be quite short to induce shear failure in circular CFTs (Xu et al. 2009; Qian et al. 2007; Xiao et al. 2012). The *a/D* ratio was varied to capture a transition from flexural failure to flexure-shear failure to shear failure. The series included Specimens 1, 2, 10, 14, 16, 17, 20, and 21.

3.2.2 *Tail Length*

Composite action in CFTs requires stress continuity across the concrete-steel interface or some other way of transferring forces between components. Most shear tests of CFTs without axial load have used end-caps, but this does not allow for relative movement of the steel tube and concrete fill. The tail length would be used to determine if end conditions, where the shear force is high, affect shear strength and behavior. The series included Specimens 2, 3, 4, 6, 10, 11, 13, 14, and 15.

3.2.3 *Internal Reinforcement Ratio*

Internal reinforcement can be used in CFTs and can often be found where they connect to other structural components such as a pile cap or reinforced concrete column. Longitudinal reinforcement increases the shear capacity of reinforced concrete members without shear reinforcement, in part by restraining diagonal crack widths (ACI 2014). Its effect on flexural capacity, however, is larger than its effect on shear capacity and could potentially change the CFT failure mode at a given shear span from flexure to shear or flexure-shear. The series included Specimens 2, 12, 19, 10, 7, and 8.

3.2.4 *Interface Condition*

The condition of the interface affects the bond action needed for composite behavior. CFTs are often used as piles and can be coated on their interior surface with mud and dirt, potentially reducing bond. The surface conditions studied were 1) clean, straight-seam; 2) muddy, straight-seam; 3) greased, straight-seam; and 4) clean, spiral-welded. The series included Specimens 2, 5, 6, and 9.

3.2.5 *Axial Load*

While a compressive axial load increases the shear capacity of concrete, the same is not true for steel. The effect of axial compression on the shear resistance of CFTs should be quantified because they are most often used as columns or piles, which are axially loaded in compression. The series included Specimens 10, 11, and 13.

3.2.6 *Concrete Strength*

Self-consolidating or low-shrinkage concretes are seldom used in deep foundations for cost reasons. A conventional concrete was employed with various compressive strengths to differentiate the distinct contributions of the steel and concrete to the shear resistance of the CFTs. The series included Specimens 2, 17, 10, 16, 21, 14, and 20.

3.2.7 *Tube-Diameter-to-Wall-Thickness Ratio*

The D/t ratio affects local stability of CFTs under axial and flexural loading conditions (Moon et al. 2012; Brown et al. 2015) and bond stress transfer (Roeder et al. 2009). While local stability was not expected to influence the shear resistance of the CFTs, as the concrete fill restrains shear

buckling, the bond stress transfer was likely to play a key role. The D/t ratio was varied to study this and any other unexpected effect. The series included Specimens 2, 18, 12, and 19.

3.2.8 *Steel Strength to Concrete Strength Ratio*

In composite sections, the strength and stiffness ratios of the steel to the concrete can influence section behavior. The ratio was studied to determine any effect it may have. The series included Specimens 2, 6, 17, 10, 16, 14, and 20.

3.3 MATERIAL PROPERTIES

Two types of steel tube were used in the experimental program. Twenty of the tests were performed using a dual-specification, mild steel tube conforming to API 5L X42 and ASTM A53B. The other steel tube was spirally welded from ASTM A1011 HSLAS Gr 70 C1/C2 coil steel using a double submerged arc weld. Specimens 6 and 22 were tested using the higher strength steel tube. The steel tube for Specimen 22 was galvanized and filled with a high-strength, self-consolidating, low-shrinkage concrete mix with a 28-day design strength of 10,000 psi. It was previously fabricated for use in a different research program (Thody 2006) and was used to validate the testing apparatus and procedure. Specimen 6 used the same ungalvanized steel tube and was filled with concrete as part of the current testing program. The reinforcing bar used in the four RCFTs conformed to either ASTM A615 Gr 60 or ASTM A706 Gr 60.

Coupons were cut from each 40 foot length of steel tube and tension tested until failure on a 110 kip MTS testing machine. The stress-strain plots for each is included in Appendix F. Three concrete design mixes were used in the testing program. All three mixes utilized normal weight aggregate and were neither self-consolidating nor low-shrinkage mixes. The mix designs were scanned and included in Appendix G. Standard 6 in. diameter by 12 in. long cylinders were

prepared at each casting date and tested in compression until failure. Samples were cut from at least two reinforcing bars in each RCFT specimen and tested in tension until failure on a 300 kip Baldwin UTM. Table 3.2 shows the nominal yield and specified compressive strengths in addition to the results of the steel tube and concrete strength tests for each specimen. Table 3.4 shows nominal yield strength and the results of the reinforcing bar tension tests.

The concrete used in the third casting had a 28-day specified strength of 12,000 psi, but the test cylinders resulted in much lower strengths than expected. The cylinders for two of the CFTs, Specimens 17 and 19, had test results that varied significantly from the rest in the casting

Table 3.2: CFT material properties

Specimen	Steel Tube				Concrete Fill				
	Tube ID	f_y (ksi)	f_{ym} (ksi)	f_{um} (ksi)	Mix ID	f'_c (psi)	f'_{cm} (psi)	f_{tm} (psi)	Age (days)
1	SS-1	42	49.6	61.0	563375	6000	6012	630	22
2	SS-1	42	49.6	61.0	563375	6000	6220	561	31
3	SS-2	42	50.1	61.0	563375	6000	6655	554	45
4	SS-2	42	50.1	61.0	563375	6000	6558	N/A	59
5	SS-1	42	49.6	61.0	563375	6000	7041	704	101
6	SW-1	70	70.8	83.5	563375	6000	7182	554	115
7	SS-2	42	50.1	61.0	563375	6000	6447	704	50
8	SS-3	42	53.9	66.1	563375	6000	6484	552	56
9	SS-2	42	50.1	61.0	563375	6000	6317	506	33
10	SS-3	42	53.9	66.1	563375	6000	6151	608	42
11	SS-4	42	56.8	66.4	563375	6000	6609	645	47
12	SS-3	42	53.9	66.1	563375	6000	6177	592	28
13	SS-3	42	53.9	66.1	563375	6000	5326	570	64
14	SS-6	42	55.4	71.3	880378X	12000	8596	694	41
15	SS-6	42	55.4	71.3	880378X	12000	8792	796	47
16	SS-4	42	56.8	66.4	880378X	12000	8609	737	34
17	SS-6	42	55.4	71.3	880378X	12000	9450	753	50
18	SS-5	42	57.2	70.2	880378X	12000	8641	760	54
19	SS-5	42	57.2	70.2	880378X	12000	9131	706	56
20	SS-4	42	56.8	66.4	3051	2500	2787	347	37
21	SS-4	42	56.8	66.4	N/A	0	0	0	N/A
22	N/A	70	75.6	84.8	N/A	10000	13000	N/A	N/A

Table 3.3: CFT rebar properties

Specimen	Reinforcing Steel			
	ASTM Spec	f_y (ksi)	f_{ym} (ksi)	f_{um} (ksi)
7	A615	60	72.3	107.8
8	A706	60	68.4	96.7
12	A615	60	71.5	107.6
19	A706	60	68.5	98.4

Table 3.4: Calculated moment capacities and maximum expected shear demands

Specimen	Nominal Material Strengths		Measured Material Strengths	
	$M_{p,PSDM}$ (kip-in)	$V_{pr,\ M_{p,PSDM}}$ (kip)	$M_{p,PSDM}$ (kip-in)	$V_{pr,\ M_{p,PSDM}}$ (kip)
1	5203	271	6069	316
2	5203	465	6085	546
3	5203	465	6174	551
4	5203	465	6167	551
5	5203	465	6143	549
6	8326	743	8533	762
7	6342	689	7524	818
8	7350	800	9016	980
9	5203	465	6149	549
10	5203	566	6564	719
11	5203	566	6926	753
12	6441	575	8019	716
13	6211	675	7362	800
14	5452	757	6910	960
15	5452	757	6922	961
16	5452	593	7069	768
17	5452	487	6958	621
18	7817	698	10165	908
19	8902	795	11434	1021
20	4846	673	6451	896
21	4096	445	5539	602
22	8672	452	9495	495

Table 3.5: Comparison of maximum expected shears and WSDOT shear capacity

Specimen	Nominal Material Strengths			Measured Material Strengths		
	$V_{pr,\ M_{p,PSDM}}$ (kip)	$V_{n\ (WSDOT)}$ (kip)	V_{pr} / V_n	$V_{pr,\ M_{p,PSDM}}$ (kip)	$V_{n\ (WSDOT)}$ (kip)	V_{pr} / V_n
1	271	219	1.24	316	254	1.24
2	465	219	2.13	546	254	2.14
3	465	219	2.13	551	258	2.14
4	465	219	2.13	551	257	2.14
5	465	219	2.13	549	256	2.14
6	743	349	2.13	762	355	2.15
7	689	218	3.16	818	257	3.18
8	800	218	3.67	980	274	3.57
9	465	219	2.13	549	257	2.14
10	566	219	2.59	719	274	2.60
11	566	219	2.59	753	289	2.61
12	575	218	2.63	716	274	2.61
13	675	219	3.09	800	273	2.93
14	757	228	3.32	960	286	3.36
15	757	228	3.32	961	286	3.36
16	593	228	2.60	768	292	2.63
17	487	228	2.13	621	287	2.16
18	698	323	2.16	908	424	2.14
19	795	323	2.46	1021	424	2.41
20	673	210	3.20	896	280	3.20
21	445	195	2.28	602	264	2.28
22	452	356	1.27	495	386	1.28

Table 3.6: Concrete core strengths

Specimen	Location	Age (days)	f'_{cm} (psi)	$f'_{cm}/0.85$ (psi)	Potential overstrength
17	south	103	10302	12120	1.23
17	south	103	9973	11733	1.19
17	north	103	10570	12436	1.26
18	south	103	10972	12908	1.31
cylinder	N/A	104	9838	N/A	N/A

group, indicating that something other than weaker-than-expected concrete might be happening. It is possible that there was an issue in the curing process that reduced the strength of the cylinders such that they did not accurately represent the concrete strength in the CFTs. A total of four cores were drilled, three from Specimen 17 and one from Specimen 18, and tested at an age of 103 days to verify the in situ strength of the concrete. An additional 6 in. x 12 in. cylinder was tested for comparison. According to ACI 318 (2014), it is realistic to expect the strength of core tests to be about 85% of the specified strength due to size differences in specimens and the core drilling process. The results of the core testing are shown in Table 3.6 and the average potential overstrength is 125% of a cylinder at the same age. The results from the cylinder tests will be used throughout the analysis, but the actual compressive strength in the CFTs was likely higher than reported.

3.4 Specimen Instrumentation

3.4.1 *External Instrumentation*

TML steel strain gauges were employed on each specimen to measure local steel strains. Single element gauges were employed at mid-span and at the top and bottom of the shear spans for the shorter shear span to depth ratios of 0.375 and 0.25, to develop strain profiles. Three-element rosettes were employed at the center of the shear spans on each side of the steel tube. Unimeasure cable linear position transducers, Duncan linear potentiometers, and inclinometers were used on each specimen and on the apparatus to measure displacements. The strain gauges

were only capable of measuring small strains, so a non-contact motion capture system, the NDI Optotrak Certus system, was used to capture displacement at over 130 discrete locations. These displacements can be used to calculate large strains throughout each test and allow further validation of future analytical models. A grid was drawn on each specimen to aid in the visualization and understanding of the deformation patterns and to provide discrete locations for the Optotrak targets. Figures 3.6 and 3.7 show the grid and instrumentation elements that are common to all specimens. Figures 3.8 - 3.11 show the external instrumentation layout specific to each *a/D* ratio. Figures 3.12 - 3.15 show the non-contact instrumentation specific to each *a/D* ratio.

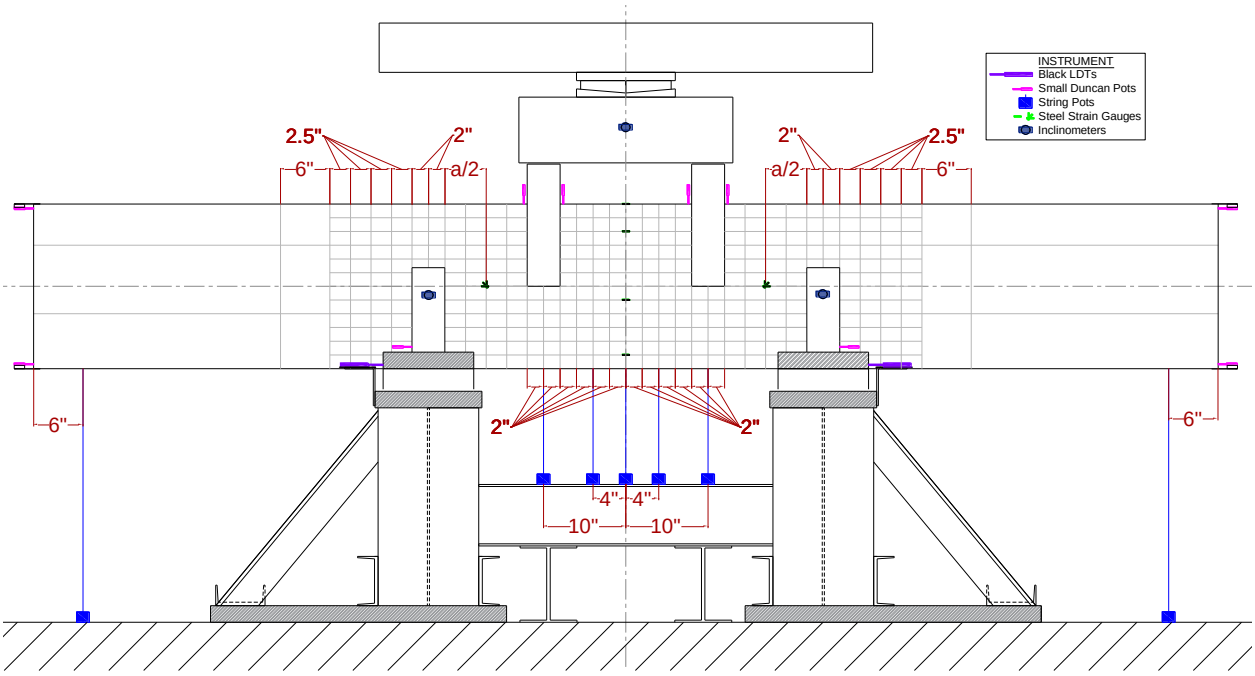

Figure 3.6: Contact instrumentation and grid layout common to all specimens

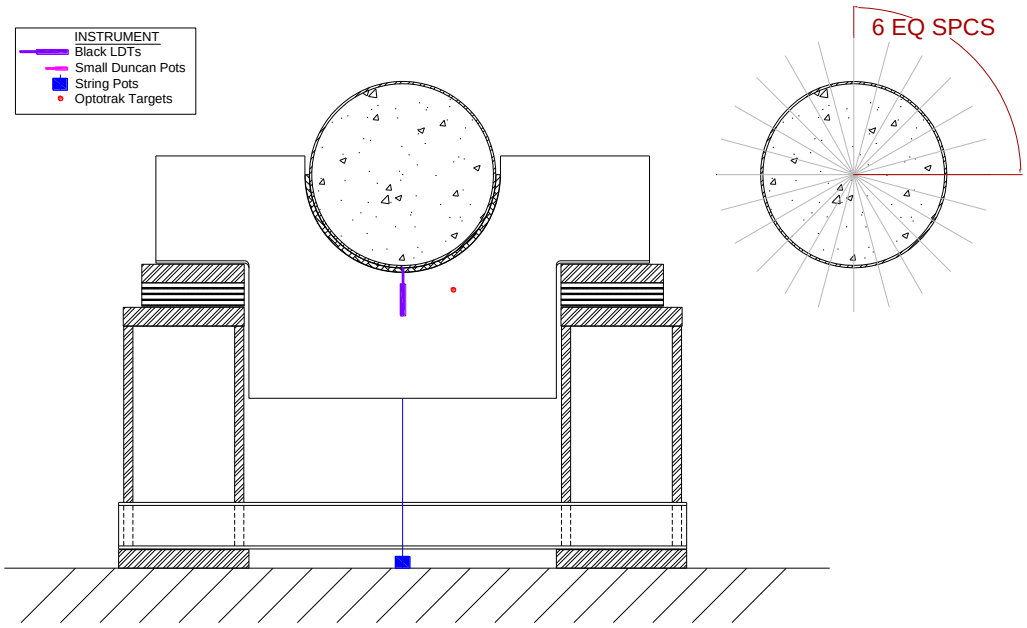

Figure 3.7: Instrumentation and grid layout common to all specimens (end view)

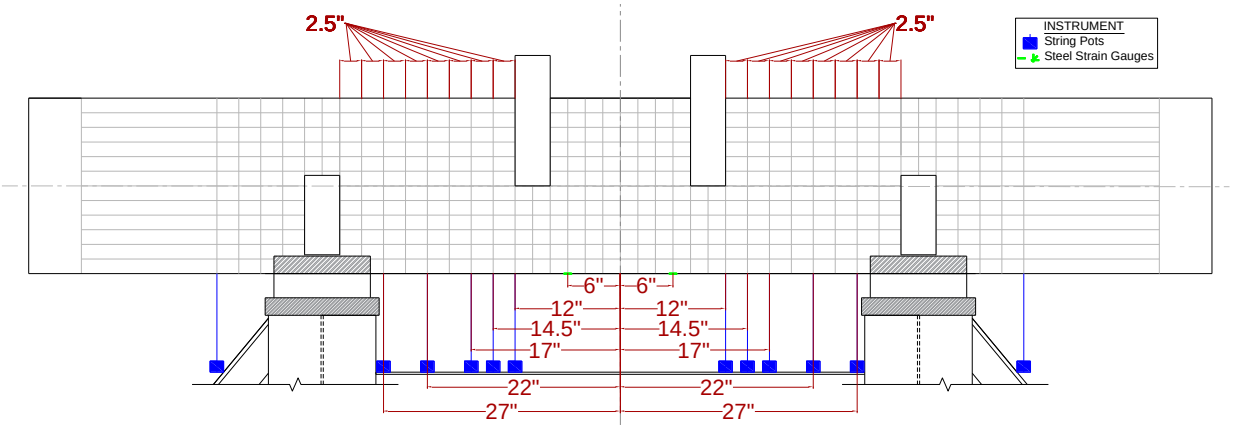

Figure 3.8: Contact instrumentation and grid layout specific to *a/D*=1.0

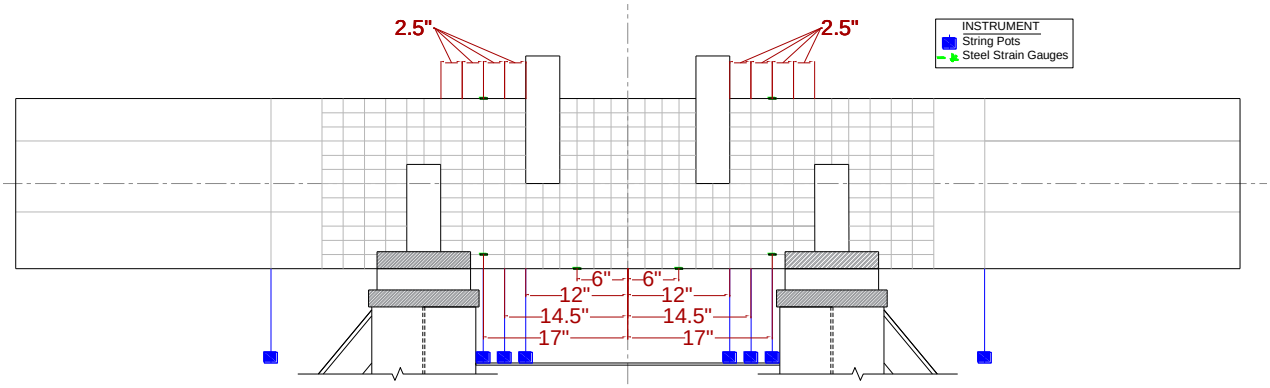

Figure 3.9: Contact instrumentation and grid layout specific to *a/D*=0.5

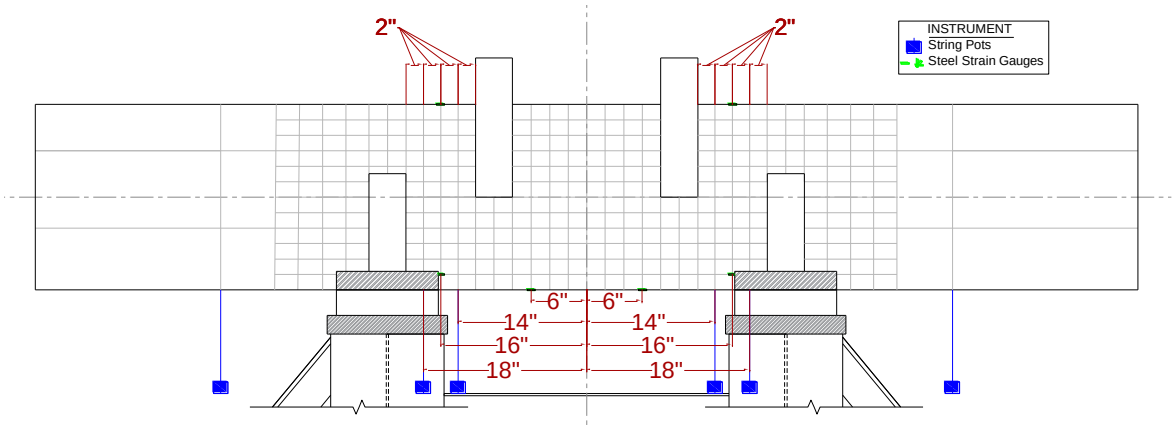

Figure 3.10: Contact instrumentation and grid layout specific to *a/D*=0.375

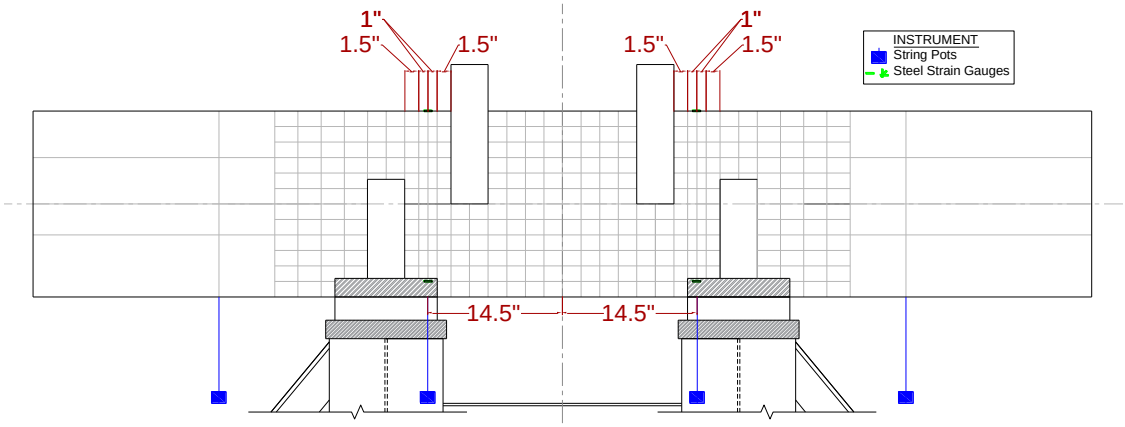

Figure 3.11: Contact instrumentation and grid layout specific to *a/D*=0.25

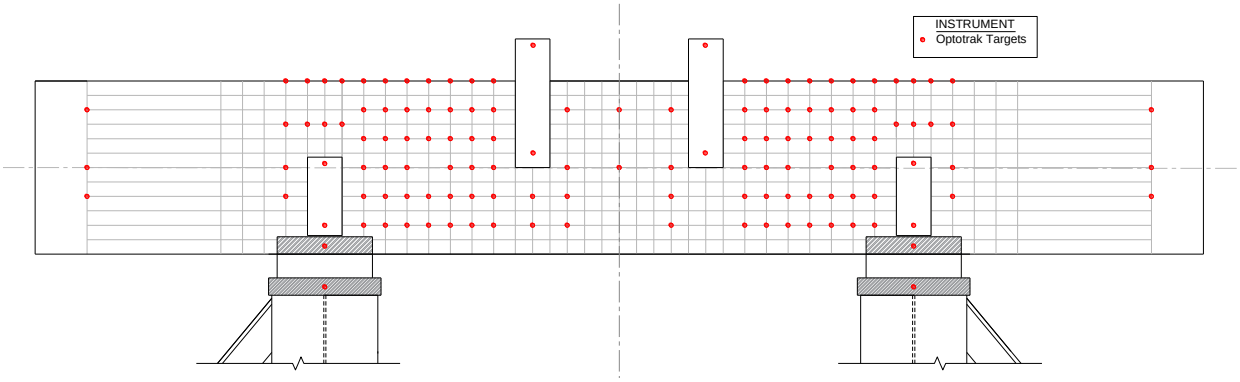

Figure 3.12: Non-contact instrumentation layout specific to *a/D*=1.0

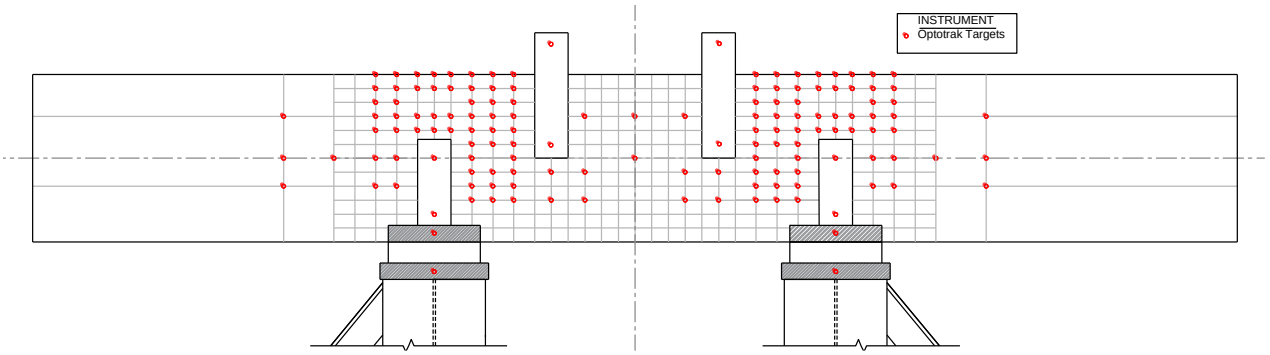

Figure 3.13: Non-contact instrumentation layout specific to *a/D*=0.5

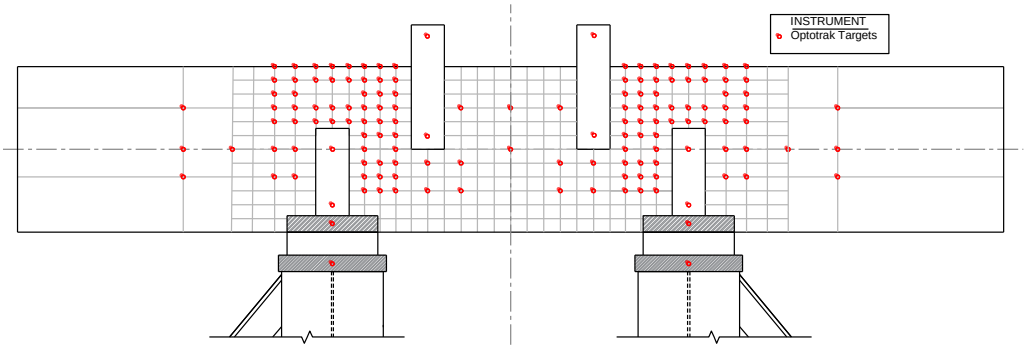

Figure 3.14: Non-contact instrumentation layout specific to *a/D*=0.375

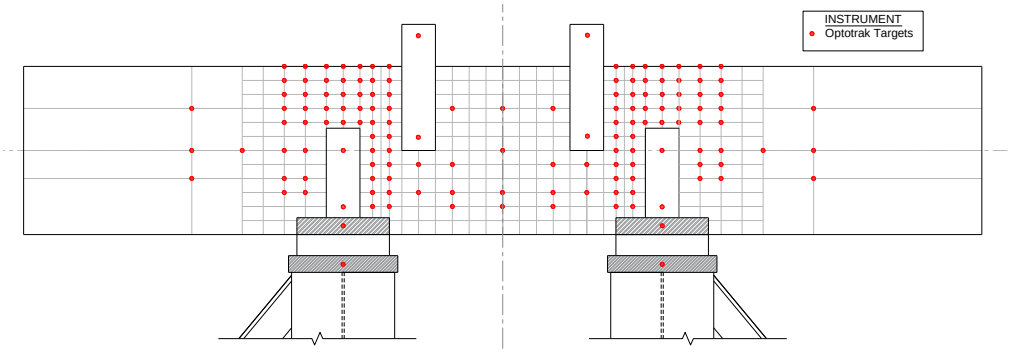

Figure 3.15: Non-contact instrumentation layout specific to *a/D*=0.25

3.4.2 *Internal Instrumentation*

Geokon vibrating wire strain gauges were placed in several CFTs before the concrete was cast to better understand the concrete strain behavior at discrete locations. They were primarily employed in the shear spans, with some gauges placed at mid-span. The diagonally-placed gauges in the shear spans were oriented perpendicularly to an assumed shear strut in order to

Table 3.7: Geokon strain gauge locations

Specimens	Geokon Vibrating Wire Strain Gauge Schematic
1,6	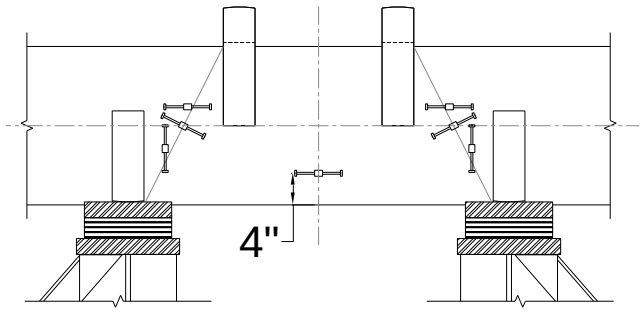
3, 4, 5	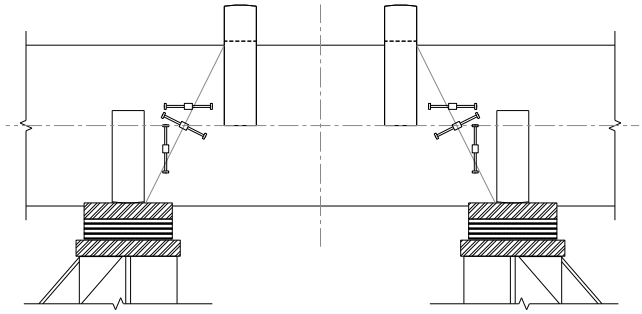
10	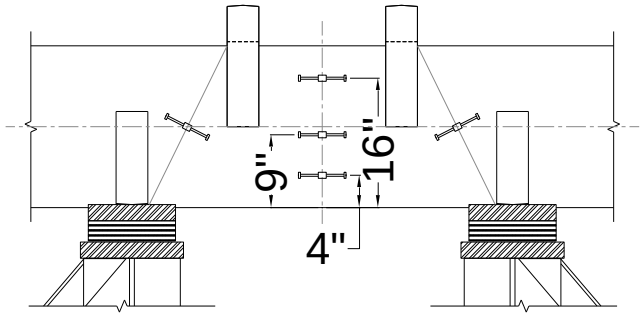
11, 14, 15	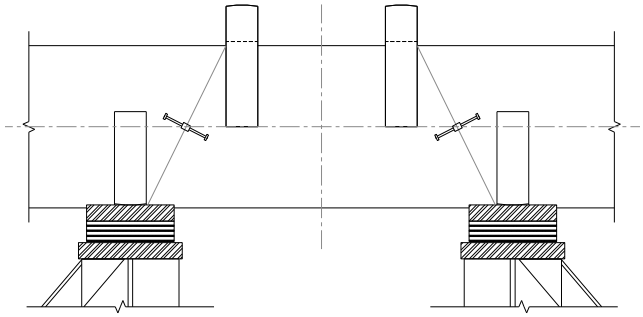
16	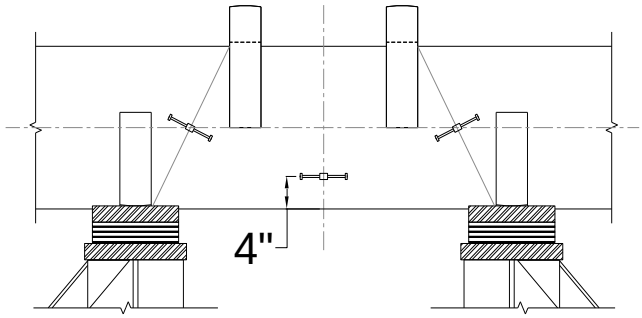

capture the tensile strains and cracking that occur during strutting action. Table 3.7 describes the Geokon gauge locations for each specimen that utilized them.

3.5 Specimen Construction

The steel tubes were cut to length using an oxygen-acetylene pipe-cutting torch. They were placed vertically on a wood base and strapped down. They were also strapped together at two heights to provide stability during the pouring and curing of concrete. The concrete was pumped through a 4 in. hose and only allowed to freefall from a maximum height of 4 ft. All specimens were left in the vertical position for at least 28 days, except Specimens 1 and 12, which remained for at least twenty days. The top ends of the CFTs were covered with wet burlap while the concrete was curing. See Figures 3.16 - 3.19.

A plug consisting of two 3/4 in. plywood layers was placed at one end of each tube to offset the concrete from the end and to provide support for the Geokon gauges and the internal reinforcing bars, where present. Specimens 1 through 6 were cast first, on 17 February 2015, followed by Specimens 7 through 13 on 21 May 2015, then Specimens 14 through 21 on 1 July 2015. No cleaning or special procedure was undertaken to prepare the insides of the tubes at the interface with the concrete, excepting Specimens 5 and 9, which were muddied and greased, respectively. The dirt applied to Specimen 5 was of a relatively well-graded aggregate. The tube was placed at an inclined position on rollers, and was then rotated as the wetted dirt coated the inside face of the tube wall until even and thorough coverage was achieved. See Figures 3.20 and 3.21. The grease was applied to Specimen 9 via rags on the end of a pole.

Figure 3.16: Specimen casting support

Figure 3.17: Specimen casting support

Figure 3.18: Specimen casting support

Figure 3.19: Concrete pumping

Figure 3.20: Muddied CFT interface

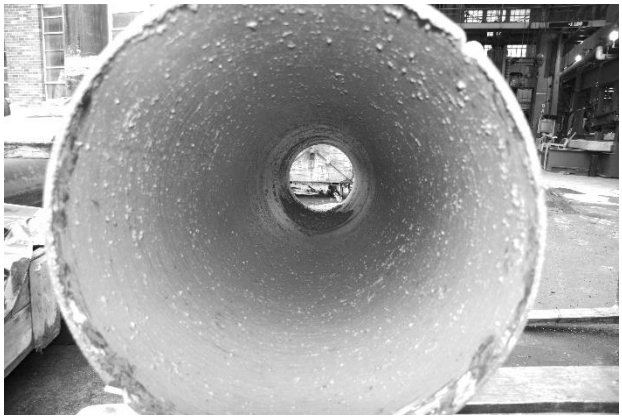

Figure 3.21: Muddied CFT interface

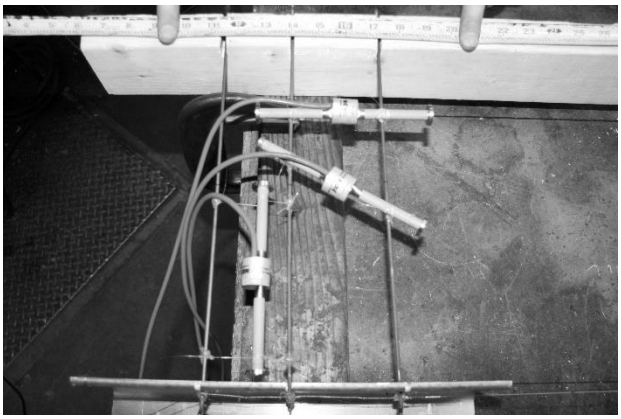

Figure 3.22: Geokon strain gauges

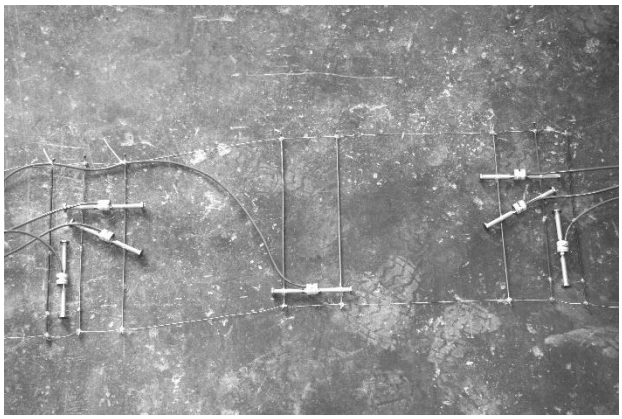

Figure 3.23: Geokon strain gauge support

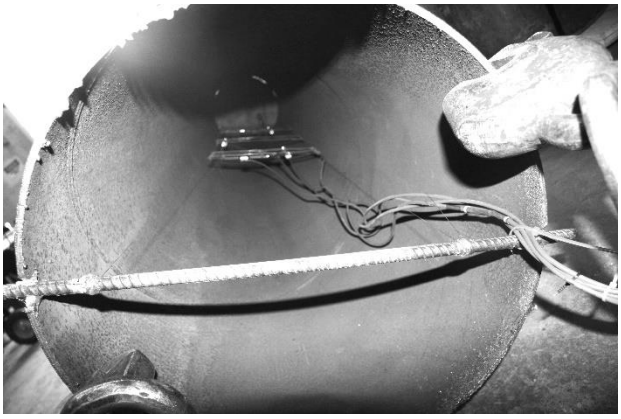

Figure 3.24: Geokon strain gauge support

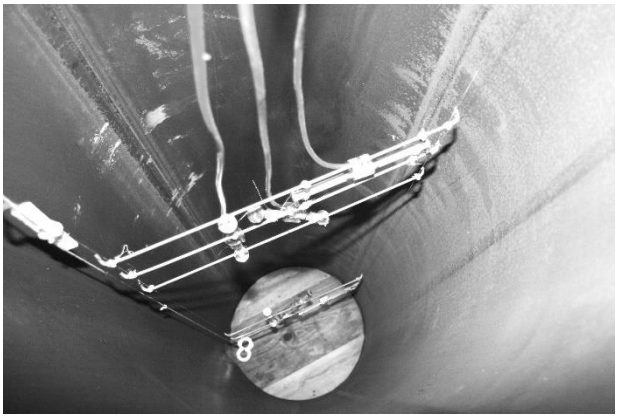

Figure 3.25: Geokon strain gauge support

The Geokon vibrating wire strain gauges were placed in several of the specimens using a ladder consisting of small-diameter wire rope and mild steel rods, as shown in Figures 3.22 – 3.25. The ladders were secured to the plywood plugs and tightened by tensioning the wire rope once the tubes were in the vertical casting position, so as to locate them more accurately. The

wire rope did not provide substantial longitudinal reinforcement as the tensile capacity of the wire rope was approximately 80 lbs. The Geokon gauges were arranged in various configurations, as shown in Table 3.7.

3.6 LOADING PROTOCOL

A combination of load control and displacement control was used to test the CFTs until failure occurred. Each test was initiated under load control of the Baldwin testing machine at a 5 kip increment. The 5 kip increment continued until the applied load, equal to $2V_{exp}$, reached 40 kips. The increment increased to 10 kips until the applied load was 80 kips. At 80 kips applied load, the increment was increased again to 20 kips. The 20 kip increment was maintained until the specimen started displaying substantial non-linearity in the force-displacement plot. At that point, the Baldwin was operated under continuous displacement control until failure occurred. The initial loading rate of 0.5 kips/sec was maintained until the applied load was 100 kips. The load rate was then increased to 1.0 kips/sec. The displacement rate was set at 0.002 in./sec.

Chapter 4. OBSERVED RESPONSE

Twenty-two tests were performed under load control in the elastic region, and under displacement control as the CFTs softened and eventually reached failure. The typical loading protocol is described in Section 3.6. Failure is defined as the tube steel tearing, coupled with a significant drop in flexural or shear resistance in the case of unreinforced CFTs. In CFTs with internal longitudinal reinforcement, failure is defined as tensile rupture of at least two layers of the reinforcing steel in addition to the tube steel tearing and a significant drop, approximately 20%, in the flexural or shear resistance. Normalized moment is plotted against normalized displacement, and the shear force is plotted against measured displacement for each of the specimens. The experimental moment is normalized by the moment capacity as calculated by the plastic stress distribution method, $M_{p,PSDM}$, which is defined in Section 2.1.3.

Due to the high levels of plastic deformation, the short spans of the testing apparatus, and the vertical location of the supports' bearing surfaces—i.e. not at the level of the plastic neutral

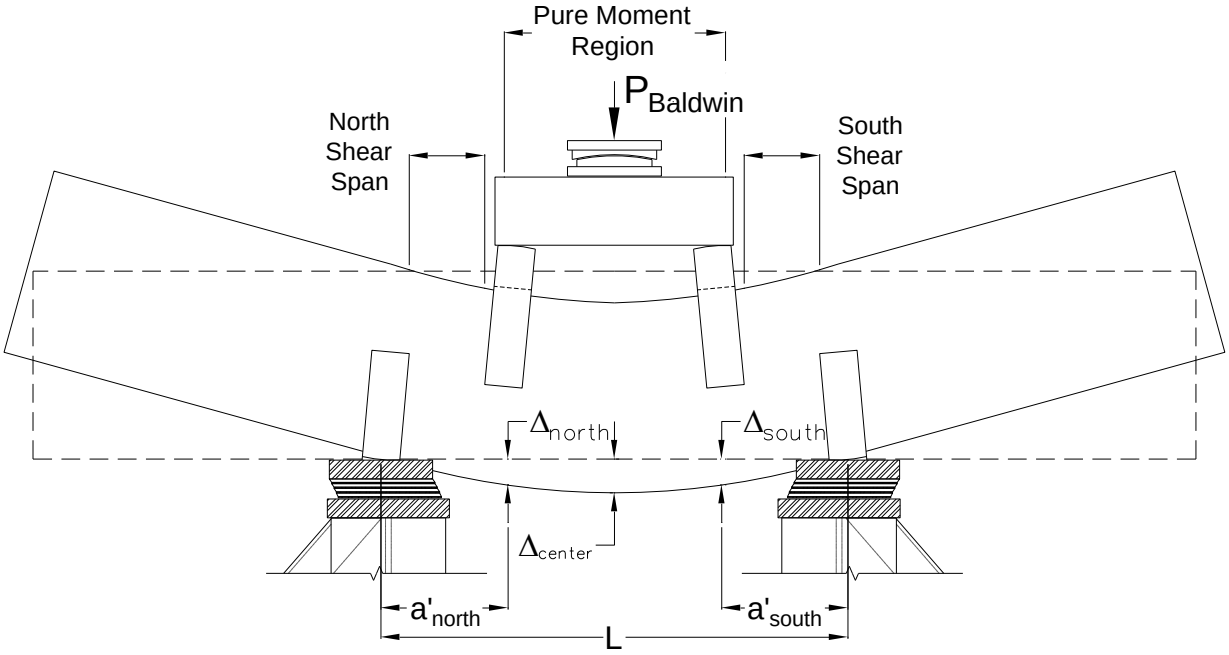

Figure 4.1: Displacement and span measurement diagram

axis—the total span, L, and the shear spans, a'_{north} and a'_{south}, were not constant throughout each test. They vary from the initial lengths, L_0 and a'_0, and were measured at each time step with the Optotrak targets. Example values are plotted in Figures 4.2a, 4.2b, and 4.2c, respectively, for each of the shear span to depth ratios.

In order to more easily compare the specimens, normalized measures of displacement at mid-span and at the load points are defined. The normalized experimental displacement at mid-span, $\bar{\Delta}_{center}$, is similar to a traditional drift measurement except that it includes significant shear deformation in a majority of the tested specimens. The normalized displacements at the north

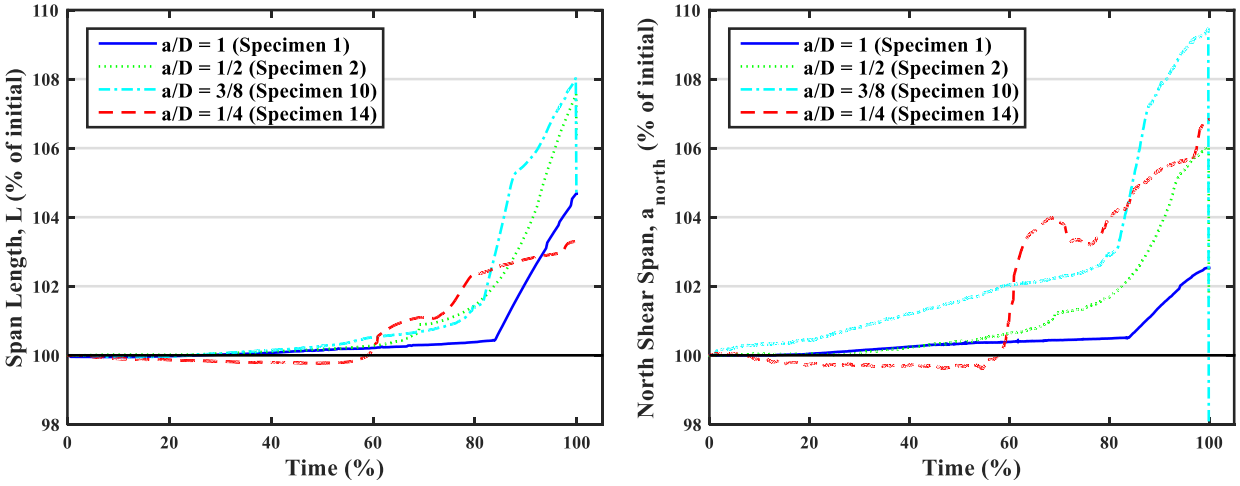

a) Span length, L b) North shear span length, a'_{north}

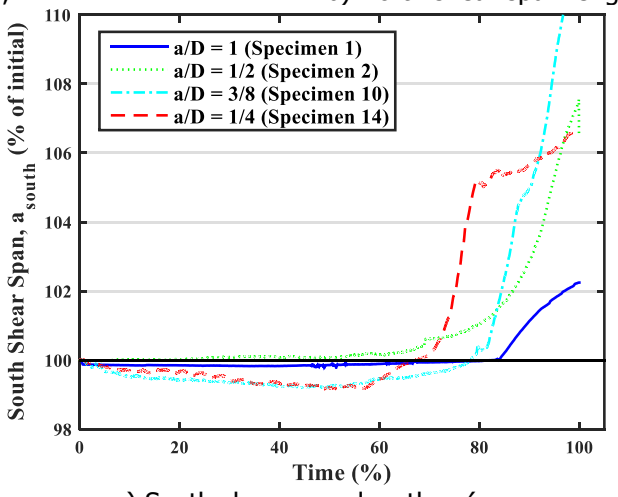

c) South shear span length, a'_{south}

Figure 4.2: Span lengths

load, $\bar{\Delta}_{north}$, and at the south load, $\bar{\Delta}_{south}$, are similar to a shear angle in cases where only pure shearing exists, but are calculated using a' instead of the shear span, a. This underestimates the shear angle, as the CFT is restrained by the load and support cradles as seen in Figure 4.3. The normalized displacements are calculated as shown in Equations 4.1 - 4.3

$$\bar{\Delta}_{center} = \frac{\Delta_{center}}{L/2} \times 100\% \quad (4.1)$$

$$\bar{\Delta}_{north} = \frac{\Delta_{north}}{a'_{north}} \times 100\% \quad (4.2)$$

$$\bar{\Delta}_{south} = \frac{\Delta_{south}}{a'_{south}} \times 100\% \quad (4.3)$$

where Δ_{center} is the measured deflection at mid-span, Δ_{north} is the measured deflection at the north load point, and Δ_{south} is the measured deflection at the south load point. The measurement and span locations are shown in Figure 4.1.

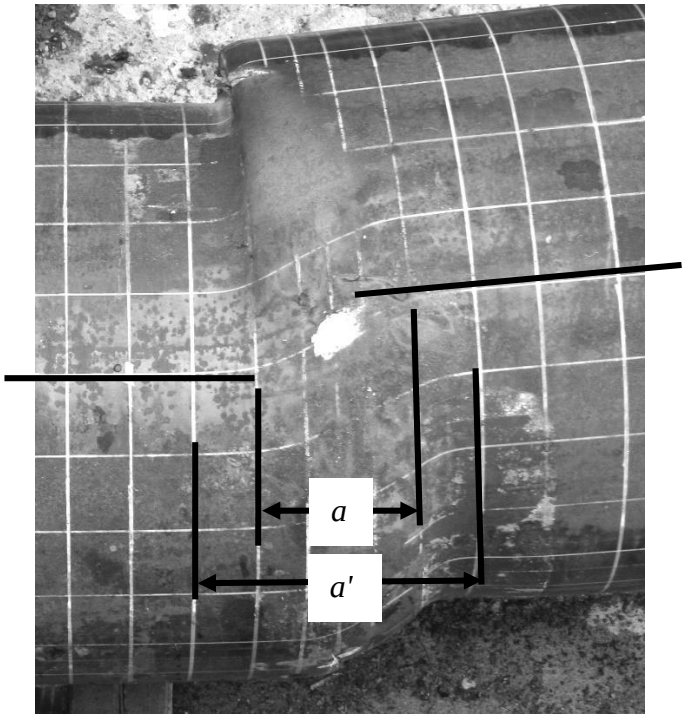

Figure 4.3: Shear span deformation and restraint

The experimental shear and experimental moment at the north load point, south load point, and mid-span, V_{north}, V_{south}, V_{center}, M_{north}, M_{south}, and M_{center}, respectively, are calculated according to Equations 4.4 – 4.9

$$V_{north} = \frac{P_{Baldwin}}{2 \times L}(L - a'_{north} + a'_{south}) \tag{4.4}$$

$$V_{south} = \frac{P_{Baldwin}}{2 \times L}(L - a'_{south} + a'_{north}) \tag{4.5}$$

$$V_{center} = \frac{P_{Baldwin}}{2 \times L}(a'_{south} - a'_{north}) \tag{4.6}$$

$$M_{north} = V_{south} \times a'_{north} \tag{4.7}$$

$$M_{south} = V_{south} \times a'_{south} \tag{4.8}$$

$$M_{center} = \frac{M_{north} + M_{south}}{2} \tag{4.9}$$

where $P_{Baldwin}$ is the total force applied by the Baldwin UTM. It is assumed that the total Baldwin load is divided evenly between the two load cradles, as there were no load cells included in the testing apparatus. The load spherical bearing used to load the system was placed in the center between the load cradles to nominally achieve this goal.

As discussed in Section 3.1, there was significant deformation in the elastomeric and cotton duck bearing pads. These deformations affected the displacement measurements. The measured displacements used in calculating the normalized displacements in Equations 4.1 – 4.3 have been corrected using the procedure detailed in Appendix C in order to isolate the CFT deformation.

The NDI Optotrak system did not function properly during the testing of Specimen 15, so a standard first order analysis was done to calculate the moment, shear, and displacement quantities of interest. The data from the string potentiometers and linear displacement

transducers were used to plot the moment-displacement and shear-displacement response of the specimen. Only the values at mid-span are calculated and reported.

Table 4.1 summarizes the moment and mid-span displacement and corresponding shear values at first yield, M_{yield}, V_{yield}, and $\bar{\Delta}_{yield}$, at the proportional limit, M_{prop}, V_{prop}, and $\bar{\Delta}_{prop}$, and at the point of maximum moment, M_{ult}, V_{ult}, and $\bar{\Delta}_{ult}$, for each specimen. The mid-span displacement at failure, $\bar{\Delta}_{fail}$, is also included. The normalized moment-normalized displacement figures for each specimen include these four key performance points. Point A corresponds to $\bar{\Delta}_{yield}$, point B corresponds to $\bar{\Delta}_{prop}$, point C corresponds to $\bar{\Delta}_{ult}$, and point D corresponds to $\bar{\Delta}_{fail}$. The point at which the bottom-most reinforcing bar yields at mid-span is also included on the plots for the internally reinforced specimens and is labeled point E. Figure 4.4 shows the normalized displacement plotted against normalized moment for Specimen 10, while Figure 4.5 shows the longitudinal steel strain at mid-span plotted versus the normalized moment for the

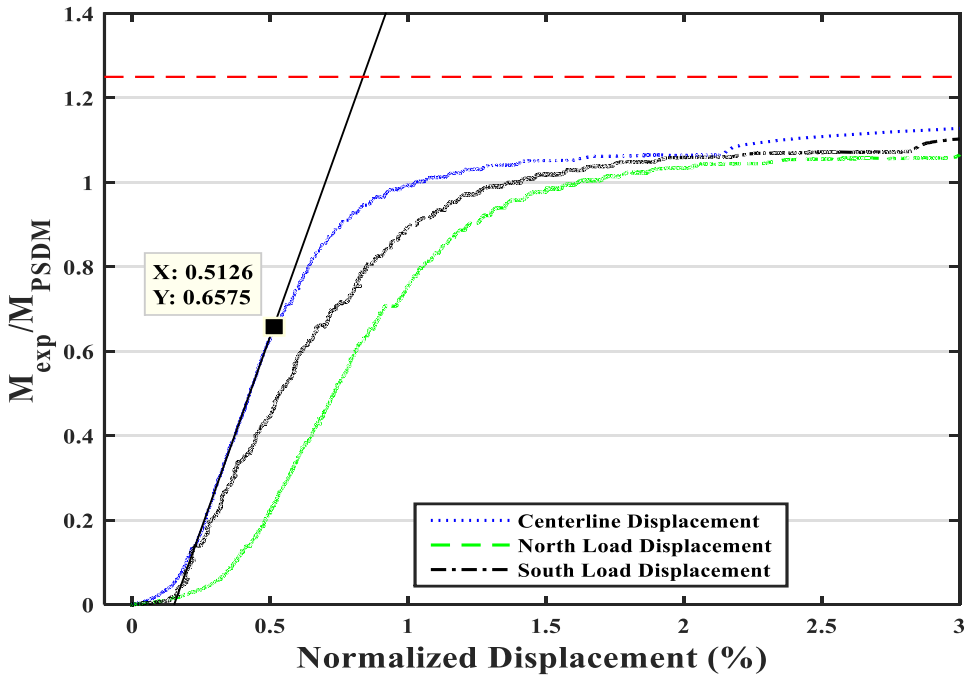

Figure 4.4: Proportional limit for Specimen 10

same specimen. The proportional limit is defined by plotting a best-fit line to the linear-elastic portion of the normalized moment-normalized displacement plot and determining when the curve departs from linear. The measured yield stress for the steel tube of Specimen 10 was 53.9 ksi and the elastic modulus was 29,308 ksi, resulting in a yield strain of 0.00184. The bending moment at first yield—i.e. when the bottom strain gauges first reach the yield strain—is 3,572 in-kips. This is lower than M_{prop} = 4,316 in-kips, when the cross section begins to noticeably soften. Plots of the steel strain gauges at mid-span for each specimen are included in Appendix D.

Table 4.2 shows the shear force, bending moment, and normalized displacement at mid-span when the concrete cracks in the pure flexural region, and as the compression struts in the shear spans form cracks. In specimens with Geokon gauges, it is known explicitly when the concrete forms its first major crack in each location. These specimens are noted with an asterisk in the table. For the others, audible evidence during the test and force-displacement data

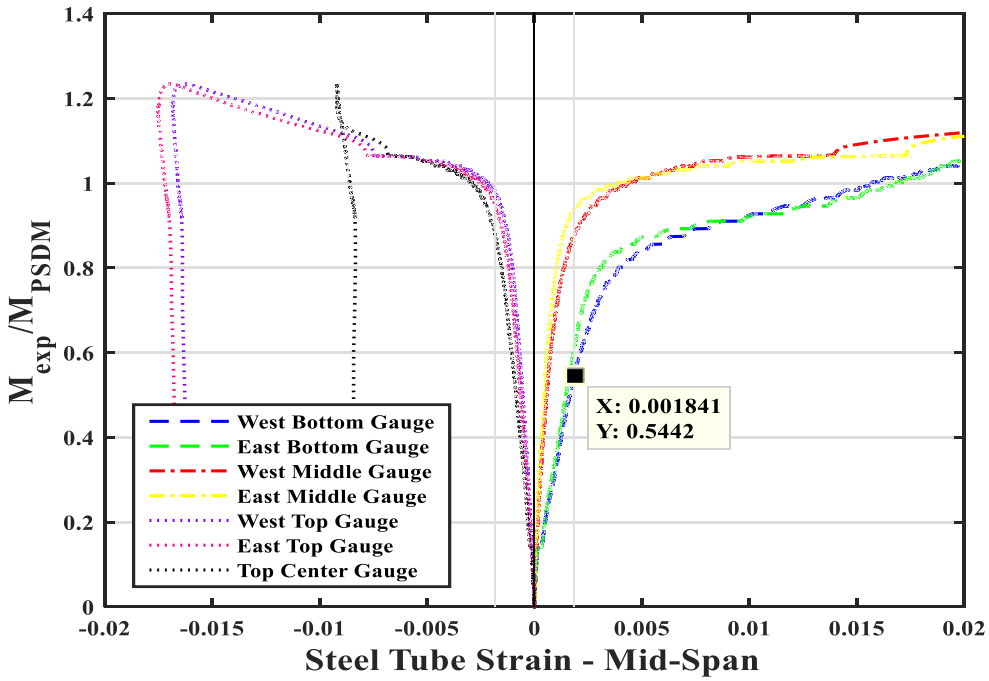

Figure 4.5: Strain in steel tube at mid-span in Specimen 10

was used to determine when the cracks occurred. The inferred values correlate well with the explicitly known values. In cases where cracking was not visible upon inspection of the concrete, the table reads N/A in the appropriate location. The table reads “unknown” when cracks were present but, for various reasons, load and drift at cracking was undetermined. Reasons included high ambient noise in the lab, a lack of clarity in the data, or cracking occurring while the test was under continuous displacement control. Figure 4.6 plots the concrete strain versus the normalized moment for Specimen 10. Table 3.7 shows the Geokon layout for Specimen 10. Most notable is the timing of the major cracking, represented as large jumps in the strains. Also of note is the shape of the Mid-Span Top curve; after the normalized moment reaches 0.35 the strain decreases until the concrete struts crack. The plastic neutral axis is potentially shifting as a result of the flexure-shear interaction. All concrete strain gauge plots are included in Appendix E.

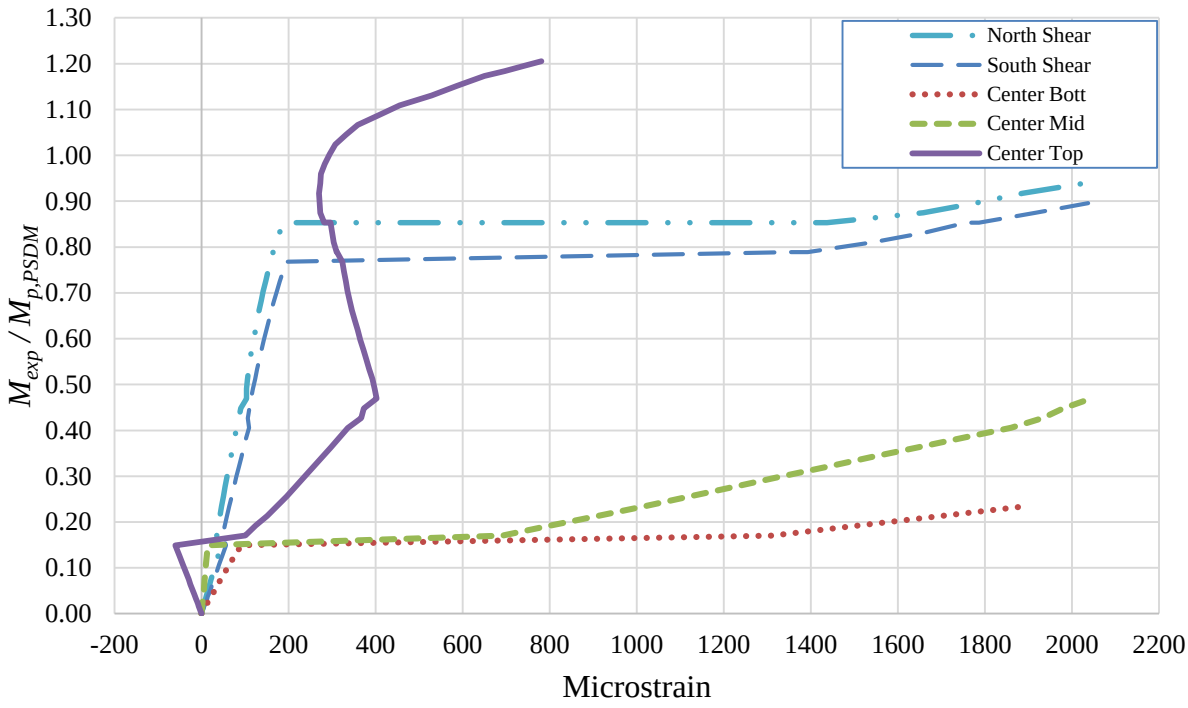

Figure 4.6: Concrete strain for Specimen 10

Table 4.1: Summary of key performance states

Specimen	**1**	**2**	**3**	**4**	**5**	**6**	**7**	**8**
a/D	1.0	0.5	0.5	0.5	0.5	0.5	0.375	0.375
D/t	80	80	80	80	80	80	80	80
ρ_{int}	0%	0%	0%	0%	0%	0%	1.04%	2.00%
L_T	2D	2D	D/2	D	2D	2D	2D	2D
M_{yield} (k-in)	4209	3825	3699	2988	3794	5753	4328	4996
V_{yield} (k)	175	270	264	249	271	409	371	431
$\bar{\Delta}_{yield}$ (%)	0.331	0.339	0.350	0.286	0.384	0.568	0.360	0.417
M_{prop} (k-in)	4209	3930	4025	3915	4027	5916	3903	5432
V_{prop} (k)	175	280	286	280	287	420	335	471
$\bar{\Delta}_{prop}$ (%)	0.331	0.344	0.375	0.320	0.390	0.570	0.318	0.443
M_{ult} (k-in)	7893	8099	8111	8035	8124	11665	8807	9239
V_{ult} (k)	322	550	552	543	556	779	705	802
$\bar{\Delta}_{ult}$ (%)	9.37	7.96	8.94	10.23	5.60	4.70	12.08	12.71
$\bar{\Delta}_{fail}$ (%)	11.40	11.32	11.02	11.56	6.22	9.04	16.19	15.51

Specimen	**9**	**10**	**11**	**12**	**13**	**14**	**15**	**16**
a/D	0.5	0.375	0.375	0.5	0.375	0.25	0.25	0.375
D/t	80	80	80	80	80	80	80	80
ρ_{int}	0%	0%	0%	1.13%	0%	0%	0%	0%
L_T	2D	2D	D/2	2D	2D	2D	5D/8	2D
M_{yield} (k-in)	3646	3572	3847	4899	5172	4894	4052	4764
V_{yield} (k)	261	309	336	346	451	546	450	415
$\bar{\Delta}_{yield}$ (%)	0.385	0.452	0.830	0.417	0.484	0.743	0.162*	0.385
M_{prop} (k-in)	3647	4316	3665	4539	3784	3497	3421	5051
V_{prop} (k)	261	372	320	321	330	390	380	441
$\bar{\Delta}_{prop}$ (%)	0.383	0.513	0.812	0.380	0.359	0.623	0.135*	0.400
M_{ult} (k-in)	6528	8159	7024	9679	8270	76788	7164	9204
V_{ult} (k)	442	665	600	651	710	826	796	765
$\bar{\Delta}_{ult}$ (%)	7.50	6.23	3.26	10.00	22.87	2.58	0.56	6.61
$\bar{\Delta}_{fail}$ (%)	17.08	14.57	10.71	11.92	5.66	9.48	1.26*	10.36

Specimen	**17**	**18**	**19**	**20**	**21**	**22**
a/D	0.5	0.5	0.5	0.25	0.375	1.0
D/t	80	53.3	53.3	80	80	80
ρ_{int}	0%	0%	1.07%	0%	0%	0%
L_T	2D	2D	2D	D/2	2D	4.5D
M_{yield} (k-in)	4536	5980	6626	4244	3479	N/A
V_{yield} (k)	324	430	473	462	305	N/A
$\bar{\Delta}_{yield}$ (%)	0.557	0.579	0.560	0.484	7.783	N/A
M_{prop} (k-in)	4489	6159	7144	3772	2272	5509
V_{prop} (k)	321	443	511	420	198	230
$\bar{\Delta}_{prop}$ (%)	0.552	0.590	0.587	0.427	0.392	0.307
M_{ult} (k-in)	8056	12444	13816	6838	5211	11579
V_{ult} (k)	547	832	952	712	449	477
$\bar{\Delta}_{ult}$ (%)	8.25	8.72	7.00	14.37	16.23	6.15
$\bar{\Delta}_{fail}$ (%)	10.64	10.97	10.72	16.69	17.16	7.06

* Optotrak system did not function properly—displacements are not comparable to other specimens

Table 4.2: Summary of concrete cracking states

Specimen	Crack Location	V_{cr} (kips)	M_{cr} (in-k)	$\bar{\Delta}_{cr}$ (%)
1	Mid-span Flexure	36	853	0.050
	North Shear	N/A	N/A	N/A
	South Shear	N/A	N/A	N/A
2*	Mid-span Flexure	60	838	0.091
	North Shear	430	6066	0.652
	South Shear	430	6066	0.652
3*	Mid-span Flexure	60	835	0.132
	North Shear	448	6310	0.792
	South Shear	unknown	unknown	unknown
4*	Mid-span Flexure	67	939	0.087
	North Shear	451	6327	0.770
	South Shear	456	6395	0.831
5*	Mid-span Flexure	69	969	0.159
	North Shear	440	6223	0.971
	South Shear	487	6881	1.611
6*	Mid-span Flexure	60	837	0.165
	North Shear	461	6487	0.626
	South Shear	438	6167	0.591
7	Mid-span Flexure	110	1281	0.137
	North Shear	308	3590	0.284
	South Shear	308	3590	0.284
8	Mid-span Flexure	135	1555	0.207
	North Shear	unknown	unknown	unknown
	South Shear	unknown	unknown	unknown
9	Mid-span Flexure	58	812	0.126
	North Shear	unknown	unknown	unknown
	South Shear	unknown	unknown	unknown
10*	Mid-span Flexure	79	911	0.220
	North Shear	403	4674	0.568
	South Shear	373	4318	0.520
11*	Mid-span Flexure	74	851	0.562
	North Shear	390	4473	0.895
	South Shear	380	4357	0.875
12	Mid-span Flexure	75	1062	0.144
	North Shear	322	4556	0.390
	South Shear	322	4556	0.390
13	Mid-span Flexure	140	1606	0.222
	North Shear	unknown	unknown	unknown
	South Shear	unknown	unknown	unknown
14*	Mid-span Flexure	104	929	0.446
	North Shear	390	3499	0.630
	South Shear	391	3502	0.637
15*	Mid-span Flexure	110	989	0.036
	North Shear	450	4050	0.161
	South Shear	480	4327	0.172

Table 4.2 cont.

Specimen	Crack Location	V_{cr} (kips)	M_{cr} (in-k)	$\bar{\Delta}_{cr}$ (%)
16*	Mid-span Flexure	77	887	0.137
	North Shear	440	5051	0.400
	South Shear	451	5166	0.418
17	Mid-span Flexure	69	966	0.262
	North Shear	428	6028	0.823
	South Shear	430	6028	0.823
18	Mid-span Flexure	76	1063	0.302
	N/S Shear	470	6540	0.627
	N/S Shear	560	7792	0.728
19	Mid-span Flexure	74	1080	0.245
	North Shear	unknown	unknown	unknown
	South Shear	unknown	unknown	unknown
20	Mid-span Flexure	80	719	0.149
	North Shear	unknown	unknown	unknown
	South Shear	unknown	unknown	unknown
22	Mid-span Flexure	47	1137	0.057
	North Shear	N/A	N/A	N/A
	South Shear	N/A	N/A	N/A

* Indicates that Geokon strain gauges were used to determine when cracking occurred

4.1 SPECIMEN 1

Specimen 1 was the baseline specimen for a/D = 1.0 and was tested 11 March 2015. It had a clean interface, a tail length of 40 inches, a straight seam weld, and no internal reinforcement. It achieved 1.30 times $M_{p,PSDM}$ and 1.27 times $V_{n\ (WSDOT)}$ and failed in flexure. The tube tore at the bottom in flexure approximately 0.5 inches south of mid-span after significant flexural deformations occurred. The tear in the steel was vertical. There were no visible shear deformations in the steel nor apparent strutting cracks in the concrete. There was extensive flexural cracking in the concrete fill and the tube steel buckled symmetrically on both the north and the south ends of the pure moment region. Figure 4.7 shows the normalized moment-normalized displacement plot. Figure 4.8 shows the shear-displacement plot. Figures 4.9 a – f show the CFT at final deformation states and the condition of the concrete at the end of the test. North is to the left in each photograph.

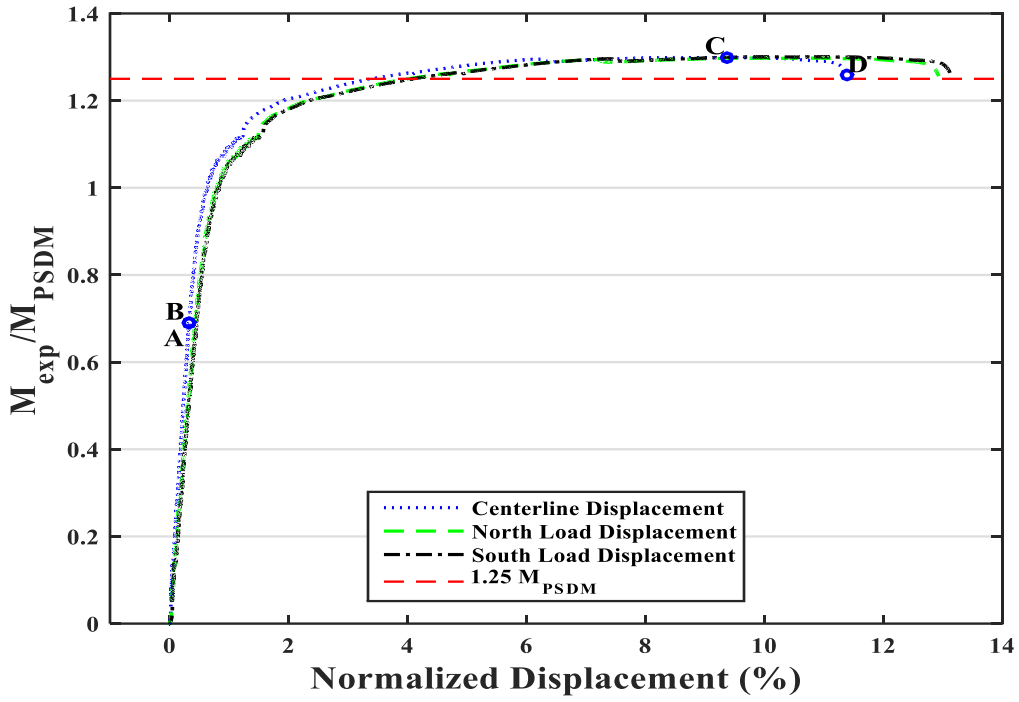

Figure 4.7: Specimen 1 moment-displacement plot

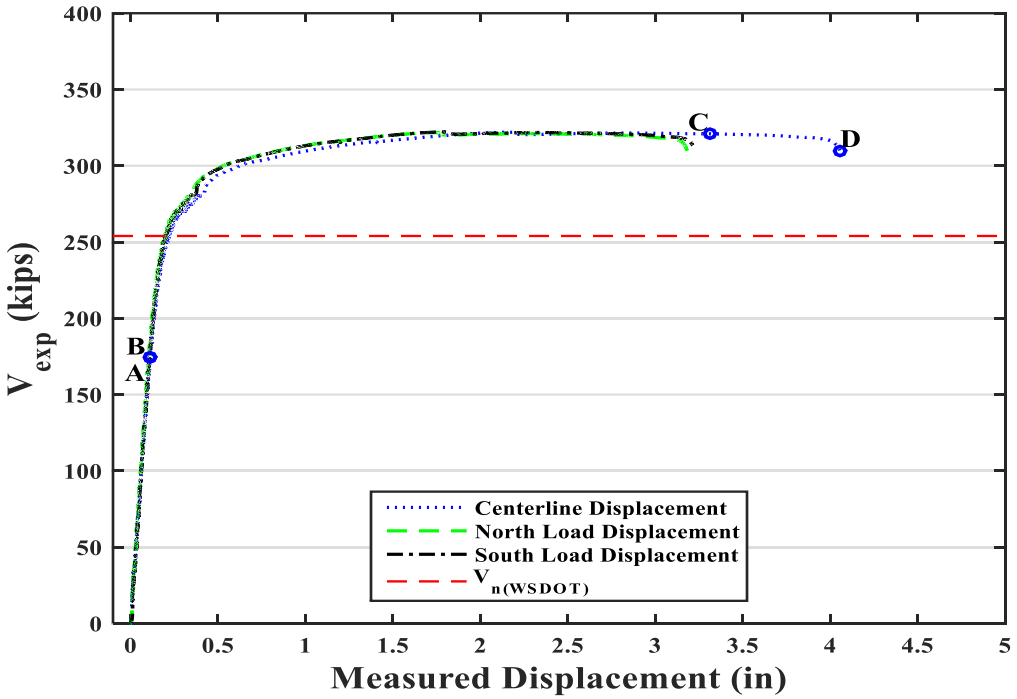

Figure 4.8: Specimen 1 shear-displacement plot

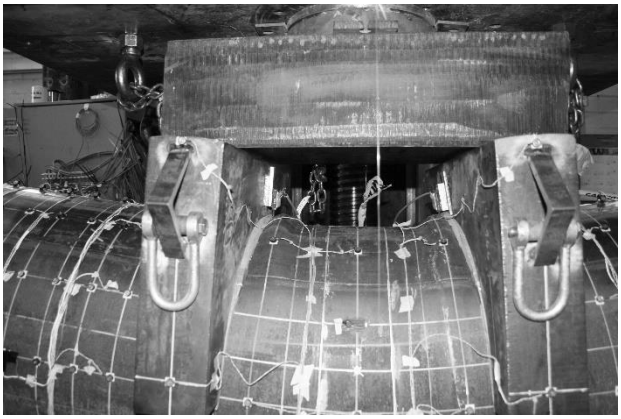

a) Specimen 1 final state

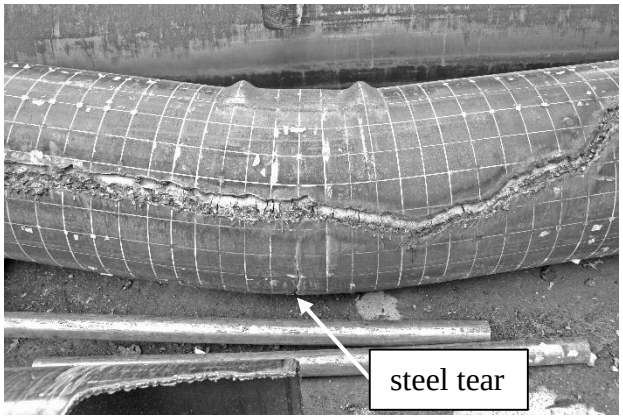

b) Specimen 1 final state

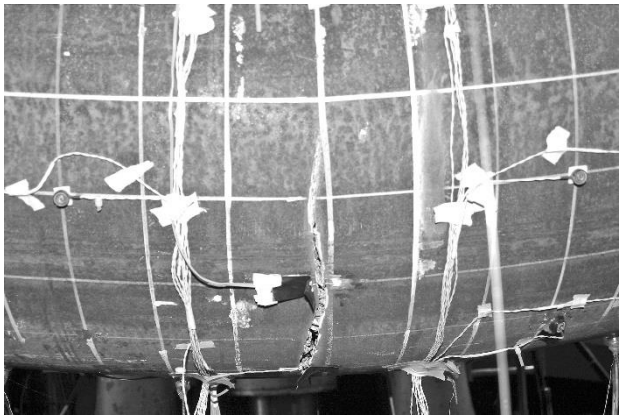

c) Specimen 1 steel tear

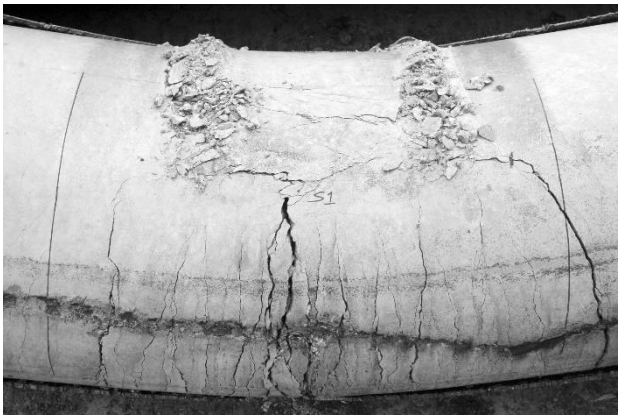

d) Specimen 1 mid-span concrete cracking

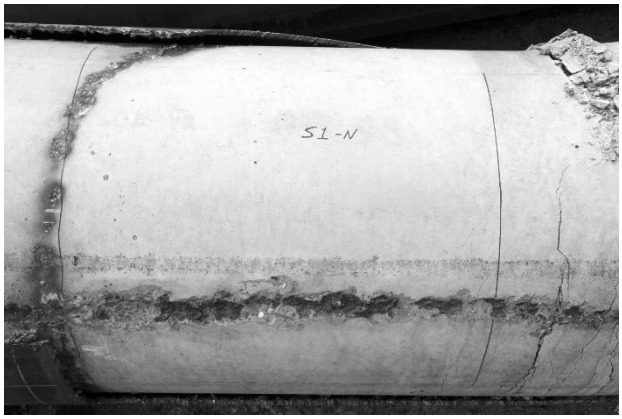

e) Specimen 1 north span concrete cracking

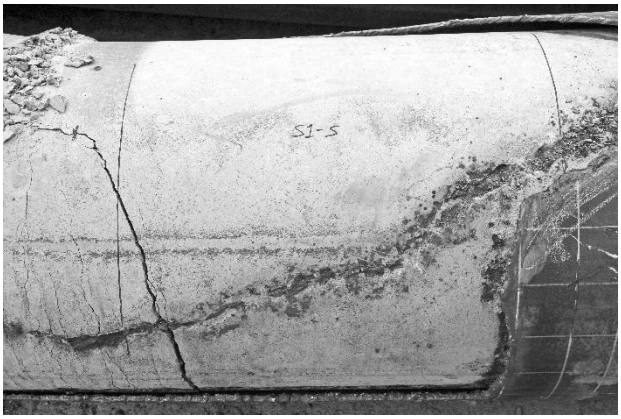

f) Specimen 1 south span concrete cracking

Figure 4.9: Specimen 1 state photos
(*a/D* = 1.0, D/t=80, ρ_{int}=0%)

4.2 SPECIMEN 2

Specimen 2 was the baseline specimen for a/D = 0.5 and was tested 20 March 2015. It had a clean interface, a tail length of 40 inches, a straight seam weld, and no internal reinforcement. It achieved 1.33 times $M_{p,PSDM}$ and 2.16 times $V_{n\ (WSDOT)}$ and failed in flexure. The tube tore at the bottom in flexure approximately 4 inches south of mid-span after significant flexural deformations occurred. The tear in the steel was vertical. There were no visible shear deformations in the steel but limited diagonal shear cracking formed in the concrete in the shear spans. The tube steel buckled on both the north and the south ends of the pure moment region with a more prominent buckle on the south. Extensive flexural cracking of the concrete fill was also noted in the pure flexural region. Figure 4.10 shows the normalized moment-normalized displacement plot. Figure 4.11 shows the shear-displacement plot. Figures 4.12 a – f show the CFT at final deformation states and the condition of the concrete at the end of the test. North is to the left in each photograph.

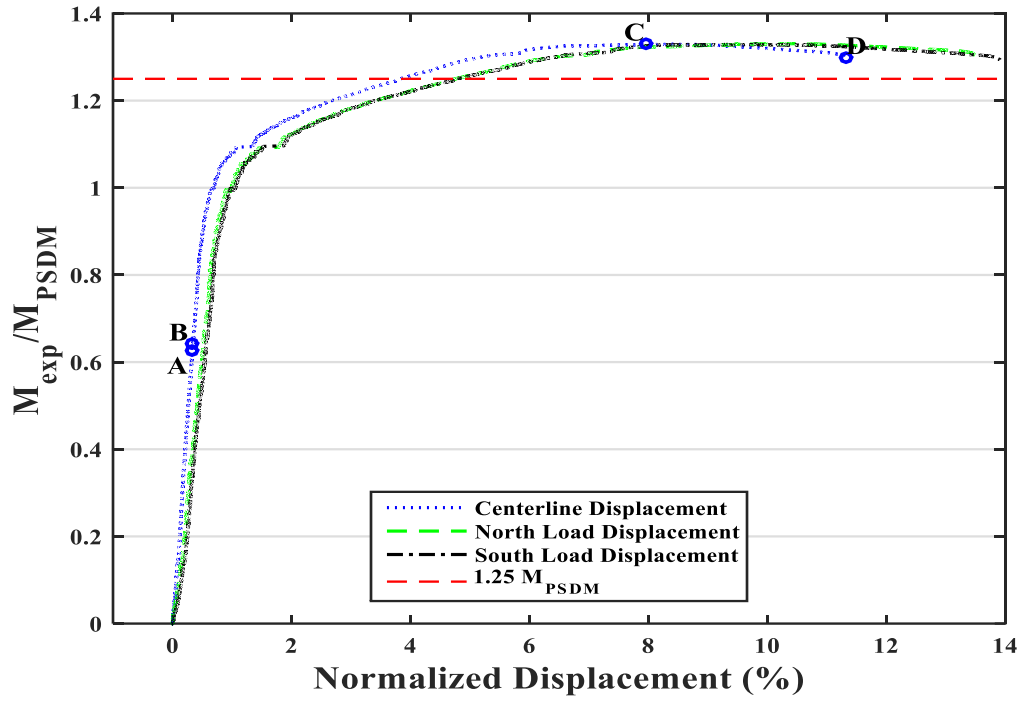

Figure 4.10: Specimen 2 moment-displacement plot

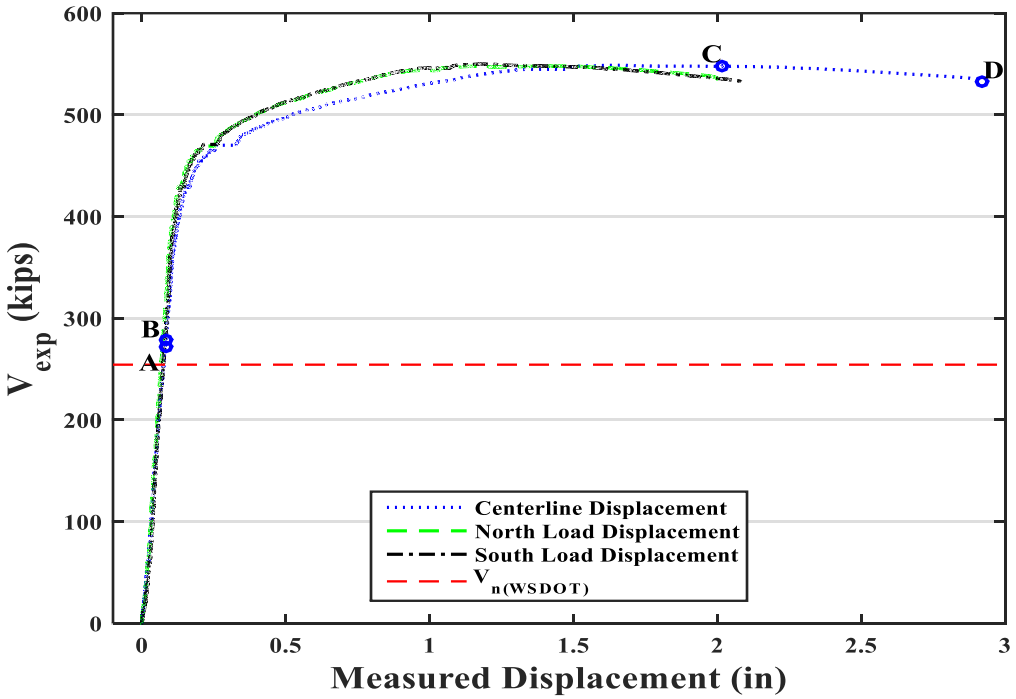

Figure 4.11: Specimen 2 shear-displacement plot

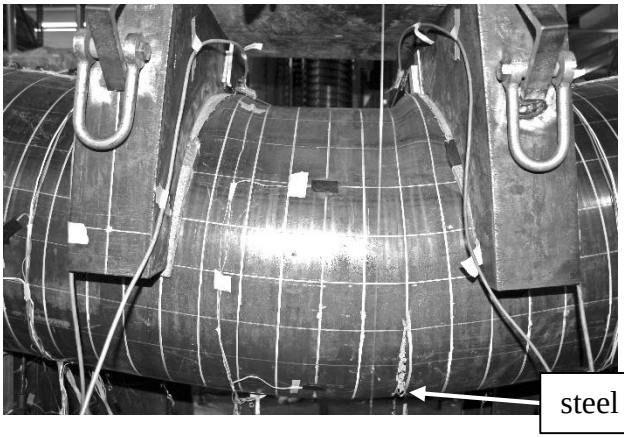

a) Specimen 2 final state

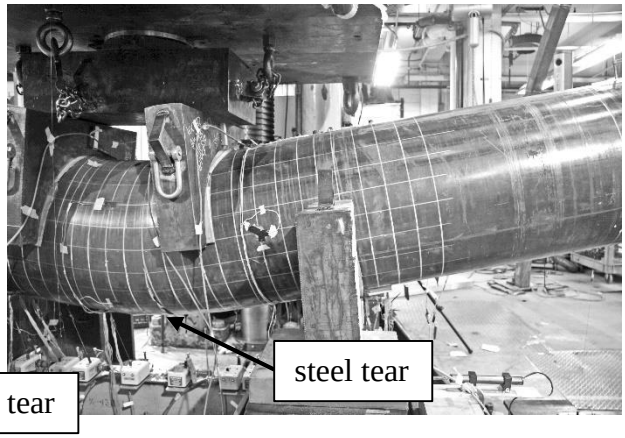

b) Specimen 2 final state

c) Specimen 2 steel tear

d) Specimen 2 mid-span concrete cracking

e) Specimen 2 north span concrete cracking

f) Specimen 2 south span concrete cracking

Figure 4.12: Specimen 2 state photos
(*a/D* = 0.5, D/t=80, ρ_{int}=0%)

4.3 SPECIMEN 3

Specimen 3 was a tail length variation of Specimen 2, the baseline specimen for a/D = 0.5, and was tested 3 April 2015. It had a clean interface, a tail length of 10 inches, a straight seam weld, and no internal reinforcement. It achieved 1.31 times $M_{p,PSDM}$ and 2.14 times $V_{n\ (WSDOT)}$ and failed in flexure. The tube tore at the bottom in flexure approximately 0.5 inches south of mid-span after significant flexural deformations occurred. The tear in the steel was vertical. There were no visible shear deformations in the steel but limited diagonal shear cracks formed in the concrete in the shear spans. The tube steel buckled on both the north and the south ends of the pure moment region symmetrically. Extensive flexural cracking of the concrete fill was also noted in the pure flexural region. Figure 4.13 shows the normalized moment-normalized displacement plot. Figure 4.14 shows the shear-displacement plot. Figures 4.15 a – f show the CFT at final deformation states and the condition of the concrete at the end of the test. North is to the left in each photograph.

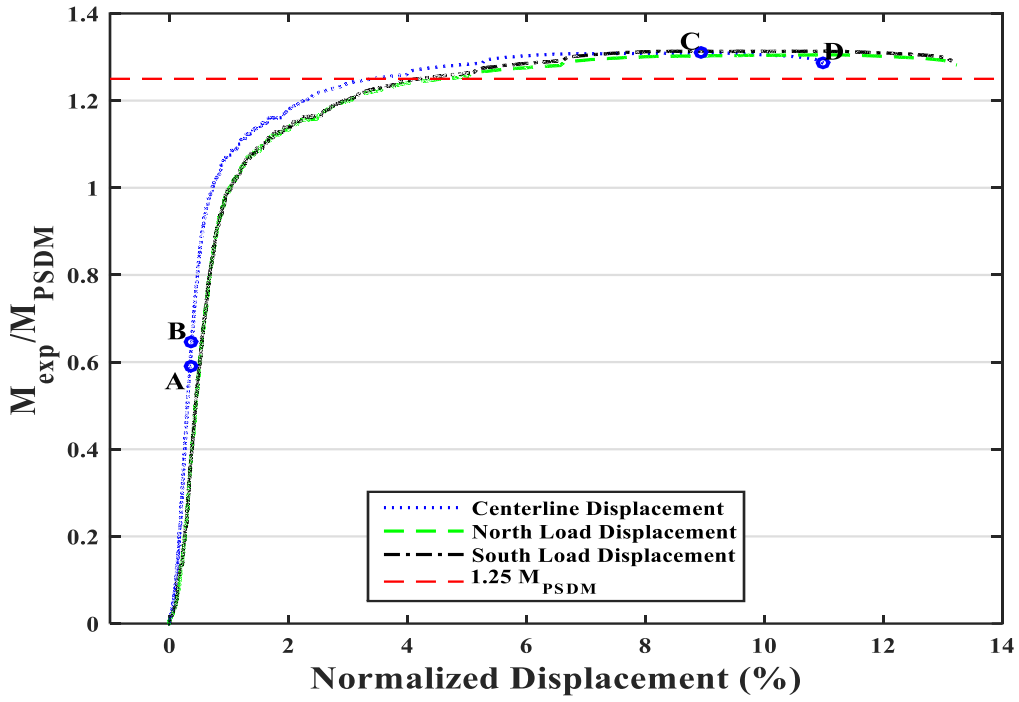

Figure 4.13: Specimen 3 moment-displacement plot

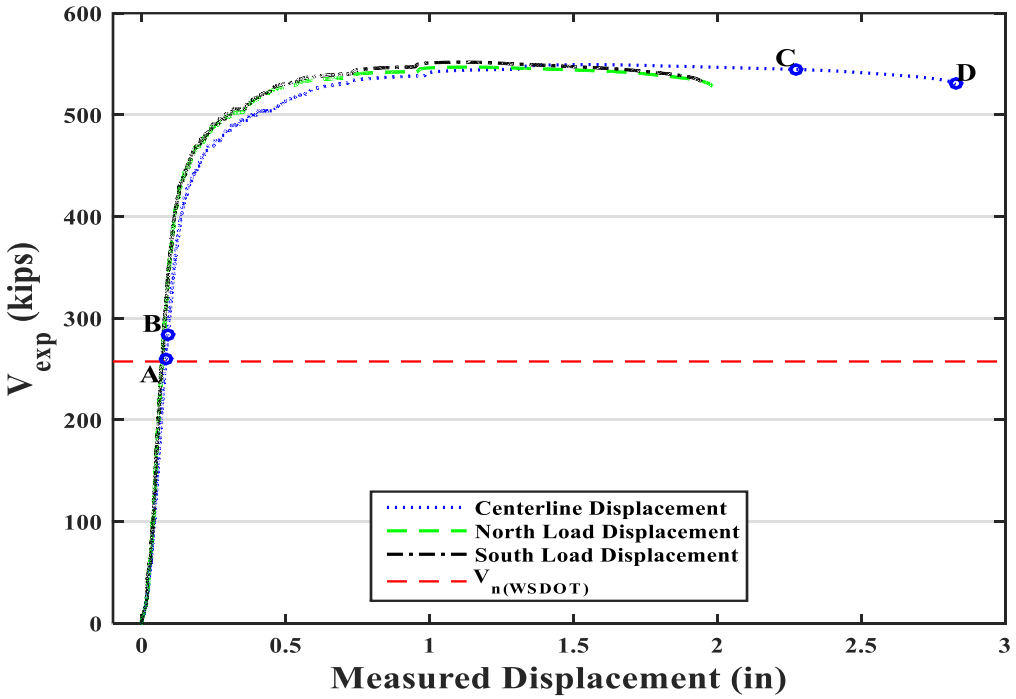

Figure 4.14: Specimen 3 shear-displacement plot

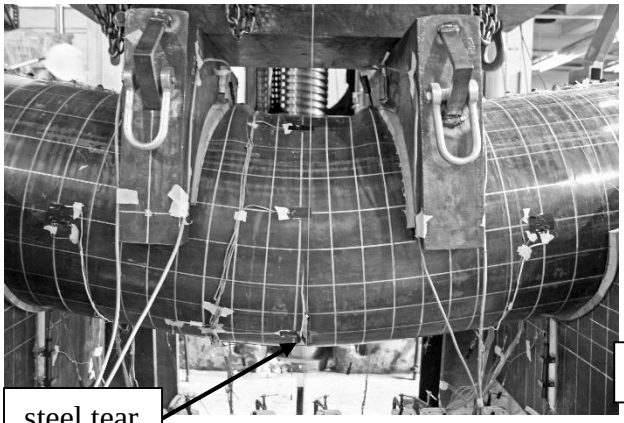

a) Specimen 3 final state

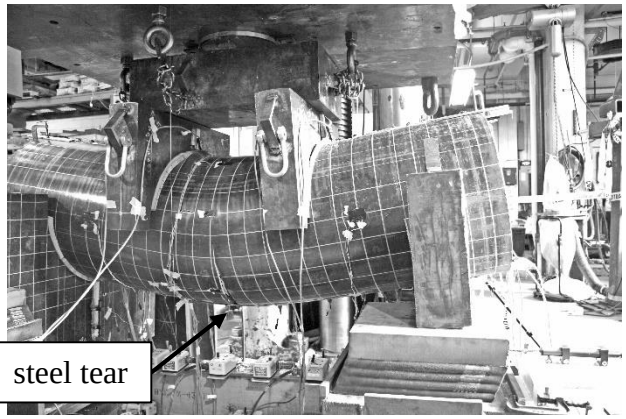

b) Specimen 3 final state

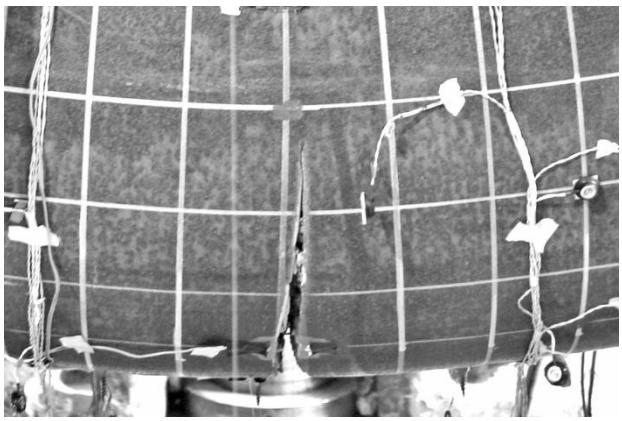

c) Specimen 3 steel tear

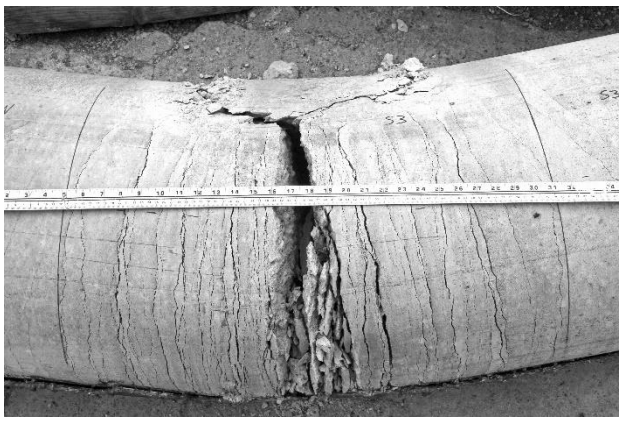

d) Specimen 3 mid-span concrete cracking

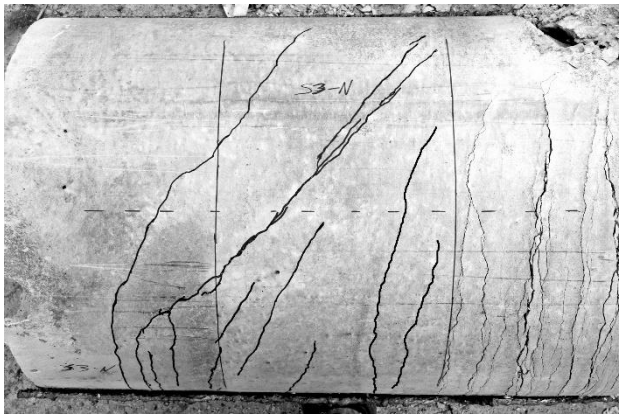

e) Specimen 3 north span concrete cracking

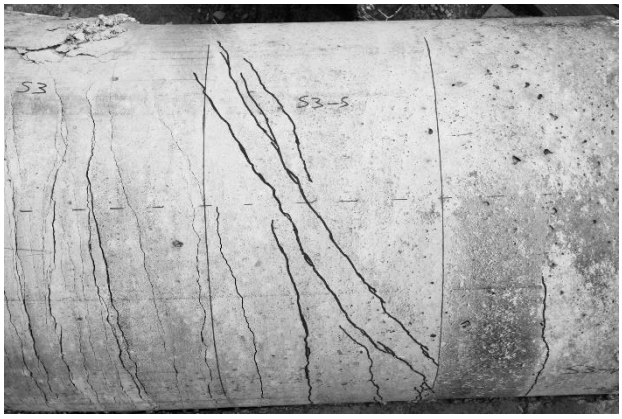

f) Specimen 3 south span concrete cracking

Figure 4.15: Specimen 3 state photos
(*a/D* = 0.5, D/t=80, L_T=D/2)

4.4 SPECIMEN 4

Specimen 4 was a tail length variation of Specimen 2, the baseline specimen for a/D = 0.5, and was tested 17 April 2015. It had a clean interface, a tail length of 20 inches, a straight seam weld, and no internal reinforcement. It achieved 1.30 times $M_{p,PSDM}$ and 2.11 times $V_{n\ (WSDOT)}$ and failed in flexure. The tube tore at the bottom in flexure approximately 0.5 inches south of mid-span after significant flexural deformations occurred. The tear in the steel was vertical. There were no visible shear deformations in the steel but limited diagonal shear cracks formed in the concrete in the shear spans. The tube steel buckled on both the north and the south ends of the pure moment region with more prominent buckling on the south. Extensive flexural cracking of the concrete fill was also noted in the pure flexural region. Figure 4.16 shows the normalized moment-normalized displacement plot. Figure 4.17 shows the shear-displacement plot. Figures 4.18 a – f show the CFT at final deformation states and the condition of the concrete at the end of the test. North is to the left in each photograph.

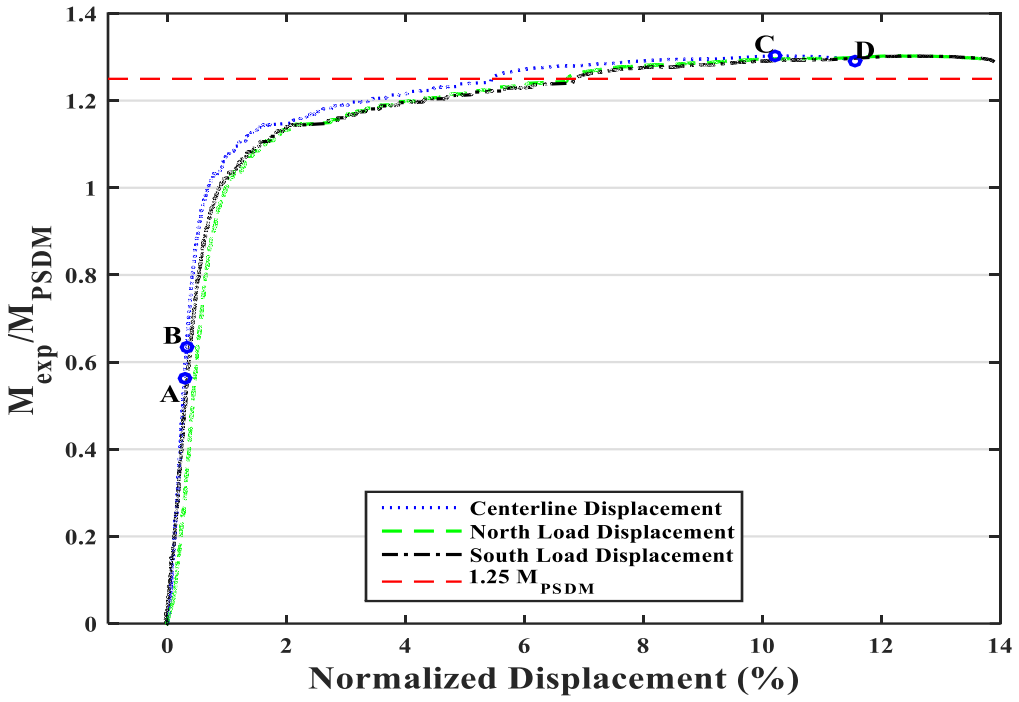

Figure 4.16: Specimen 4 moment-displacement plot

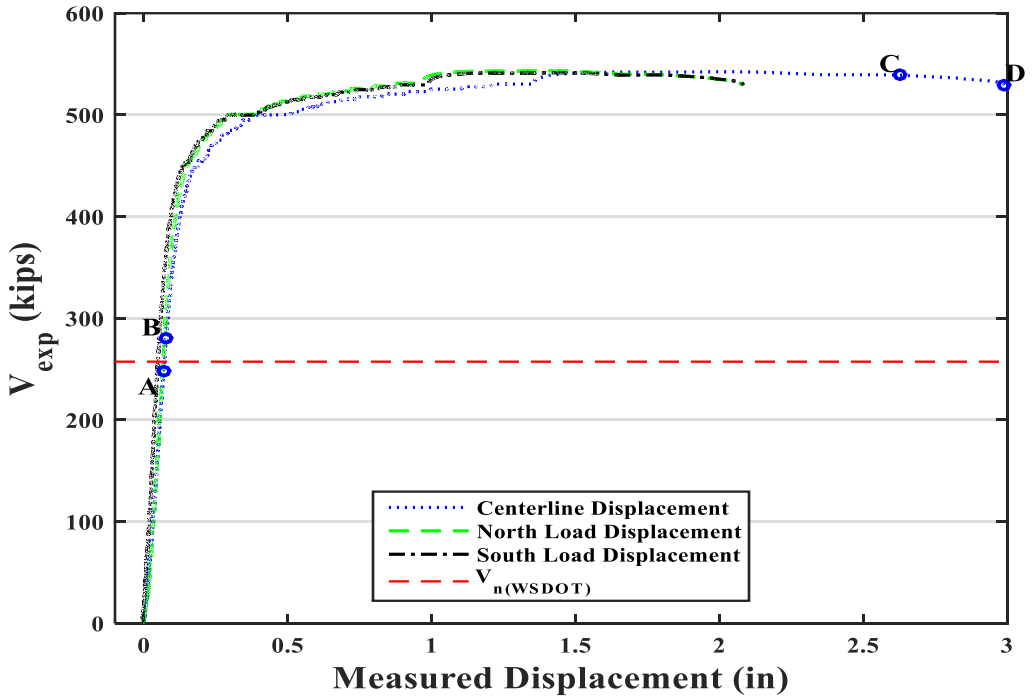

Figure 4.17: Specimen 4 shear-displacement plot

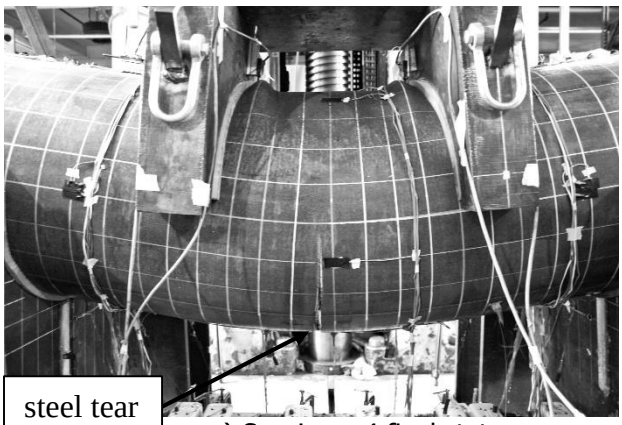

a) Specimen 4 final state

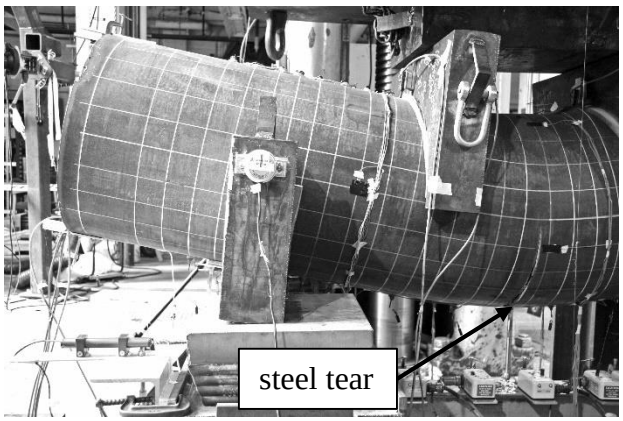

b) Specimen 4 final state

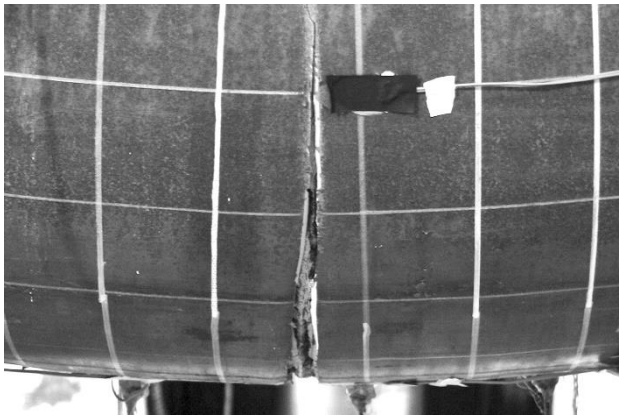

c) Specimen 4 steel tear

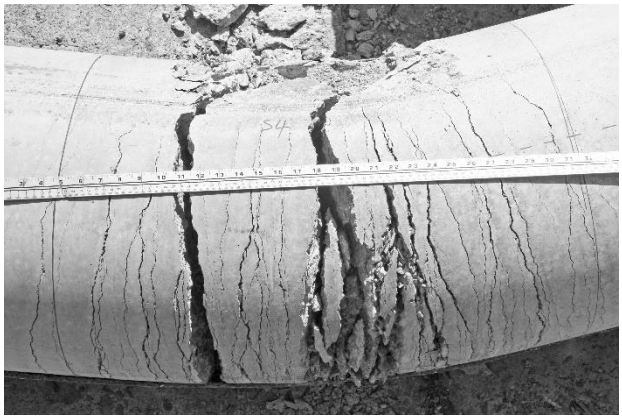

d) Specimen 4 mid-span concrete cracking

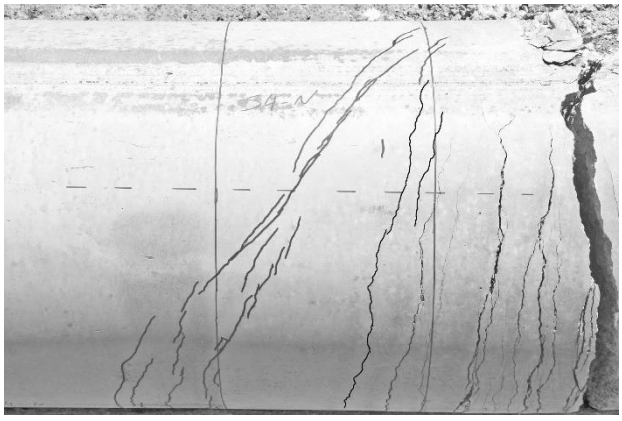

e) Specimen 4 north span concrete cracking

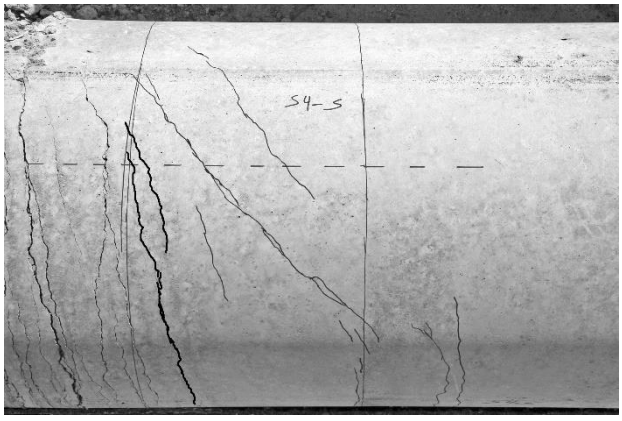

f) Specimen 4 south span concrete cracking

Figure 4.18: Specimen 4 state photos
(*a/D* = 0.5, D/t=80, L_T=D)

4.5 SPECIMEN 5

Specimen 5 was a tube steel-concrete interface variation of Specimen 2, the baseline specimen for a/D = 0.5, and was tested 29 May 2015. It had a muddied interface, a tail length of 40 inches, a straight seam weld, and no internal reinforcement. It achieved 1.32 times $M_{p,PSDM}$ and 2.17 times

$V_{n\ (WSDOT)}$ and failed in flexure. The tube tore at the bottom in flexure approximately 0.5 inches north of mid-span after significant flexural deformations occurred. The tear in the steel was vertical. There were no visible shear deformations in the steel but limited diagonal shear cracks formed in the concrete in the shear spans. The tube steel buckled on both the north and the south ends of the pure moment region symmetrically. Extensive flexural cracking of the concrete fill was also noted in the pure flexural region. Figure 4.19 shows the normalized moment-normalized displacement plot. Figure 4.20 shows the shear-displacement plot. Figures 4.21 a – f show the CFT at final deformation states and the condition of the concrete at the end of the test. South is to the left in each photograph.

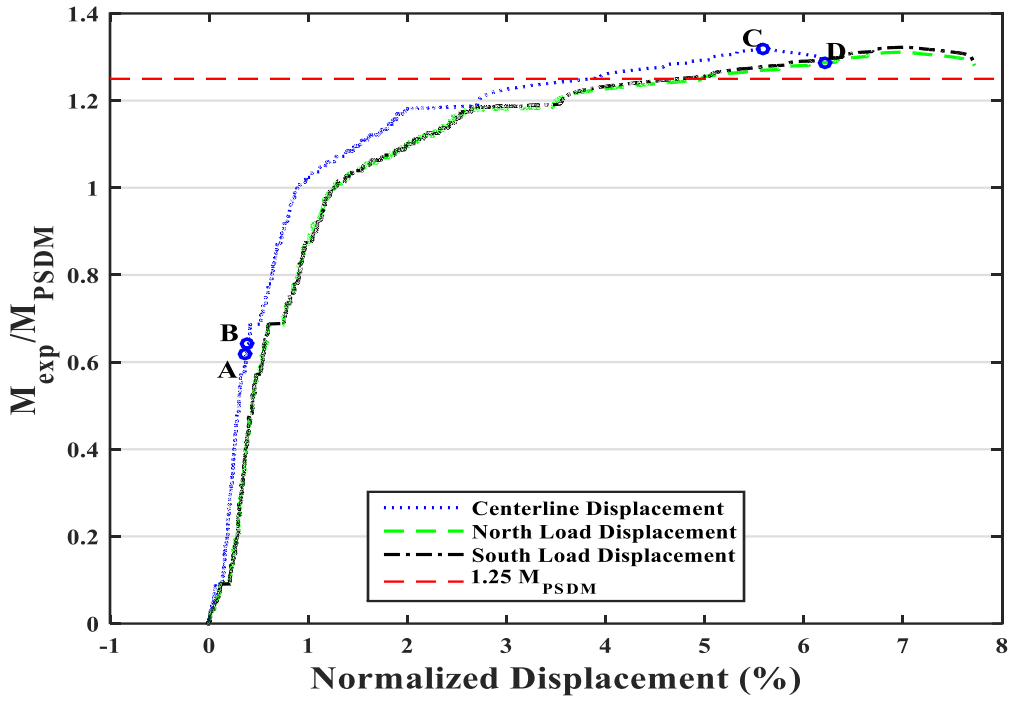

Figure 4.19: Specimen 5 moment-displacement plot

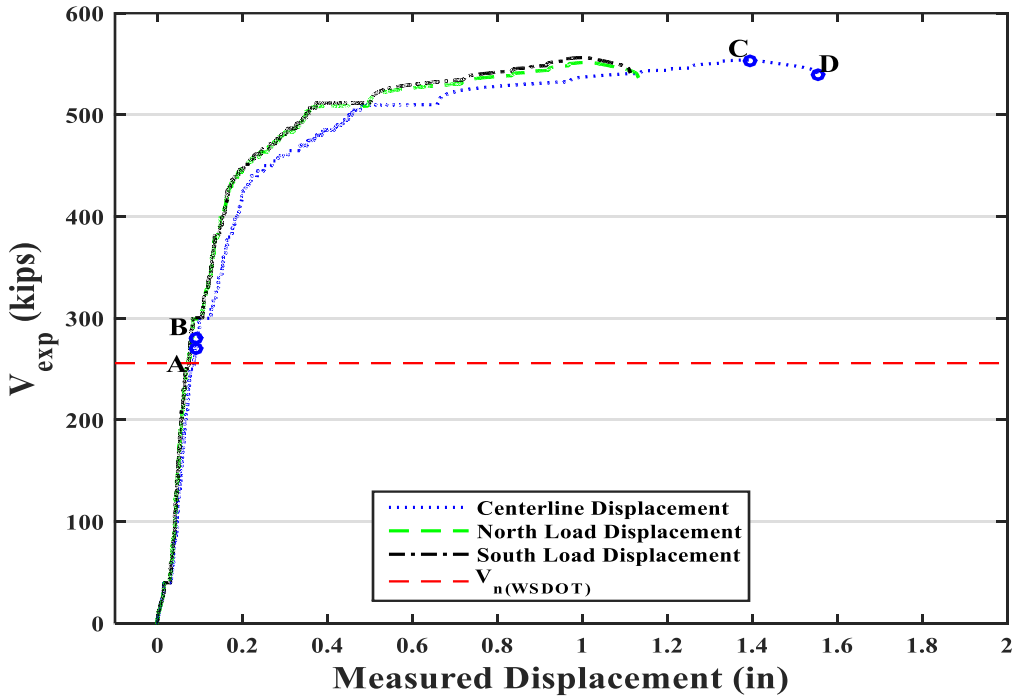

Figure 4.20: Specimen 5 shear-displacement plot

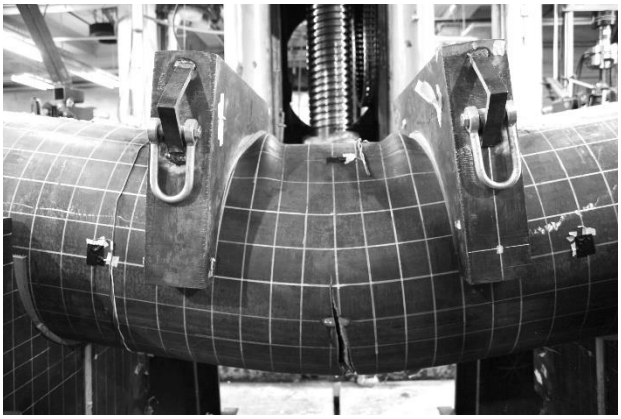

a) Specimen 5 final state

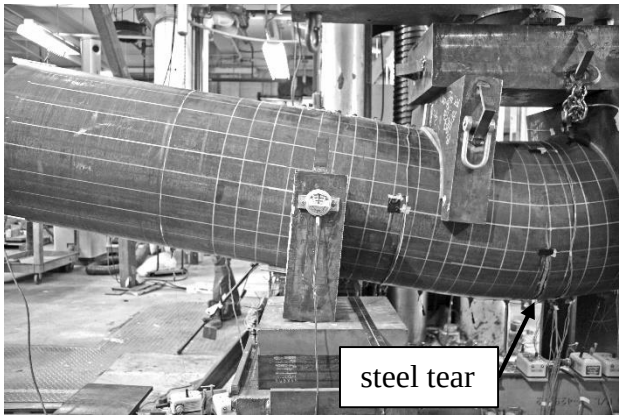

b) Specimen 5 final state

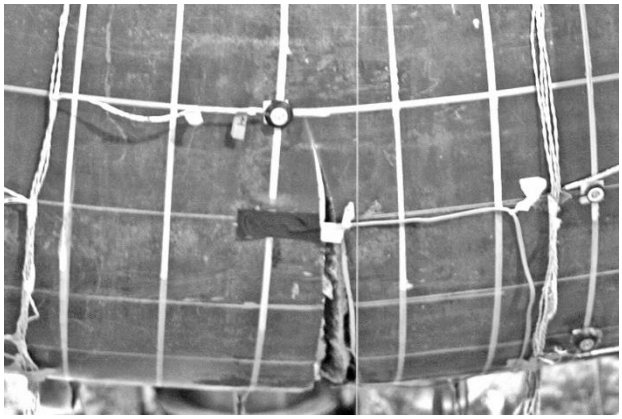

c) Specimen 5 steel tear

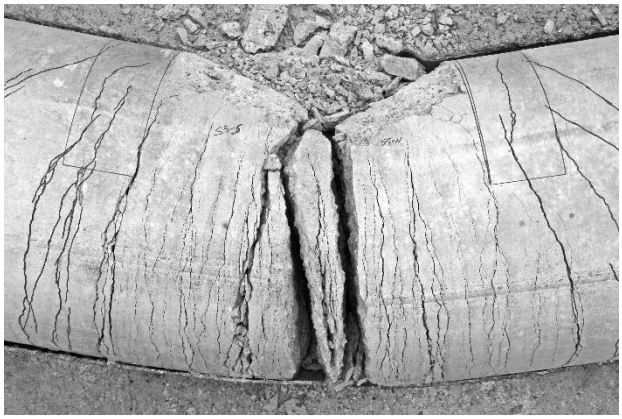

d) Specimen 5 mid-span concrete cracking

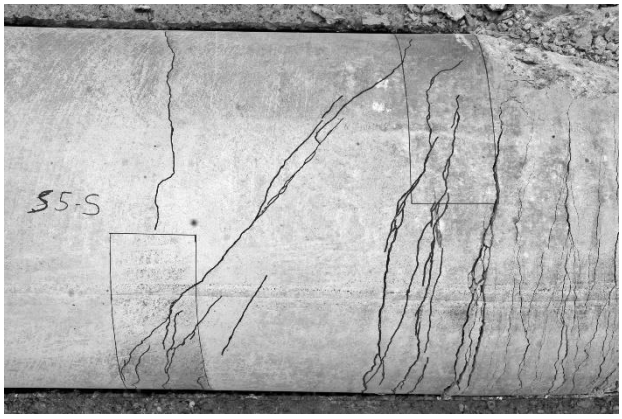

e) Specimen 5 south span concrete cracking

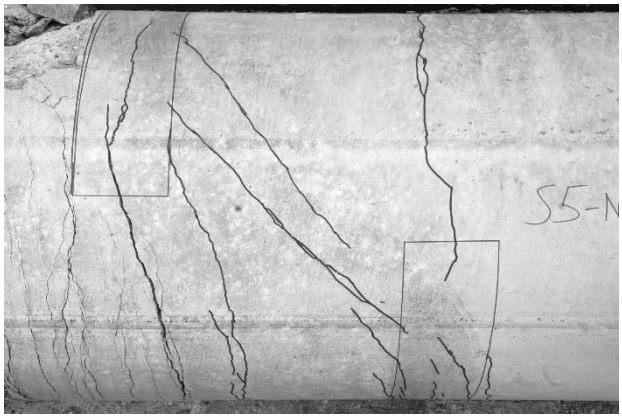

f) Specimen 5 north span concrete cracking

Figure 4.21: Specimen 5 state photos
(*a/D* = 0.5, D/t=80, muddied interface)

4.6 SPECIMEN 6

Specimen 6 was a steel tube type variation of Specimen 2, the baseline specimen for a/D = 0.5, and was tested 12 June 2015. It had a clean interface, a tail length of 40”, a spiral seam weld, a higher yield stress, and no internal reinforcement. It achieved 1.37 times $M_{p,PSDM}$ and 2.20 times $V_{n\ (WSDOT)}$ and failed in flexure. The tube tore at the bottom in flexure approximately 1.5 inches north of mid-span after significant flexural deformations occurred. The tear in the steel was vertical and extended farther up the tube than in any of the other specimens. This likely due to the presence of the spiral weld. There were no visible shear deformations in the steel but limited diagonal shear cracks formed in the concrete in the shear spans. The tube steel buckled on both the north and the south ends of the pure moment region symmetrically. Extensive flexural cracking of the concrete fill was also noted in the pure flexural region. Figure 4.22 shows the normalized moment-normalized displacement plot. Figure 4.23 shows the shear-displacement plot. Figures 4.24 a – f show the CFT at final deformation states and the condition of the concrete at the end of the test. South is to the left in each photograph.

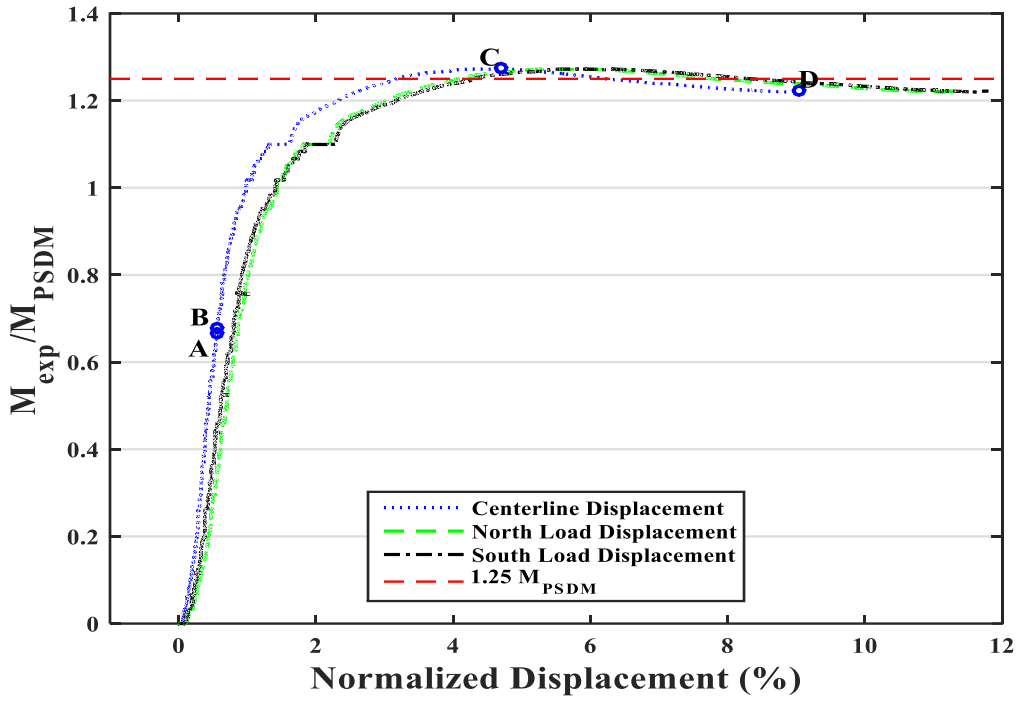

Figure 4.22: Specimen 6 moment-displacement plot

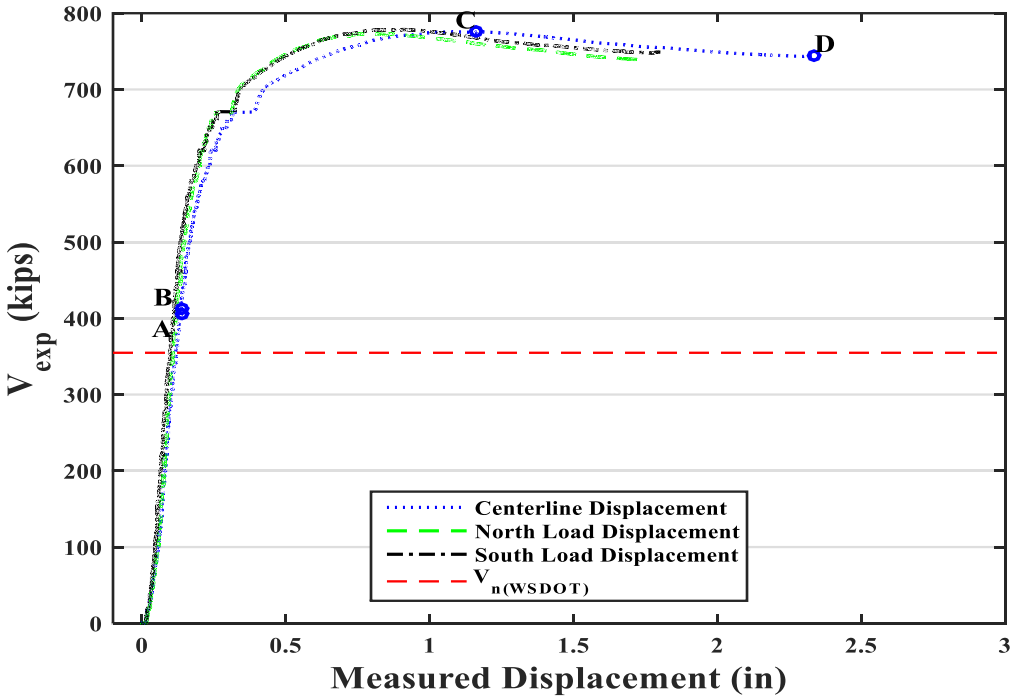

Figure 4.23: Specimen 6 shear-displacement plot

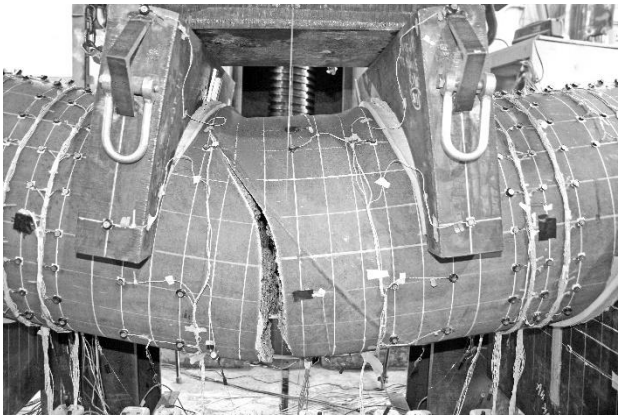

a) Specimen 6 final state

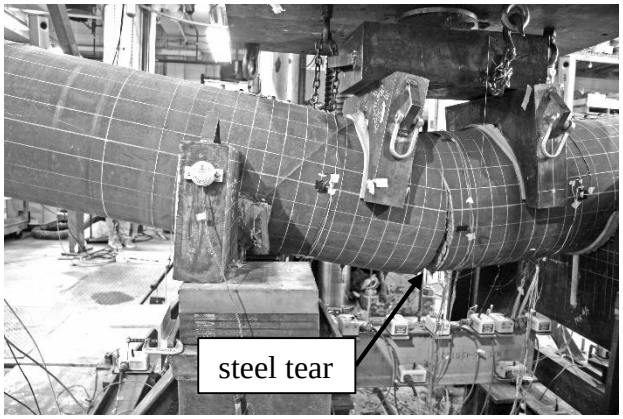

b) Specimen 6 final state

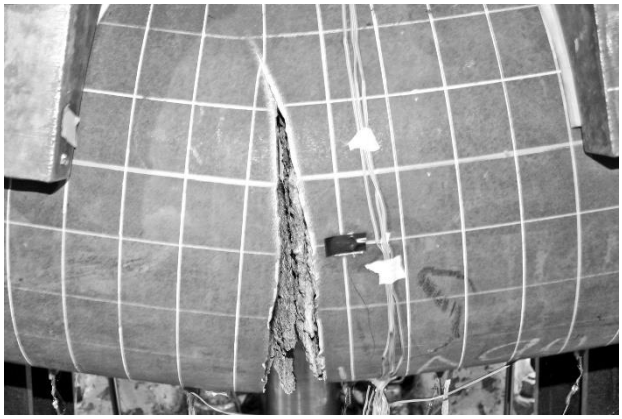

c) Specimen 6 steel tear

d) Specimen 6 mid-span concrete cracking

e) Specimen 6 south span concrete cracking

f) Specimen 6 north span concrete cracking

Figure 4.24: Specimen 6 state photos
(*a/D* = 0.5, D/t=80, spiral weld)

4.7 SPECIMEN 7

Specimen 7 was an internally reinforced variation of Specimen 10, the baseline specimen for *a/D* = 0.375, and was tested 10 July 2015. It had a clean interface, a tail length of 40", a straight seam weld, and 1.04% internal reinforcement. The amount of internal reinforcement was chosen as a practical minimum for RCFTs based on discussions with engineers at WSDOT. It achieved 1.17 times $M_{p,PSDM}$ and 2.74 times $V_{n\ (WSDOT)}$ and failed due to flexure-shear interaction. The tube tore at the bottom approximately 10 inches north of mid-span after significant flexural and shear deformations occurred. The tear was inclined slightly from the vertical at roughly half the angle of the concrete strut. Three layers of reinforcing bars ruptured along the inclined plane of the crack in the concrete strut. The shear deformations were seen primarily in the steel in the north shear span. The concrete experienced extensive diagonal shear cracking and deformations in both shear spans. The tube steel buckled on the north end of the pure moment region with no visible buckling on the south end. Extensive flexural cracking of the concrete fill was also noted in the pure flexural region. Figure 4.25 shows the normalized moment-normalized displacement plot. Figure 4.26 shows the shear-displacement plot. Figures 4.27 a – f show the CFT at final deformation states and the condition of the concrete at the end of the test. The images of the concrete cracks were lost for this specimen but they were similar in nature to Specimen 8 except with more vertical cracks in the pure moment region. North is to the left in each photograph.

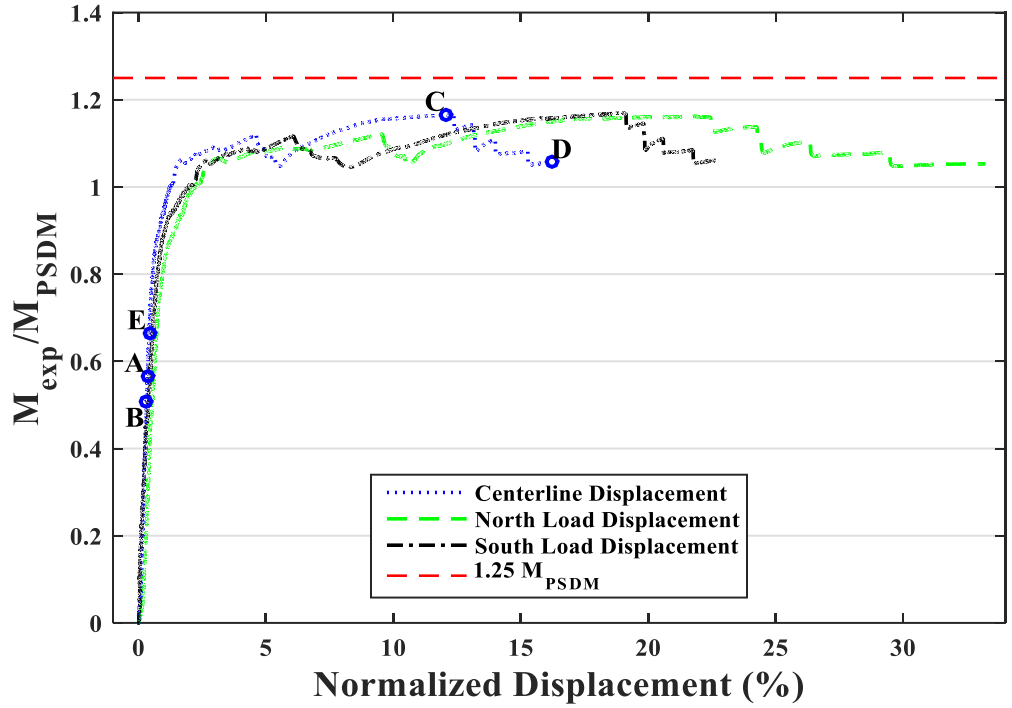

Figure 4.25: Specimen 7 moment-displacement plot

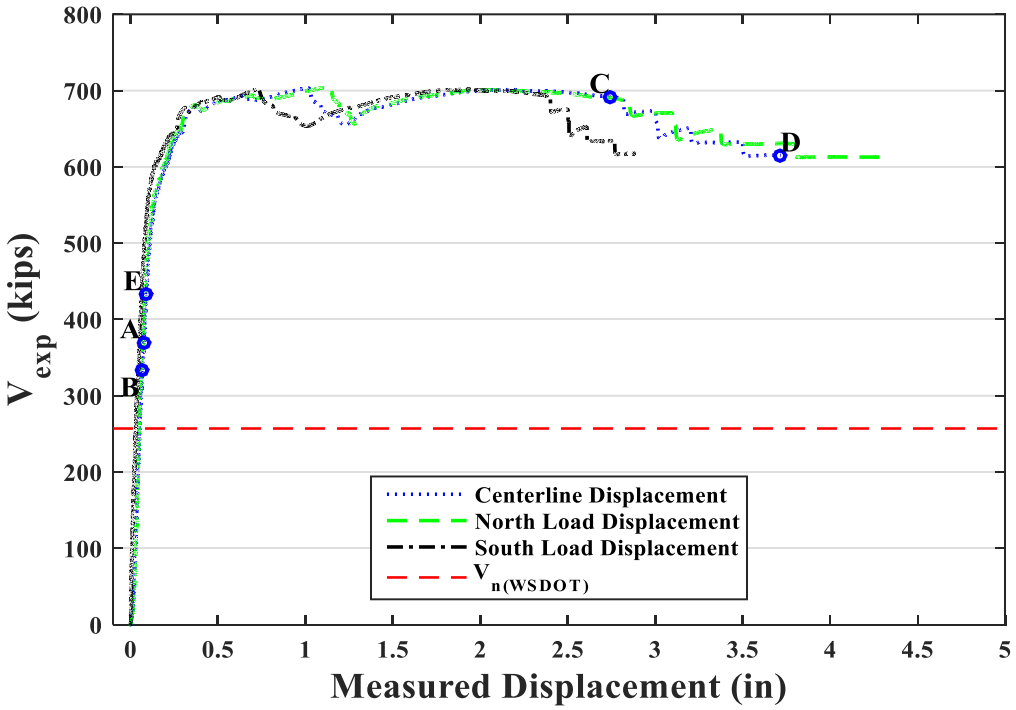

Figure 4.26: Specimen 7 shear-displacement plot

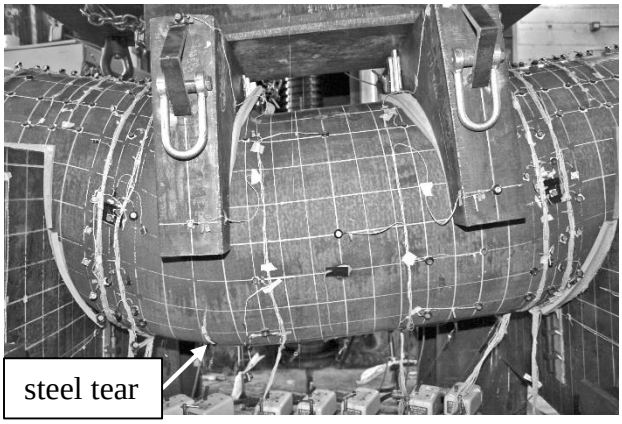

a) Specimen 7 final state

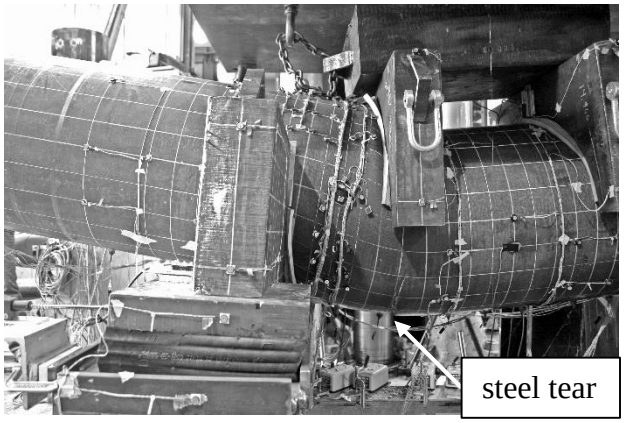

b) Specimen 7 final state

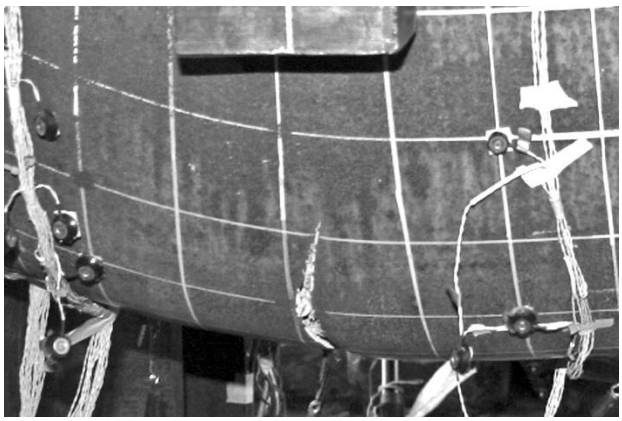

c) Specimen 7 steel tear

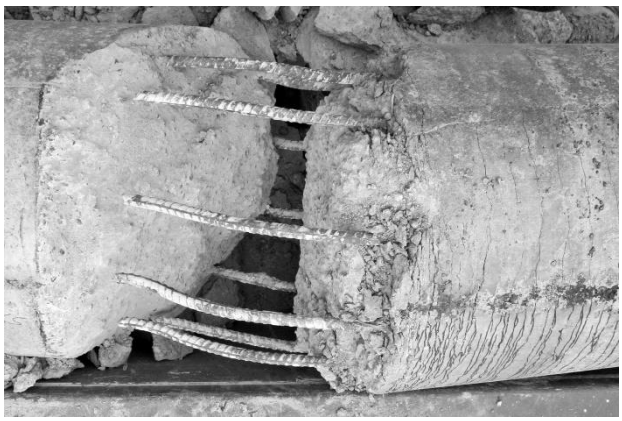

d) Specimen 7 north span reinforcement

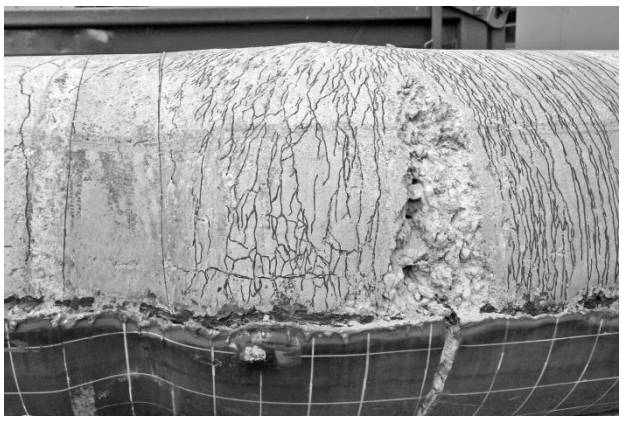

e) Specimen 7 north span cracking from bottom

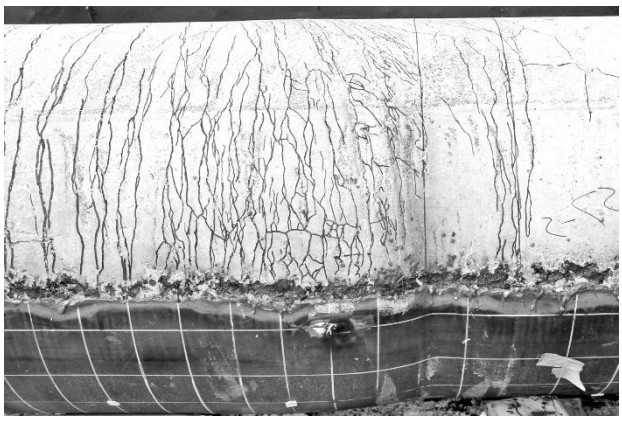

f) Specimen 7 south span cracking from bottom

Figure 4.27: Specimen 7 state photos
(*a/D*=0.375, D/t=80, ρ_{int}=1.04%)

4.8 SPECIMEN 8

Specimen 8 was an internally reinforced variation of Specimen 10, the baseline specimen for *a/D* = 0.375, and was tested 16 July 2015. It had a clean interface, a tail length of 40”, a straight seam weld, and 2.00% internal reinforcement. The amount of internal reinforcement was chosen as a practical maximum for RCFTs based on discussions with engineers at WSDOT. It achieved 1.03 times $M_{p,PSDM}$ and 2.92 times $V_{n\ (WSDOT)}$ and failed in shear. The tube tore at the bottom approximately 12 inches south of mid-span after significant shear deformations occurred. The tear in the steel was inclined from the vertical at generally the same angle as the concrete strut. Three layers of reinforcing bars ruptured along the inclined plane of the tear in the tube steel. The shear deformations were seen in the steel in both shear spans, and the concrete experienced extensive diagonal shear cracking and deformations in both shear spans. The tube steel experienced minor flexural buckling on the south end of the pure moment region with no visible buckling on the north end. There was limited flexural cracking in the pure moment region. Figure 4.28 shows the normalized moment-normalized displacement plot. Figure 4.29 shows the shear-displacement plot. Figures 4.30 a – f show the CFT at final deformation states and the condition of the concrete at the end of the test. South is to the left in each photograph.

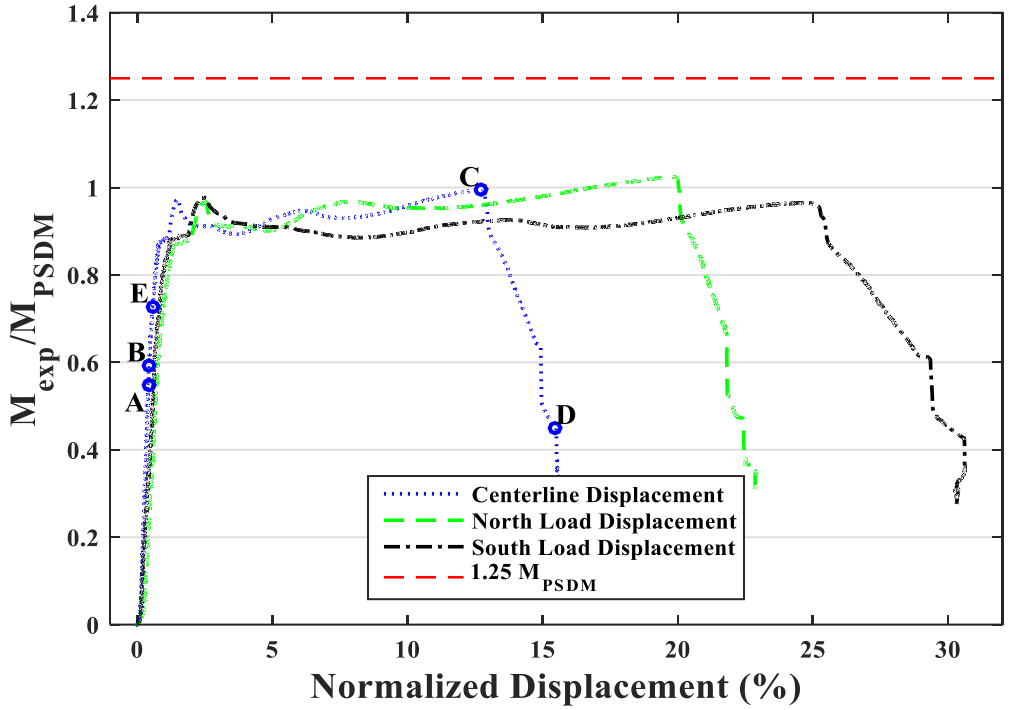

Figure 4.28: Specimen 8 moment-displacement plot

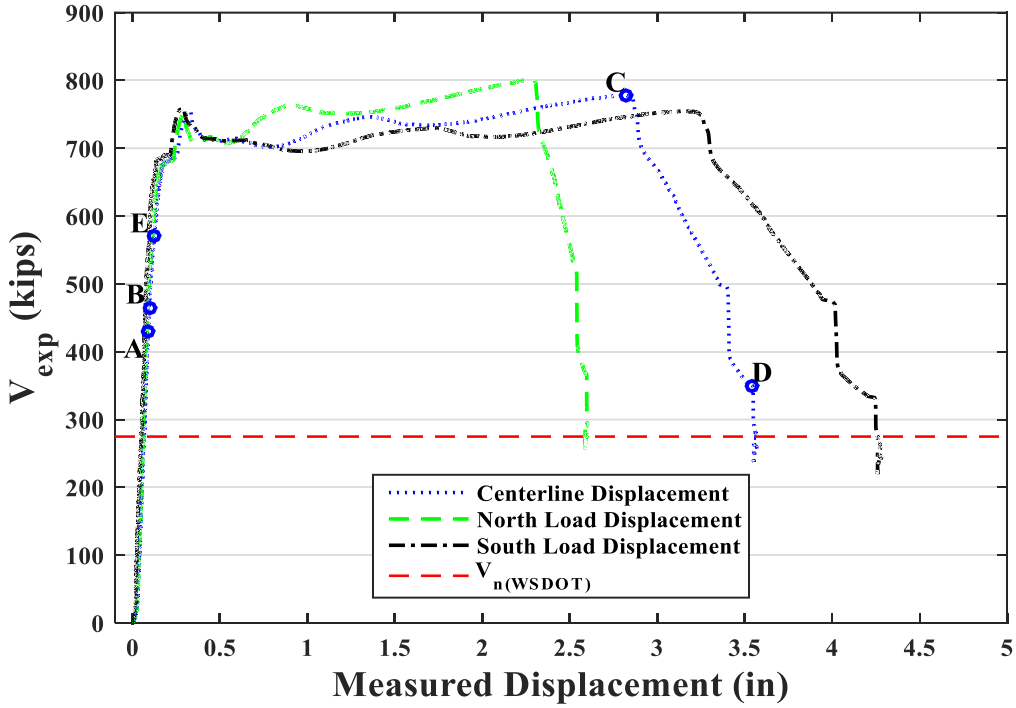

Figure 4.29: Specimen 8 shear-displacement plot

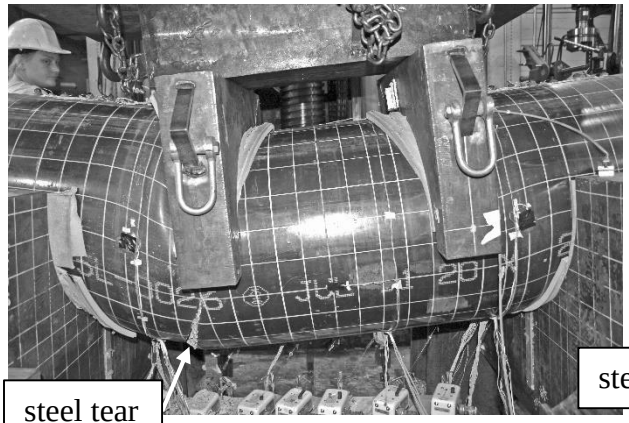

a) Specimen 8 final state

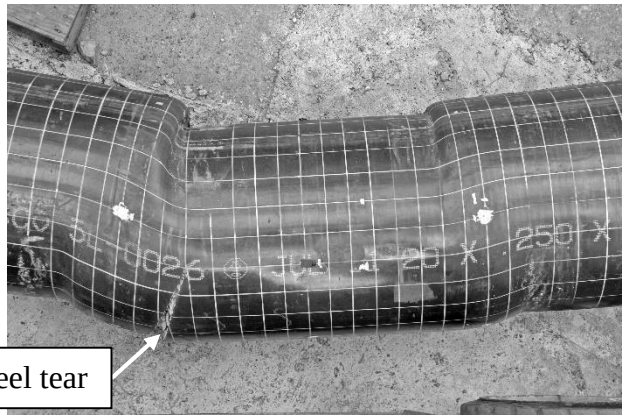

b) Specimen 8 final state

c) Specimen 8 steel tear

d) Specimen 8 mid-span concrete cracking

e) Specimen 8 south span concrete cracking

f) Specimen 8 north span concrete cracking

Figure 4.30: Specimen 8 state photos
(*a/D*=0.375, D/t=80, ρ_{int}=2.00%)

4.9 SPECIMEN 9

Specimen 9 was a tube steel-concrete interface variation of Specimen 2, the baseline specimen for a/D = 0.5, and was tested 23 June 2015. It had a greased interface, a tail length of 40 inches, a straight seam weld, and no internal reinforcement. It achieved 1.06 times $M_{p,PSDM}$ and 1.72 times $V_{n\ (WSDOT)}$ and failed in flexure due to a loss of bond. The tube tore at the bottom due to flexure-shear interaction approximately 6 inches south of mid-span after significant flexural deformations, flexural buckling, and shear deformations occurred. The tear was approximately vertical. The composite action was greatly reduced by the greased interface, and sections of the concrete fill exhibited large rigid body displacements, e.g. the concrete in the south tail slipped over 4 inches at the end. The reduction in composite action effectively concentrated the cracking in the concrete fill into a few, large cracks in contrast to the widely distributed crack pattern seen in the other CFT tests. Figure 4.31 shows the normalized moment-normalized displacement plot. Figure 4.32 shows the shear-displacement plot. Figures 4.33 a – f show the CFT at final deformation states and the condition of the concrete at the end of the test. North is to the left in each photograph.

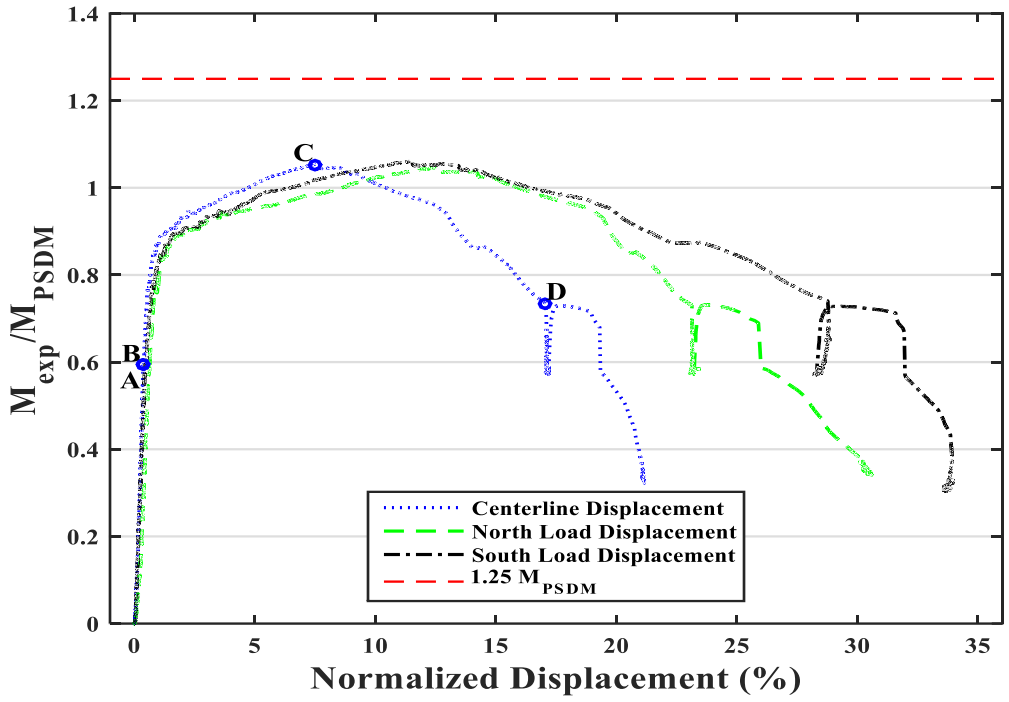

Figure 4.31: Specimen 9 moment-displacement plot

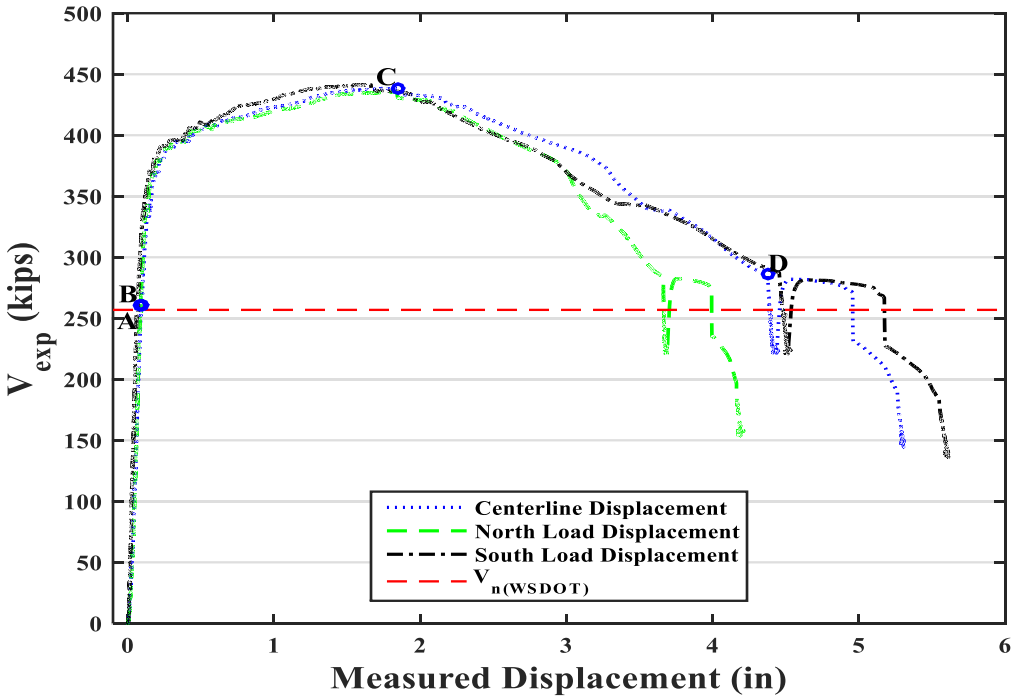

Figure 4.32: Specimen 9 shear-displacement plot

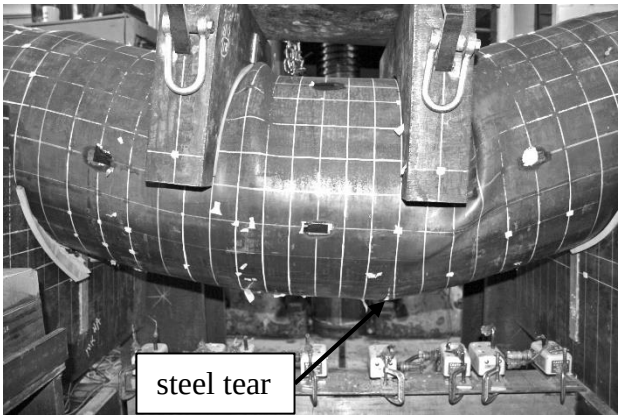

a) Specimen 9 final state

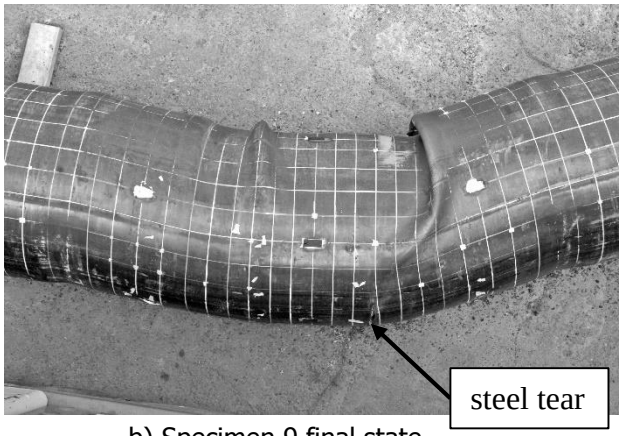

b) Specimen 9 final state

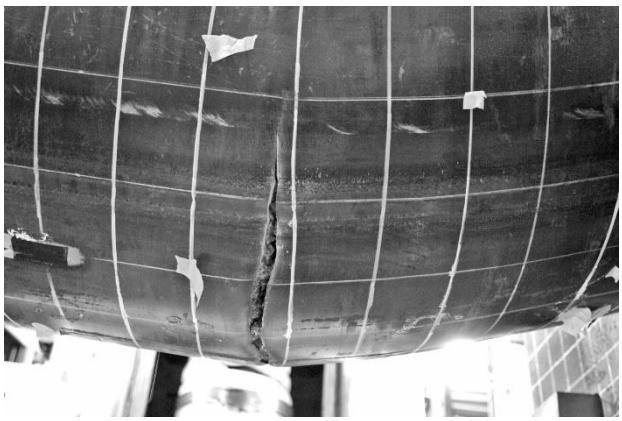

c) Specimen 9 steel tear

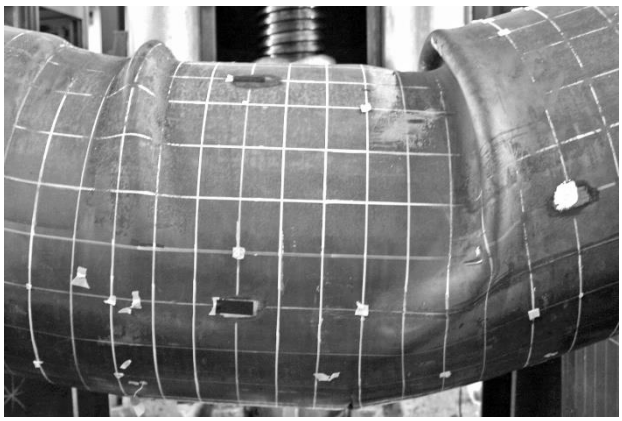

d) Specimen 9 steel buckling

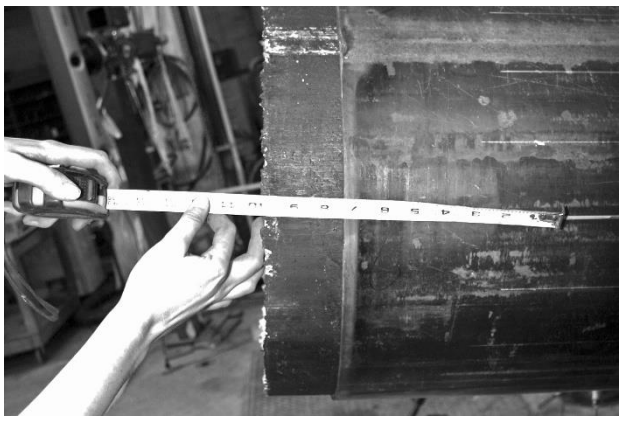

e) Specimen 9 south end concrete slip

f) Specimen 9 concrete cracking

Figure 4.33: Specimen 9 state photos
(*a/D* = 0.5, D/t=80, greased interface)

4.10 SPECIMEN 10

Specimen 10 is the baseline specimen for a/D = 0.375 and was tested 2 July 2015. It had a clean interface, a tail length of 40 inches, a straight seam weld, and no internal reinforcement. It achieved 1.29 times $M_{p,PSDM}$ and 2.49 times $V_{n\ (WSDOT)}$ and failed due to flexure-shear interaction. The tube tore at the bottom approximately 15.5 inches south of mid-span after significant flexural and shear deformations occurred. The shear deformations were seen in both shear spans but were more substantial in the south shear span. Diagonal shear cracking and deformation were clearly noted in the north shear span and were particularly severe in the south shear span. The tear was inclined slightly away from vertical. The tube steel buckled on both the north and the south ends of the pure moment region with more significant buckling on the north end. Flexural cracking of the concrete fill was also noted in the pure moment region. Figure 4.34 shows the normalized moment-normalized displacement plot. Figure 4.35 shows the shear-displacement plot. Figures 4.36 a – f show the CFT at final deformation states and the condition of the concrete at the end of the test. North is to the left in each photograph.

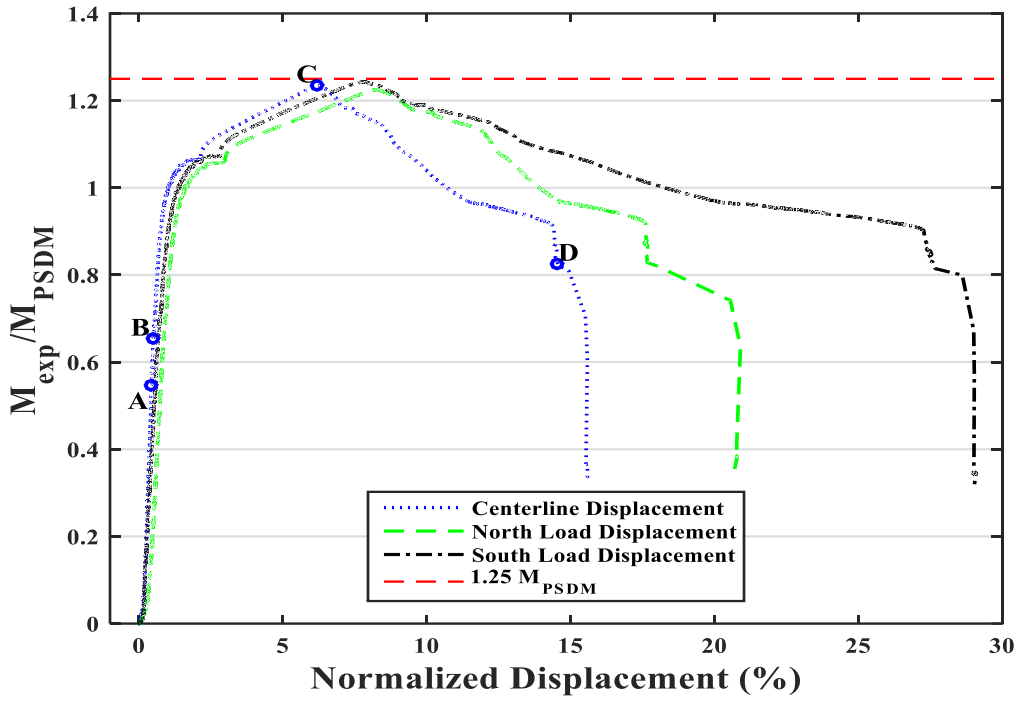

Figure 4.34: Specimen 10 moment-displacement plot

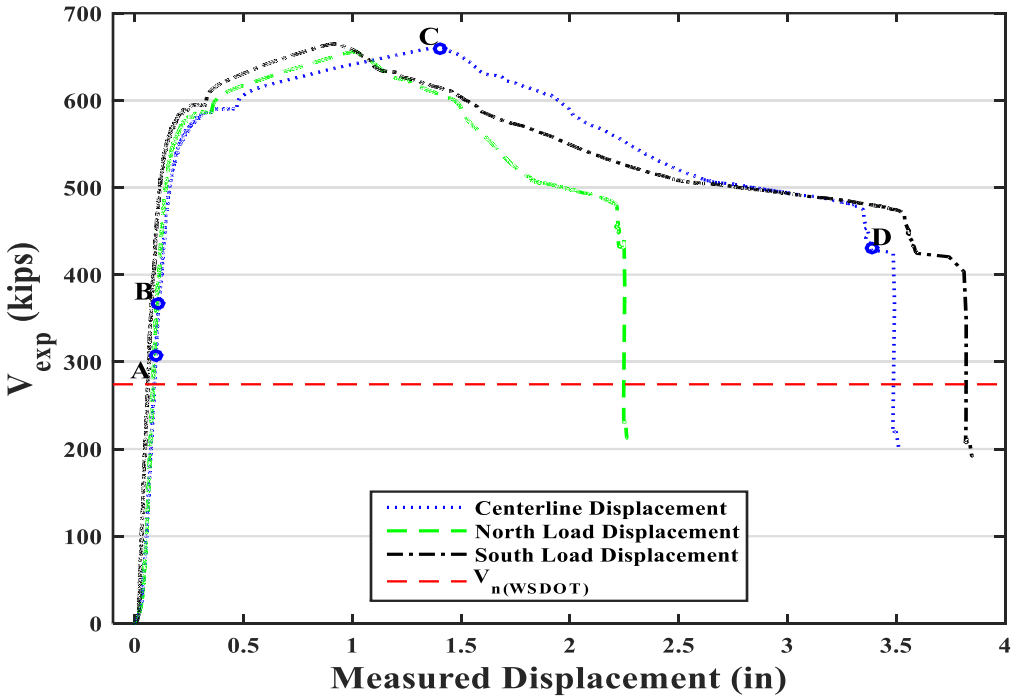

Figure 4.35: Specimen 10 shear-displacement plot

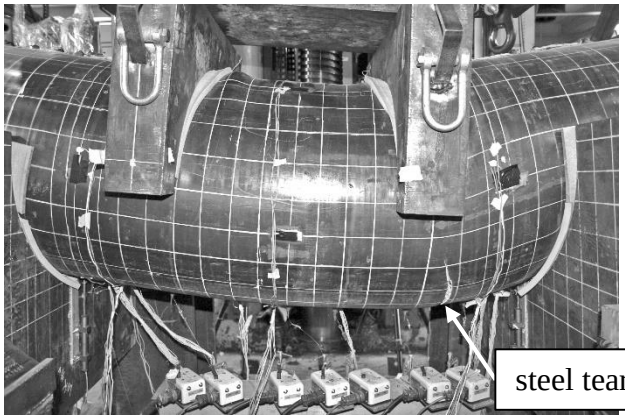

a) Specimen 10 final state

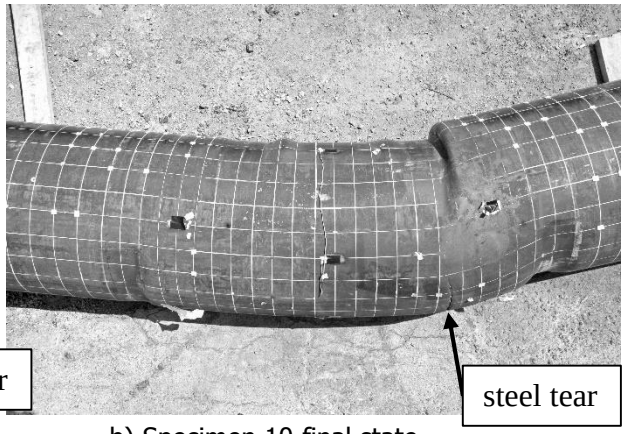

b) Specimen 10 final state

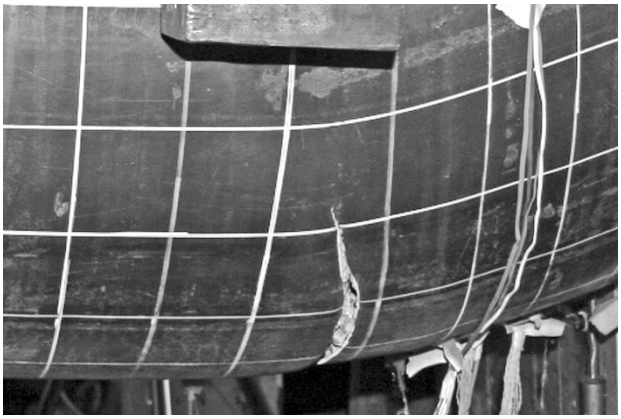

c) Specimen 10 steel tear

d) Specimen 10 mid-span concrete cracking

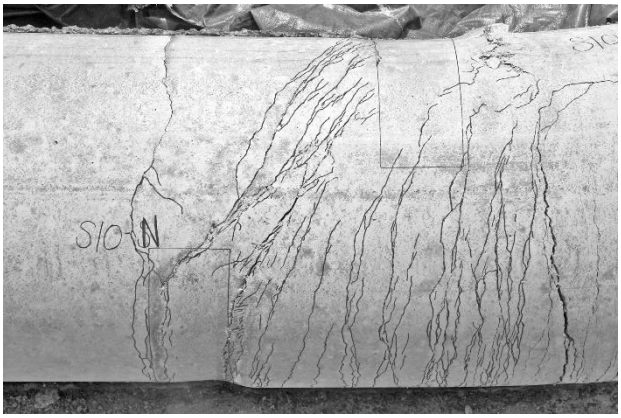

e) Specimen 10 north span concrete cracking

f) Specimen 10 south span concrete cracking

Figure 4.36: Specimen 10 state photos
(a/D = 0.375, D/t=80, ρ_{int}=0%)

4.11 SPECIMEN 11

Specimen 11 was a tail length variation of Specimen 10, the baseline specimen for a/D = 0.375, and was tested 7 July 2015. It had a clean interface, a tail length of 10", a straight seam weld, and no internal reinforcement. It achieved 1.01 times $M_{p,PSDM}$ and 2.08 times $V_{n\ (WSDOT)}$ and failed in shear due to a loss of bond strength on the south end. The tube tore at the bottom approximately 13 inches south of mid-span after significant shear deformations occurred. The tear was inclined from the vertical at an angle slightly less than the angle of the concrete strut. The shear deformations were seen almost exclusively in the south shear span. Extensive diagonal shear cracking and deformations occurred in the south shear span concrete while limited diagonal cracking was noted in the north shear span concrete. There were no visible signs of permanent flexural deformations or of flexural buckling of the tube steel in the pure moment region. Very limited flexural cracking of the concrete fill was also noted in the pure moment region. The south end of the tube experienced significant distortion of the circular cross-section as seen in Figure 4.37. Figure 4.38 shows the normalized moment-normalized displacement plot. Figure 4.39 shows the shear-displacement plot. Figures 4.40 a – f show the CFT at final deformation states and the condition of the concrete at the end of the test. North is to the left in each photograph.

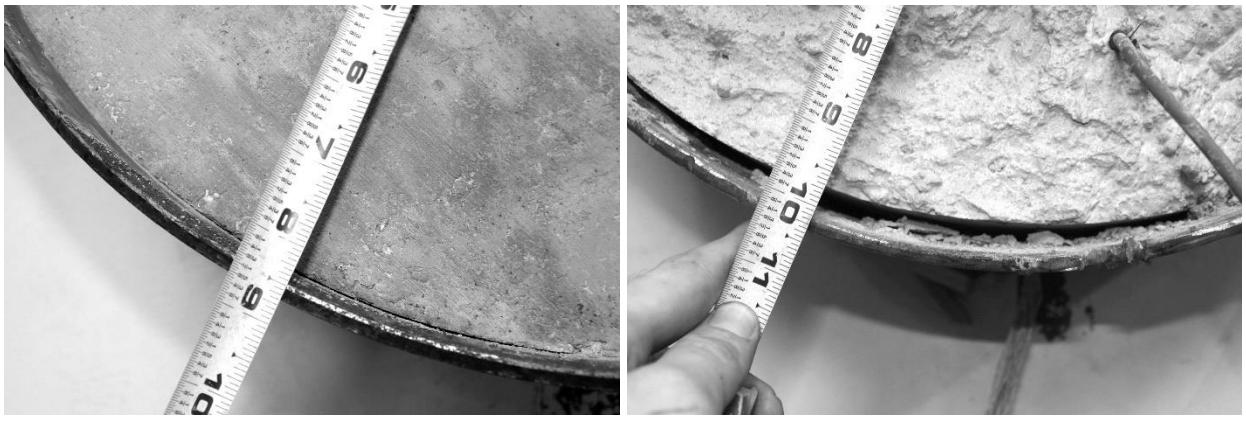

a) North end of CFT b) South end of CFT

Figure 4.37: Cross-sectional distortion of Specimen 11

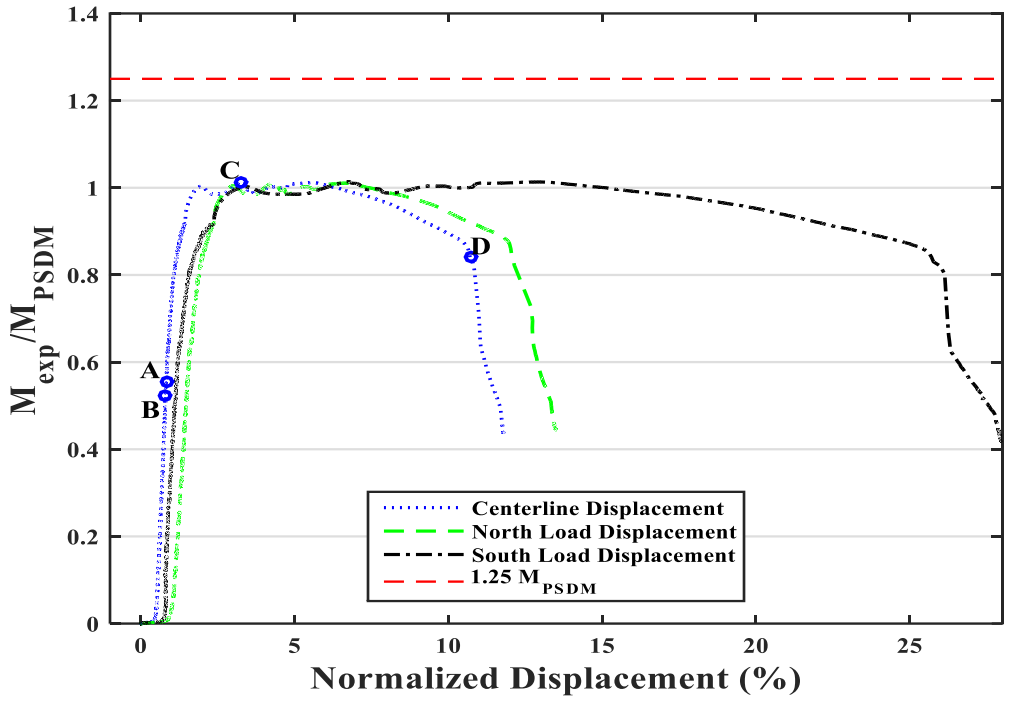

Figure 4.38: Specimen 11 moment-displacement plot

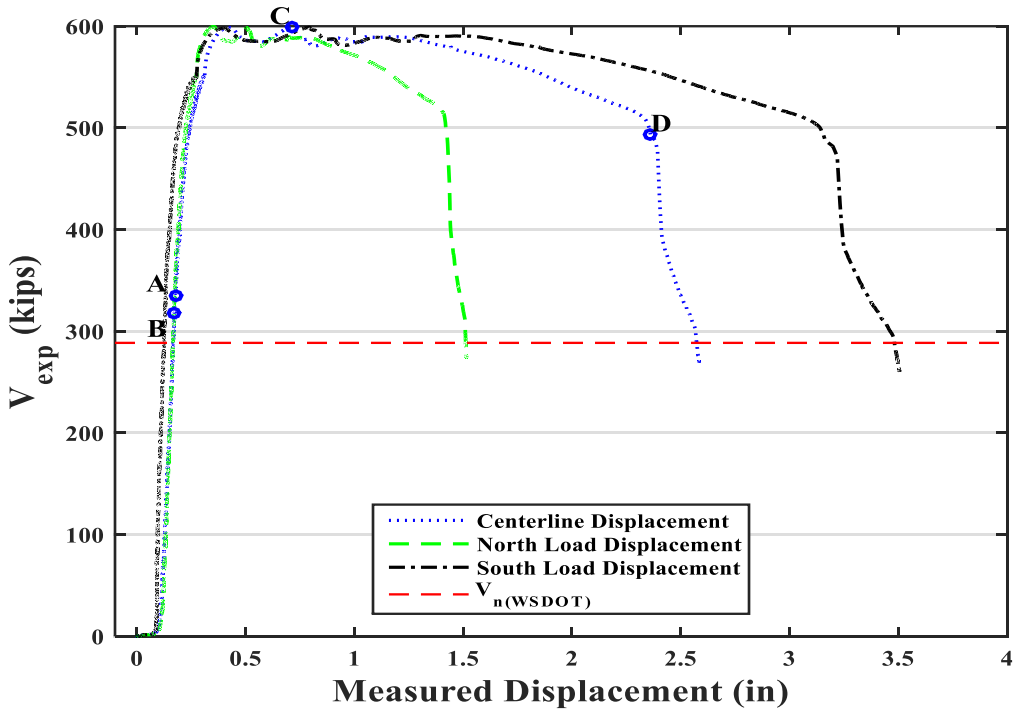

Figure 4.39: Specimen 11 shear-displacement plot

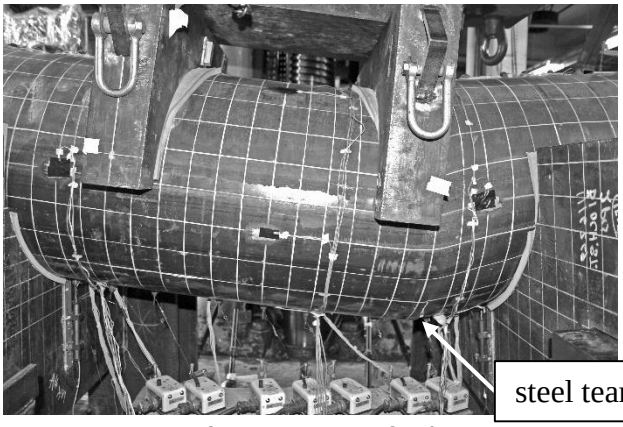

a) Specimen 11 final state

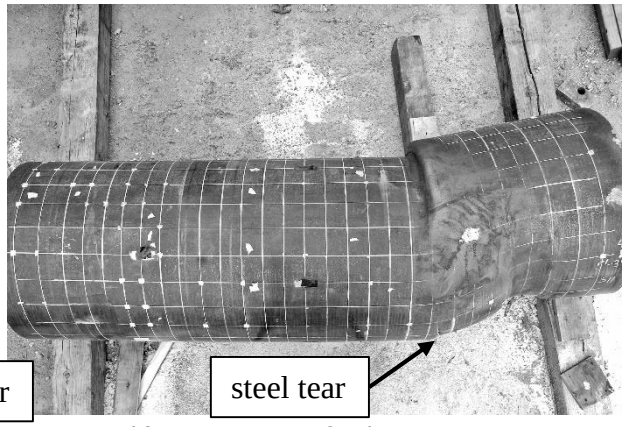

b) Specimen 11 final state

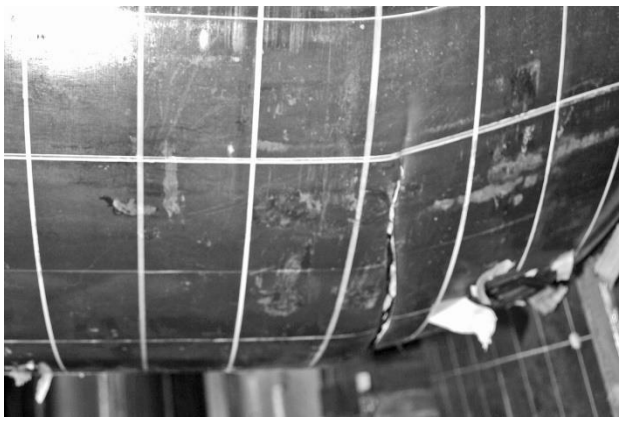

c) Specimen 11 steel tear

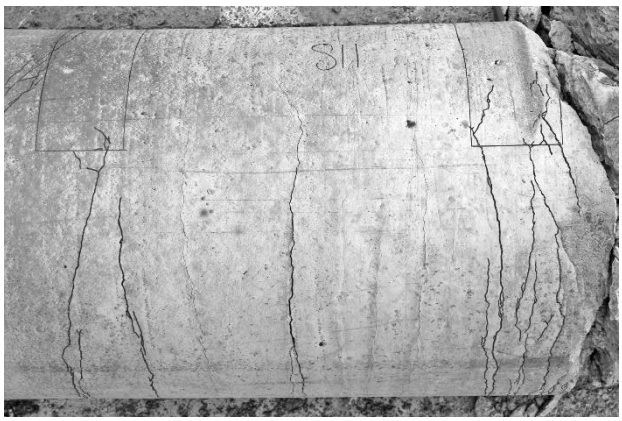

d) Specimen 11 mid-span concrete cracking

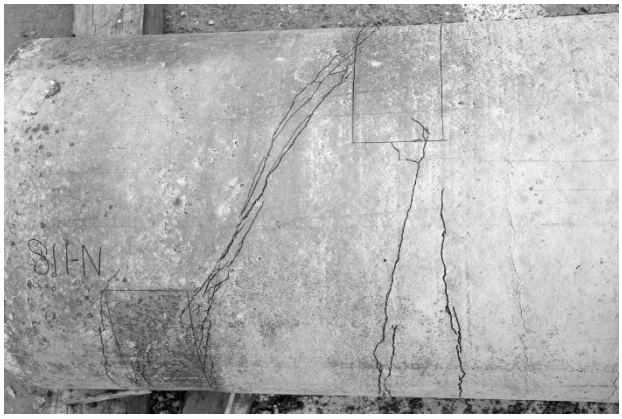

e) Specimen 11 north span concrete cracking

f) Specimen 11 south span concrete cracking

Figure 4.40: Specimen 11 state photos
(a/D = 0.375, D/t=80, L_T=D/2)

4.12 SPECIMEN 12

Specimen 12 was an internally reinforced variation of Specimen 2, the baseline specimen for a/D = 0.5, and was tested 18 June 2015. It had a clean interface, a tail length of 40”, a straight seam weld, and 1.13% internal reinforcement. The amount of internal reinforcement was chosen such that the required shear demand corresponding the plastic moment capacity would be equivalent to the required shear demand corresponding to the plastic moment capacity of Specimen 10, the baseline specimen for a/D = 0.375. It achieved 1.21 times $M_{p,PSDM}$ and 2.37 times $V_{n\ (WSDOT)}$ and failed due to flexure-shear interaction. The tube tore at the bottom approximately 11 inches south of mid-span after significant flexural and shear deformations occurred. The shear deformations were seen primarily in the south shear span and the tear was inclined from the vertical at roughly half the angle of the concrete strut. Extensive diagonal shear cracking and deformations occurred in the south shear span concrete while moderate, restrained diagonal shear cracking was noted in the north shear span. The tube steel buckled on both the north and the south ends of the pure moment region with approximately equal amplitude. Extensive flexural cracking of the concrete fill was also noted in the pure moment region. Figure 4.41 shows the normalized moment-normalized displacement plot. Figure 4.42 shows the shear-displacement plot. Figures 4.43 a – f show the CFT at final deformation states and the condition of the concrete at the end of the test. North is to the left in each photograph.

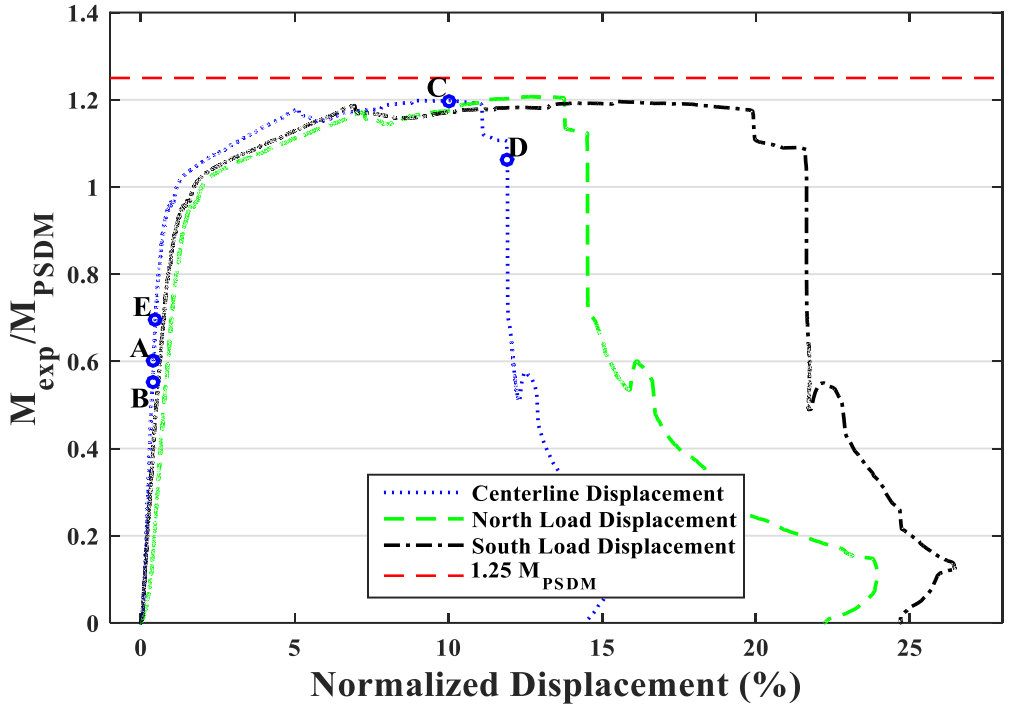

Figure 4.41: Specimen 12 moment-displacement plot

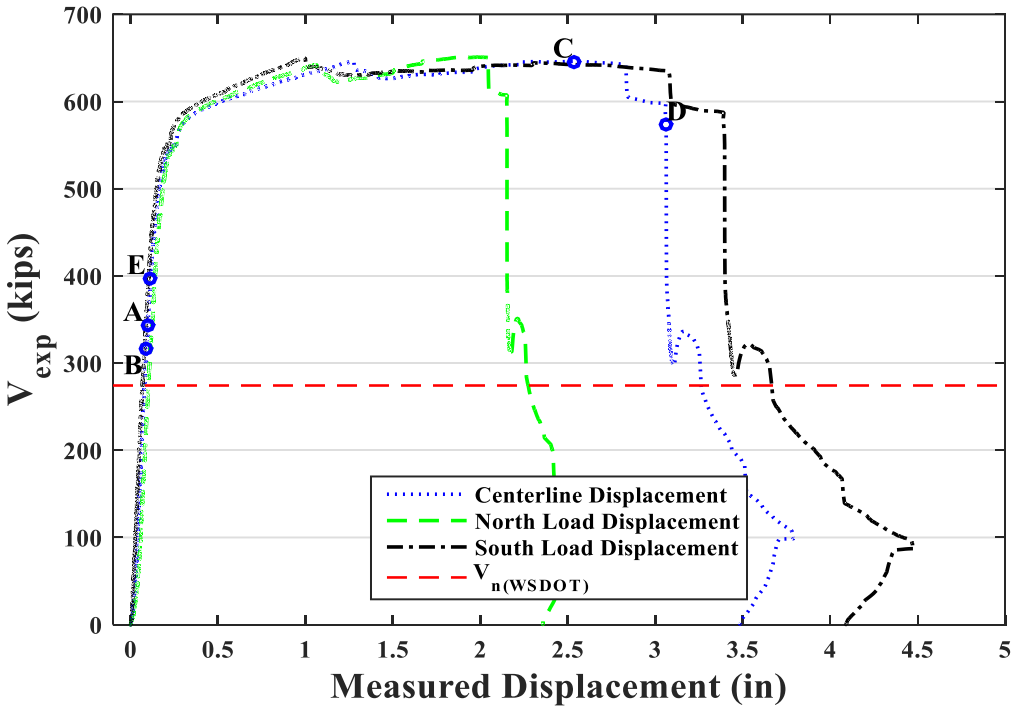

Figure 4.42: Specimen 12 shear-displacement plot

a) Specimen 12 final state

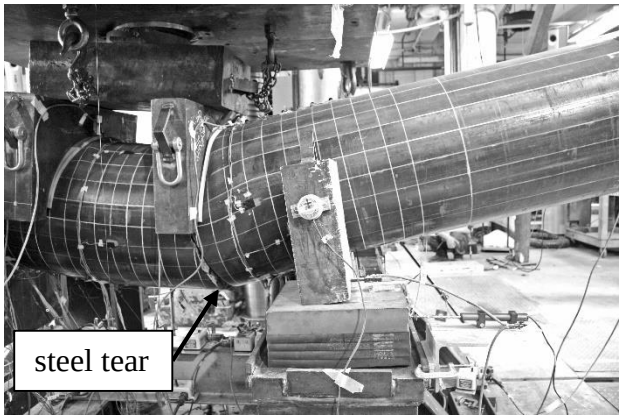

b) Specimen 12 final state

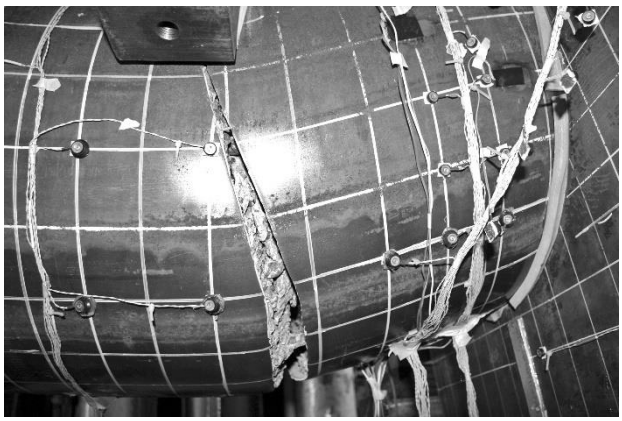

c) Specimen 12 steel tear

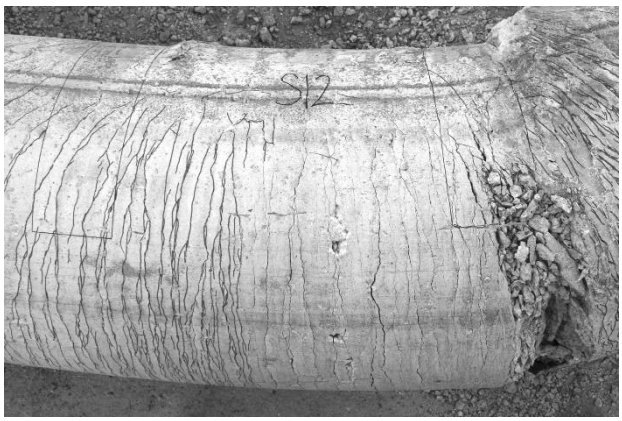

d) Specimen 12 mid-span concrete cracking

e) Specimen 12 north span concrete cracking

f) Specimen 12 south span concrete cracking

Figure 4.43: Specimen 12 state photos
(*a/D* = 0.5, D/t=80, ρ_{int}=1.13%)

4.13 SPECIMEN 13

Specimen 13 was an axial load variation of Specimen 11, the *a/D* = 0.375 specimen with the short tail length, and was tested 24 July 2015. It had a clean interface, a tail length of 10", a straight seam weld, no internal reinforcement, and an axial load of 8.5% of the compression capacity of the CFT. It achieved 1.12 times $M_{p,PSDM}$ and 2.60 times $V_{n\ (WSDOT)}$ and failed due to flexure-shear interaction. The tube did not tear since the test was stopped to avoid damaging the Williams rod used to apply the axial load. There were significant shear deformations in addition to less severe flexural deformations. The shear deformations were seen primarily in the south shear span. Extensive diagonal shear cracking and deformations occurred in the concrete fill in the south shear span while significant diagonal cracking was noted in the north shear span concrete. Flexural buckling only just initiated by the end of the test. Moderate flexural cracking was noted in the concrete fill in the pure moment region. The axial load was applied manually via a center-hole hydraulic ram. The axial load was maintained within +/-3% of the intended target until the normalized moment reached 1.10, at a normalized displacement of 1.58%, at which point the load dropped to 78% of the target and became difficult to control with the manual setup. Pressure was released from the ram four times in an attempt to maintain the axial load as constant as possible, at displacements of 1.58%, 2.17%, 2.48%, and 2.93%, which accounts for some of the sawtooth pattern in the plots. Other factors caused the sawtooth response about half of the time. The axial load was completely released at a displacement of 5.77% and then transverse loading was continued until 6.53%. Figure 4.44 shows the normalized moment-normalized displacement plot. Figure 4.45 shows the shear-displacement plot. Figures 4.46 a – f show the CFT at final deformation states and the condition of the concrete at the end of the test. North is to the left in each photograph.

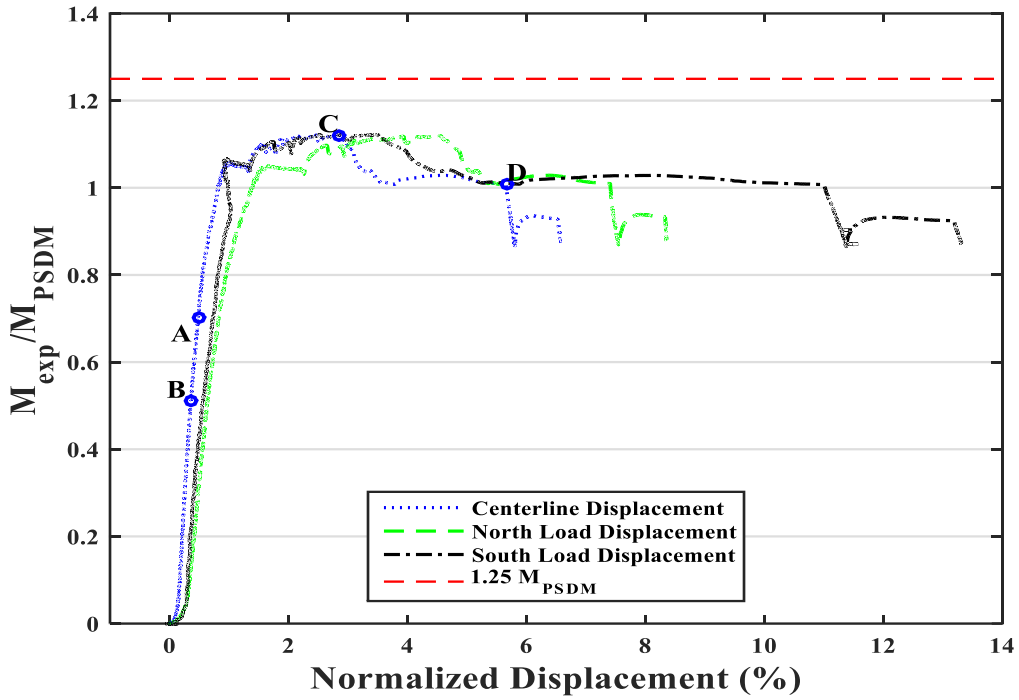

Figure 4.44: Specimen 13 moment-displacement plot

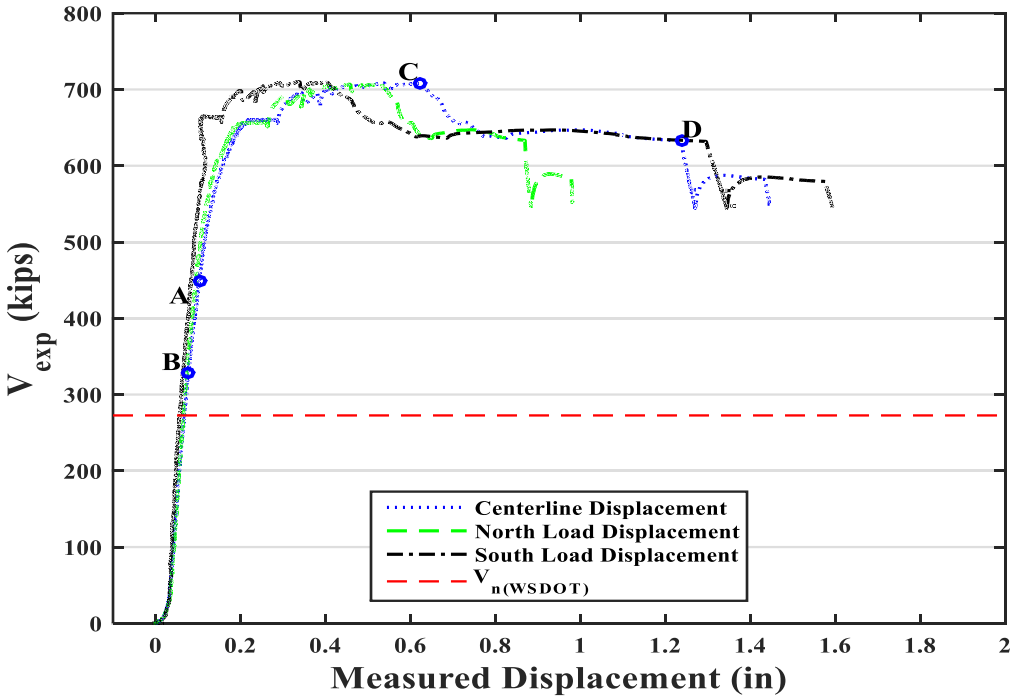

Figure 4.45: Specimen 13 shear-displacement plot

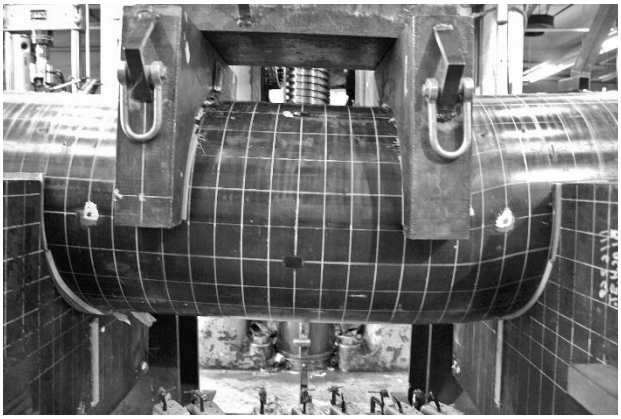

a) Specimen 13 final state

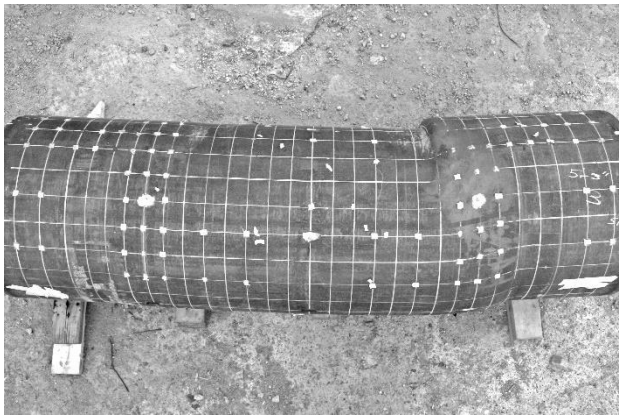

b) Specimen 13 final state

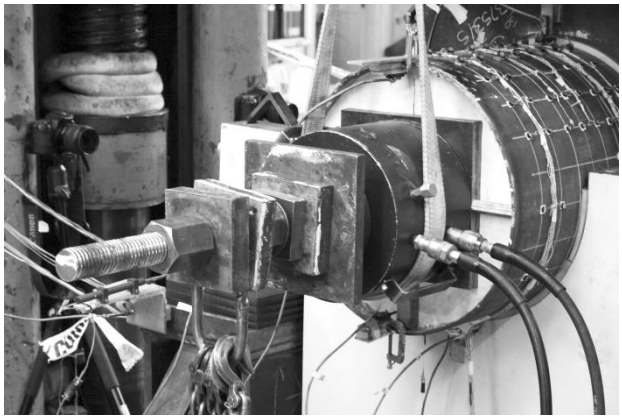

c) Specimen 13 jacking setup

d) Specimen 13 mid-span concrete cracking

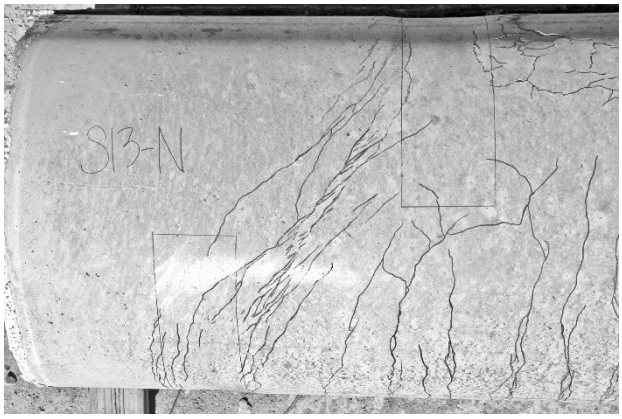

e) Specimen 13 north span concrete cracking

f) Specimen 13 south span concrete cracking

Figure 4.46: Specimen 13 state photos
(a/D = 0.375, D/t=80, L_T=D/2, P/P_0=0.085)

4.14 SPECIMEN 14

Specimen 14 is the baseline specimen for a/D = 0.25 and was tested 11 August 2015. It had a clean interface, a tail length of 40”, a straight seam weld, and no internal reinforcement. It achieved 1.11 times $M_{p,PSDM}$ and 2.89 times $V_{n\ (WSDOT)}$ and failed in shear. The tube tore at the bottom approximately 16 inches north of mid-span after significant shear deformations occurred. The shear deformations were visible in the north shear span. Extensive diagonal shear cracking and deformations occurred in the concrete fill in the north shear span while significant diagonal cracking was noted in the south shear span concrete. The tube also tore on the top at the north load cradle, a likely relic of the boundary condition. The tube steel exhibited no signs of flexural buckling in the pure moment region. Very limited flexural cracking of the concrete fill was also noted in the pure moment region. Figure 4.47 shows the normalized moment-normalized displacement plot. Figure 4.48 shows the shear-displacement plot. Figures 4.49 a – f show the CFT at final deformation states and the condition of the concrete at the end of the test. South is to the left in each photograph.

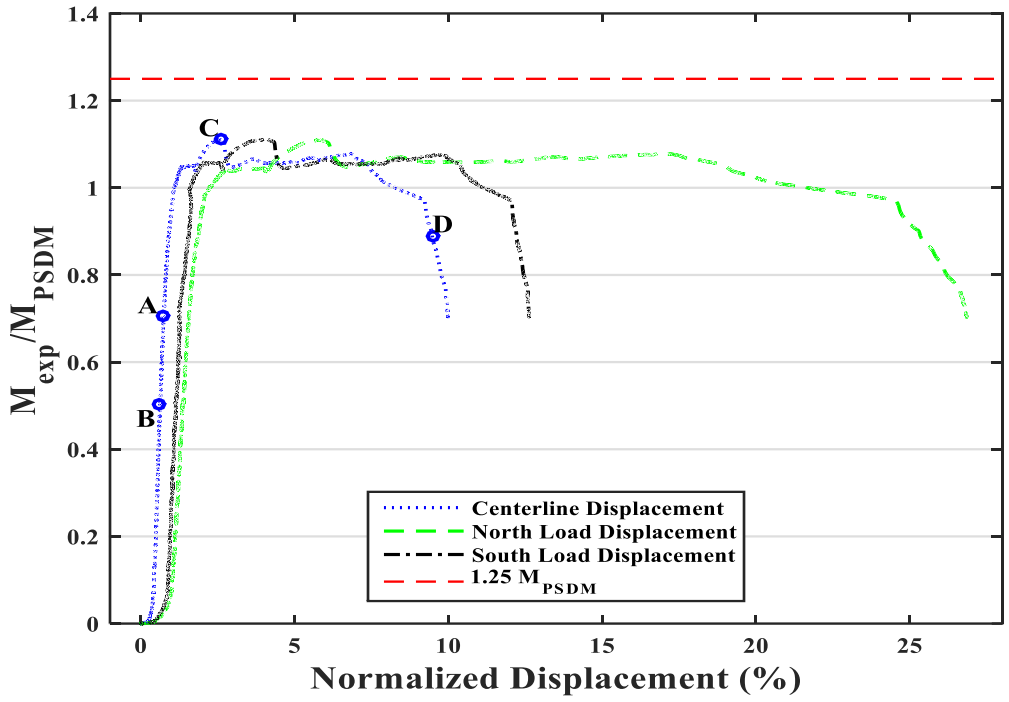

Figure 4.47: Specimen 14 moment-displacement plot

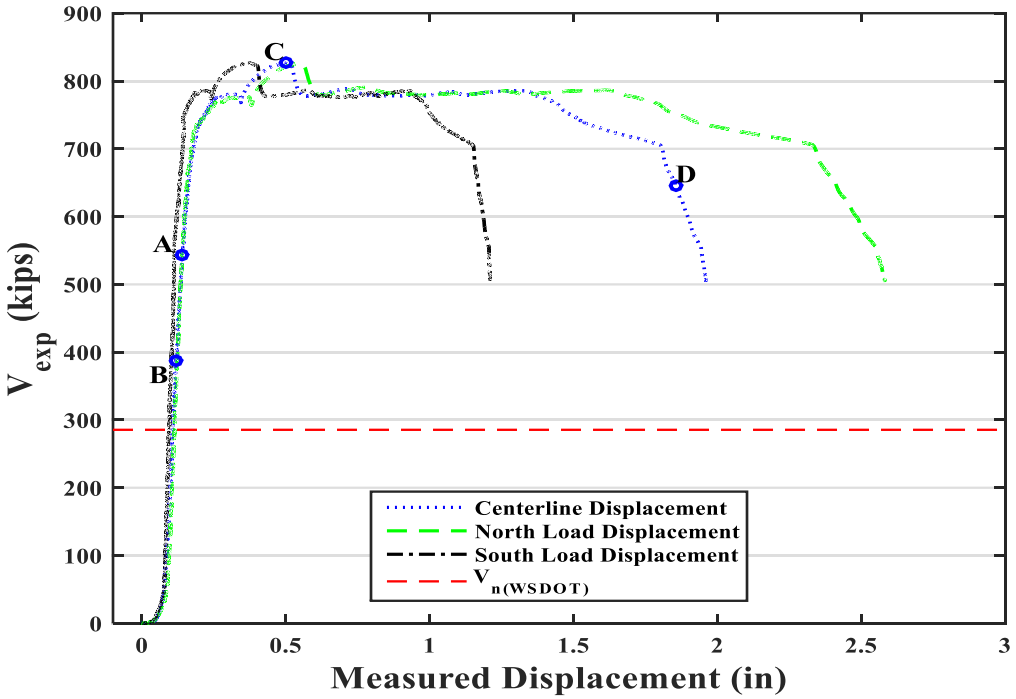

Figure 4.48: Specimen 14 shear-displacement plot

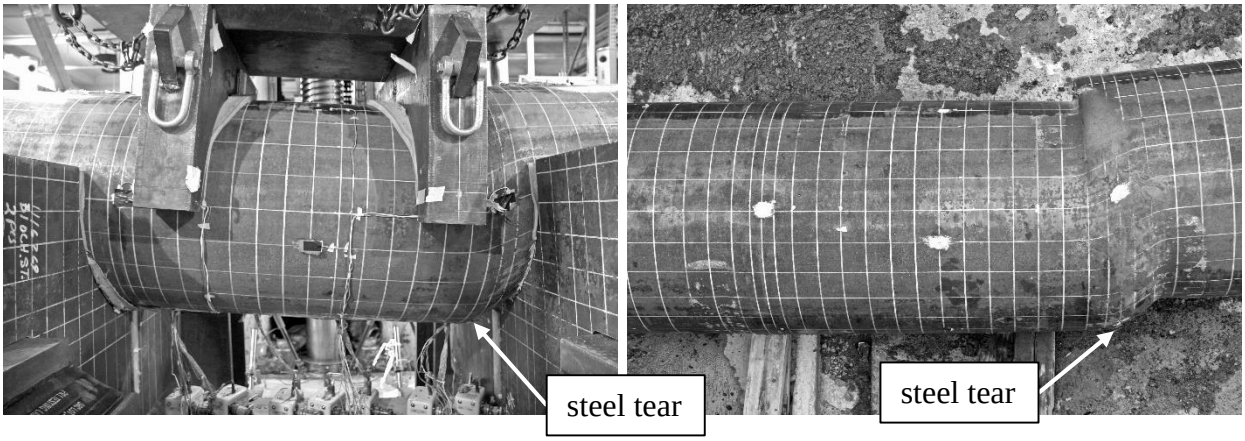

a) Specimen 14 final state

b) Specimen 14 final state

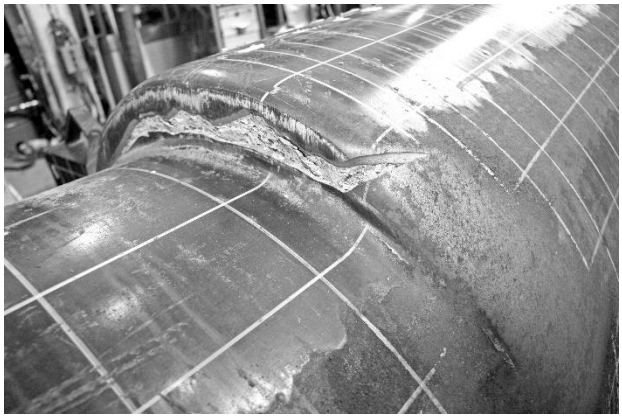

c) Specimen 14 top steel tear

d) Specimen 14 mid-span concrete cracking

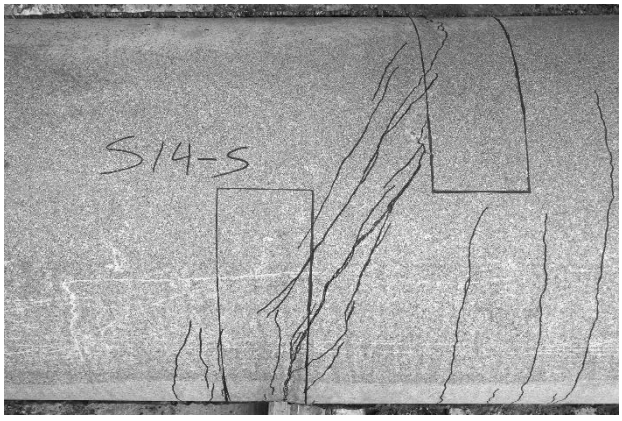

e) Specimen 14 south span concrete cracking

f) Specimen 14 north span concrete cracking

Figure 4.49: Specimen 14 state photos
(a/D = 0.25, D/t=80, L_T=2D)

4.15 SPECIMEN 15

Specimen 15 was the tail length variation of Specimen 14, the baseline specimen for a/D = 0.25, and was tested 17 August 2015. It had a clean interface, a tail length of 12.5”, a straight seam weld, and no internal reinforcement. It achieved 1.04 times $M_{p,PSDM}$ and 2.78 times $V_{n\ (WSDOT)}$ and failed in shear. The tube tore at the bottom approximately 17 inches north of mid-span, at the north support cradle, after significant shear deformations occurred. The tear was oriented at approximately the same angle as the concrete strut. The steel tube also tore at the top at the north load cradle, a likely relic of the boundary condition. The shear deformations were seen primarily in the north shear span. Extensive diagonal shear cracking and deformations occurred in the concrete fill in the north shear span while moderate diagonal cracking was noted in the south shear span concrete. The tube steel did not experience visible flexural buckling in the pure moment region and limited flexural cracking was noted in the concrete fill. The north end of the tube experienced significant distortion of the circular cross-section as seen in Figure 4.50. Figure 4.51 shows the normalized moment-normalized displacement plot. Figure 4.52 shows the shear-displacement plot. Figures 4.53 a – f show the CFT final deformation states and the condition of the concrete at the end of the test. South is to the left in each photograph.

a) South end of CFT b) North end of CFT

Figure 4.50: Cross-sectional distortion of Specimen 15

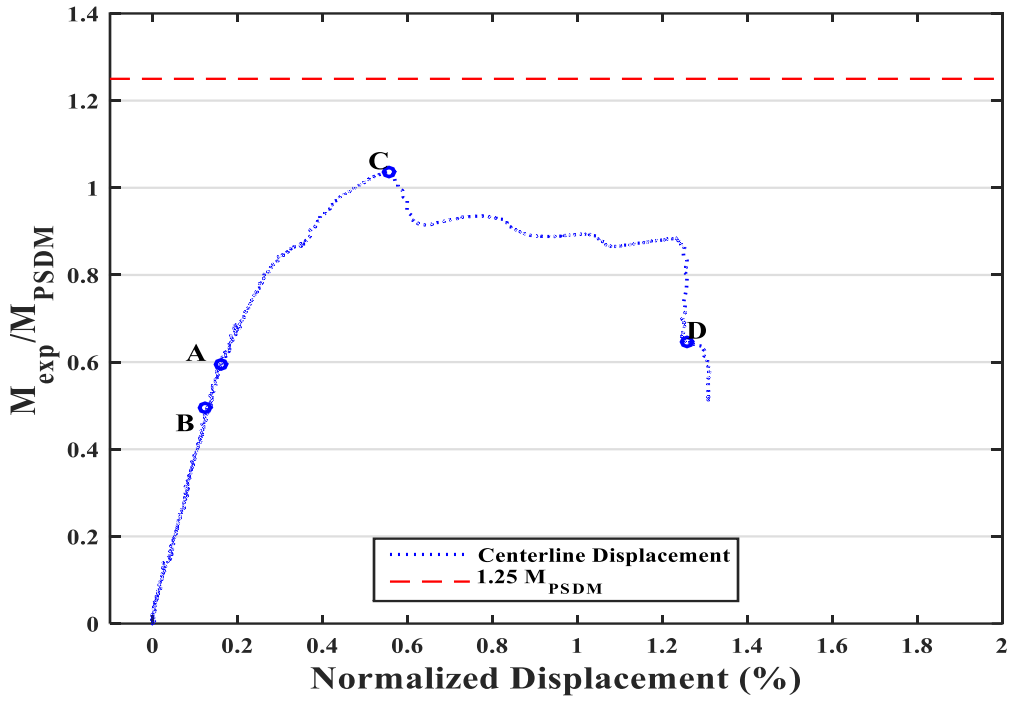

Figure 4.51: Specimen 15 moment-displacement plot

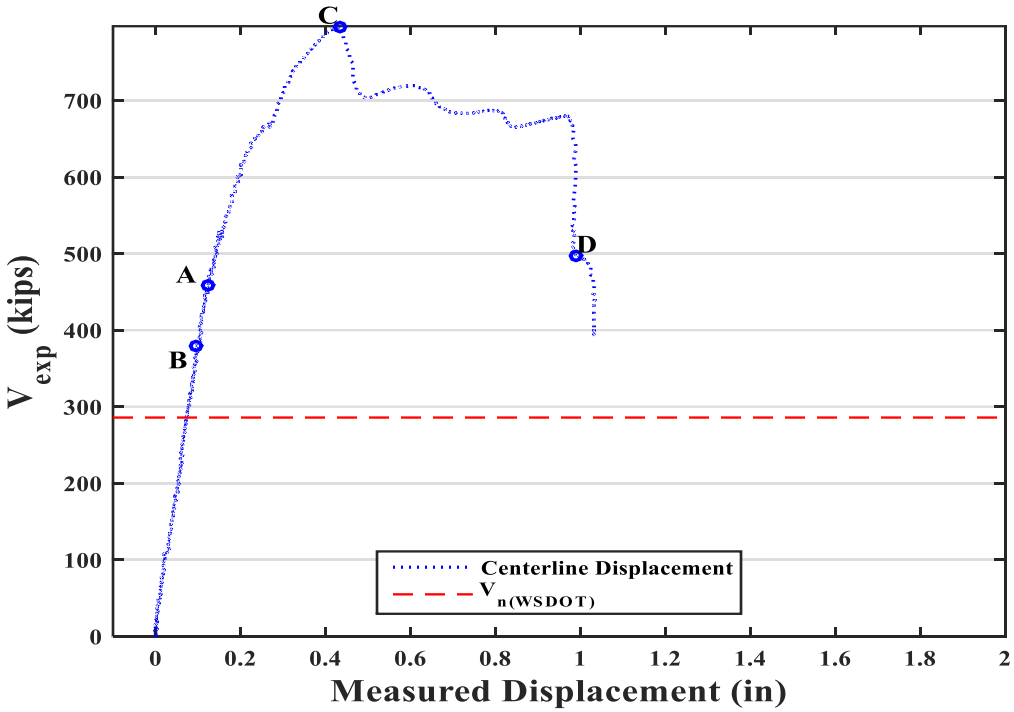

Figure 4.52: Specimen 15 shear-displacement plot

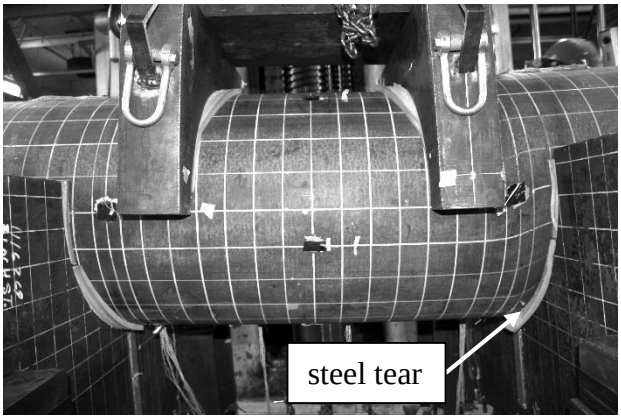

a) Specimen 15 final state

b) Specimen 15 final state

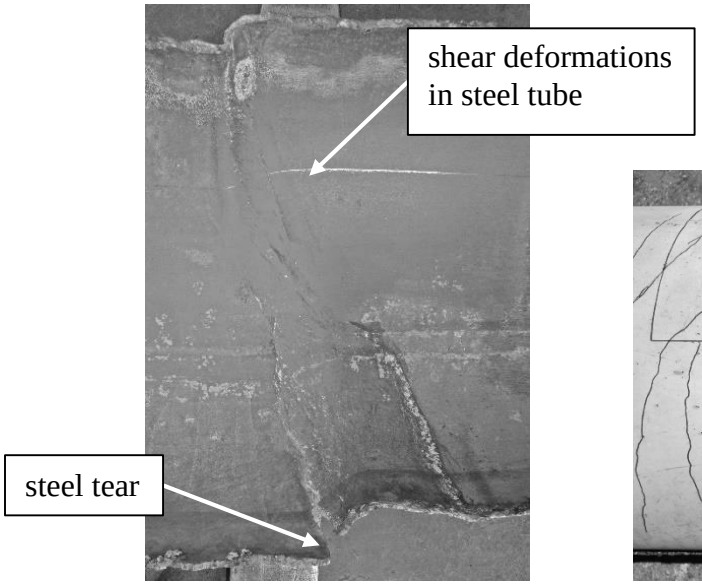

c) Specimen 15 steel tear and deformation at north span, inside face of tube

d) Specimen 15 mid-span concrete cracking

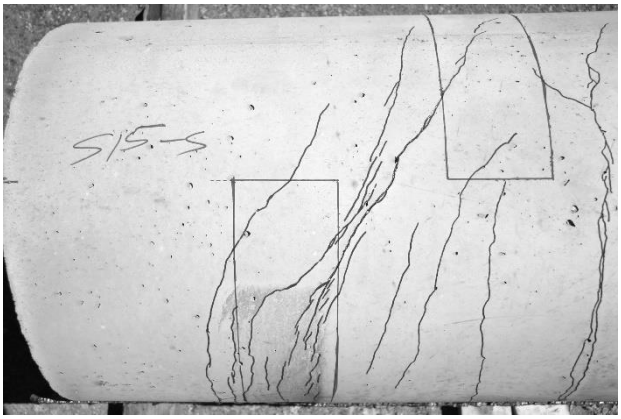

e) Specimen 15 south span concrete cracking

f) Specimen 15 north span concrete cracking

Figure 4.53: Specimen 15 state photos
(a/D = 0.25, D/t=80, L_T=D/2)

4.16 SPECIMEN 16

Specimen 16 was a concrete type variation of Specimen 10, the baseline specimen for a/D = 0.375, and was tested 4 August 2015. It had a clean interface, a tail length of 40”, a straight seam weld, no internal reinforcement, and a specified 28-day concrete strength of 12000 psi, twice that of Specimen 10. It achieved 1.30 times $M_{p,PSDM}$ and 2.62 times $V_{n\ (WSDOT)}$ and failed due to flexure-shear interaction. The tube tore at the bottom approximately 14 inches north of mid-span after significant flexural and shear deformations occurred. The shear deformations were seen primarily in the north shear span, but were clearly noted in the south shear span, and the tear was inclined from the vertical at roughly half the angle of the concrete strut. Extensive diagonal shear cracking and deformations occurred in the concrete fill in the north shear span while significant diagonal cracking was noted in the south shear span concrete. The tube steel buckled on both the north and the south ends of the pure moment region with more significant buckling on the north end. Significant flexural cracking of the concrete fill was also noted in the pure moment region. Figure 4.54 shows the normalized moment-normalized displacement plot. Figure 4.55 shows the shear-displacement plot. Figures 4.56 a – f show the CFT at deformation states and the condition of the concrete at the end of the test. South is to the left in each photograph.

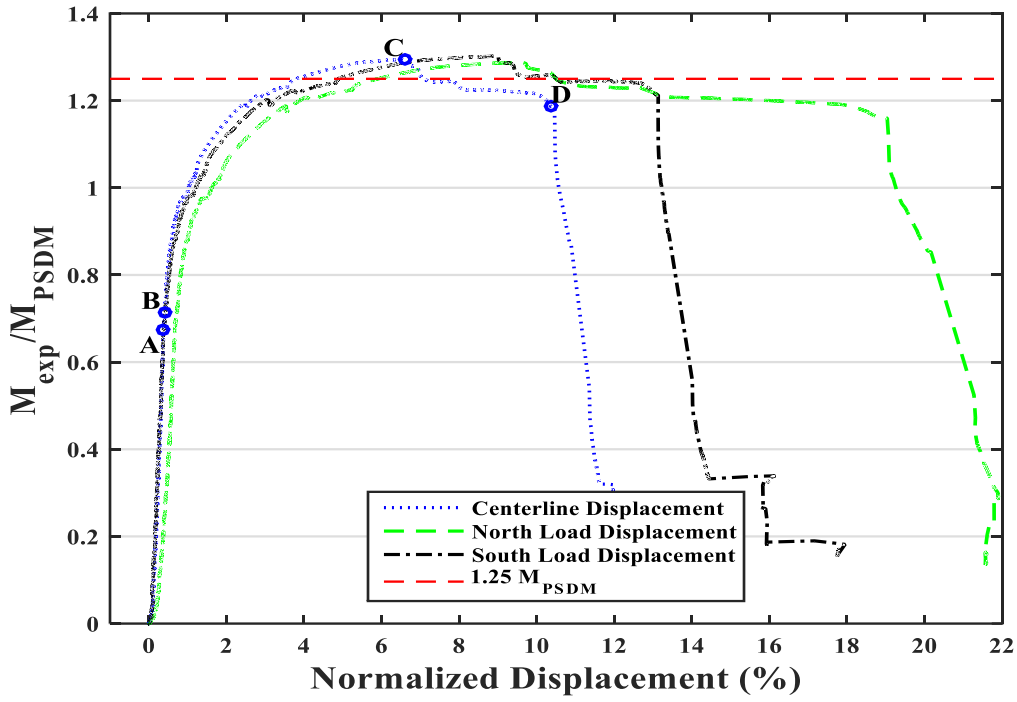

Figure 4.54: Specimen 16 moment-displacement plot

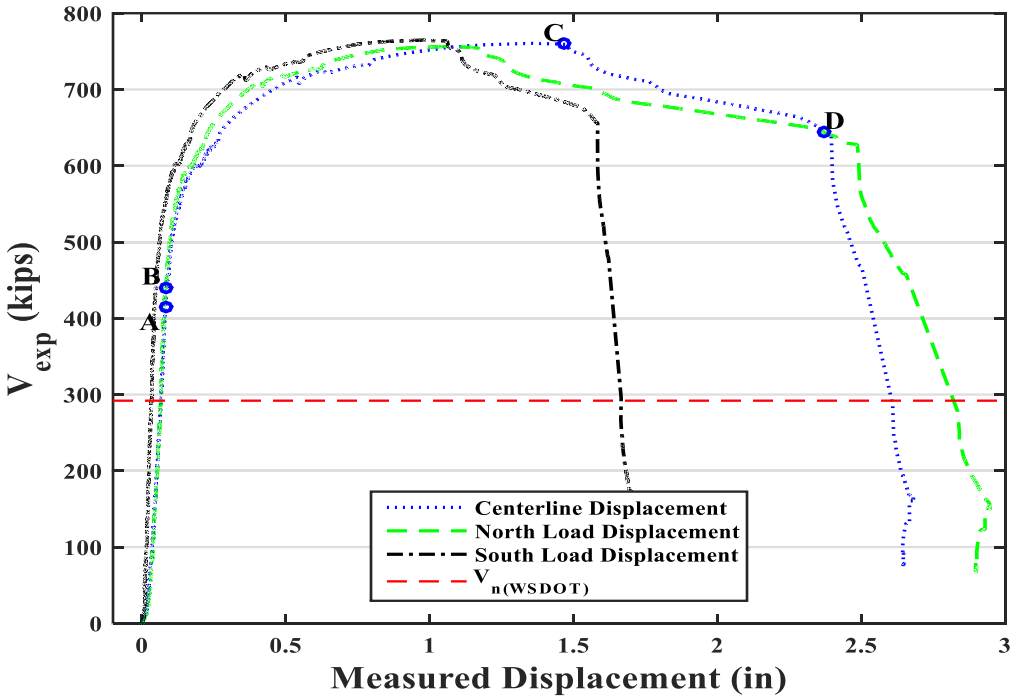

Figure 4.55: Specimen 16 shear-displacement plot

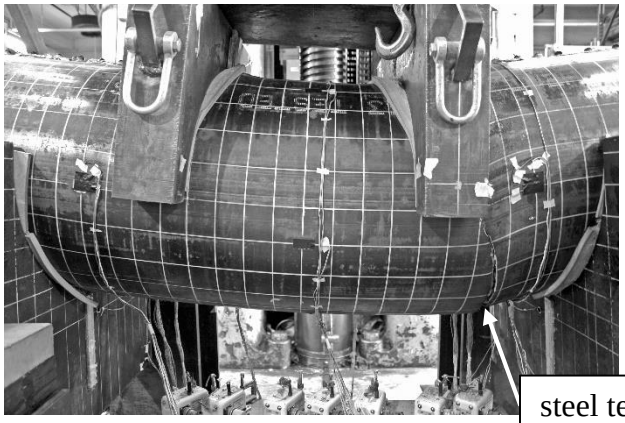

a) Specimen 16 final state

b) Specimen 16 final state

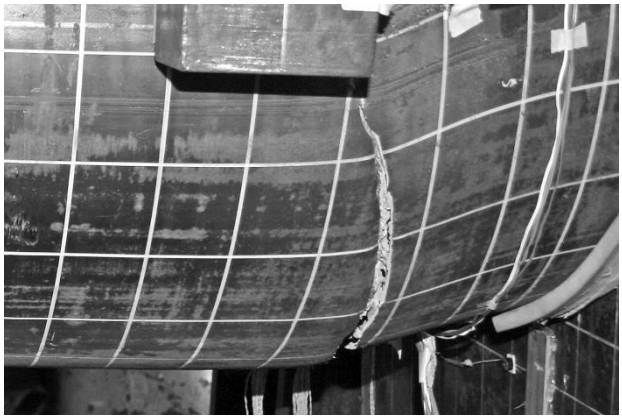

c) Specimen 16 steel tear

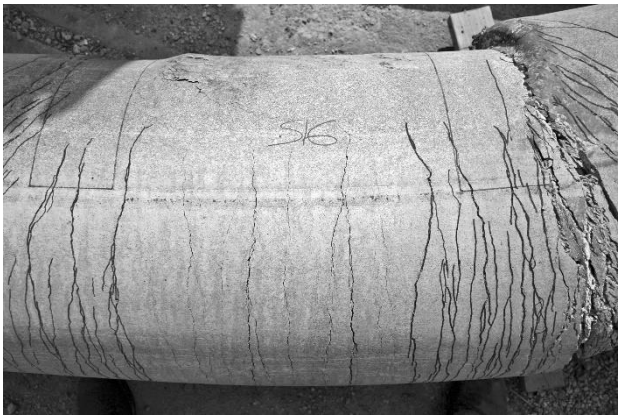

d) Specimen 16 mid-span concrete cracking

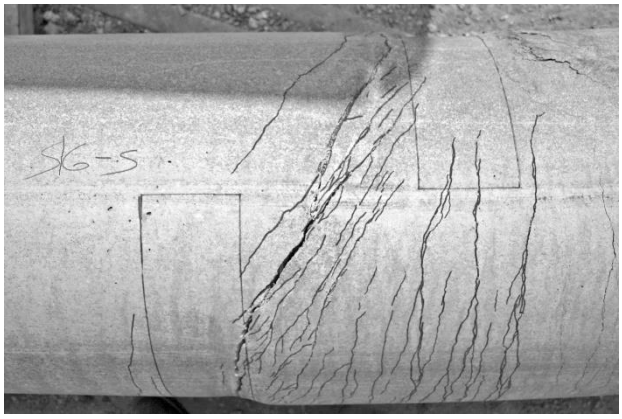

e) Specimen 16 south span concrete cracking

f) Specimen 16 north span concrete cracking

Figure 4.56: Specimen 16 state photos
(*a/D* = 0.375, D/t=80, f'_c=12 ksi)

4.17 SPECIMEN 17

Specimen 17 was a concrete type variation of Specimen 2, the baseline specimen for a/D = 0.5, and was tested 20 August 2015. It had a clean interface, a tail length of 40”, a straight seam weld, no internal reinforcement, and a specified 28-day concrete strength of 12000 psi, twice that of Specimen 2. It achieved 1.16 times $M_{p,PSDM}$ and 1.91 times $V_{n\ (WSDOT)}$ and failed in flexure. The tube tore at the bottom in flexure approximately 2 inches south of mid-span after significant flexural deformations occurred. The tear was oriented vertically. The tube steel buckled on both the north and the south ends of the pure moment region symmetrically. Extensive flexural cracking of the concrete fill occurred in the pure moment region while limited diagonal shear cracking was also noted in the concrete fill in both shear spans. Figure 4.57 shows the normalized moment-normalized displacement plot. Figure 4.58 shows the shear-displacement plot. Figures 4.59 a – f show the CFT at final deformation states and the condition of the concrete at the end of the test. South is to the left in each photograph.

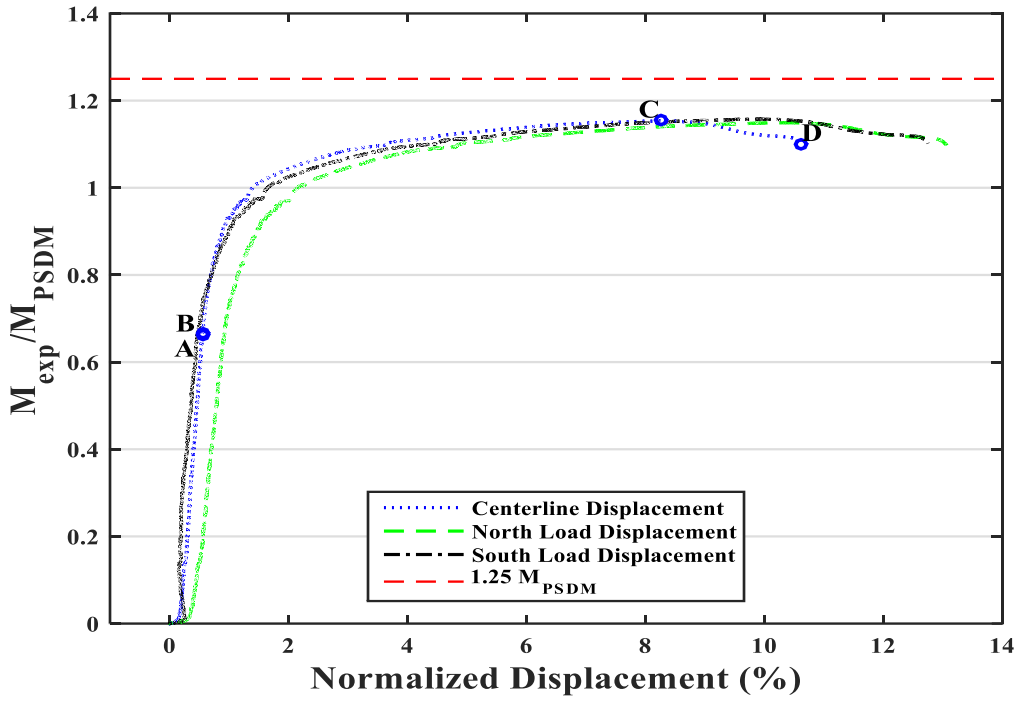

Figure 4.57: Specimen 17 moment-displacement plot

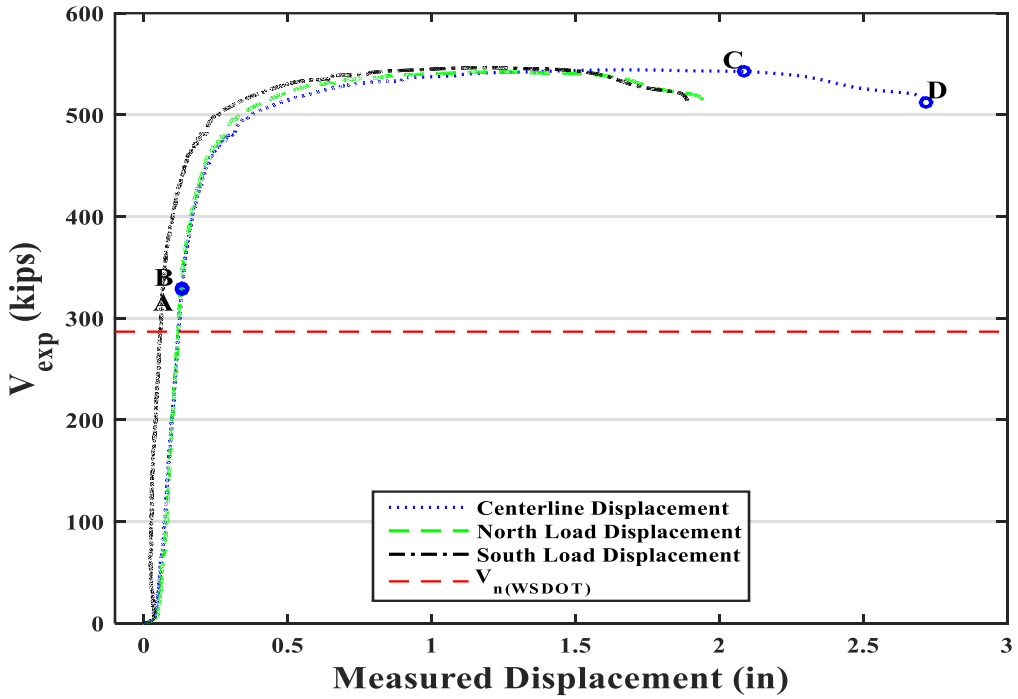

Figure 4.58: Specimen 17 shear-displacement plot

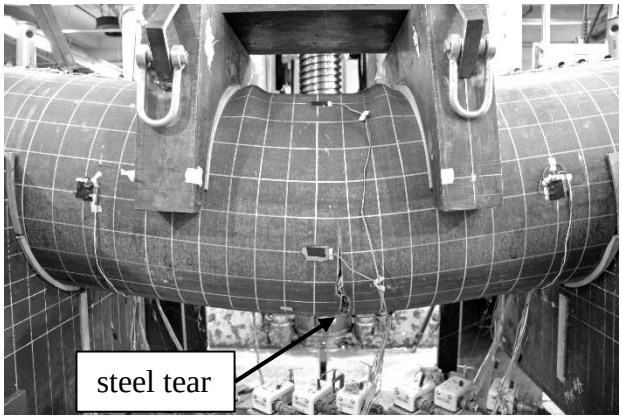

a) Specimen 17 final state

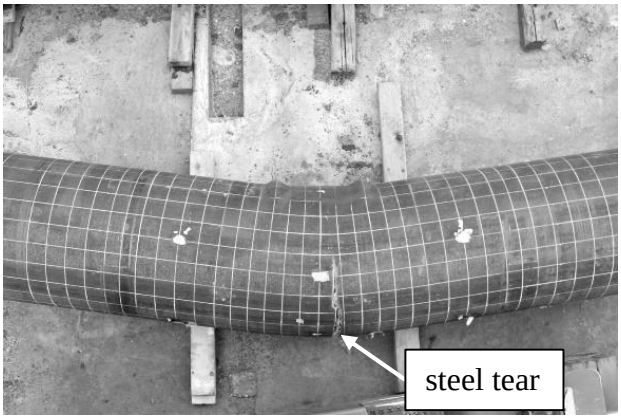

b) Specimen 17 final state

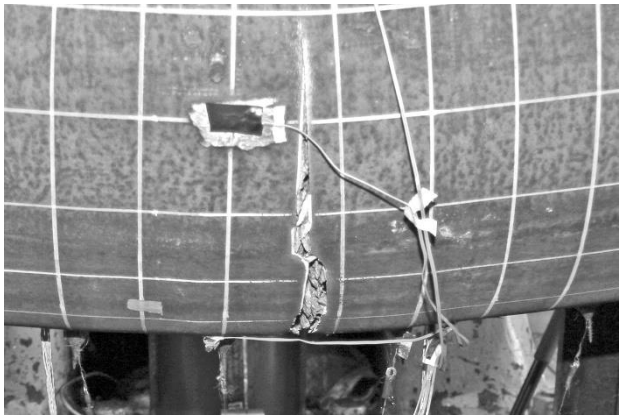

c) Specimen 17 steel tear

d) Specimen 17 mid-span concrete cracking

e) Specimen 17 south span concrete cracking

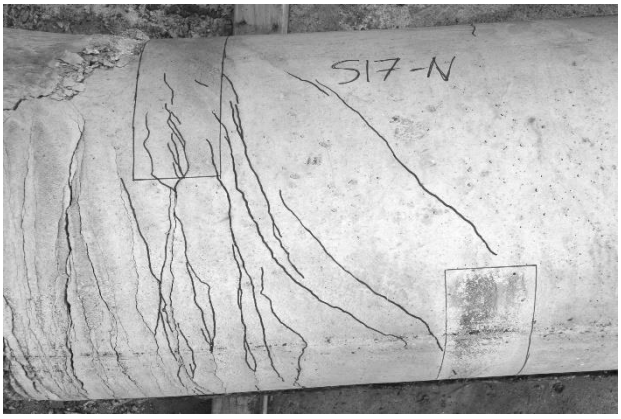

f) Specimen 17 north span concrete cracking

Figure 4.59: Specimen 17 state photos
(*a/D* = 0.5, D/t=80, f'_c=12 ksi)

4.18 SPECIMEN 18

Specimen 18 was a D/t variation of Specimen 2, the baseline specimen for a/D = 0.5, and was tested 24 August 2015. It had a D/t = 53.3, a clean interface, a tail length of 40”, a straight seam weld, no internal reinforcement, and a specified 28-day concrete strength of 12000 psi, twice that of Specimen 2. It achieved 1.22 times $M_{p,PSDM}$ and 1.96 times $V_{n\ (WSDOT)}$ and failed due in flexure. The tube tore at the bottom in flexure approximately 4 inches south of mid-span after significant flexural deformations occurred. The tear was vertical. The tube steel buckled extensively on the south end of the pure moment region while the north end just initiated buckling at failure. Extensive flexural cracking of the concrete fill occurred in the pure moment region while very limited diagonal shear cracking was also noted in the concrete fill in both shear spans. Figure 4.60 shows the normalized moment-normalized displacement plot. Figure 4.61 shows the shear-displacement plot. Figures 4.62 a – f show the CFT at final deformation states and the condition of the concrete at the end of the test. North is to the left in each photograph.

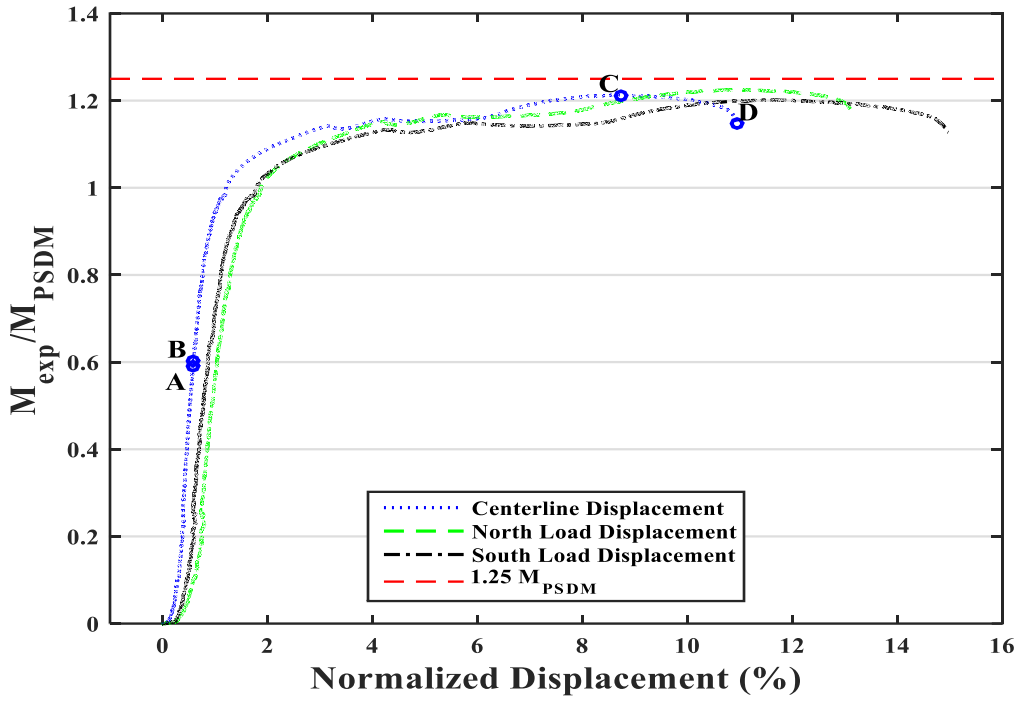

Figure 4.60: Specimen 18 moment-displacement plot

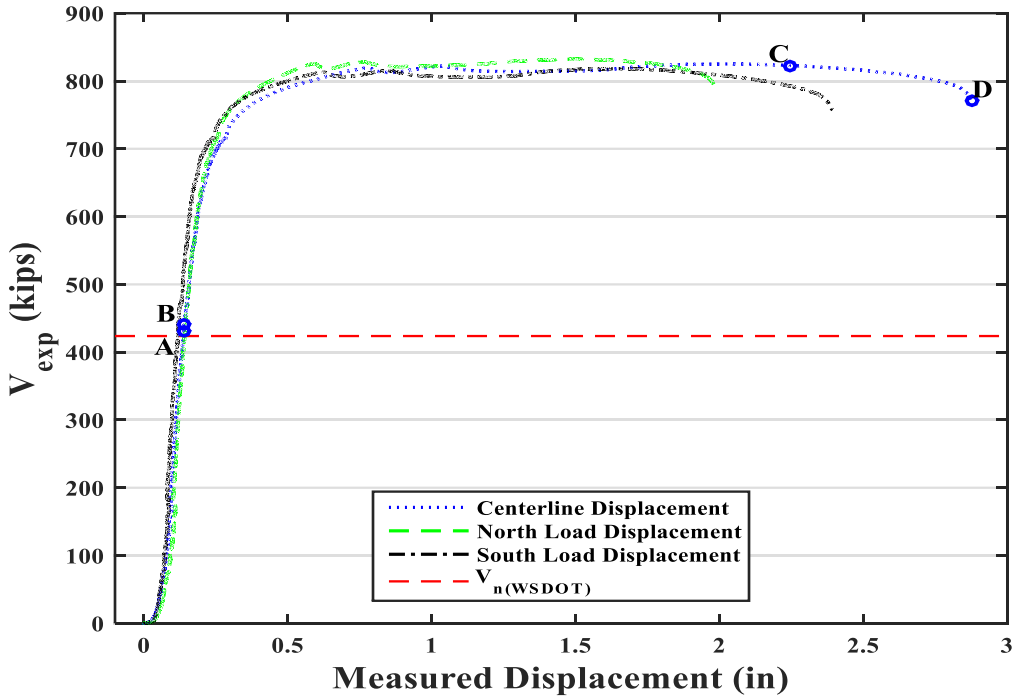

Figure 4.61: Specimen 18 shear-displacement plot

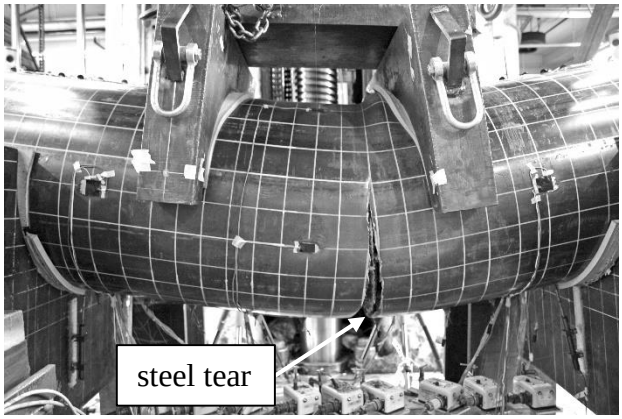

a) Specimen 18 final state

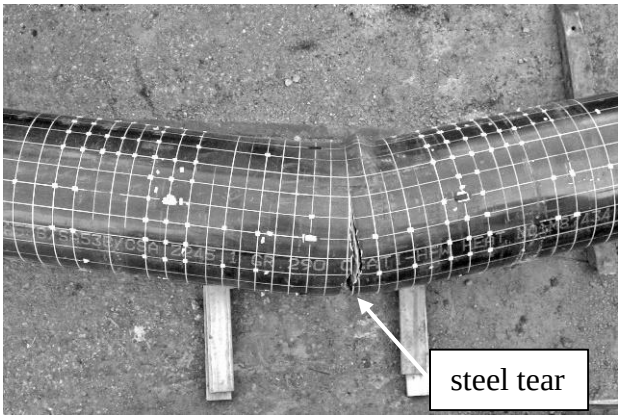

b) Specimen 18 final state

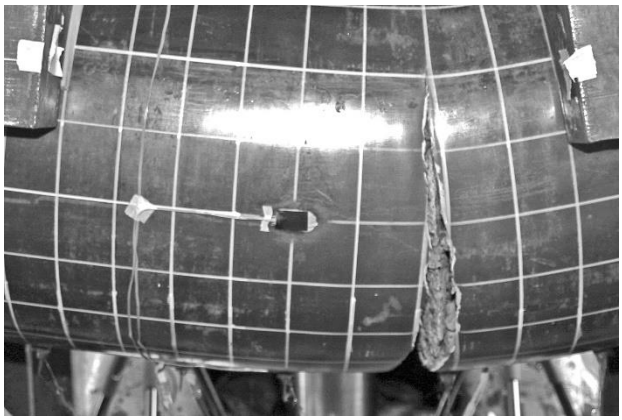

c) Specimen 18 steel tear

d) Specimen 18 mid-span concrete cracking

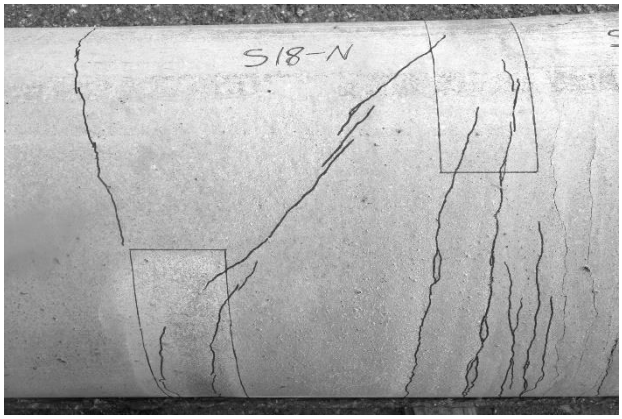

e) Specimen 18 north span concrete cracking

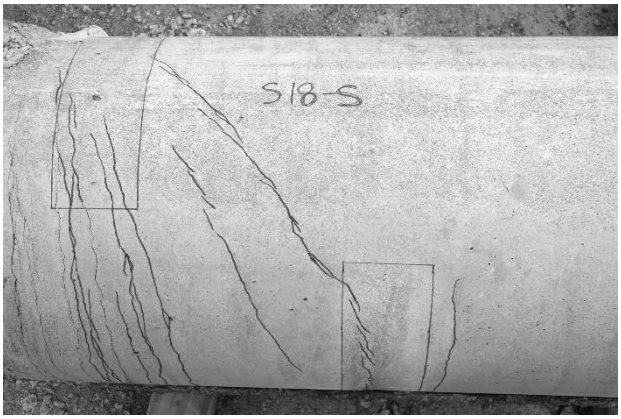

f) Specimen 18 south span concrete cracking

Figure 4.62: Specimen 18 state photos
(*a/D* = 0.5, D/t=53.3, f'_c=12 ksi)

4.19 SPECIMEN 19

Specimen 19 was an internally reinforced variation of Specimen 18, the baseline specimen for *a/D* = 0.5 and D/t = 53.3, and was tested 26 August 2015. It had a clean interface, a tail length of 40”, a straight seam weld, and 1.07% internal reinforcement. It achieved 1.22 times $M_{p,PSDM}$ and 2.24 times $V_{n\ (WSDOT)}$ and failed due to flexure-shear interaction. The tube tore at the bottom approximately 12.5 inches south of mid-span after significant flexural and shear deformations occurred. The shear deformations were seen primarily in the south shear span and the tear was oriented slightly off of vertical. Extensive diagonal shear cracking and deformations occurred in the concrete fill in the south shear span while very limited diagonal cracking was noted in the north shear span concrete. The tube steel buckled significantly on the south end of the pure moment region while the north end just initiated buckling at failure. Extensive flexural cracking of the concrete fill was also noted in the pure moment region. Figure 4.63 shows the normalized moment-normalized displacement plot. Figure 4.64 shows the shear-displacement plot. Figures 4.65 a – f show the CFT at final deformation states and the condition of the concrete at the end of the test. North is to the left in each photograph.

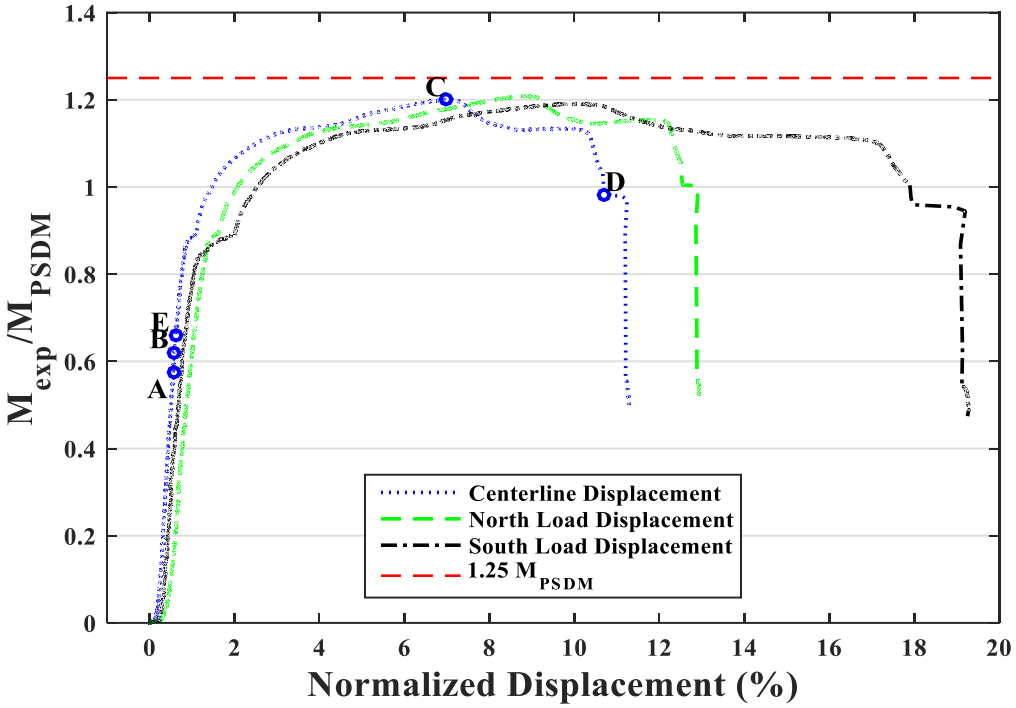

Figure 4.63: Specimen 19 moment-displacement plot

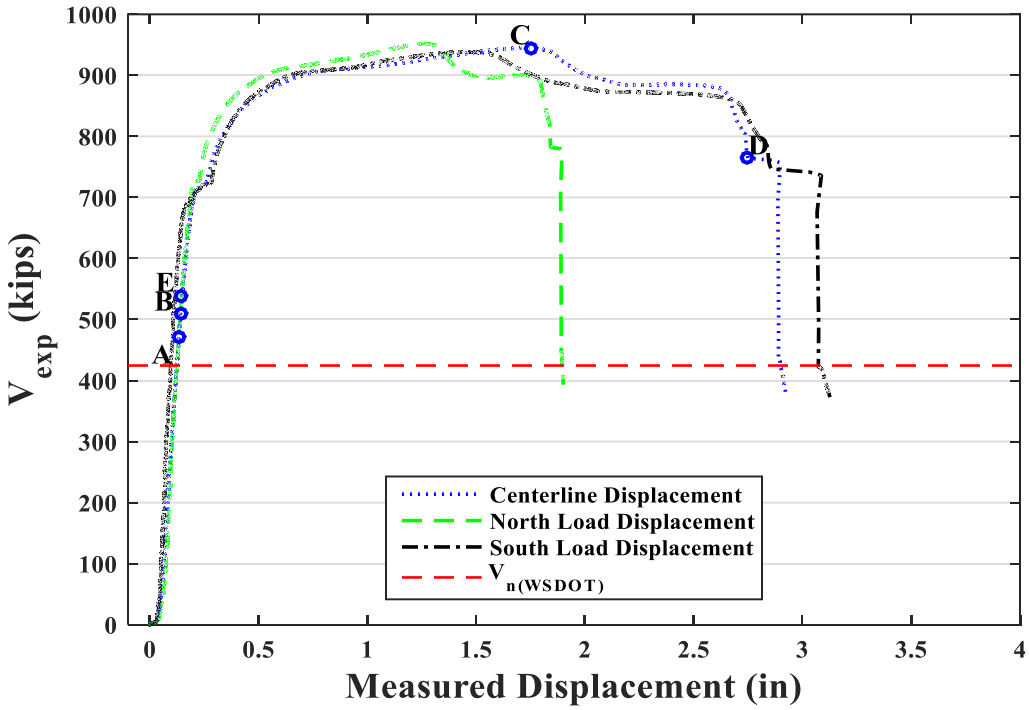

Figure 4.64: Specimen 19 shear-displacement plot

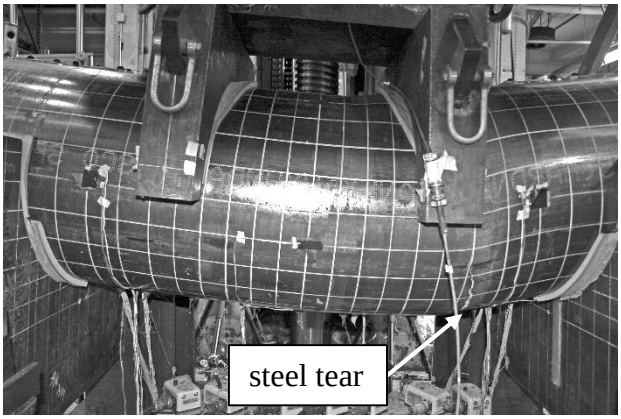

a) Specimen 19 final state

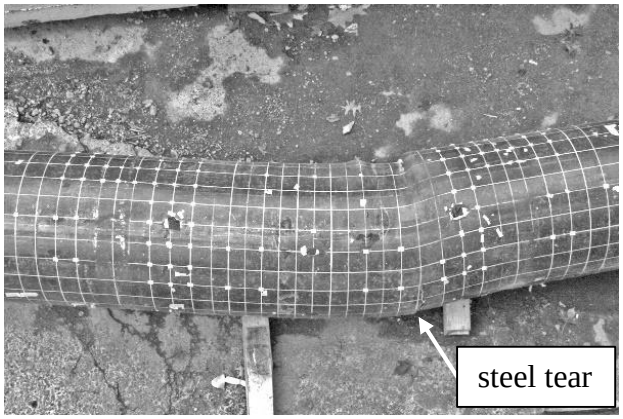

b) Specimen 19 final state

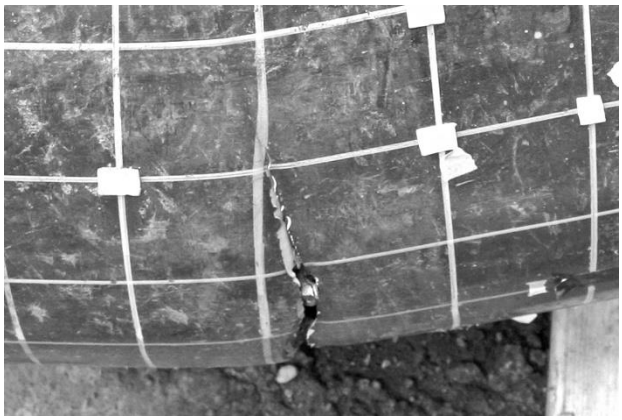

c) Specimen 19 steel tear

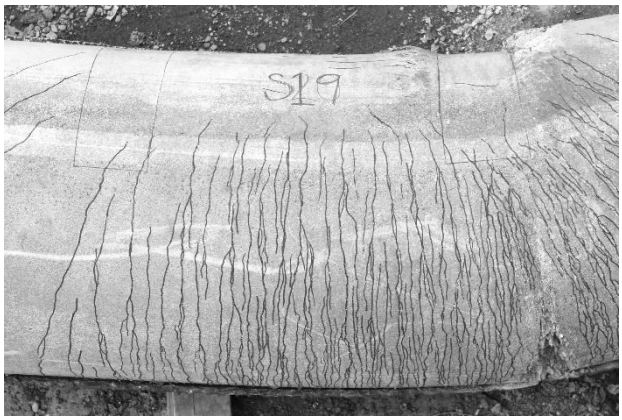

d) Specimen 19 mid-span concrete cracking

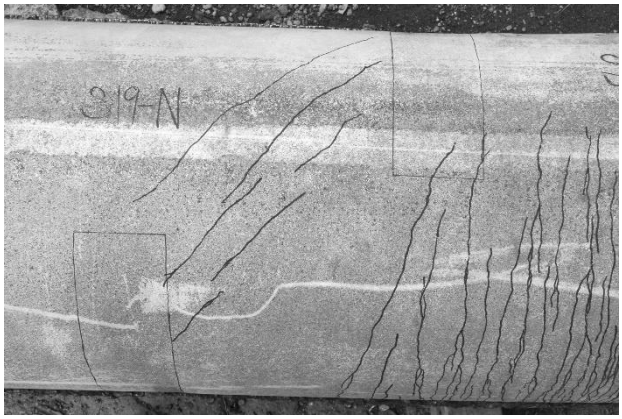

e) Specimen 19 north span concrete cracking

f) Specimen 19 south span concrete cracking

Figure 4.65: Specimen 19 state photos
(*a/D* = 0.5, D/t=53.3, ρ_{int}=1.07%)

4.20 SPECIMEN 20

Specimen 20 was a concrete type variation of Specimen 14, the baseline specimen for *a/D* = 0.25, and was tested 7 August 2015. It had a clean interface, a tail length of 40”, a straight seam weld, no internal reinforcement, and a specified 28-day concrete strength of 2500 psi, one fifth that of Specimen 14. It achieved 1.06 times $M_{p,PSDM}$ and 2.54 times $V_{n\ (WSDOT)}$ and failed in shear. The tube tore at the bottom approximately 13 inches north of mid-span after significant shear deformations occurred. The shear deformations were seen in both spans with larger deformations in the north shear span and the tear was oriented at an angle similar to the concrete strut. The concrete fill in the shear spans experienced extensive deformation and damage but the damage patterns are different than the other specimens. Significant cracks formed in the concrete fill in the north shear span along with large deformations or extrusions of the concrete without large, visible cracks. The concrete fill in the south shear span appeared to extrude or flow without large, visible cracks as the CFT experienced shear deformation. This was likely an effect of the weaker, less stiff concrete. The tube steel did not experience visible flexural buckling in the pure moment region. Very mild flexural cracking of the concrete fill was also noted in the pure moment region. Figure 4.66 shows the normalized moment-normalized displacement plot. Figure 4.67 shows the shear-displacement plot. Figures 4.68 a – f show the CFT at final deformation states and the condition of the concrete at the end of the test. South is to the left in each photograph.

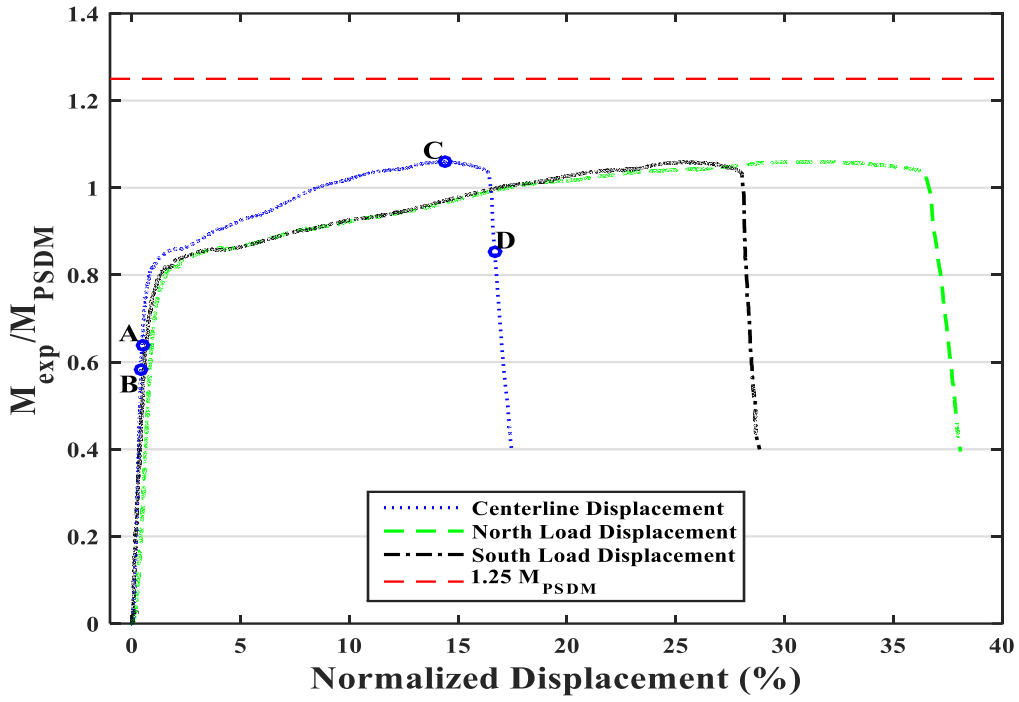

Figure 4.66: Specimen 20 moment-displacement plot

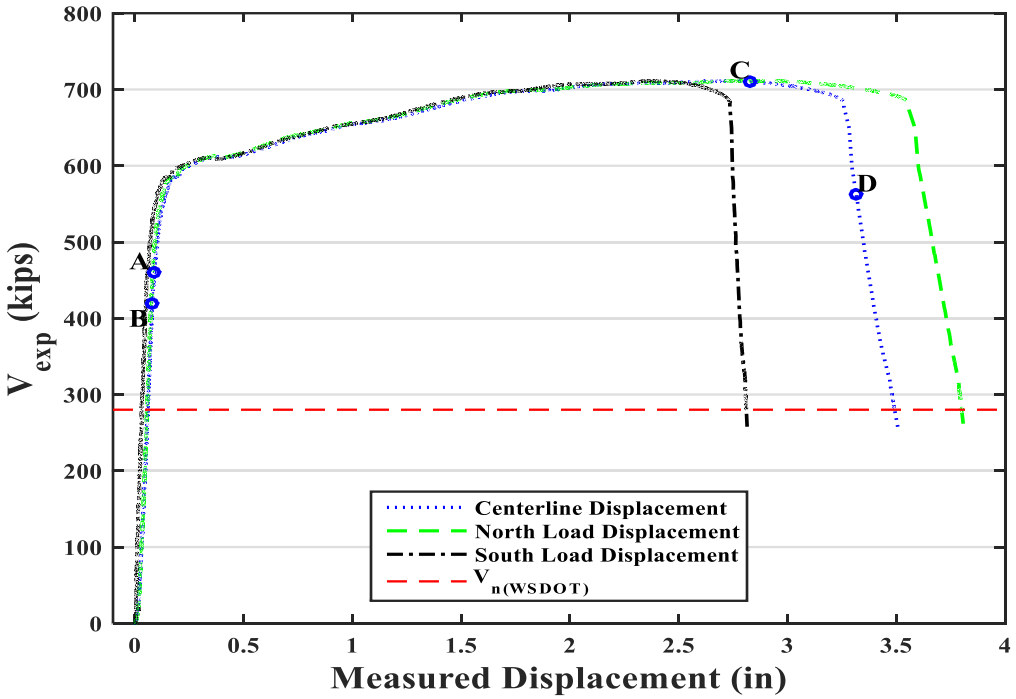

Figure 4.67: Specimen 20 shear-displacement plot

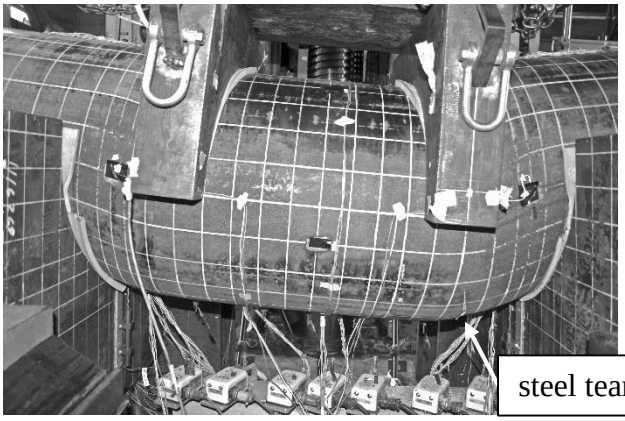

a) Specimen 20 final state

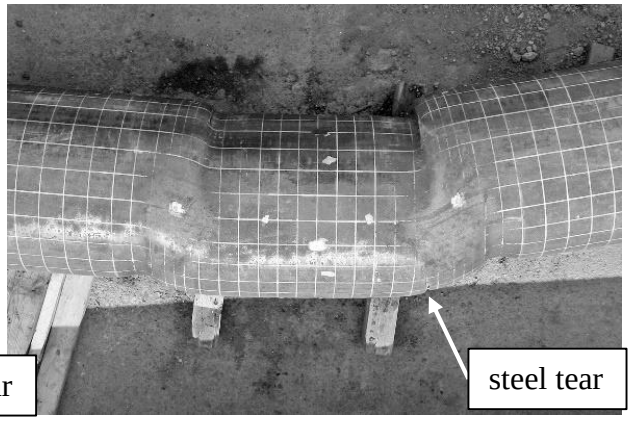

b) Specimen 20 final state

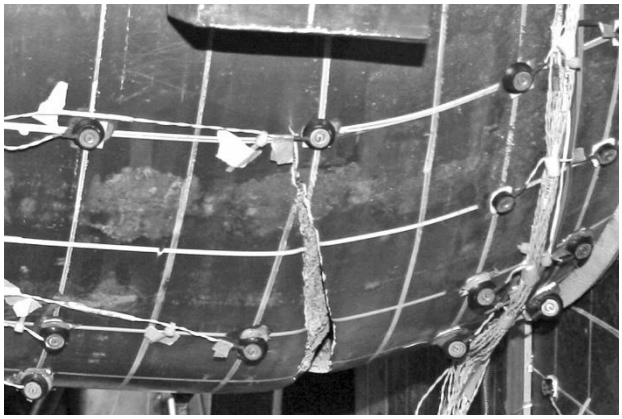

c) Specimen 20 steel tear

d) Specimen 20 mid-span concrete cracking

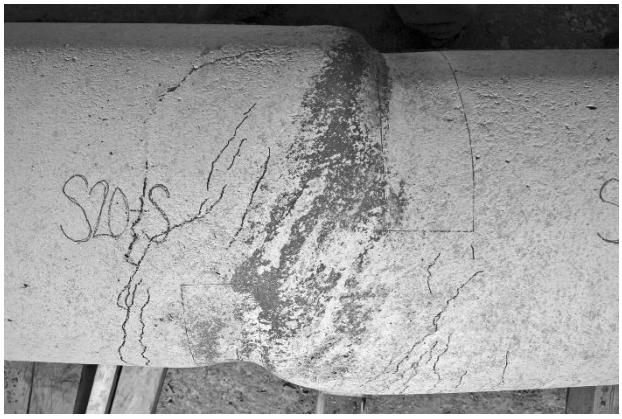

e) Specimen 20 south span concrete cracking

f) Specimen 20 north span concrete cracking

Figure 4.68: Specimen 20 state photos
(*a/D* = 0.25, D/t=80, f'_c=2.5 ksi)

4.21 SPECIMEN 21

Specimen 21 had gravel in the shear spans in lieu of concrete in order to determine the distinct contributions of the concrete and steel to the shear resistance of CFTs. It was not a true CFT but it will be compared to the calculated CFT values for consistency with the rest of the research specimens. It was a variation on Specimen 10, the baseline specimen for a/D = 0.375, and was tested 29 July 2015. It had a clean interface, a tail length of 40”, a straight seam weld, and no internal reinforcement. It achieved 0.94 times $M_{p,PSDM}$ of the CFT and 1.70 times $V_{n\ (WSDOT)}$ of the CFT and failed in shear. The tube tore at the bottom approximately 11 inches south of mid-span after significant shear deformations occurred. Shear buckling initiated when the normalized moment reached approximately 0.5 and the shear force was approximately 0.9 times $V_{n\ (WSDOT)}$. Tension-field action developed and provided increased shear resistance. The tear was oriented at roughly half the angle of the tension field. There was no visible flexural buckling in the pure moment region. The concrete fill experienced very minor cracking and damage. Figure 4.69 shows the normalized moment-normalized displacement plot. Figure 4.70 shows the shear-displacement plot. Figures 4.71 a – f show the CFT at final deformation states and the condition of the concrete and gravel at the end of the test. South is to the left in each photograph.

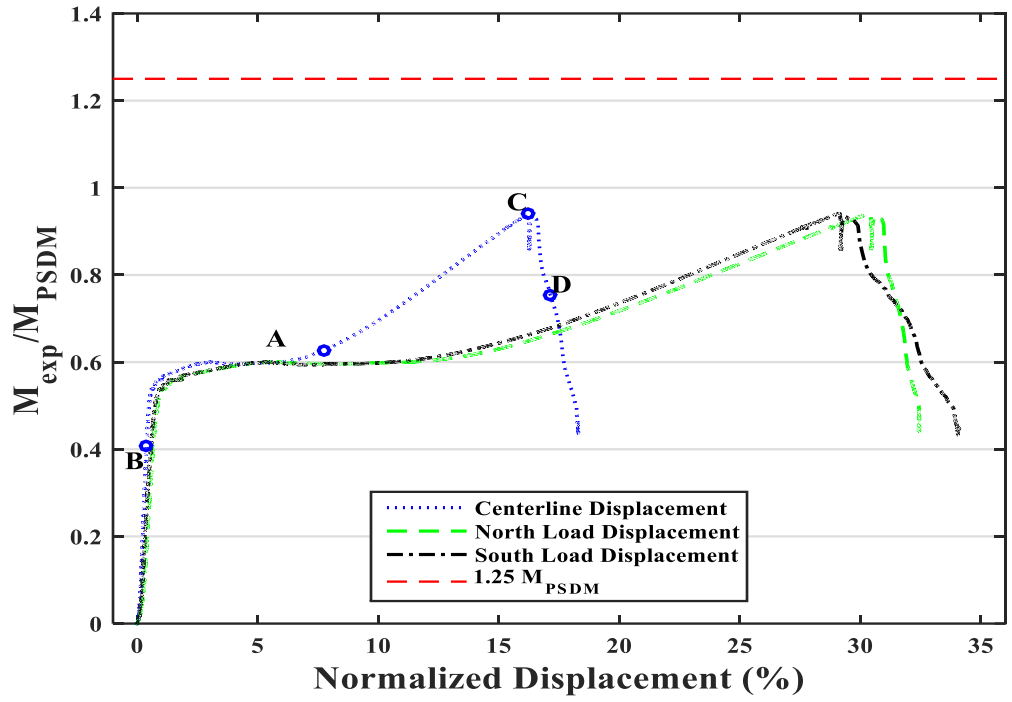

Figure 4.69: Specimen 21 moment-displacement plot

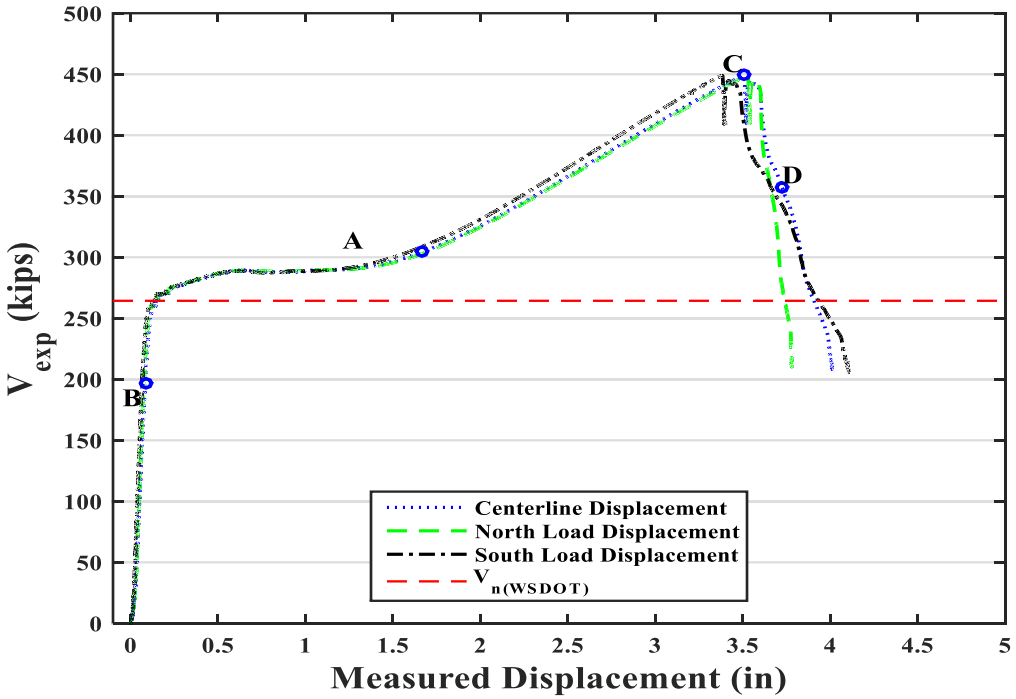

Figure 4.70: Specimen 21 shear-displacement plot

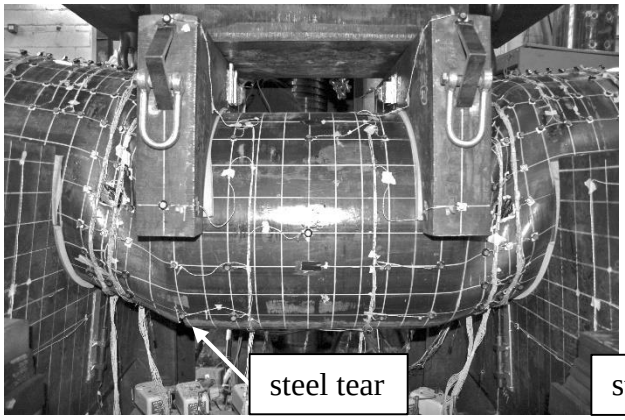

a) Specimen 21 final state

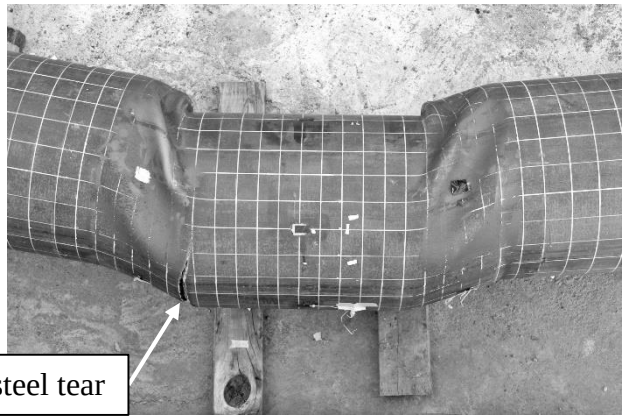

b) Specimen 21 final state

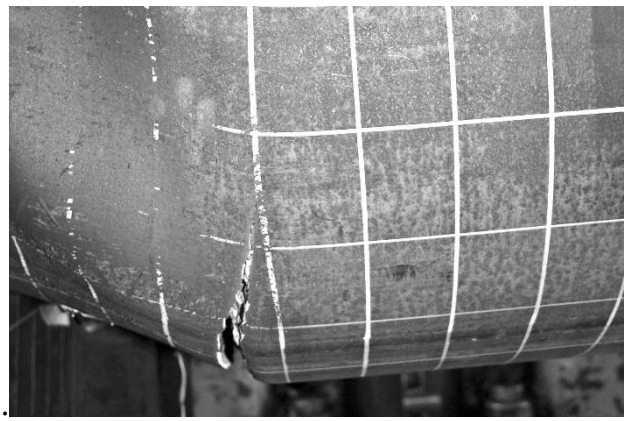

c) Specimen 21 steel tear

d) Specimen 21 mid-span concrete cracking

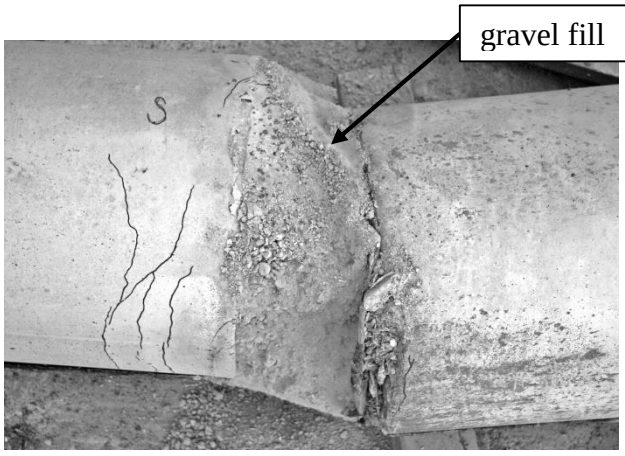

e) Specimen 21 south span concrete cracking

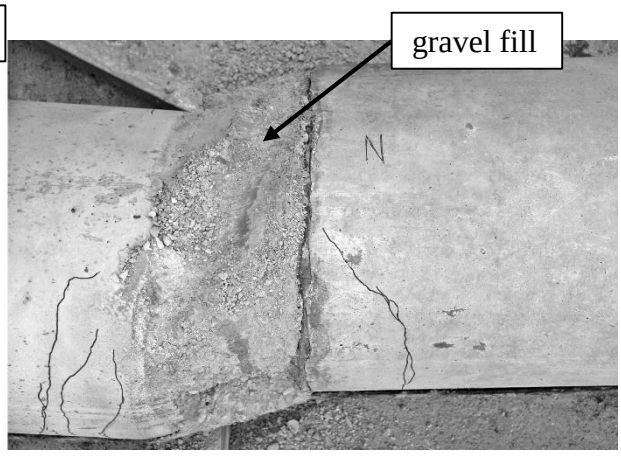

f) Specimen 21 north span concrete cracking

Figure 4.71: Specimen 21 state photos
(*a/D* = 0.375, D/t=80, no concrete in shear span)

4.22 SPECIMEN 22

Specimen 22 was a steel tube-type variation of Specimen 1, the baseline specimen for *a/D* = 1.0 and was tested 19 January 2015. It had a clean, galvanized interface, a tail length of ~90”, a spiral seam weld, a high steel yield stress, a high concrete strength – greater than 13000 psi, and no internal reinforcement. The CFT was constructed for previous research and was used to verify the testing apparatus and procedure. It achieved 1.22 times $M_{p,PSDM}$ and 1.24 times $V_{n\ (WSDOT)}$ and failed in flexure. The tube tore at the bottom in flexure approximately 2 inches north of mid-span. The tube steel buckled on both the north and the south ends of the pure moment region. The buckle on the north end occurred in the usual location next to the load cradle while the buckle on the south end followed the spiral weld over the top of the tube. The state of the concrete fill is not known as the specimen was not cut open for inspection. Figure 4.73 shows the normalized moment-normalized displacement plot. Figure 4.74 shows the shear-displacement plot. The yield point A is not shown on the figures as there were no strain gauges used during the test. Figures 4.72 a – b show the CFT at final deformation states. South is to the left in each photograph.

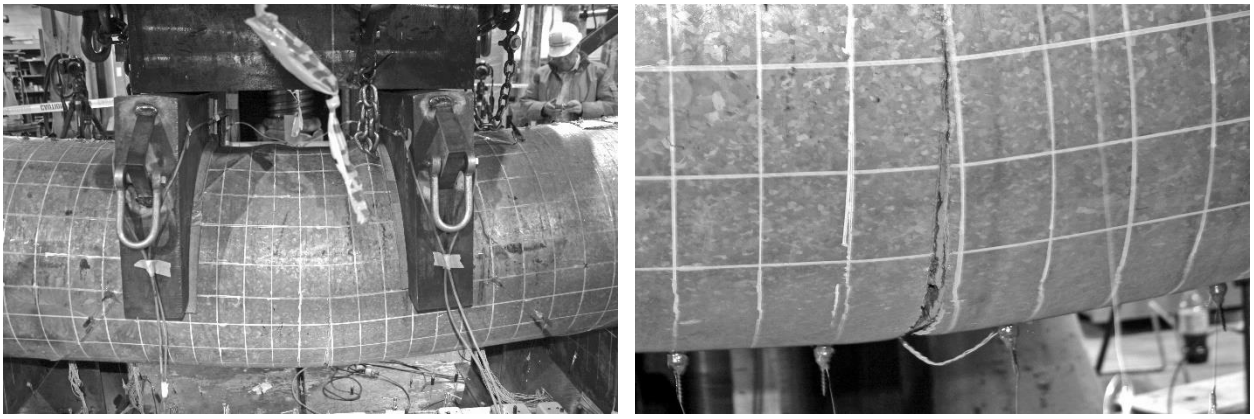

a) Specimen 22 final state b) Specimen 22 steel tear

Figure 4.72: Specimen 22 state photos
(*a/D* = 1.0, D/t=80, spiral weld tube)

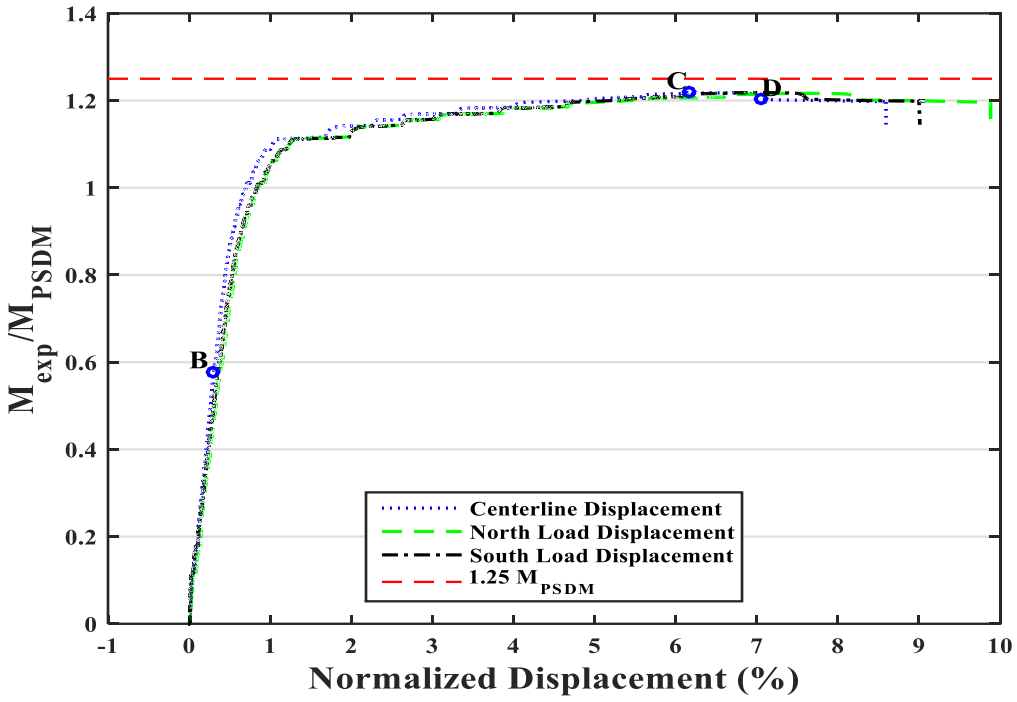

Figure 4.73: Specimen 22 moment-displacement plot

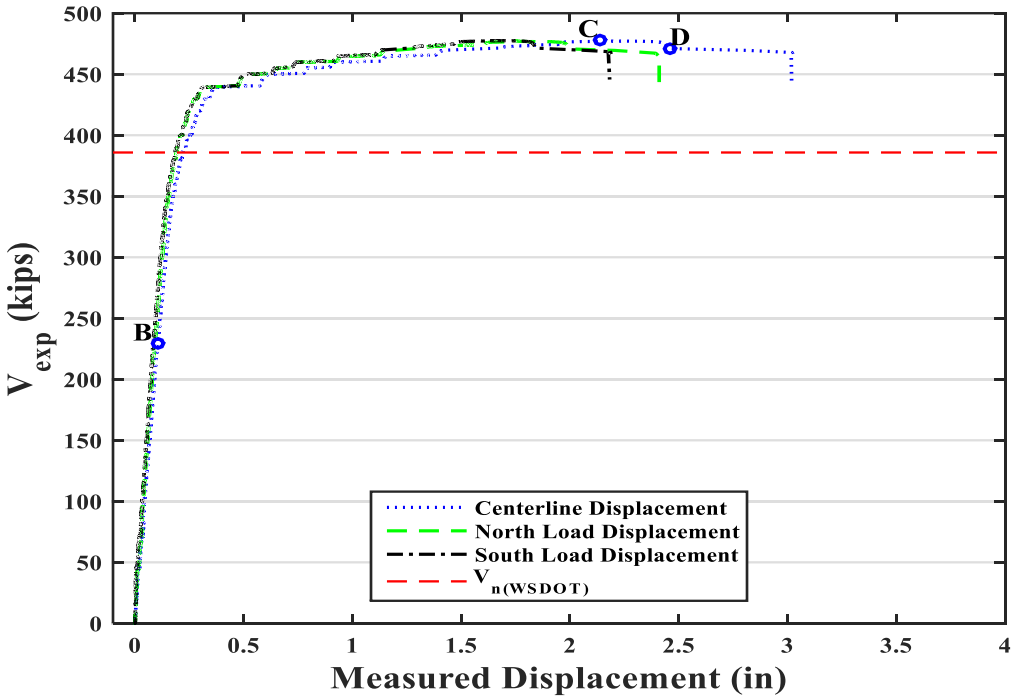

Figure 4.74: Specimen 22 shear-displacement plot

Chapter 5. DATA INTERPRETATION AND DESIGN EXPRESSIONS

The purpose of this experimental program was to evaluate the shear resistance and deformation of CFTs and RCFTs subjected to transverse loading and to investigate the effect of various parameters on their behavior. This chapter discusses the failure modes, moment-displacement and shear-displacement responses, study parameter influence, and evaluates several potential design expressions. Table 5.1 shows the experimental bending moments and shears for each specimen. All specimens had a diameter, D, of 20 in. and a/D and measured material strengths as shown. All specimens had a clean straight-seam interface, $P/P_0 = 0$, $D/t = 80$, $L_T = 2D$, and $\rho_{int} = 0\%$ unless noted otherwise. Parameters that vary from the specific a/D baseline are noted.

Table 5.1: Experimental moments and shears

Specimen	a/D	Varied Parameters	f_{ym} (ksi)	f'_{cm} (ksi)	$M_{p,PSDM}$ (k-in)	$V_{n\ (WSDOT)}$ (kip)	$V_{pr,\ M_{p,PSDM}}$ (kip)	M_{exp} (k-in)	V_{exp} (kip)
1	1.0	baseline	49.6	6.0	6069	254	316	7893	322
22		spiral weld conc. strength	75.6	13.0	9495	386	495	11654	477
2	0.5	baseline	49.6	6.2	6085	254	543	8099	550
3		L_T = D/2	50.1	6.7	6174	258	551	8111	552
4		L_T = D	50.1	6.6	6167	257	551	8035	543
5		muddied	49.6	7.0	6143	256	549	8124	556
6		spiral weld	70.8	7.2	8533	355	762	11665	779
9		greased	50.1	6.3	6149	257	549	6528	442
12		ρ_{int} = 1.13%	53.9	6.2	8019	274	716	9679	651
17		conc. strength	55.4	9.5	6958	287	621	8056	547
18		D/t = 53.3 conc. strength	57.2	8.6	10165	424	908	12444	832
19		ρ_{int} = 1.07% D/t = 53.3 conc. strength	57.2	9.1	11434	424	1021	13816	952
10	0.375	baseline	53.9	6.2	6564	274	713	8159	665
11		L_T = D/2	56.8	6.6	6926	289	753	7024	600
7		ρ_{int} = 1.04%	50.1	6.4	7524	257	818	8807	705
8		ρ_{int} = 2.01%	53.9	6.5	9016	274	980	9239	802
13		P/P_0 = 8.5% L_T = D/2	53.9	5.3	7362	273	800	8270	710
16		conc. strength	56.8	8.6	7069	292	769	9204	765
21		no concrete	56.8	0.0	5539	264	602	5211	449
14	0.25	baseline	55.4	8.6	6910	286	960	7678	826
15		L_T = D/2	55.4	8.8	6922	286	961	7164	796
20		conc. strength	56.8	2.8	6451	280	896	6838	712

5.1 FAILURE MODES

There were four failure modes that occurred during the test program: flexure, shear, flexure-shear interaction, and bond. The characteristics of each failure mode are identified in this section.

5.1.1 *Flexural Failure*

The predominant characteristics of flexural failures in CFTs include:

- Flexural buckling of the tube steel due to compressive flexural stresses at the location of maximum bending moment. The amount of buckling is affected by the local stability of the tube section, often described with the *D/t* ratio. See Figure 5.1.
- Rupture of the tube steel due tensile flexural stresses at the location of maximum bending moment. The tear in the steel is close to vertical as the stresses are primarily longitudinal. See Figure 5.1.
- Flexural deformation at the location of maximum bending moment coupled with a lack of shear deformation in the tube steel in the shear spans.
- Flexural cracking in the concrete fill exhibiting as a uniform pattern of dense, transverse cracks where the bending moment is high as shown in Figure 5.2.
- Either a lack of cracking or the presence of minor diagonal cracking in the concrete fill in the shear spans as shown in Figure 5.3.

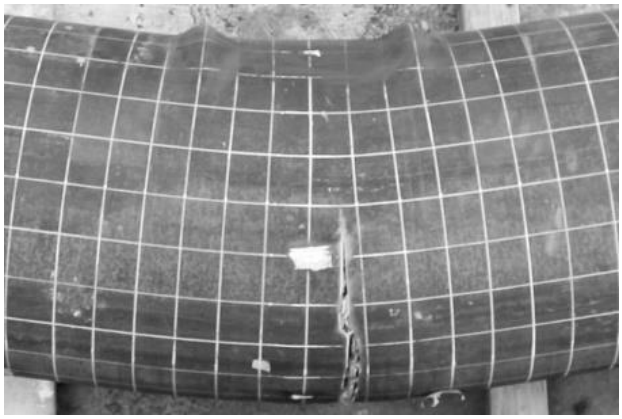

Figure 5.1: Flexural buckling and tensile rupture

Figure 5.2: Dense flexural cracking

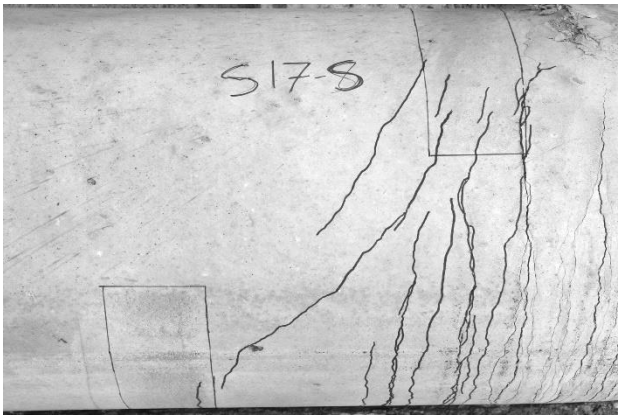

Figure 5.3: Minimal shear cracking

5.1.2 *Shear Failure*

The predominant characteristics of shear failures in CFTs include:

- Shear deformation in the tube steel in at least one shear span as shown in Figure 5.4.
- An inclined rupture in the tube steel located in a shear span as shown in Figure 5.5.
- A lack of visible flexural deformation, including flexural buckling, at the location where the bending moment is the highest.
- Relatively minor flexural cracking in the concrete fill where the bending moment is high as shown in Figure 5.6.
- Extensive diagonal cracking in the concrete fill in the shear spans as the concrete effectively flows as shown in Figure 5.7.

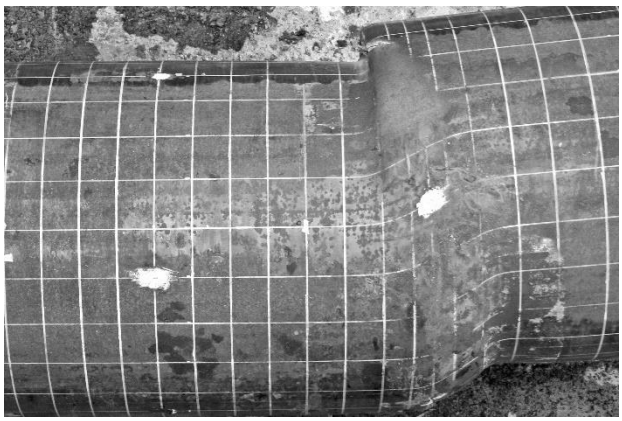

Figure 5.4: Shear deformation

Figure 5.5: Inclined steel tear

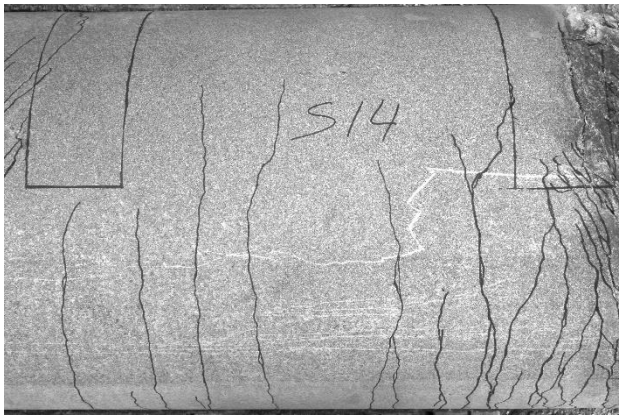

Figure 5.6: Minor flexural cracking

Figure 5.7: Extensive shear cracking

5.1.3 *Flexure-Shear Interaction*

In CFTs, failure due to flexure-shear interaction occurs as the member yields in flexure, experiences an increase in flexural capacity due to strain hardening, and then ultimately fails as the applied shear force exceeds a reduced shear capacity of the section. The predominant characteristics of flexure-shear failures in CFTs include:

- Flexural buckling and flexural deformations at the location of maximum bending moment coupled with shear deformation in at least one shear span as shown in Figure 5.8.
- Significant flexural cracking where the bending moment is high and extensive diagonal cracking in at least one of the shear spans as shown in Figures 5.9 and 5.10.

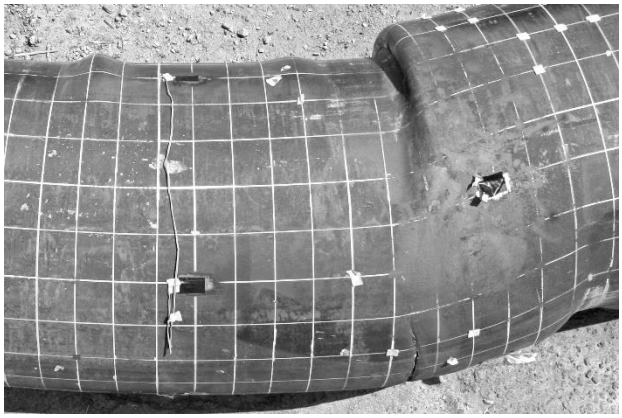

Figure 5.8: Flexure and shear deformations

Figure 5.9: Dense flexural cracking

Figure 5.10: Extensive shear cracking

5.1.4 *Bond Failure*

CFTs, like all composite members, require continuity of stress at the material interfaces. The bond stresses allow the different constituents to jointly resist the internal forces and moments that are developed to resist external loads. A bond failure means the cross-section no longer acts jointly, but as separate and distinct components. The predominant characteristics of bond failures in CFTs include:

- Significant relative displacement of the concrete fill and the steel tube, also called slip, as shown in Figure 5.11.
- Large portions of the concrete fill break away and exhibit rigid body motion as shown in Figure 5.12 due to the lack of horizontal stress transfer at the concrete-steel interface.
- A reduction in moment and shear capacity as the section is no longer fully composite.

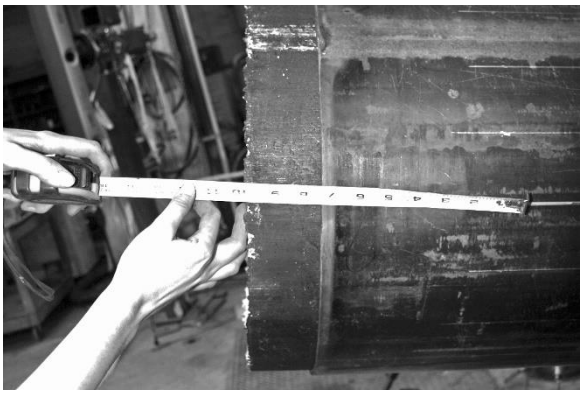

Figure 5.11: Concrete slip

Figure 5.12: Concrete rigid-body motions

5.2 SPECIMEN CLASSIFICATION

Several specimens appeared to fail in shear, but much of the CFT behavior was dominated by flexure. A method was needed in order to determine into which failure category each specimen fit. The flexural failures were easily identified, as were the bond failures, but differentiating between flexure-shear and shear failures was more difficult. A set of criteria was developed to identify the different failure modes. The criteria are: 1) whether the orientation of the steel tear is inclined or vertical, 2) whether the ratio M_{yield} / M_{prop} (both defined in Chapter 4) is greater than 1.0, 3) the presence of visible, permanent flexural deformation in the steel tube, 4) whether the ratio M_{exp} / $M_{p,PSDM}$ is less than 1.1, and 5) whether the ratio V_{exp} / $V_{n\ WSDOT}$ is greater than 2.5. The values for criteria 4 and 5 are arbitrarily chosen bins but appear to fit the data well. If a specimen fits all five criteria it is assigned a score of 5 and a shear failure mode. If it fits none, its score is 0 and it is a flexural failure. A score of 1 to 4 is classified as flexure-shear interaction. Bond failures are identified by the amount of relative slip between the concrete fill and the steel tube and are exempted from this classification process. They are discussed later in this section. Figures 5.13 and 5.14 show the normalized moment and normalized shear values for each specimen. Throughout this chapter, filled symbols on the plots will indicate a shear failure while open symbols will indicate all the other failure modes.

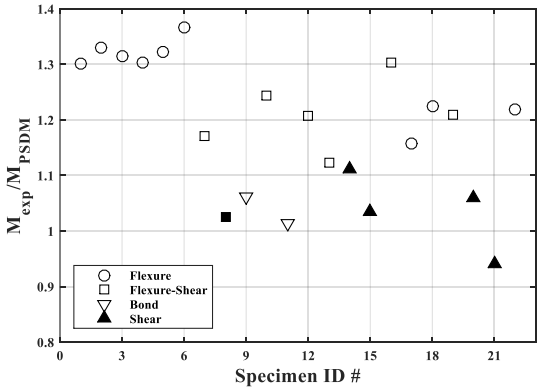

Figure 5.13: Normalized moment

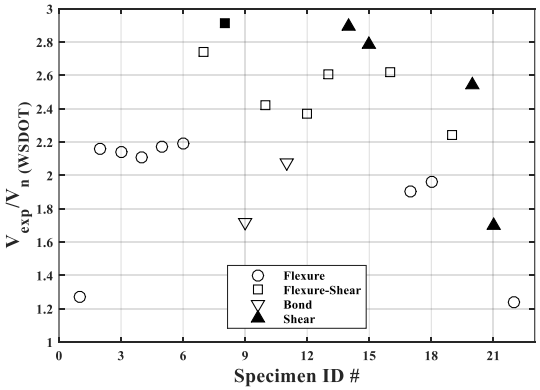

Figure 5.14: Normalized shear

The orientation of the steel tear indicates if it occurred under predominantly flexural stresses, as is the case for vertical tears, or if there was a significant contribution from shear stresses, as well. The location of the tear corresponded to the orientation for every specimen, i.e. the vertical tears all happened in the pure flexural regions, while inclined tears all happened in a shear span or under a load cradle.

The M_{yield} / M_{prop} ratio determines if there is non-linearity in the section before the tube steel yields in flexural tension at the mid-span. This is a rough indicator of shear yielding versus flexural yielding. The strain gauge rosettes in the shear zone could be used to calculate a surficial Von Mises stress, then be compared to the longitudinal strain at mid-span in order to more accurately predict the yielding magnitude and sequence. Additionally, the Optotrak data could be used to form strain fields which could then be used to determine the yielding magnitude and sequence. Neither of these procedures will be included here, as this thesis focuses more on the experimental procedure and global behavior of the CFTs and less on localized deformation.

The use of visible, permanent flexural deformation is reasonably straight forward. The normalized moment and normalized shear values are used as additional measures to highlight possible different failure modes, as in the case of Specimen 11, where V_{exp} / $V_{n\ WSDOT}$ = 2.08, which is significantly less than the other shear failures.

Duncan potentiometers were used at the north and south ends of the CFTs to measure the longitudinal slip of the concrete fill relative to the steel tube. These measurements were used to help determine the composite nature of the CFT behavior. Figures 5.15 a-b show the maximum values of slip and the maximum values normalized by the tail length, L_T, for each specimen. The normalized values are analogous to an average strain measurement at the bond surface and indicate which specimens are most likely affected by a bond failure. Specimens 9 and 11 were

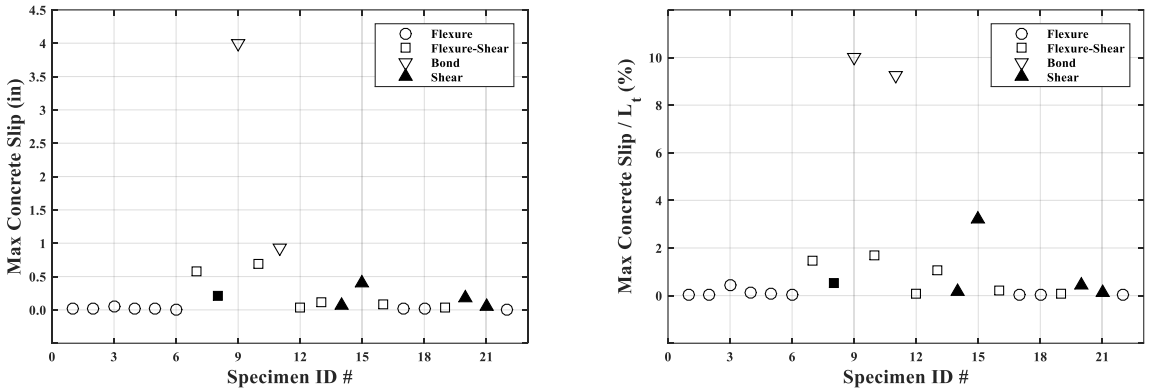

a) Maximum concrete slip b) Maximum normalized concrete slip

Figure 5.15: Concrete slip measures

classification criteria indicated a shear failure. There were no slip readings for Specimen 22, but it is reasonable to assign it the slip values for Specimen 6 as a worst case in order to include it in the comparison, because both were spirally welded tubes that failed in flexure and the tail length for Specimen 22 was more than twice that of Specimen 6.

Using the above procedure, nine specimens failed in flexure, five failed in shear (including Specimen 8), six failed due to flexure-shear interaction, and two failed due to a significant loss of bond stress. Table 5.2 shows the results and failure classifications. Four things to note about this process are:

- Specimen 17 had a M_{yield} / M_{prop} ratio of 1.01 but was likely a flexural failure given the location of the tear in the steel, the shape of the moment-drift plots, and the cracking pattern in the concrete. It will be classified as such herein.
- Specimen 13, with the axial load, was assigned a flexure-shear failure but had a high M_{yield} / M_{prop} ratio of 1.37, which aligns more closely with the shear specimens. Further investigation of the test images shows that the visible plastic flexural deformation occurred before the shear deformations and before the axial load was released, confirming the classification.

- Specimen 21 had gravel in the shear spans in an attempt to quantify the steel-supplied shear resistance versus that provided by the concrete and as such is not a CFT for the entire length. It did not meet criterion 5 because of this, but was still a shear failure. Its response was dominated by shear buckling and tension-field action.
- Specimen 8, with the internal reinforcement ratio of 2%, met all but the M_{yield} / M_{prop} ratio criterion for a shear failure. Its moment-displacement and shear-displacement curves, as well as its capacity ratios, are similar to those of the shear failures and it will be grouped with the shear failures for analysis of the shear design expressions.

Table 5.2: Specimen failure classification

Specimen	*a/D*	M_{yield} / M_{prop}	Inclined Tear	Visible Flex Deform.	M_{exp} / $M_{p,PSDM}$	V_{exp} / $V_{n\ WSDOT}$	Score	Failure Mode	Max Slip / L_T
1	1.0	1.00	No	Yes	1.30	1.27	0	Flexure	0.06%
2	0.5	0.97	No	Yes	1.33	2.16	0	Flexure	0.04%
3	0.5	0.92	No	Yes	1.31	2.14	0	Flexure	0.44%
4	0.5	0.76	No	Yes	1.30	2.11	0	Flexure	0.13%
5	0.5	0.94	No	Yes	1.32	2.17	0	Flexure	0.06%
6	0.5	0.97	No	Yes	1.37	2.20	0	Flexure	0.02%
17	0.5	1.01	No	Yes	1.16	1.91	1	Flexure	0.03%
18	0.5	0.97	No	Yes	1.22	1.96	0	Flexure	0.03%
22	1.0	N/A	No	Yes	1.23	1.24	0	Flexure	0.02%
7	0.375	1.11	Yes	Yes	1.17	2.74	3	Flex-Shear	1.46%
10	0.375	0.83	Yes	Yes	1.24	2.42	1	Flex-Shear	1.71%
12	0.5	1.08	Yes	Yes	1.21	2.38	2	Flex-Shear	0.07%
13	0.375	1.37	N/A	Yes	1.12	2.60	3	Flex-Shear	1.07%
16	0.375	0.94	Yes	Yes	1.30	2.62	2	Flex-Shear	0.22%
19	0.5	0.93	Yes	Yes	1.21	2.24	1	Flex-Shear	0.08%
8	0.375	0.91	Yes	No	1.03	2.92	4	Flex-Shear	0.55%
14	0.25	1.40	Yes	No	1.11	2.89	5	Shear	0.18%
15	0.25	1.18	Yes	No	1.04	2.78	5	Shear	3.23%
20	0.25	1.10	Yes	No	1.06	2.54	5	Shear	0.43%
21	0.375	1.53	Yes	No	0.94	1.70	4	Shear	0.11%
9	0.5	1.00	No	Yes	1.06	1.72	N/A	Bond	10.0%
11	0.375	1.05	Yes	No	1.01	2.08	N/A	Bond	9.26%

5.3 MOMENT-DISPLACEMENT RESPONSE

The normalized moment-normalized displacement response is presented for five groups of specimens: 1) flexural failures, 2) flexure-shear failures, 3) internally reinforced specimens, 4) shear failures, and 5) bond failures. They are found in figures 5.16 – 5.20. A reference line at 125% $M_{p,PSDM}$ is plotted in each figure and represents the expected average value for a CFT that fails in flexure. Bishop (2009) found the mean ultimate moment for flexural tests to be 123% of $M_{p,PSDM}$ across several experimental programs. Behaviors to note in the figures include:

- The long, smooth plateau and sudden loss of resistance in the flexural failures as the steel tube experienced a tensile rupture due to flexural tension.
- The prominent peak in the middle of the drift range and gradual tapering of resistance for flexure-shear failures.
- The flat then increasing plateau and gradual loss of resistance for the shear failures.

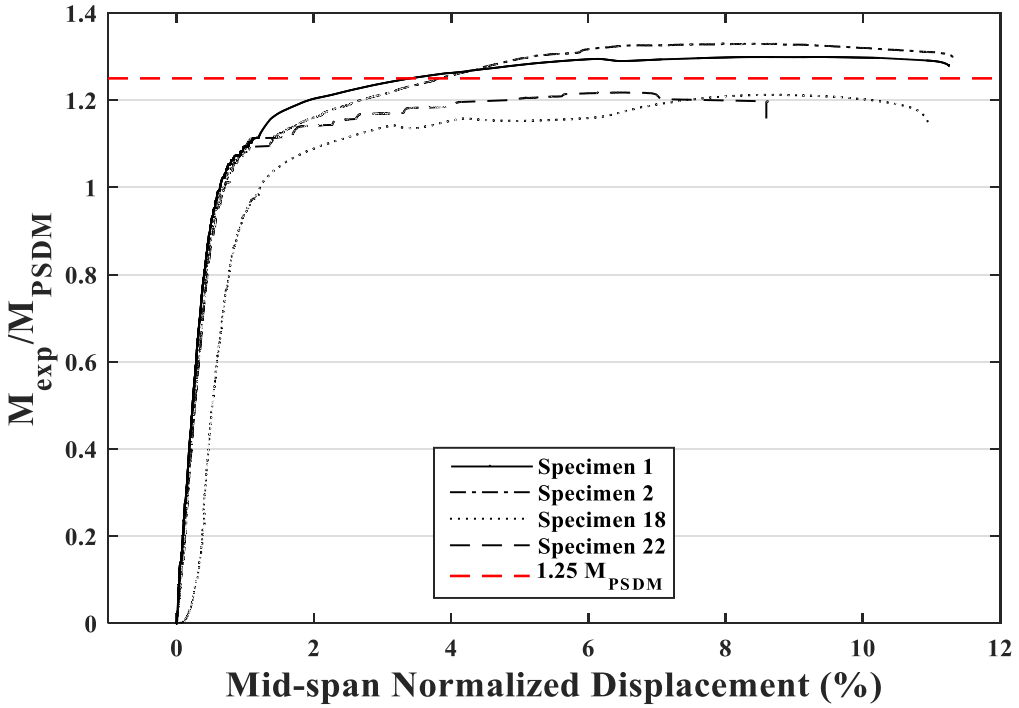

Figure 5.16: Moment-displacement response for flexural failures

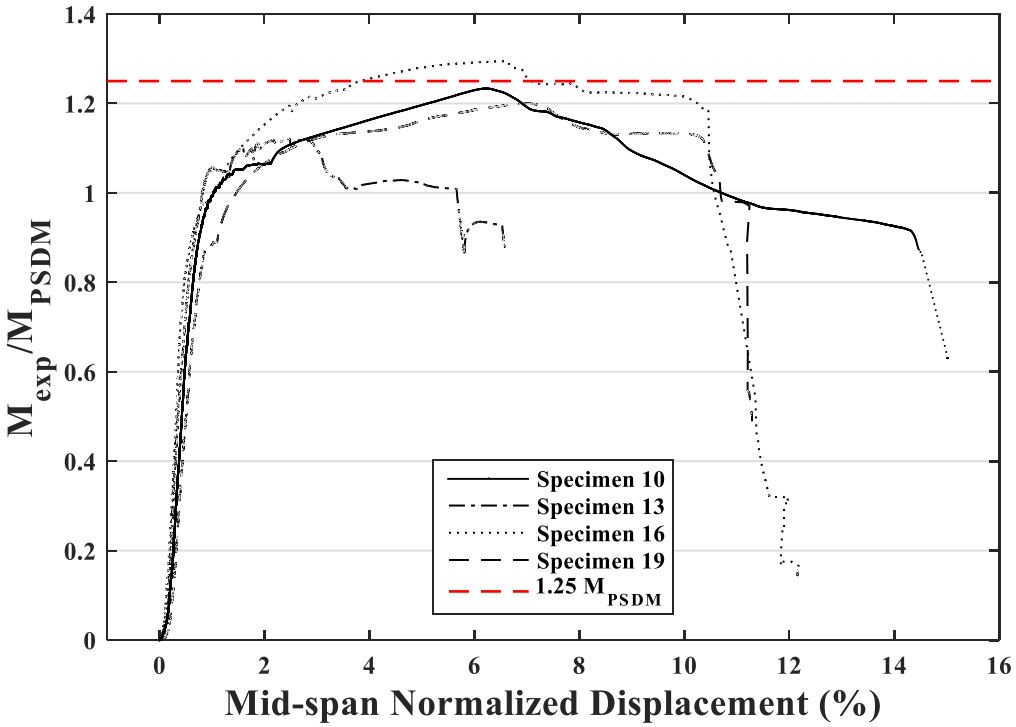

Figure 5.17: Moment-displacement response for flexure-shear failures

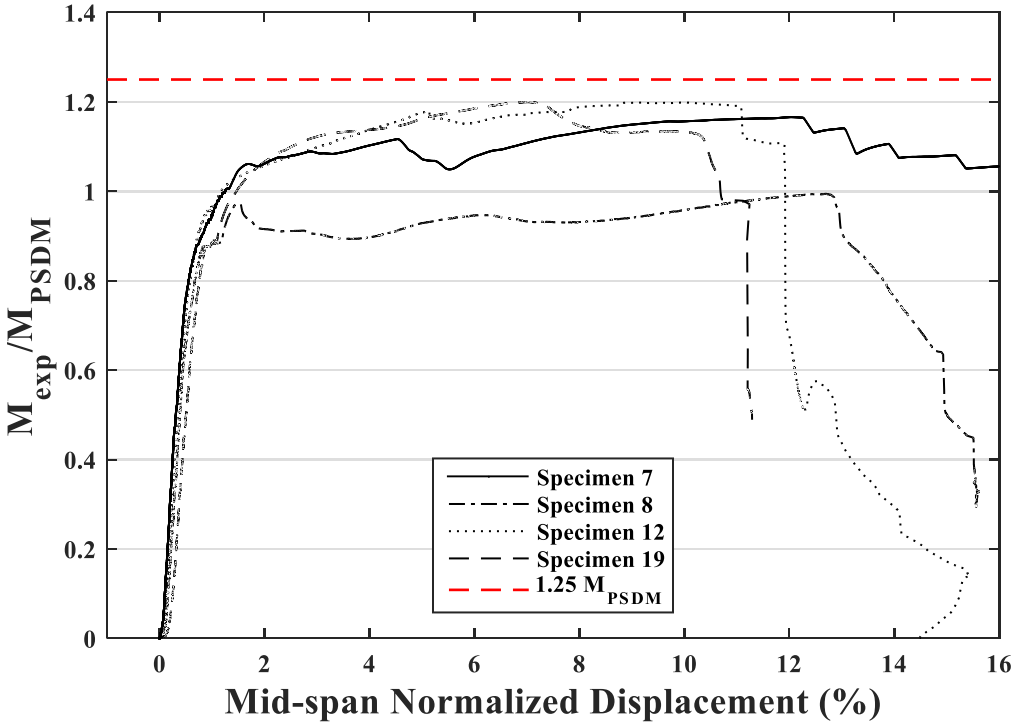

Figure 5.18: Moment-displacement response for RCFTs

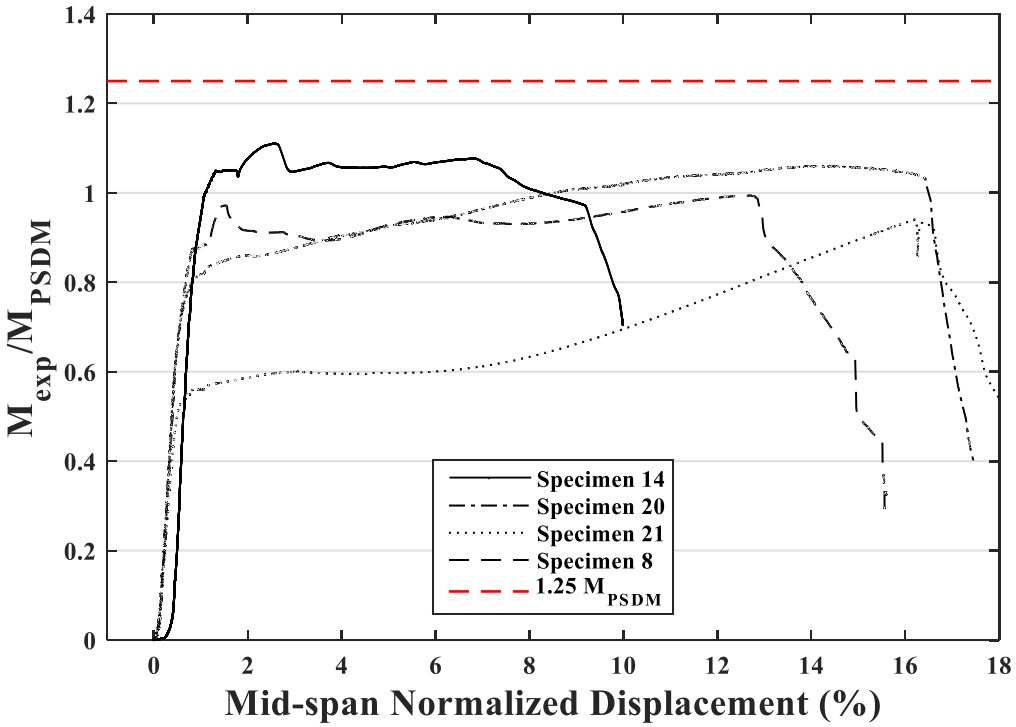

Figure 5.19: Moment-displacement response for shear failures

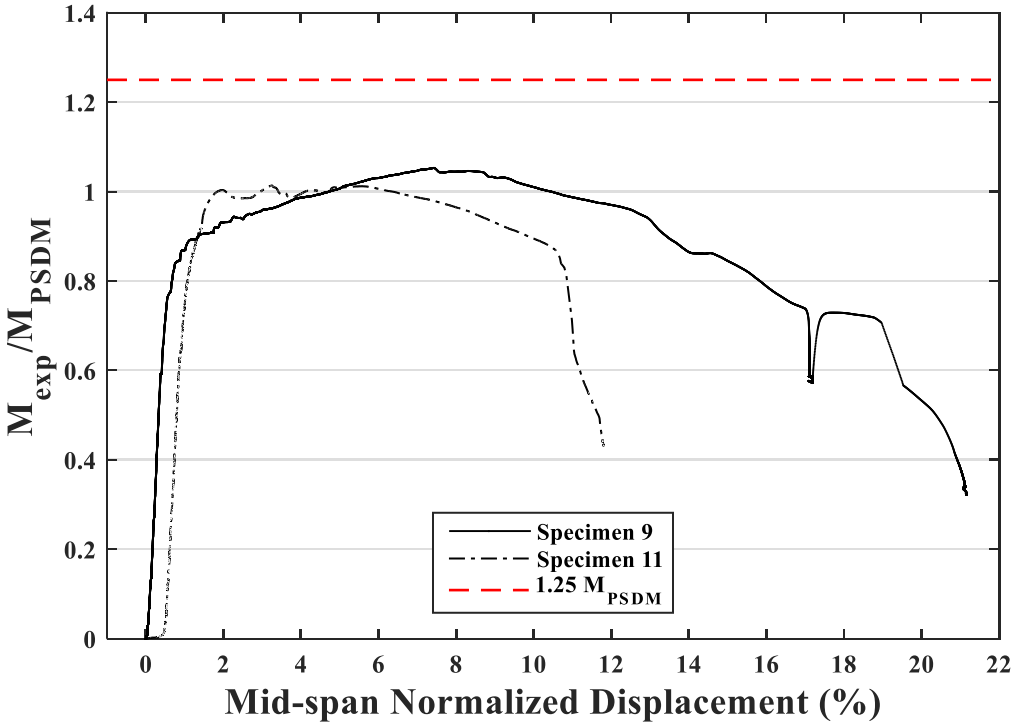

Figure 5.20: Moment-displacement response for bond failures

5.4 SHEAR-DISPLACEMENT RESPONSE

The normalized shear-normalized displacement response is presented for five groups of specimens: 1) flexural failures, 2) flexure-shear failures, 3) internally reinforced specimens, 4) shear failures, and 5) bond failures. They are found in figures 5.21 – 5.25. Two curves are plotted for each specimen depicting shear-displacement at both the north and south load cradles. A reference line at 170% V_s is plotted in each figure. It is approximately the maximum shear achieved for Specimen 21 and represents a possible value for the shear resistance contributed by the steel alone. Behaviors to note in the figures include:

- The items listed in the moment-displacement section.
- The flexural failures never reached a shear force sufficient to cause shear deformations.
- In Figure 5.24, the max shear force for Specimen 14 peaks earlier in the displacement range than the other three specimens. It appears that there might not have been sufficient bond strength in the tail to permit full development of the shear resistance.

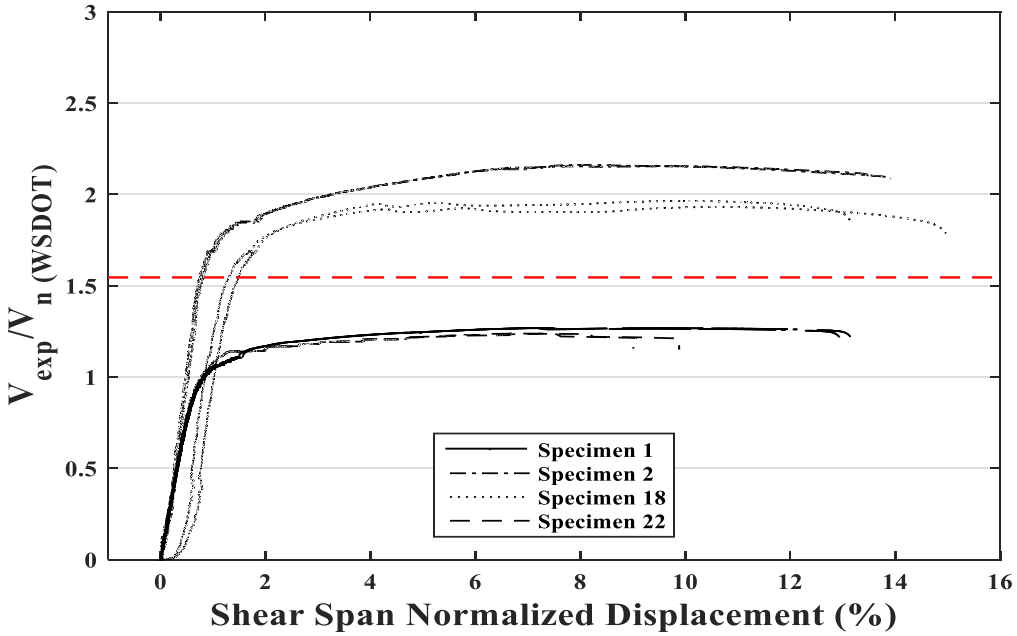

Figure 5.21: Shear-displacement response for flexural failures

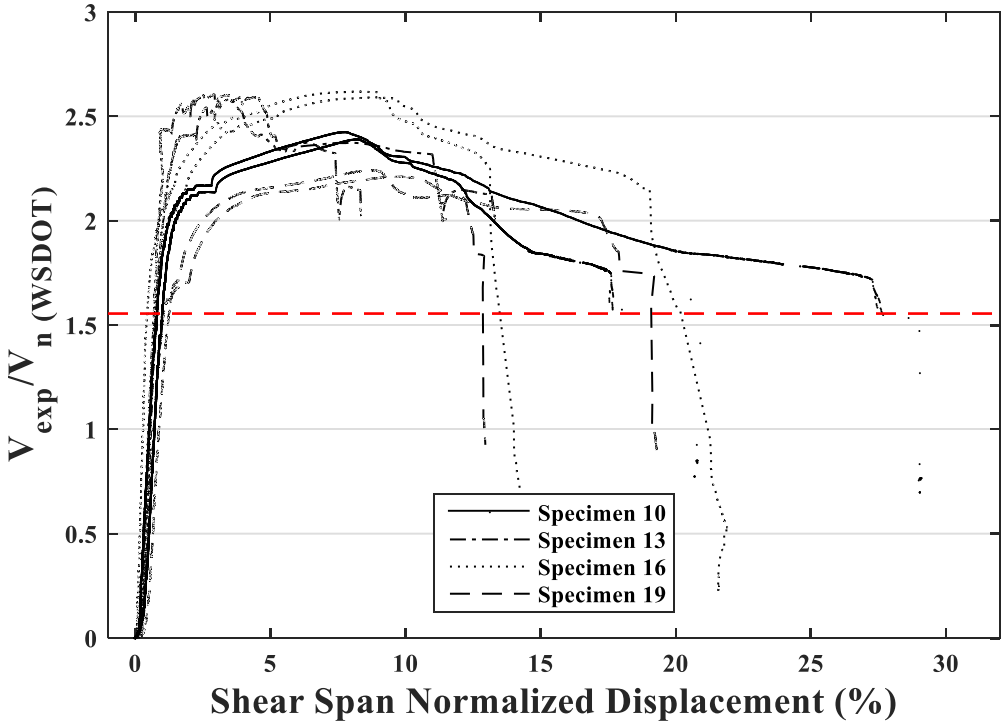

Figure 5.22: Shear-displacement response for flexure-shear failures

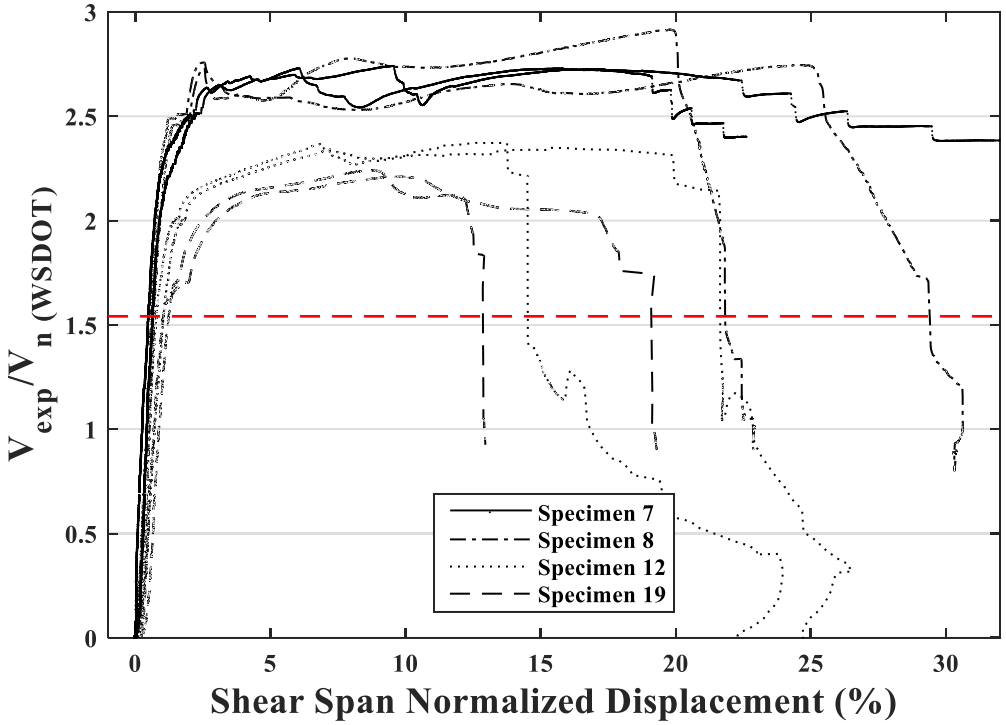

Figure 5.23: Shear-displacement response for RCFTs

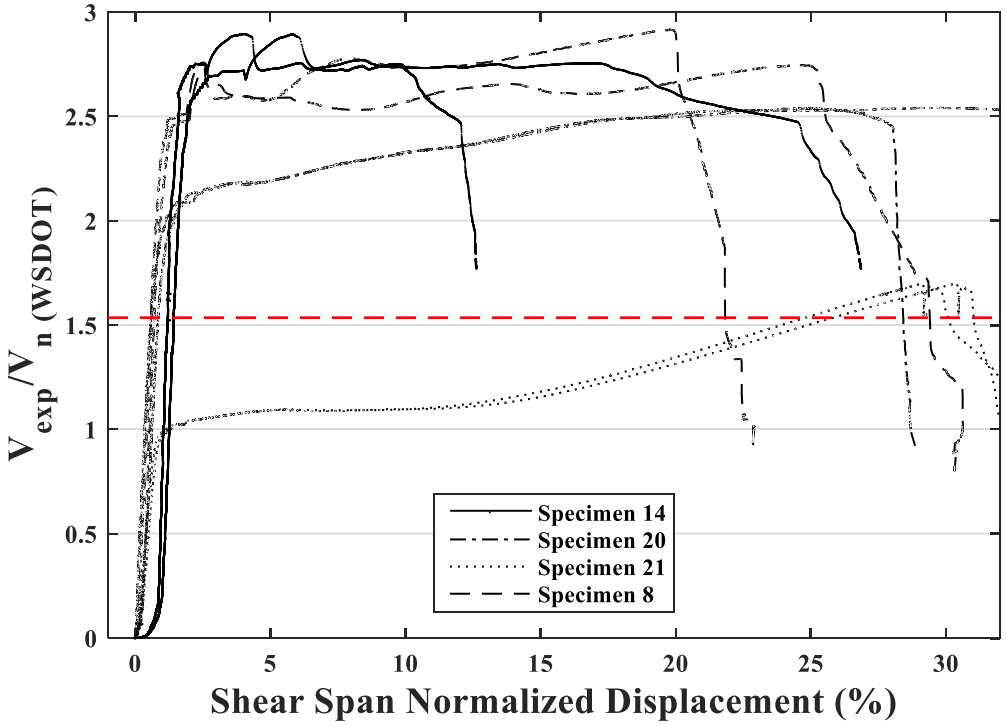

Figure 5.24: Shear-displacement response for shear failures

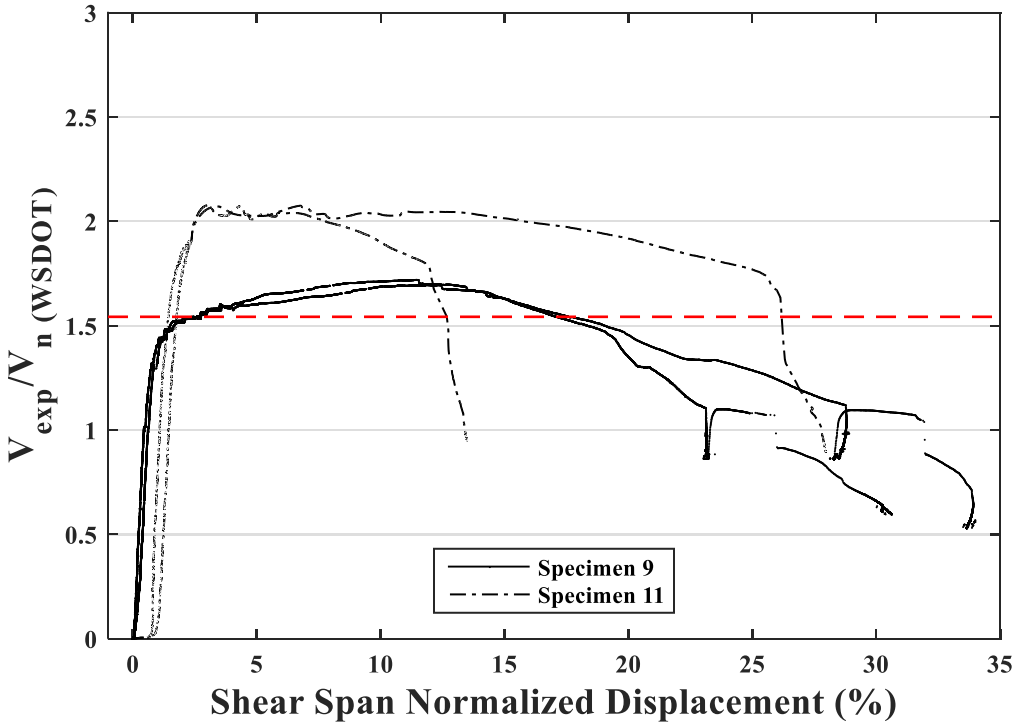

Figure 5.25: Shear-displacement response for bond failures

5.5 PARAMETER INFLUENCE

5.5.1 *Shear Span to Depth Ratio (a/D)*

Four shear span to depth ratios were studied in the experimental program: 1.0, 0.5, 0.375, and 0.25. The shear span is defined as the clear distance from the load cradle to the support cradle. This parameter had the greatest effect on the failure mode of the specimens, with the smaller *a/D* ratios exhibiting more shear deformation than the larger ones. The specimens with *a/D* ratios of 0.25 failed in shear, while the specimens with *a/D* ratios of 1.0 failed in flexure. All specimens with *a/D* = 0.5—except Specimen 9, with the greased interface, and those with internal reinforcement—failed in flexure. Specimens with *a/D* = 0.375 failed due to flexure-shear interaction with the exception of the RCFTs, Specimen 21 (with only gravel in the shear spans), and Specimen 11, which suffered a bond-type failure. The effect of internal reinforcement will be discussed further in Section 5.5.3. Table 5.3 lists the failure modes for each specimen and their respective *a/D* ratios. Figure 5.26 shows the normalized moments and normalized shears for this series, binned by specified concrete strength. Figure 5.27 shows the normalized moment and shear demands for all the specimens along with their failure modes.

Table 5.3: Shear span ratio series specimen properties

Specimen	1	2	17	10	16	21	14	20
a/D	1.0	0.5		0.375			0.25	
f'_c **(ksi)**	6.0	6.0	12.0	6.0	12.0	0	12.0	2.5
f'_{cm} **(ksi)**	6.01	6.22	9.45	6.15	8.61	0	8.60	2.79
f_{ym} **(ksi)**	49.6	49.6	55.4	53.9	56.8	56.8	55.4	56.8
$M_{p,PSDM}$ **(k-in)**	6069	6085	6958	6564	7069	5539	6910	6451
$V_{pr,\,M_{p,PSDM}}$ **(kip)**	316	543	621	713	768	602	960	896
V_{exp} **(kip)**	322	550	547	665	765	449	826	712
Failure Mode	flexure	flexure	flexure	flex-shear	flex-shear	shear	shear	shear
M_{exp} / $M_{p,PSDM}$	1.30	1.33	1.16	1.24	1.30	0.94	1.11	1.06
V_{exp} / $V_{n\,(WSDOT)}$	1.27	2.16	1.91	2.42	2.62	1.70	2.89	2.54

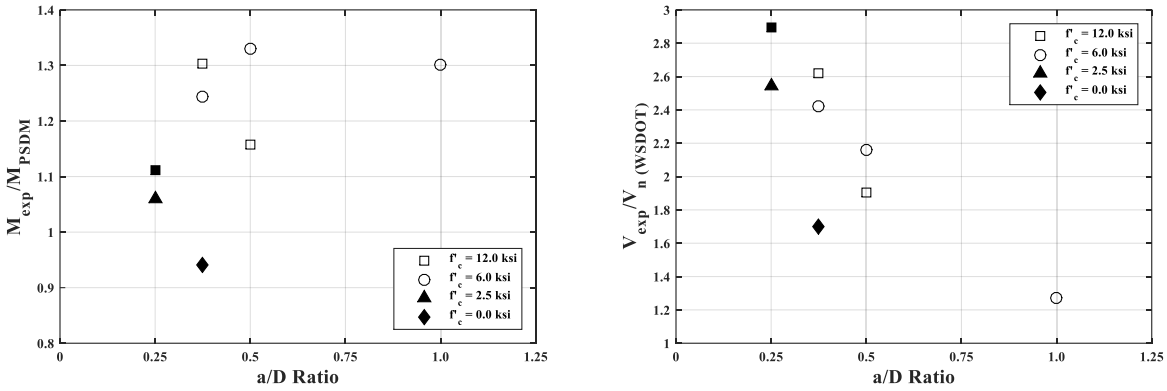

a) Normalized moment response b) Normalized shear response

Figure 5.26: Shear span to depth ratio series by concrete strength

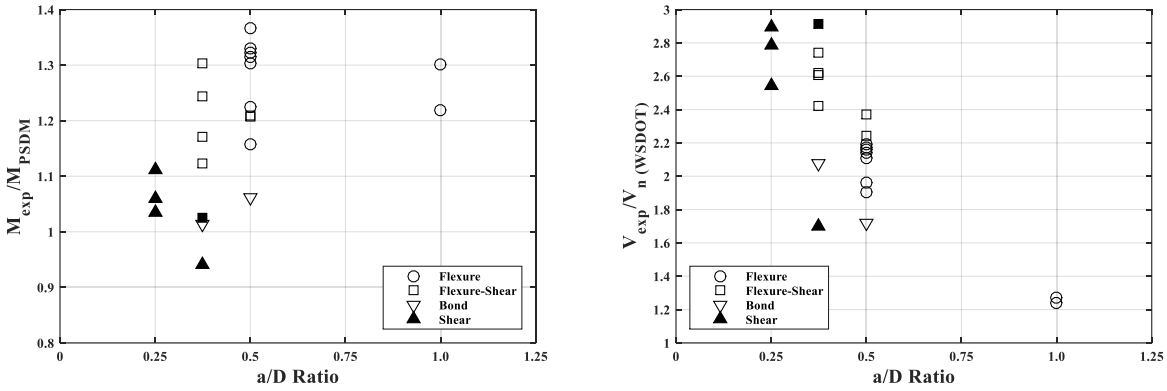

a) Normalized moment response b) Normalized shear response

Figure 5.27: Shear span to depth ratio series by failure mode

5.5.2 *Tail Length (L_T)*

An important source of shear resistance in CFTs comes from internal strutting action in the concrete fill. These strutting actions result in horizontal shear forces that need to be transferred from the concrete to the steel tube. Much of the previous shear research used end-caps, which can emulate conditions away from the ends but do not allow for the differential movement of the steel tube and concrete fill that may be present, especially near the ends of CFTs. A tail length, L_T, for the majority of the specimens was set at 2D to represent this in-field condition. There were five specimens that had shorter tail lengths to study the effects near the end of the CFTs. Table 5.4 describes the specimens used in the tail length series. Specimen 13, with the axial

Table 5.4: Tail length series specimen properties

Specimen	2	3	4	6	10	11	13	14	15
a/D	0.5				0.375			0.25	
P/P_0	0%				0%		8.5%	0%	
L_T	2D	D/2	D	2D	2D	D/2	D/2	2D	D/2
Failure Mode	flexure	flexure	flexure	flexure	flex-shear	bond	flex-shear	shear	shear
$M_{exp} / M_{p,PSDM}$	1.33	1.31	1.30	1.37	1.24	1.01	1.12	1.11	1.04
$V_{exp} / V_{n\ (WSDOT)}$	2.16	2.14	2.11	2.20	2.42	2.08	2.60	2.89	2.78
Max Slip (in)	0.018	0.044	0.026	0.007	0.683	0.926	0.107	0.070	0.404
Max Slip / L_t	0.04%	0.44%	0.13%	0.02%	1.71%	9.26%	1.07%	0.18%	3.23%

load, had a short tail length to enable use of the Williams rod and limit potential bending in the rod due to the specimen deformation. Specimen 15 had a tail length of 12.5 inches, compared to a standard length of 10 inches for the shortest tails, due to a fabrication error.

The relative slip between the steel tube and the concrete fill was measured at the north and south ends. Maximum values for all specimens can be seen in Figure 5.15. The variable tail length had little effect on the behavior and capacity of the three specimens that failed in flexure, as evidenced by their maximum normalized moment and normalized shear values and concrete slip measurements. The horizontal shear transfer required for composite flexural action is transferred via frictional bond and the binding action that occurs as CFTs deform (Roeder et al. 2009; Roeder et al. 1999). The CFTs that failed in flexure had sufficient length in the shear spans and tails to develop the horizontal shear forces required to maintain composite behavior.

The remaining specimens in the series show that the end condition, in addition to the shear span length, can have a significant effect on the shear capacity, and even the failure mode, of CFTs. Specimen 15 has a minor reduction in shear resistance when compared to Specimen 14, and Specimen 11 has a large reduction when compared to Specimen 10. There was cross-sectional distortion visible at one end of Specimens 11 and 15, as seen in Figures 4.37 and 4.50, respectively, likely due to some prying action from the concrete wedge at the end. This distortion reduced the available bond, allowing the concrete to slip and the shear cracks to open wider than

in their respective baseline specimens. The effect is more pronounced in Specimen 11, which had *a/D* = 0.375.

Figures 5.28 and 5.29 plot moment versus concrete slip and shear versus concrete slip, respectively. Figure 5.30 shows the normalized moments and normalized shears for the tail-length series. The shorter end condition provides less length for the horizontal shear transfer and allows for more distortion of the cross-section as prying action occurs near the end of the tube.

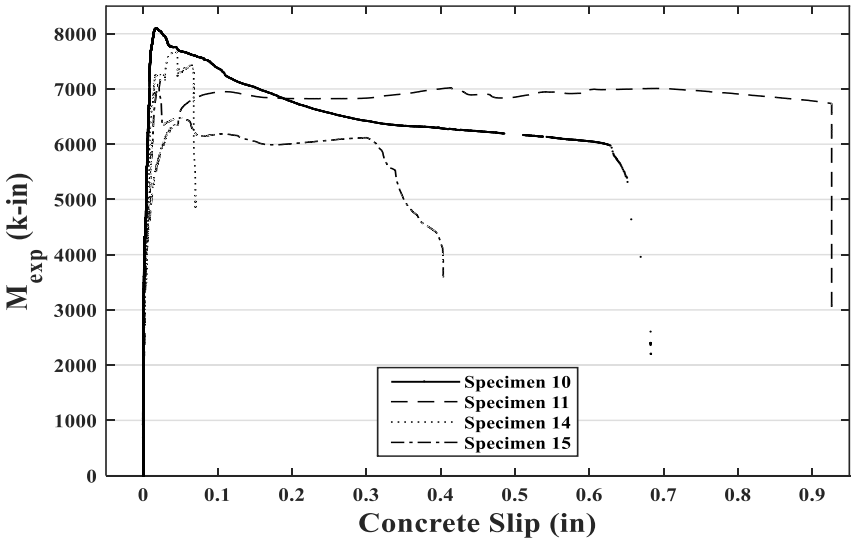

Figure 5.28: Moment vs. max concrete slip

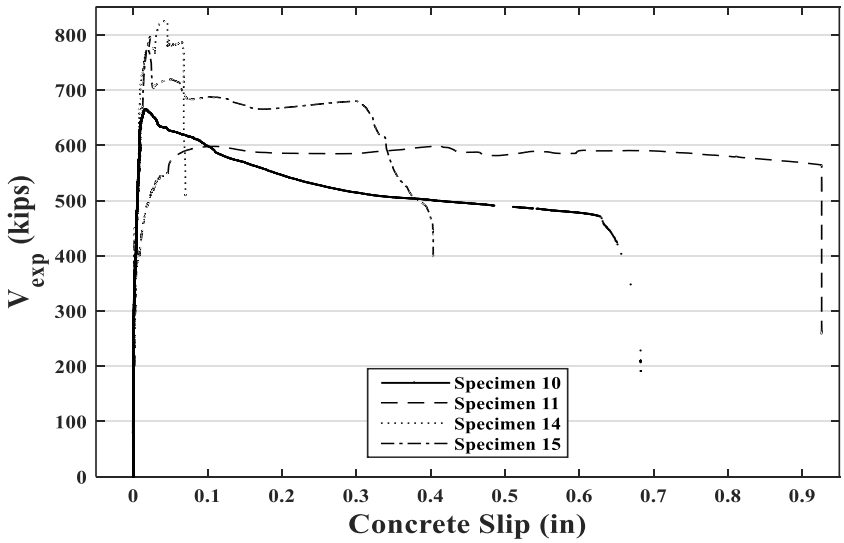

Figure 5.29: Shear vs. max concrete slip

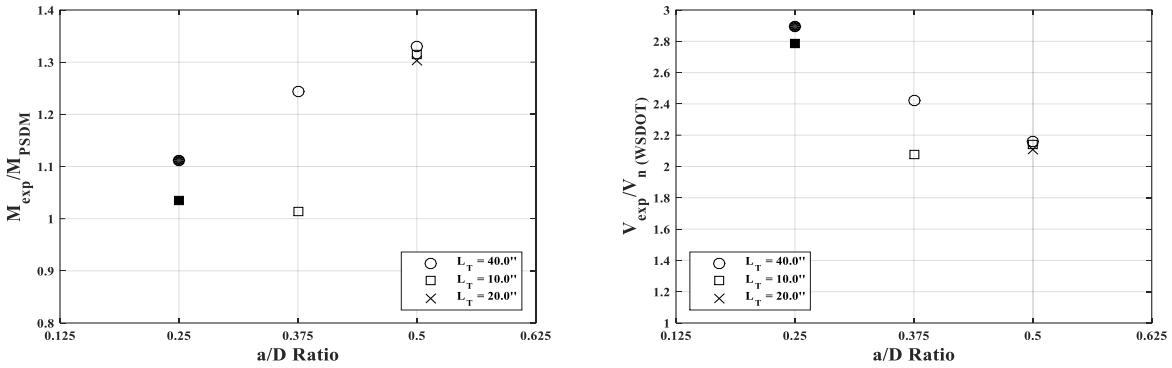

a) Normalized moment response b) Normalized shear response

Figure 5.30: Tail length series specimens

All specimens in the series had a D/t ratio of 80, and testing should be done to assess the effect of different D/t ratios, especially on cross-sectional distortion. The tail length parameter should also be tested with spiral-welded tubes, as the weld provides excellent engagement with the concrete fill.

5.5.3 *Internal Reinforcement Ratio (ρ_{int})*

The literature review found no available research on the shear behavior of reinforced concrete-filled steel tubes. Four internally reinforced specimens with two different shear span to depth ratios and two different tube-diameter-to-wall-thickness ratios were tested. Table 5.5 outlines the series specimen properties. The reinforcement increased the moment capacity sufficiently to shift the failure mode from flexure to flexure-shear for the *a/D*=0.5 specimens and significantly changed the behavior of all four specimens with respect to their baseline specimens. Specimen 8, with 2.01% reinforcement and *a/D*=0.375, is likely a shear failure even though its preliminary classification is flexure-shear. Figure 5.31 shows the moment-displacement responses for RCFT specimens and their baselines. Figure 5.32 shows the shear-displacement responses for RCFT specimens and their baselines. Note that three of the four RCFTs—Specimens 7, 8, and 12—experience their peak bending moment near the end of the displacement range, and two of the

four—Specimens 8 and 12—experience their peak shear at the same point. The late shear peak for Specimen 7 is nearly as high as the early peak. This behavior is typical for the response curves of the unreinforced CFT specimens that fail in shear. Specimen 19's response fits with the more typical unreinforced CFT flexure-shear response seen in the experimental program and is identified by a pronounced peak in the middle of the displacement range. Its response is not influenced by the internal reinforcement as much as that of the other specimens. The ratio of reinforcement area to the tube steel area, A_{sr}/A_s, shown in Table 5.5, explains this phenomenon.

Table 5.5: Reinforcement series specimen properties

Specimen	*D/t*	*a/D*	ρ_{int}	f'_c (ksi)	M_{exp} / $M_{p,PSDM}$	V_{exp} / $V_{n\ WSDOT}$	Failure Mode	A_{sr} / A_s
2	80	0.5	0%	6.22	1.33	2.16	flexure	0%
12	80		1.13%	6.18	1.21	2.37	flex-shear	21.5%
19	53.3		1.07%	9.13	1.21	2.24	flex-shear	13.2%
10	80	0.375	0%	6.15	1.24	2.42	flex-shear	0%
7			1.04%	6.45	1.17	2.74	flex-shear	19.7%
8			2.01%	6.48	1.02	2.92	shear	38.2%

Figure 5.33 shows the normalized moments and normalized shears for the specimens in this series. In addition to changing the failure mode at lower *a/D* ratios, internal longitudinal reinforcement increases the shear capacity of the concrete fill by restraining crack openings in the shear span.

The reinforcement was fully developed in the concrete before it reached the shear span in all the RCFTs. More research should be done with short development and tail lengths to assess the impact at an end condition. Research is also needed to determine the impact that internal reinforcement coupled with a spiral-welded tube would have on resistance and deformation capacity.

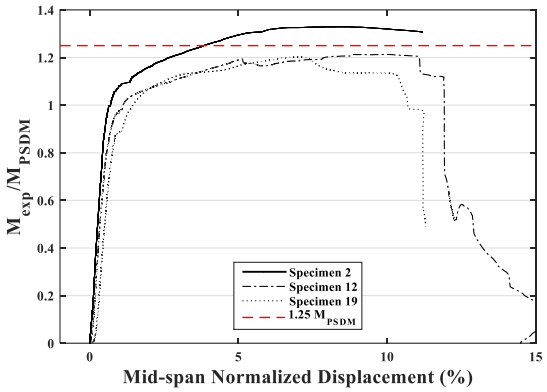

a) Moment-displacement for *a/D*=0.5

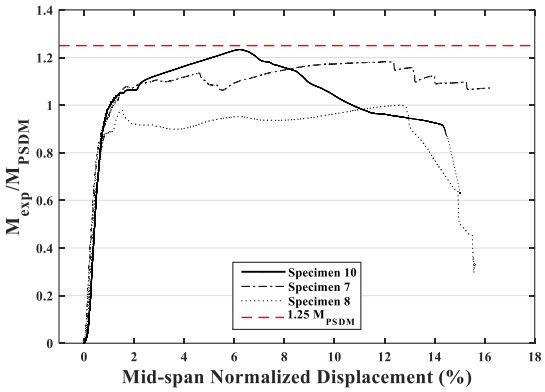

b) Moment-displacement for *a/D*=0.375

Figure 5.31: Moment-displacement response plots for internal reinforcement series

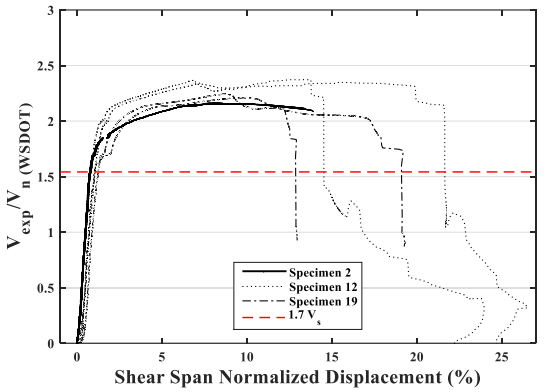

a) Shear-displacement for *a/D*=0.5

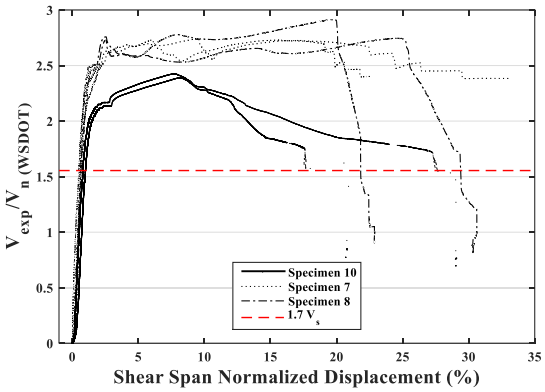

b) Shear-displacement for *a/D*=0.375

Figure 5.32: Shear-displacement response plots for internal reinforcement series

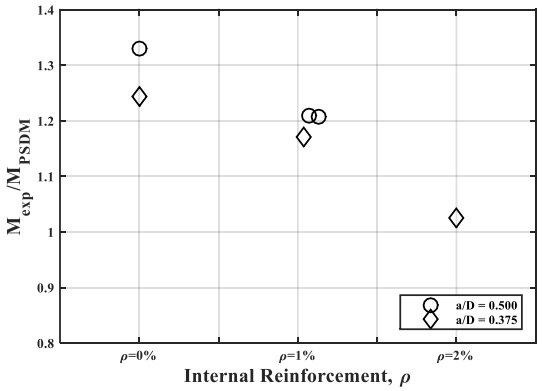

a) Normalized moment response

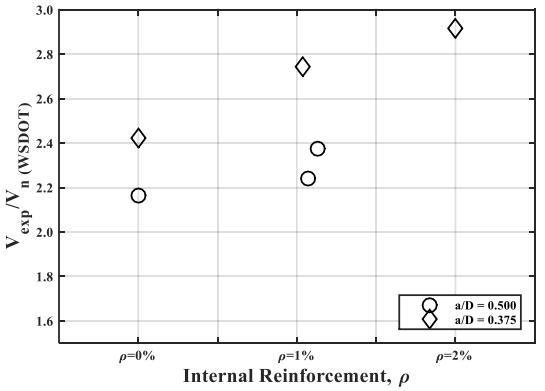

b) Normalized shear response

Figure 5.33: Internal reinforcement series

5.5.4 *Interface Condition*

There were four distinct interface conditions represented in the experimental program: 1) clean interior tube surface with a straight-seam welded tube, 2) clean interior tube surface with a spirally welded tube, 3) muddied interior tube surface with a straight-seam welded tube, and 4) greased interior tube surface with a straight-seam welded tube. The normalized moment-normalized displacement curves for each of the four specimens are shown in Figure 5.34. Shear was not a significant factor in this series as all of the specimens had an $a/D = 0.5$.

The CFT with the greased interface, Specimen 9, exhibited very little composite behavior as it experienced a bond failure but, while only attaining 106% of the plastic moment of the composite section, still reached 134% of the plastic moment capacity of the steel tube. Specimen 9 shows that, at a minimum, the concrete provides for good local stability for the steel and provides a conservative lower bound for the flexural capacity, even if there is essentially no horizontal shear stress transfer at the concrete-steel tube interface. The maximum shear resistance was 1.89 V_s.

The ultimate moment capacities of the other three specimens in the series were very similar. The primary difference appears to be in the initial yielding slope as the spiral-welded tube retains more stiffness than the straight-seamed ones between yield moment and peak moment. The interlock between the concrete and the internal weld seam adds significant force

Table 5.6: Interface series specimen properties

Specimen	2	5	6	9
a/D	0.5			
Interface	clean SS	muddied SS	clean SW	greased SS
L_T	2D			
Failure Mode	flexure	flexure	flexure	bond
M_{exp} / $M_{p,PSDM}$	1.33	1.32	1.37	1.06
V_{exp} / $V_{n\ (WSDOT)}$	2.16	2.17	2.20	1.72
Max Slip (in)	0.018	0.024	0.007	4
Max Slip / L_t	0.04%	0.06%	0.02%	10%

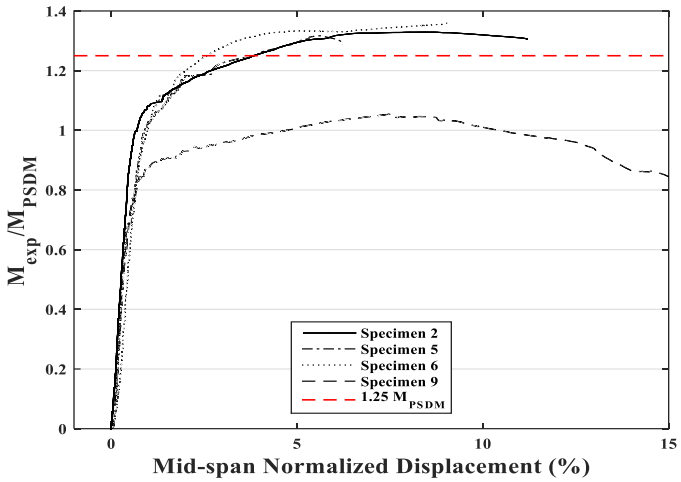

Figure 5.34: Moment-displacement for concrete-tube interface series

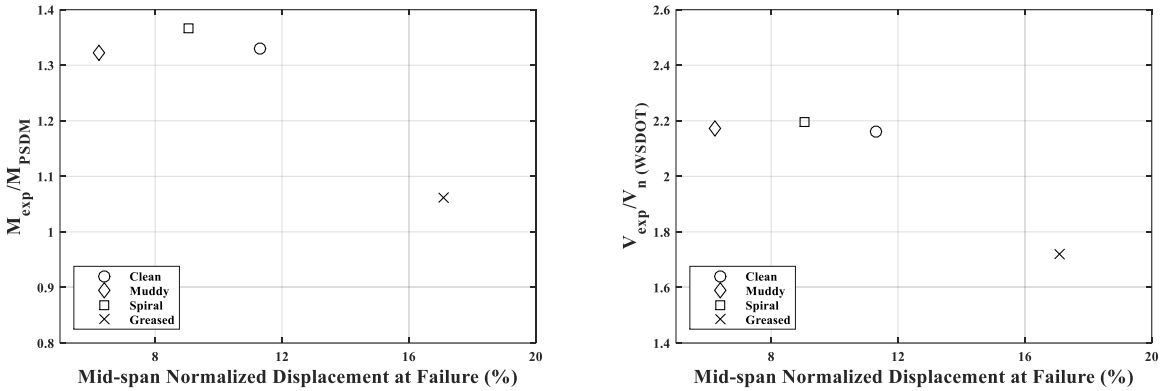

a) Normalized moment response b) Normalized shear response

Figure 5.35: Failure displacement of interface series

transfer between the tube and the concrete. The muddied interface also appears to have increased the force transfer as the post-yield stiffness for Specimen 5 is slightly greater than Specimen 2 and its clean interface. Figure 5.35 shows the normalized moments and normalized shears for the CFTs in this series plotted against the normalized displacement at failure.

There was little difference in the behavior of the CFTs in the tube-concrete interface series for the specimens with likely real-world conditions, but all of the failures were flexural in nature. The same conditions should be tested at an *a/D* ratio of 0.5 or lower as that will result in

global shear behavior and impose different stress conditions on the interface. This is an interesting issue for CFTs experiencing shear, as the strutting that forms in the concrete fill exerts a significant demand on the horizontal shear force transfer across the interface. The interface condition should also be tested with CFTs that have a shorter tail lengths.

5.5.5 *Axial Load*

CFTs are most often used as columns or piles in deep foundations and subject to axial loading in addition to flexure and shear. The presence of an axial compression increases the shear strength of concrete but not of steel, and it was desired to study its effect on a composite CFT. The project budget did not allow for a self-reacting frame to apply a constant axial load, but an attempt was made to simulate axial compression using post-tensioning with a high-strength Williams rod and a center-hole ram. The load was applied via a 12 in. square plate centered on the specimen ends. The loaded area of concrete was 131 in^2., accounting for the center duct in the CFT. One CFT, Specimen 13, had an axial load of 200 kips applied via the Williams rod in addition to the transverse loads. A description of the load variation can be found in Section 4.13. The specimens used for comparison are Specimen 10, the baseline a/D=0.375, and Specimen 11, the short-tail version of Specimen 10. Figure 5.36 shows the moment-displacement and shear-displacement plot for the axial load series. Figure 5.37 shows the normalized moments and normalized shears for the axial load series. Table 5.7 outlines the properties of the specimens used in this series.

Table 5.7: Axial load series specimen properties

Specimen	10	11	13
a/D	0.375		
P/P_0	0%	0%	8.5%
L_T	2D	D/2	D/2
Failure Mode	flex-shear	bond	flex-shear
M_{exp} / $M_{p,PSDM}$	1.24	1.01	1.12
V_{exp} / $V_{n\ (WSDOT)}$	2.42	2.08	2.60

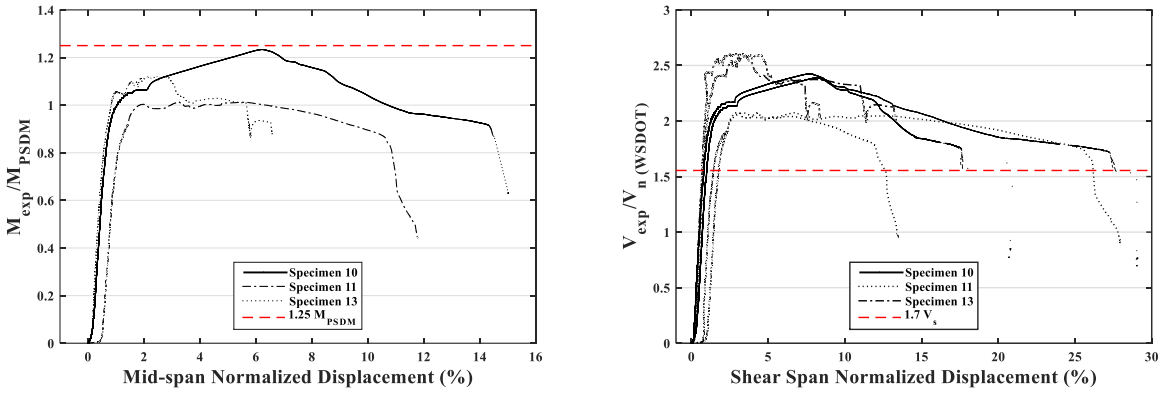

a) Moment-displacement response b) Shear-displacement response

Figure 5.36: Moment- and shear-displacement plots for axial load series

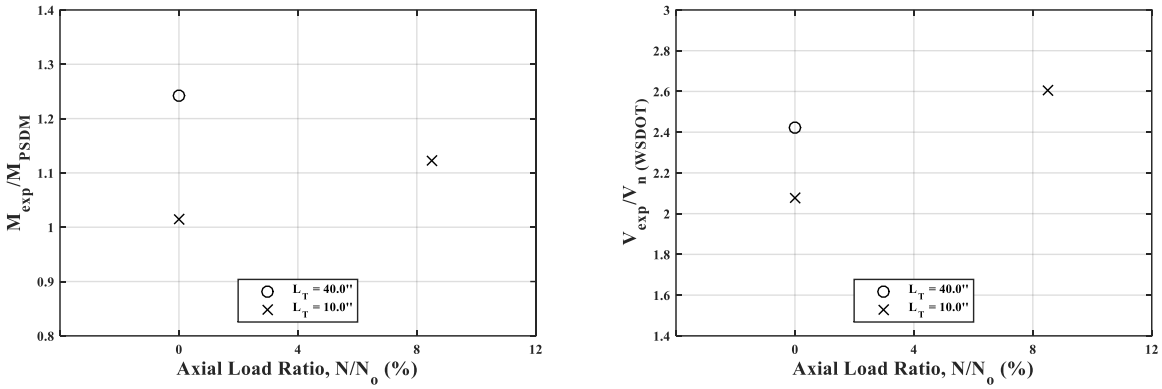

a) Normalized moment response b) Normalized shear response

Figure 5.37: Effect of axial load

The axial load moderately increases the flexural capacity of the CFT above the baseline specimen before the capacity drops to approximately match that of Specimen 11. The shear capacity is significantly increased over that of the baseline specimen until the shear stresses overcome the axial load effect and the shear capacity matches that of the baseline. It never falls to the level of Specimen 11 as the axial load still helps restrain the cracks from opening too wide. There is a definite increase in shear resistance due to the axial compression load but it is not easily quantified given the limitations of the test setup and the limited number of specimens. The absence of provisions for axial load in the shear design expressions in this thesis is conservative as the ultimate capacity is initially increased but then settles down to match that of a baseline

specimen. Future experimental or analytical studies should be undertaken to quantify the axial load effect and should consider the effects of axial tension.

5.5.6 *Concrete Strength*

Three different specified concrete strengths were used in the experimental program to determine the parameter's effect on behavior. The specimen with the gravel in the shear spans, Specimen 21, could be said to have a concrete with zero strength at those locations, adding a fourth concrete strength. Table 5.8 outlines the properties of the specimens used in this series. The specimens were grouped by *a/D* ratio and their response curves are shown in figures 5.38, 5.39, and 5.40. The normalized moment and normalized shear demands are plotted in Figure 5.41. Figure 5.42 shows the normalized mid-span displacement at failure plotted against the specimen concrete strength.

Noting that the sample size is small, the following observations are made:

- Flexural overstrength of CFTs that fail in flexure decreases as the concrete strength increases.
- Shear overstrength of CFTs that fail in shear increases as the concrete strength increases when the WSDOT shear expression is employed, demonstrating that the expression doesn't capture well the concrete contribution to the shear capacity.
- For CFTs that fail due to flexure-shear interaction, both apparent shear overstrength and apparent moment overstrength increase as the concrete strength increases.
- As concrete strength increases, ultimate deformation capacity decreases.

Table 5.8: Concrete strength series specimen properties

Specimen	*a/D*	D/t	f'$_c$ (ksi)	f'$_{cm}$ (ksi)	M_{exp} / $M_{p,PSDM}$	V_{exp} / $V_{n\ WSDOT}$	$\bar{\Delta}_{fail}$ (%)
2	0.5	80	6.0	6.22	1.33	2.16	11.32
17		53.3	12.0	9.45	1.16	1.91	10.64
10	0.375	80	6.0	6.15	1.24	2.42	14.57
16			12.0	8.61	1.30	2.62	10.36
21			0	0	0.94	1.70	17.16
14	0.25	80	12.0	8.60	1.11	2.89	9.48
20			2.5	2.79	1.06	2.54	16.69

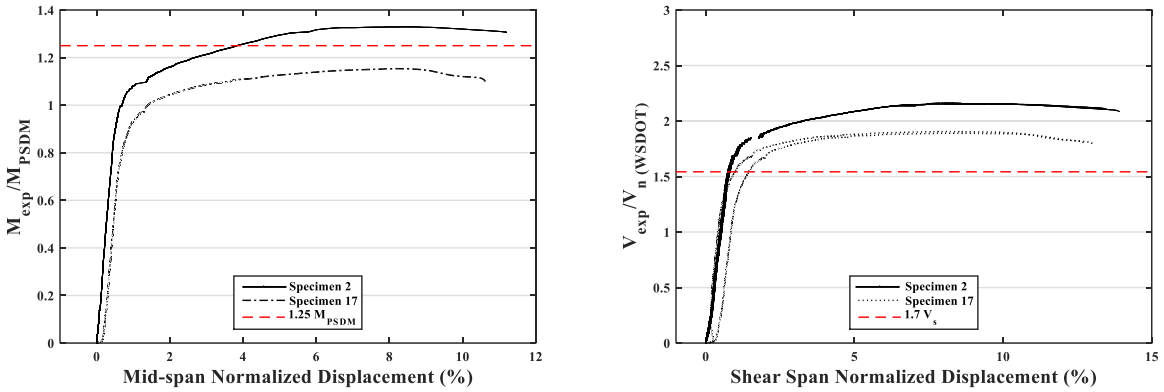

a) Moment-displacement b) Shear-displacement

Figure 5.38: Response curves for *a/D*=0.5 in concrete strength series

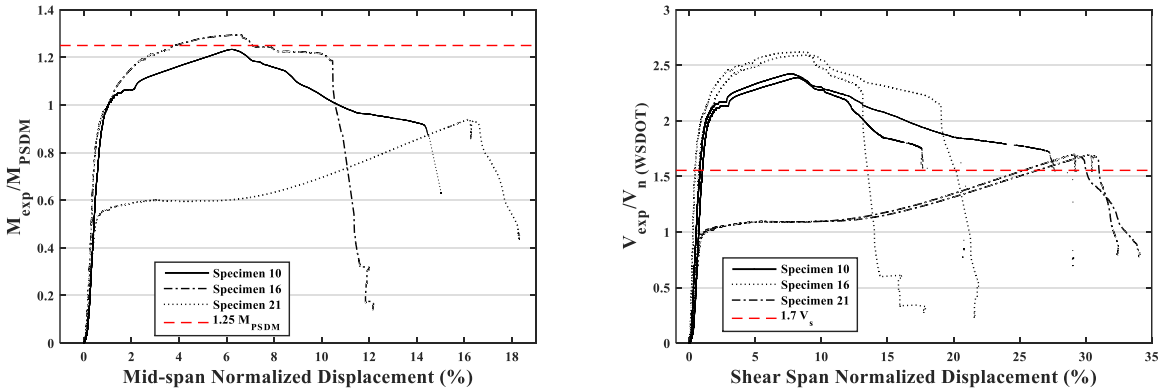

a) Moment-displacement b) Shear-displacement

Figure 5.39: Response curves for *a/D*=0.375 in concrete strength series

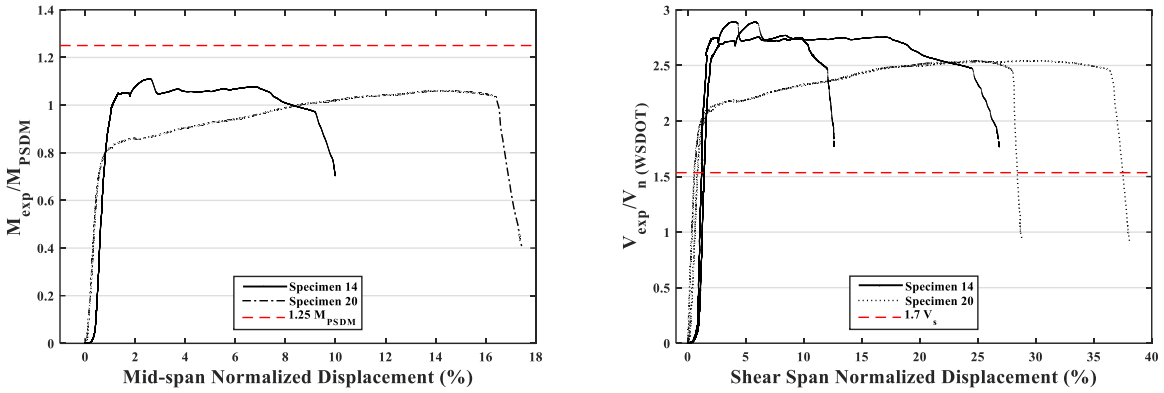

a) Moment-displacement b) Shear-displacement

Figure 5.40: Response curves for *a/D*=0.25 in concrete strength series

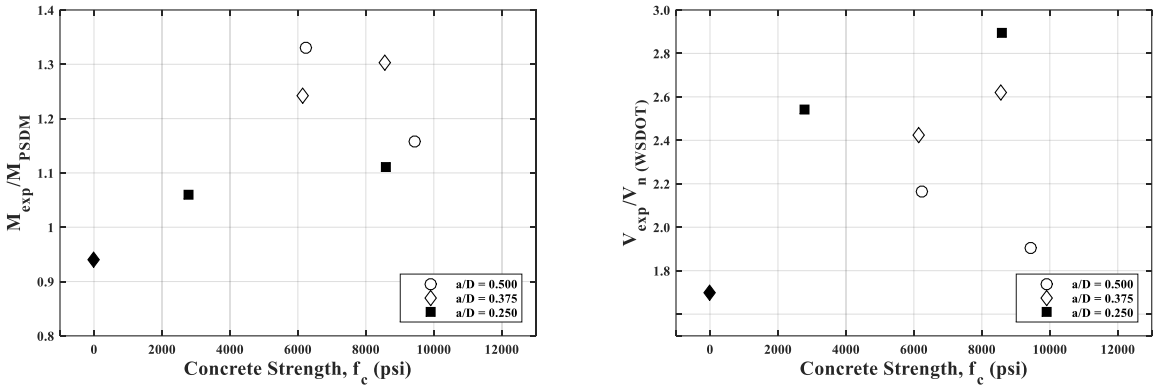

a) Normalized moment response b) Normalized shear response

Figure 5.41: Effect of concrete strength

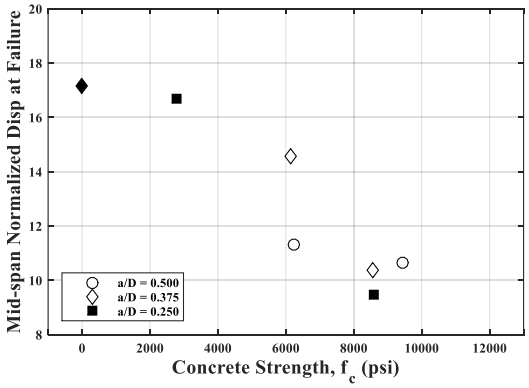

Figure 5.42: Effect of concrete strength on ultimate displacement

5.5.7 *Tube Diameter to Thickness Ratio (D/t)*

Availability of twenty in. diameter steel tubes that fit the requirements of the test apparatus was limited to 1/4 in. and 3/8 in. wall thicknesses so there were only two values of the D/t ratio used in testing, 80 and 53.3. The CFTs with D/t of 53.3 were only tested with an *a/D* ratio of 0.5 because their shear and moment resistance for the lower *a/D* ratios were greater than the capacity of the test apparatus.

Table 5.9 outlines the properties of the specimens used in this series. Figure 5.43 shows the moment-displacement response, and Figure 5.44 shows the normalized moments and normalized shears. There was a possible decrease in moment capacity as D/t decreased but this could also be attributed to the higher concrete strength of Specimen 18 relative to Specimen 2. More research in scenarios where shear strength is a potential failure mode, such as short shear spans and short tails lengths, is needed.

Table 5.9: D/t series specimen properties

Specimen	*a/D*	D/t	ρ_{int}	f_c (psi)	M_{exp} / $M_{p,PSDM}$	V_{exp} / $V_{n\ WSDOT}$	Failure Mode
2	0.5	80	0%	6220	1.33	2.16	flexure
18		53.3		8641	1.22	1.96	
12	0.5	80	1.13%	6177	1.21	2.37	flex-shear
19		53.3	1.07%	9131	1.21	2.24	

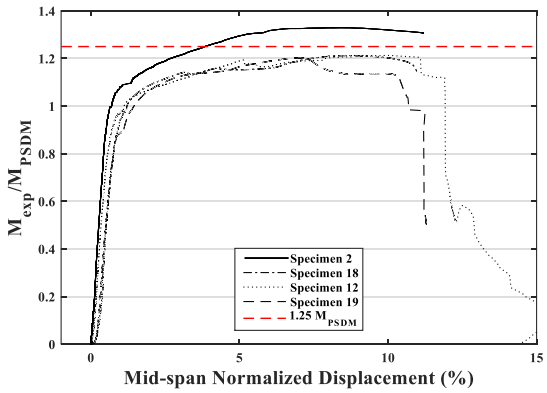

Figure 5.43: Moment-displacement response for D/t series

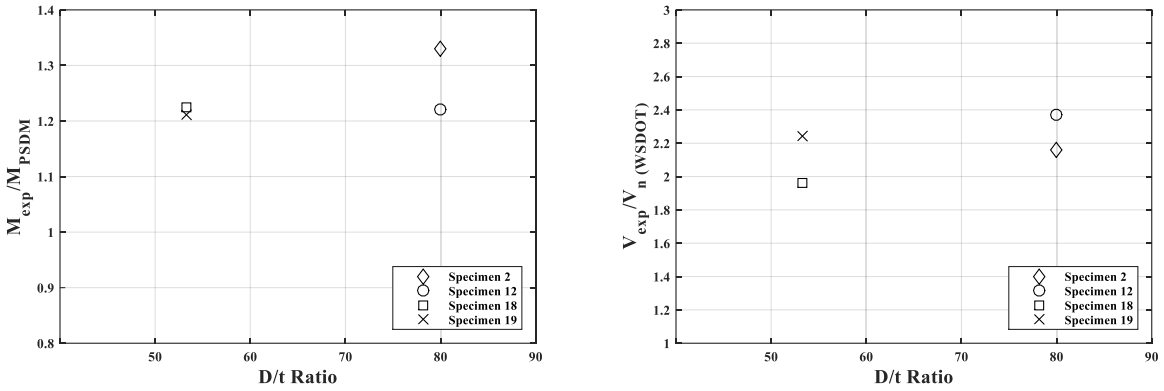

a) Normalized moment response b) Normalized shear response

Figure 5.44: Effect of D/t for a/D=0.5

5.5.8 *Steel Strength to Concrete Strength Ratio*

For steel-concrete composite members, the ratio of steel strength to concrete strength, f_{ym} / f'_{cm}, can play a role in behavior. Table 5.10 shows the specimen properties, and figure 5.45 shows the normalized moments and normalized shears plotted against f_{ym} / f'_{cm} for all specimens except Specimen 21 (with the gravel fill), whose ratio is undefined.

Table 5.10: Material strength ratio specimen properties table

Specimen	1	2	3	4	5	6	7	8	9	10	11
a/D	1.0	0.5	0.5	0.5	0.5	0.5	0.375	0.375	0.5	0.375	0.375
f_{ym} / f'_{cm}	8.25	7.98	7.53	7.64	7.08	9.85	7.77	8.32	7.93	8.77	8.60
Failure Mode	flexure	flexure	flexure	flexure	flexure	flexure	flexure -shear	flexure -shear	bond	flexure -shear	bond
$M_{exp} / M_{p,PSDM}$	1.30	1.33	1.31	1.30	1.32	1.37	1.17	1.02	1.06	1.24	1.01
$V_{exp} / V_{n\ WSDOT}$	1.27	2.16	2.14	2.11	2.17	2.20	2.74	2.92	1.72	2.42	2.08

Specimen	12	13	14	15	16	17	18	19	20	21	22
a/D	0.5	0.375	0.25	0.25	0.375	0.5	0.5	0.5	0.25	0.375	1.0
f_{ym} / f'_{cm}	8.73	10.12	6.45	6.31	6.60	5.87	6.62	6.27	20.38	undef	5.82
Failure Mode	flexure-shear	flexure-shear	shear	shear	flexure-shear	flexure	flexure	flexure-shear	shear	shear	flexure
$M_{exp} / M_{p,PSDM}$	1.21	1.12	1.11	1.04	1.30	1.16	1.22	1.21	1.06	0.94	1.23
$V_{exp} / V_{n\ WSDOT}$	2.37	2.60	2.89	2.78	2.62	1.91	1.96	2.24	2.54	1.70	1.24

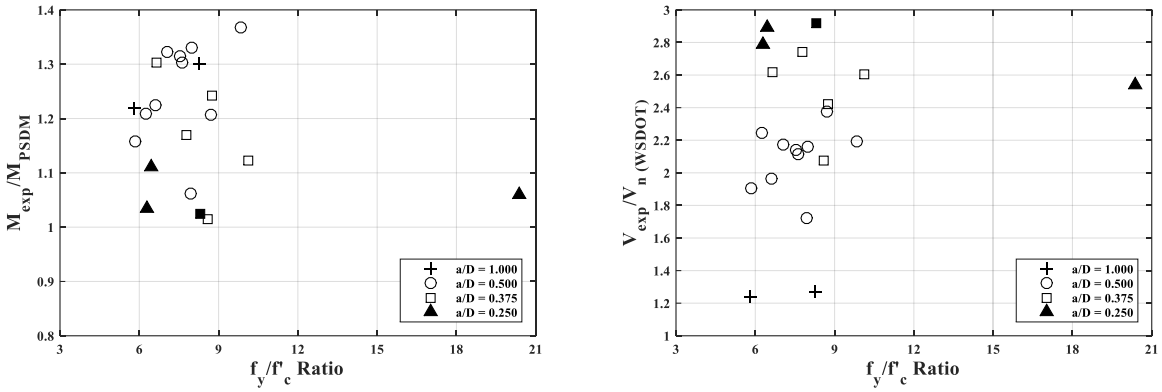

a) Normalized moment response b) Normalized shear response

Figure 5.45: Effect of steel-concrete strength ratio

5.6 Evaluation of Shear Design Expressions

The WSDOT and AISC design expressions are compared to the experimental data in this chapter. Three potential design expressions are also introduced and evaluated.

5.6.1 *Current Design Provisions*

Table 5.11 shows the experimental shears at failure normalized by the WSDOT design capacity for the shear and flexure-shear failures. Table 5.12 shows the experimental shears at failure normalized by the AISC Method 1 design capacity for the shear and flexure-shear failures. Table 5.13 shows the experimental shears at failure normalized by the AISC Method 2 design capacity for the shear and flexure-shear failures. AISC Method 3 is the same as Method 1 as none of the specimens contained hoop or spiral shear reinforcement. It is seen from the shear failures in the experimental program that the CFTs can easily exceed 2.5 times the capacity given by WSDOT provisions when using actual yield strengths of the CFT components. The multiplier increases to 3.5 when using nominal yield strengths. The AISC design expression are more even more conservative.

Table 5.11: Normalized shears for WSDOT expression

Failure Type	Specimens	V_{exp} / $V_{n\_(WSDOT)}$						
			Mean	Median	Min	Max	Std. Dev.	C.O.V.
flex-shear	8	2.92	2.783	2.837	2.541	2.917	0.172	0.062
shear	14	2.89						
shear	15	2.78						
shear	20	2.54						
shear	21	1.70	N/A					
flex-shear	7	2.74	2.500	2.514	2.242	2.741	0.185	0.074
flex-shear	10	2.42						
flex-shear	12	2.37						
flex-shear	13	2.60						
flex-shear	16	2.62						
flex-shear	19	2.24						

Table 5.12: Normalized shears for AISC Method 1

Failure Type	Specimens	V_{exp} / $V_{n\_(WSDOT)}$						
			Mean	Median	Min	Max	Std. Dev.	C.O.V.
flex-shear	8	3.20	3.044	3.141	2.692	3.202	0.241	0.079
shear	14	3.20						
shear	15	3.09						
shear	20	2.69						
shear	21	1.70	N/A					
flex-shear	7	3.02	2.732	2.740	2.399	3.023	0.227	0.083
flex-shear	10	2.65						
flex-shear	12	2.59						
flex-shear	13	2.83						
flex-shear	16	2.89						
flex-shear	19	2.40						

Table 5.13: Normalized shears for AISC Method 2

Failure Type	Specimens	V_{exp} / $V_{n\_(WSDOT)}$						
			Mean	Median	Min	Max	Std. Dev.	C.O.V.
flex-shear	8	11.17	15.72	14.56	11.17	22.57	4.849	0.308
shear	14	14.92						
shear	15	14.21						
shear	20	22.57						
shear	21	N/A						
flex-shear	7	11.94	13.77	14.00	11.49	16.23	1.807	0.131
flex-shear	10	14.20						
flex-shear	12	11.49						
flex-shear	13	16.29						
flex-shear	16	13.80						
flex-shear	19	14.90						

5.6.2 *Proposed Design Expressions*

The current design expressions for shear are overly conservative and can unnecessarily limit CFT designs that appear shear critical. Using the test results, three types of shear design expressions for CFTs and RCFTs that better represent the contribution of the steel tube, the concrete fill, and the internal reinforcement were developed and evaluated. The design expressions are for monotonically loaded CFTs. For cyclically loaded CFTs the contribution of the concrete could conservatively be assumed to be zero, as is traditional in reinforced concrete design, but there is no data in this experimental program to verify the assumption.

Figure 5.46 shows $M_{exp}/ M_{p,PSDM}$ plotted against V_uD/M_u. Figure 5.47 shows $V_{exp}/V_{n\ (WSDOT)}$ plotted against V_uD/M_u. The ratio V_uD/M_u is the inverse of the a'/D ratio and describes the interaction between flexural demand and shear demand. a' is the center to center shear span that was used for equilibrium calculations. Figure 5.47 displays a trend in the flexure-shear specimens and the RCFT specimens that the shear capacity decreases with decreasing V_uD/M_u as the failures move from shear to flexure. The trends are easily seen in Figure 5.48a, as well. The data show that $V_uD/M_u \geq 2.08$ for all CFT shear failures, $1.63 \leq V_uD/M_u \leq 1.72$ for all CFT flexure-shear failures, and $V_uD/M_u \leq 1.37$ for all CFT flexural failures. All the RCFT

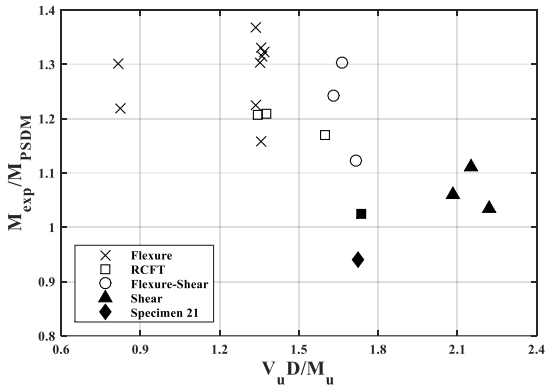

Figure 5.46: Effect of V_uD/M_u on moment

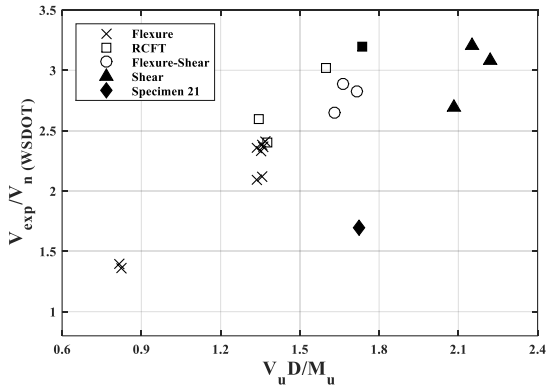

Figure 5.47 Effect of V_uD/M_u on shear

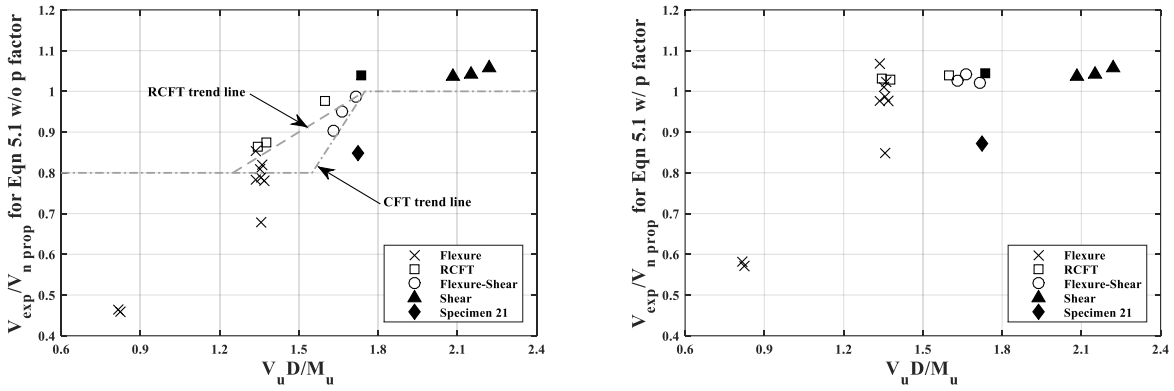

a) Shear DCRs without p-factor b) Shear DCRs with p-factor

Figure 5.48: Eqn. 5.1 normalized shears vs. V_uD/M_u for Eqn. 5.1

specimens failed in flexure-shear interaction and the data show that $1.35 \leq V_uD/M_u \leq 1.74$. As described in Section 5.1.3, the shear capacity in CFTs is reduced at higher bending moments. The aforementioned V_uD/M_u limits will be used as rough guidelines in the following shear expressions to interpolate the shear capacity for flexure-shear specimens.

The first expression to be evaluated for the nominal shear capacity of a CFT, V_n, is

$$V_n = p(V_s + V_c) \tag{5.1a}$$

$$V_s = \alpha 0.6 f_y (0.5 A_s) \tag{5.1b}$$

$$V_c = \left(\beta\lambda\sqrt{f_c'} + 5000\rho_{int}\right)A_c \tag{5.1c}$$

$$\lambda = \begin{cases} 0.85, & L_T < 2D \\ 1.0, & L_T \geq 2D \end{cases} \tag{5.1d}$$

$$p = \begin{cases} 0.8 \; if \; {V_uD}/{M_u} \leq 1.55 \\ 1.0 \; if \; {V_uD}/{M_u} \geq 1.75 \\ interpolate \; otherwise \end{cases} \quad for \; CFTs \tag{5.1e}$$

$$p = \begin{cases} 0.8 \; if \; {V_uD}/{M_u} \leq 1.25 \\ 1.0 \; if \; {V_uD}/{M_u} \geq 1.75 \\ interpolate \; otherwise \end{cases} \quad for \; RCFTs \tag{5.1f}$$

,where $\alpha = 2.0$ and $\beta = 10$ are multipliers for the steel contribution and the concrete contribution, respectively, p is a multiplier to account for flexure-shear interaction, V_s is the shear strength of the steel tube, V_c is the shear strength of the concrete fill, f_y is the yield stress of the steel tube, A_s is the cross-sectional area of the steel tube, f'_c is the compressive strength of the concrete fill in psi, ρ_{int} is the internal reinforcement ratio, A_c is the cross-sectional area of the concrete fill, and L_T is the tail length.

The factors α and β were chosen via trial and error to provide a good fit to the test data. Figures 5.48a and 5.49b show the normalized shear demands of Equations 5.1 for all but the bond failure specimens before and after the p-factor is applied to show the trending. As more experimental and analytical data is added to the database, the factors α and β, as well as the values used to calculate the p-factor, should be updated for further evaluation. The current values fit the data fairly well but the sample size is quite limited as seen in Table 5.14. The flexural specimens are not included as shear was not the critical failure mode. The values used for α and β predict the composite behavior well and appear to represent the separate steel and concrete contributions well as seen when comparing Specimen 14 to Specimen 20; both normalized shears are 1.04. The capacity may be over predicted, however, for cyclic loading when the concrete contribution is neglected.

Table 5.14: Normalized shears for Equations 5.1

Failure Type	**Specimens**	**V_uD/M_u**	**V_{exp} / V_{n_prop} for Eqn 5.1**						
				Mean	**Median**	**Min**	**Max**	**Std. Dev.**	**C.O.V.**
flex-shear	8	1.74	1.04	1.045	1.043	1.037	1.056	0.008	0.008
shear	14	2.15	1.04						
shear	15	2.22	1.06						
shear	20	2.08	1.04						
shear	21	1.72	0.85	N/A					
flex-shear	7	1.60	1.04	1.031	1.030	1.020	1.041	0.008	0.008
flex-shear	10	1.63	1.03						
flex-shear	12	1.35	1.03						
flex-shear	13	1.72	1.02						
flex-shear	16	1.66	1.04						
flex-shear	19	1.38	1.03						

The second expression to be evaluated for the nominal shear capacity of a CFT, V_n, is

$$V_n = V_s + V_c \tag{5.2a}$$

$$V_s = \alpha q 0.6 f_y (0.5 A_s) \tag{5.2b}$$

$$q = \begin{cases} 1.0 \; if \; {V_u D}/{M_u} \leq 1.5 \\ 1.25 \; if \; {V_u D}/{M_u} \geq 2.0 \\ interpolate \; otherwise \end{cases} for \; CFTs \tag{5.2c}$$

$$q = \begin{cases} 1.0 \; if \; {V_u D}/{M_u} \leq 1.35 \\ 1.25 \; if \; {V_u D}/{M_u} \geq 1.65 \\ interpolate \; otherwise \end{cases} for \; RCFTs \tag{5.2d}$$

$$V_c = \left(\beta \lambda \sqrt{f_c'} + 2500 \rho_{int} \, {V_u D}/{M_u}\right) A_c \tag{5.2e}$$

$$where \; 1.35 \leq {V_u D}/{M_u} \leq 1.65$$

$$\lambda = \begin{cases} 0.85, \; L_T < 2D \\ 1.0, \; L_T \geq 2D \end{cases} \tag{5.2f}$$

,where all variables are the same except $\alpha = 1.7$ and $\beta = 8$, and q is an additional multiplier on the steel strength while p is no longer used.

Equations 5.1 applied the moment-shear interaction adjustment to both the concrete and steel portions of the shear resistance. Equations 5.2 attempt to break out the adjustment to each portion. See Figure 5.49 for the normalized shears and Table 5.15 for the brief statistical analysis for Equations 5.2.

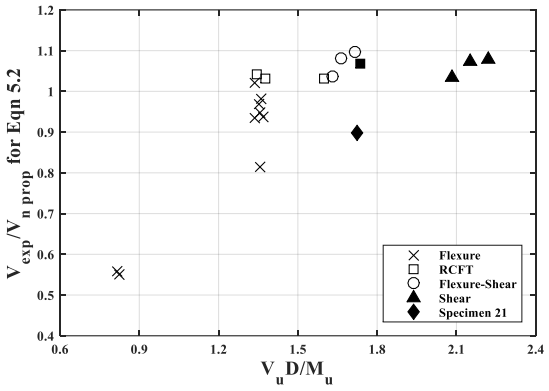

Figure 5.49: Normalized shears for Eqn. 5.2

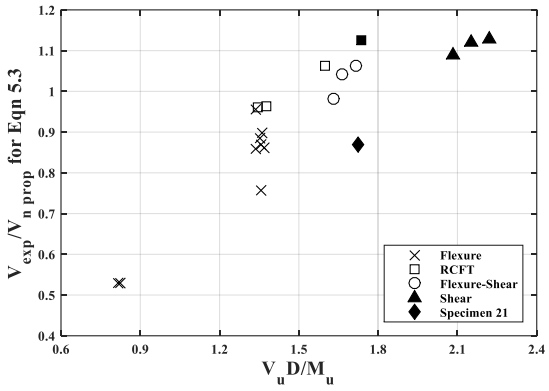

Figure 5.50: Normalized shears for Eqn. 5.3

The third expression to be evaluated for the nominal shear capacity of a CFT, V_n, treats the tube and the longitudinal reinforcement together as a total reinforcement ratio and is given by

$$V_n = V_s + V_c \tag{5.3a}$$

$$V_s = \alpha 0.6 f_y (0.5 A_s) \tag{5.3b}$$

$$V_c = \left(\beta\lambda\sqrt{f_c'} + 2500\rho_{total}\right) A_c \tag{5.3c}$$

$$where\ {}^{V_u D}/_{M_u} \leq 2.0$$

$$\rho_{total} = {}^{(A_s + A_{sr})}/_{A_c} \tag{5.3d}$$

$$\lambda = \begin{cases} 0.85, & L_T < 2D \\ 1.0, & L_T \geq 2D \end{cases} \tag{5.3e}$$

,where $\alpha = 1.7$ and $\beta = 8$, and ρ_{tot} is the total reinforcement ratio. The rest of the variables are as defined above. See Figure 5.50 for the normalized shears and Table 5.16 for the brief statistical analysis for Equations 5.3.

All expressions permit an increase in shear strength if internal longitudinal reinforcement is present. They do not include provisions for axially loaded CFTs, but it is conservative to ignore axial compression as its presence increases the shear capacity of the concrete fill

Table 5.15: Normalized shears for Equations 5.2

Failure Type	Specimen	V_uD/M_u	V_{exp} / V_{n_prop} for Eqn 5.2						
				Mean	Median	Min	Max	Std. Dev.	C.O.V.
flex-shear	8	1.74	1.07	1.064	1.071	1.035	1.078	0.020	0.018
shear	14	2.15	1.07						
shear	15	2.22	1.08						
shear	20	2.08	1.04						
shear	21	1.72	1.00	N/A					
flex-shear	7	1.60	1.03	1.053	1.038	1.031	1.097	0.029	0.027
flex-shear	10	1.63	1.04						
flex-shear	12	1.35	1.04						
flex-shear	13	1.72	1.10						
flex-shear	16	1.66	1.08						
flex-shear	19	1.38	1.03						

and reduces the likelihood of bond failure near the ends of the CFTs. None of the test specimens utilized lightweight concrete, so there is no provision included for it in the design expressions.

The shear capacity is reduced for all expressions when the critical section is within 2D of the end of the tube, as there are multiple factors that can reduce the available resistance. The reduction factor, λ, is binary because there are insufficient data points to support interpolation, but it is likely that the end effect will vary gradually depending upon conditions. Potential contributors to the need for the shear strength reduction are tail length, whether the tube is spirally welded or straight-seam, the presence of a compressive axial load, and the presence of internal reinforcement, in addition to others.

While Specimen 8, a flexure-shear failure, is included in the statistical analysis of the shear failure group, Specimen 21 (with the gravel fill) is not, even though it is a shear failure, because it is not truly a CFT. Equations 5.1 appear to provide the best fit for the current data, with its global adjustment for moment-shear interaction. Equations 5.2 and 5.3 appear to still retain some variation with V_uD/M_u. The methods used to account for flexure-shear interaction may not be sufficient. All three expressions can be re-evaluated when there is more experimental and analytical data available. Table 5.17 provides a comparison of the three potential design

expressions and the WSDOT design expression. The data set includes all of the shear and flexure-shear specimens except for Specimen 21.

Table 5.16: Normalized shears for Equations 5.3

Failure Type	Specimen	V_uD/M_u	V_{exp} / V_{n_prop} for Eqn 5.3						
				Mean	Median	Min	Max	Std. Dev.	C.O.V.
flex-shear	8	1.74	1.13	1.116	1.123	1.090	1.127	0.017	0.016
shear	14	2.15	1.12						
shear	15	2.22	1.13						
shear	20	2.08	1.09						
shear	21	1.72	0.87	N/A					
flex-shear	7	1.60	1.06	1.012	1.011	0.960	1.064	0.049	0.048
flex-shear	10	1.63	0.98						
flex-shear	12	1.35	0.96						
flex-shear	13	1.72	1.06						
flex-shear	16	1.66	1.04						
flex-shear	19	1.38	0.96						

Table 5.17: Normalized shear demand statistics for all expressions

Design Expression	Mean	Median	Min	Max	Std. Dev.	C.O.V.
Equations 5.1	1.036	1.038	1.020	1.056	0.010	0.010
Equations 5.2	1.057	1.055	1.031	1.097	0.025	0.024
Equations 5.3	1.054	1.064	0.960	1.127	0.065	0.062
$V_{n\,(WSDOT)}$	2.614	2.611	2.242	2.917	0.224	0.086
$V_{n\,(AISC\_1)}$	2.857	2.862	2.399	3.202	0.272	0.095
$V_{n\,(AISC\_2)}$	14.55	14.21	11.17	22.57	3.265	0.224

Chapter 6. CONCLUSIONS AND FUTURE WORK

While much research has been performed on the flexural and axial properties of concrete-filled steel tubes, little has been done to understand their shear capacity and deformation behavior. As such, the current design provisions for shear of circular CFTs are excessively conservative and may limit their economical and effective use in certain cases. A research program was undertaken to assess the available shear strength and deformation characteristics of CFTs and RCFTs subjected to transverse loading. Series of tests were devised to determine the effect of geometric, material, and other design parameters on CFT behavior. The experiments will be used to develop and validate high resolution finite element models in order to extend the parameter studies. Once the studies are complete, the research will conclude with recommendations of design expressions for shear strength and deformation capacity of CFTs.

6.1 RESEARCH SUMMARY

The few available studies on shear behavior of CFTs were reviewed. The research was limited in quantity and focused primarily on small-scale CFTs whose applicability to their use in bridge piers and deep foundations is questionable. A testing apparatus with sufficient capacity to test CFTs up to 20 in. was designed and constructed. Twenty-two large-scale circular CFT members were then fabricated and tested with very short shear spans at the Structural Research Laboratory at the University of Washington. The shear span was defined as the clear distance between the load and support cradles. The failure modes seen in the test results were: 1) flexure—included flexural buckling and tensile steel rupture due to flexural stresses; 2) shear—occurred when large shear deformations and steel rupture were seen in the shear spans with no apparent sign of flexural deformation or damage; 3) flexure-shear interaction—occurred when large shear

deformations and steel rupture were seen in the shear spans following significant flexural deformation; and 4) bond stress failure—occurred when there was significant relative movement between the concrete fill and the steel tube, indicating a loss of composite action. A simple procedure was outlined to determine the applicable failure mode for each specimen. Of the twenty-two tested specimens, nine failed in flexure, five failed in shear (including Specimen 8), six failed due to flexure-shear interaction, and two failed due to a significant loss of bond stress. The results were compared and three potential shear capacity design expressions were formulated to fit the test data and evaluated. Recommendations will be made after further parametric study using high-resolution finite element analysis procedures.

6.2 CONCLUSIONS

The following conclusions were made based upon the experimental results:

- The current design provisions for the shear capacity of CFTs and RCFTs are extremely conservative. For all the shear failures, the mean $V_{exp}/V_{n\,(WSDOT)} = 3.28$.
- Short shear span to depth ratios are required to produce a shear-critical configuration for CFTs and RCFTs. The addition of internal reinforcement changes the *a/D* ratio when the transition from flexure to flexure-shear to shear occurs. Table 6.1 summarizes the critical shear span to depth ratios for flexure and shear failures. Flexure-shear interaction occurs between the values listed in the table. These ratios are based on the trend data used in Equations 5.1 and described in Section 5.6.

Table 6.1: Critical shear span to depth ratios for CFTs and RCFTs

Failure Mode		**Shear**	**Flexure**
CFT	*a/D*	0.371	0.445
	a'/D	0.571	0.645
RCFT	*a/D*	0.371	0.60
	a'/D	0.571	0.80

- CFTs and RCFTs possess high strength, high stiffness, and large ductility capacities.
- There appeared to be some interaction between the shear span to depth ratio, *a/D*, and the tail length, L_T, to cause a bond failure for Specimen 11 but not for Specimen 15.
- The binding action available in CFTs subjected to flexure that increases bond is not available for shear at the ends of CFTs. The composite action is diminished necessitating a reduction in the shear capacity near the ends or detailing to restrain excessive concrete displacement.
- Internal reinforcement increases both the flexural and the shear strengths of CFTs. It can also affect the failure mode. Its effect increases as the ratio of reinforcing steel area to tube steel area, A_{sr}/A_s, increases.
- The importance of shear stress transfer at the interface is confirmed for both flexure and shear behavior. In flexure, stiffness, strength, and deformation capacity can be affected by the interface condition.
- The addition of axial load initially increases the shear capacity of the CFT as expected. There are significant limitations with the results from Specimen 13, however, as the method used to apply the load was via post-tensioning the specimen. It is unclear from the test whether the strength increase continues very far into the displacement range.
- For flexurally controlled CFTs, increased concrete strength appears to decrease the amount of available overstrength, i.e. there is a reduction in $M_{exp}/ M_{p,PSDM}$.
- Increased concrete strength decreases ultimate deformation capacity in both flexure and shear.

- The experimental shear normalized by the shear strength of the steel tube alone, V_{exp} / V_s, for Specimen 21 (with gravel in the shear spans) and for the cyclically loaded specimens of Nakahara and Tokuda (2012) were approximately equal. See Table 6.2. This could signify that a lower bound to the portion of the shear resistance contributed by the steel alone is approximately $1.7V_s$. It would seem an appropriate limit for cyclically loaded CFTs where the concrete crushes throughout the cross-section and is unable to restrain shear buckling of the steel tube. $2V_s$ would represent that the entire cross-sectional area of the steel tube is engaged in resisting shear stresses. For cases when the CFT is loaded monotonically or the cycles are insufficient to completely crush the concrete, it appears from the analysis of Equations 5.1 that more of the steel area is engaged in resisting the shear force.

Table 6.2: Effect of cyclic loading or crushed concrete on shear resistance

Specimen	a (in)	a/D	t (in)	D/t	f_{ym} (ksi)	f'_{cm} (ksi)	P/P_0	V_{exp} (kip)	V_s (kip)	V_{exp}/V_s
21	7.5	0.375	0.25	80	58.6	0	0	449	264	1.70
N1	3.27	0.5	0.193	34	77.5	9.34	0	154	89	1.73
N2	3.27	0.5	0.193	34	77.5	9.34	0.3	158	89	1.77
N3	3.25	0.5	0.197	33	78.6	7.03	0.1	152	92	1.65
N4	3.25	0.5	0.197	33	78.6	7.03	0.2	155	92	1.69
N5	3.25	0.5	0.197	33	78.6	7.03	0.4	144	92	1.57

- There was insufficient data in the experimental program to ascertain any trending with the D/t ratio.

6.3 FUTURE WORK

Recommendations for future work are divided into three categories: 1) analysis of the experimental data, 2) additional experimental testing, and 3) analytical modelling using finite element models.

6.3.1 *Experimental Data*

- A more detailed analysis of the strain gauge data should be undertaken to confirm the failure mode classification process. This includes using the Optotrak data.
- The Optotrak data should be used to formulate displacement and strain fields for each type of specimen to better understand the nature of shear deformations in CFT members.

6.3.2 *Experimental Testing*

- To better understand the effect of tube distortion on bond and shear strength when the tail length is short, additional tests with *D/t* variations should be run. Tests with short tails should also be run with spiral-welded tubes.
- More shear tests should be run using spiral-welded tubes. The weld changes the stress transfer at the concrete-steel interface significantly, thus altering the degree of composite action achieved.

6.3.3 *Analytical Modelling*

- Thorough parameter studies should be carried out using a high-resolution finite element model. Parameters should include:
    - *D/t* – The ratio was limited during experimentation due to apparatus configuration and tube availability. The study should include higher and lower ratios in shear-critical configurations to determine the effect local stability has on the shear behavior of CFTs.
    - f_y / f'_c – The relative strength and stiffness of the materials in a composite cross-section can affect how stresses are distributed. A series of simulations with

various steel and concrete strengths will help determine any effect on the strength, stiffness, or failure of the CFTs.

  - Internal longitudinal reinforcement – The research showed that internal reinforcement increases the shear strength and can change the failure mode of RCFTs. A comprehensive study will refine the understanding of its contribution.
  - P/P_0 – The research showed that the axial load ratio has an effect on the shear strength of CFTs but was not able to quantify it. A series of simulations should be run to quantify its effect.
  - *a/D* – The shear strength of CFTs and RCFTs appears dependent on the shear span to depth ratio as the bending moment and shear force interact. Simulations should be run with a/D ranging from less than 0.25 to 0.75 to capture this dependence. It will also aid in the development of a method to predict the failure mode as the shear span to depth ratio appears to be the largest factor in determining how the CFT will fail.

- CFTs that are used as deep foundation elements can aid in stiffening the soil in which they are placed. As they do so, they can develop large internal stresses and can undergo large deformations as a result of this soil-structure interaction. With the development of the high-resolution FE models and increased understanding of the shear behavior of CFTs, more refined modelling can be performed to better understand this effect.

REFERENCES

American Concrete Institute (ACI). (2011). *Building Code Requirements for Structural Concrete and Commentary.* ACI, Farmington Hills, MI.

American Institute of Steel Construction (AISC). (2010). *Specification for Structural Steel Buildings.* AISC, Chicago, Il.

Bishop, E. (2009). Evaluation of the Flexural Resistance and Stiffness Models for Circular Concrete-Filled Steel Tube Members Subjected to Axial-Flexural Loading. *MSCE Thesis, University of Washington*. Seattle, WA.

Brown, N., Kowalsky, M., & Nau, J. (2015). Impact of D/t on seismic behavior of reinforced concrete filled steel tubes. *J. Constr. Steel Res., 107*, 111-123.

Lehman, D., & Roeder, C. (2012). Initial Investigation of Reinforced Concrete Filled Tubes for use in Bridge Foundations. *WSDOT Research Report WA-RD 776.1*. Olympia, WA.

McGann, C. (2013). Numerical Evaluation of Forces on Piled Bridge Foundations in Laterally Spreading Soil. *PhD Dissertation, University of Washington*. Seattle, WA.

Moon, J., Lehman, D., Roeder, C., & Lee, H. (2012). Strength of Circular Concrete-Filled Tubes with and without Internal Reinforcement under Combined Loading. *J. Struct. Eng., 139(12)*, 1-12.

Nakahara, H., & Tokuda, S. (2012). Shearing Behavior of Circular CFT Short Columns. *Proc. of the 10th Intl. Conf. on Advances in Steel Concrete Composite and Hybrid Structures*, (pp. 362-369). Singapore.

Qian, J., Cui, Y., & Fang, X. (2007). Shear strength tests of concrete filled steel tube columns. *China Civil Engineering Journal, 40(5)*, 1-9.

Roeder, C., Cameron, B., & Brown, C. (1999). Composite Action in Concrete Filled Tubes. *J. Struct. Eng., 125(5)*, 477-484.

Roeder, C., Lehman, D., & Bishop, E. (2010). Strength and Stiffness of Circular Concrete-Filled Tubes. *J. Struct. Eng., 136(12)*, 1545-1533.

Roeder, C., Lehman, D., & Thody, R. (2009). Composite action in CFT components and connections. *Engineering Journal, 47(4)*, 229-242.

Thody, R. (2006). Experimental Investigation of the Flexural Properties of High-Strength Concrete-Filled Steel Tubes. *MSCE Thesis, University of Washington*. Seattle, WA.

Washingtion State Department of Transportation. (2012). Design Memorandum: Structural Design Recommendations of CFT and RCFT for Bridge Foundation. Olypmia, WA.

Xiao, C., Cai, S., Chen, T., & Xu, C. (2012). Experimental study on shear capacity of circular concrete filled steel tubes. *Steel Compos. Struct., 13(5)*, 437-449.

Xu, C., Haixiao, L., & Chengkui, H. (2009). Experimental study on shear resistance of self-stressing concrete filled circular steel tubes. *J. Constr. Steel Res., 65*, 801-807.

APPENDIX A: Legend of Symbols

a.....shear span; clear distance from load cradle to support cradle
a' .....the center-to-center distance from support cradle to load cradle and is used as the distance between the load resultant force and the support resultant force for equilibrium; varies during testing
a'_0 .....the initial center-to-center distance from support cradle to load cradle and is used as the distance between the load resultant force and the support resultant force for equilibrium
a/D.....shear span to depth ratio
A_c .....cross-sectional area of the concrete fill
A_s.....cross-sectional area of the tube steel
A_{sr}.....total cross-sectional area of the internal longitudinal reinforcement
D.....outside diameter of the steel tube
D/t .....tube diameter to wall thickness ratio
f_{tm} .....measured yield strength of reinforcing steel in tension
f_{um}.....measured ultimate strength of tube steel in tension
f_y.....nominal or specified yield strength of tube or reinforcing steel in tension
f_{ym}.....measured yield strength of tube or reinforcing steel in tension
f'_c .....specified peak compressive strength of concrete
f'_{cm} .....measured peak compressive strength of concrete
L .....the center-to-center distance from support cradle to support cradle; varies during testing
L_0.....the initial center-to-center distance from support cradle to support cradle
L_T .....tail length; the length of the tube extending beyond the end support
M_{exp} .....experimental bending moment
$M_{p,\ PSDM}$ .....the plastic moment of the cross section as calculated by the plastic stress distribution method
M_{prop} .....bending moment of the tests specimens at the proportional limit
M_{ult} .....peak bending moment for the test specimens
M_{yield} .....bending moment of the tests specimens when the tube steel yields in flexural tension at mid-span
P .....axial load applied to the CFT cross-section
P_0.....crushing strength of the CFT cross-section
P/P_0.....axial load ratio
$P_{Baldwin}$ .....total force applied by the 2,400 kip Baldwin hydraulic testing machine
t .....wall thickness of the steel tube
V_c .....nominal shear strength of the concrete fill alone

V_{exp} .....experimental shear force
V_n .....nominal shear strength of the CFT cross-section
$V_{n\ AISC\_1}$ .....nominal shear strength of the CFT cross-section according to the AISC design provisions Method 1
$V_{n\ AISC\_2}$ .....nominal shear strength of the CFT cross-section according to the AISC design provisions Method 2
$V_{n\ AISC\_3}$ .....nominal shear strength of the CFT cross-section according to the AISC design provisions Method 3
$V_{n\ WSDOT}$ .....nominal shear strength of the CFT cross-section according to the WSDOT design provisions
$V_{pr,\ M_{p,PSDM}}$ .....the maximum probable shear force to be attained during testing; equal to the shear force required to reach 125% of $M_{p,\ PSDM}$ of the CFT cross-section
V_{prop} .....shear force of the tests specimens at the proportional limit
V_s.....nominal shear strength of the steel tube
V_{sr}.....nominal shear strength provided by transverse shear reinforcement per ACI design provisions
V_{ult} .....peak shear force for the test specimens
V_{yield}.....shear force of the tests specimens when the tube steel yields in flexural tension at mid-span
α .....multiplication factor for the shear strength of the steel tube in the proposed design expressions
β .....multiplication factor for the shear strength of the concrete fill in the proposed design expressions
Δ .....absolute displacement of the test specimens; measured at mid-span, north load cradle, and south load cradle
$\bar{\Delta}$ .....normalized displacement of the test specimens; measured at mid-span, north load cradle, and south load cradle
$\bar{\Delta}_{fail}$.....normalized displacement of the test specimens at failure
$\bar{\Delta}_{prop}$ .....normalized displacement of the test specimens at the proportional limit
$\bar{\Delta}_{ult}$ .....normalized displacement of the test specimens at peak load
$\bar{\Delta}_{yield}$.....normalized displacement of the test specimens when the tube steel yields in flexural tension at mid-span
λ .....reduction factor in the proposed design expressions to account for reduced shear capacity near the ends
ρ_{int}.....the ratio of internal longitudinal reinforcement area to concrete area
ρ_{total}.....the ratio of internal longitudinal reinforcement area plus the area of tube steel to concrete area

APPENDIX B: CFT Shear Test Rig and Instrumentation Details

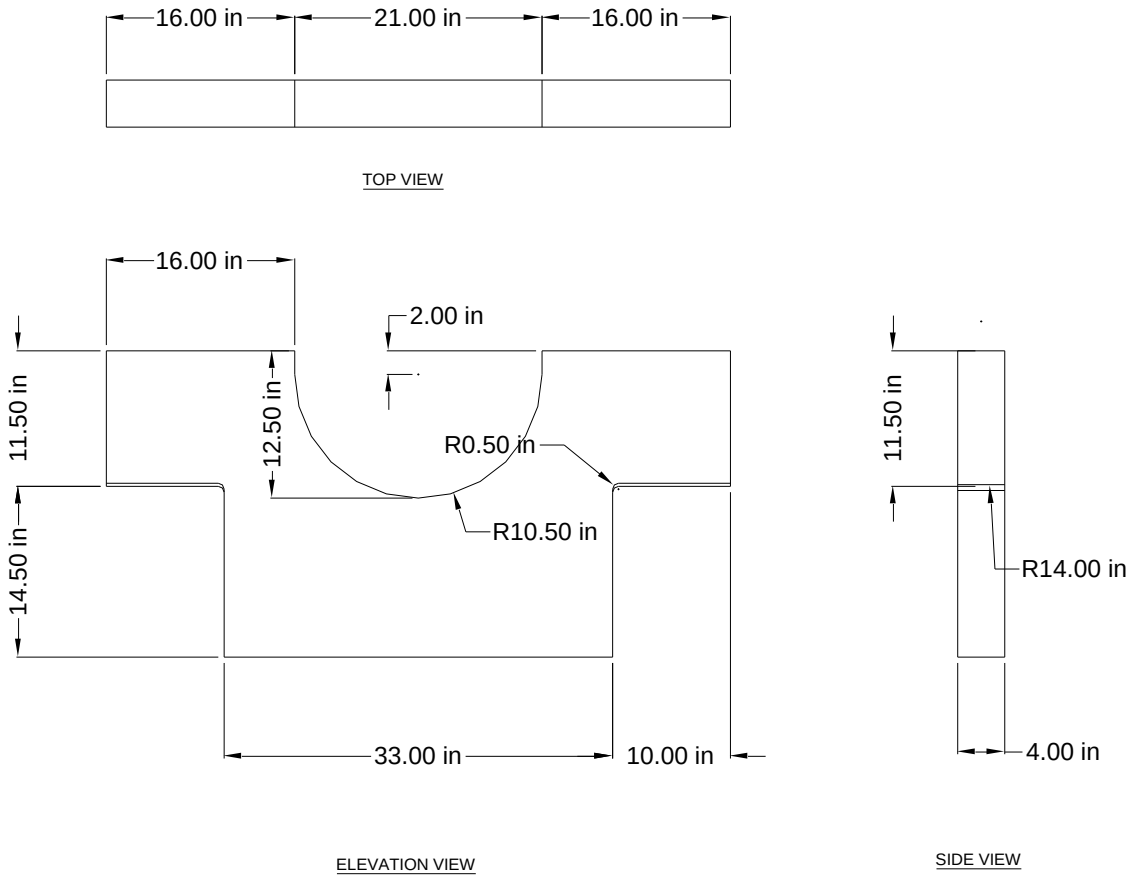

Figure B-1: Support cradle

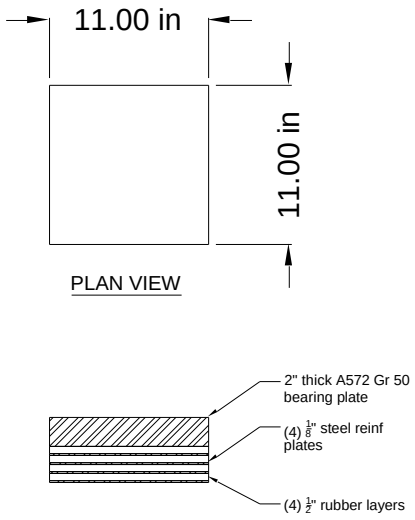

Figure B-2: Elastomeric bearing

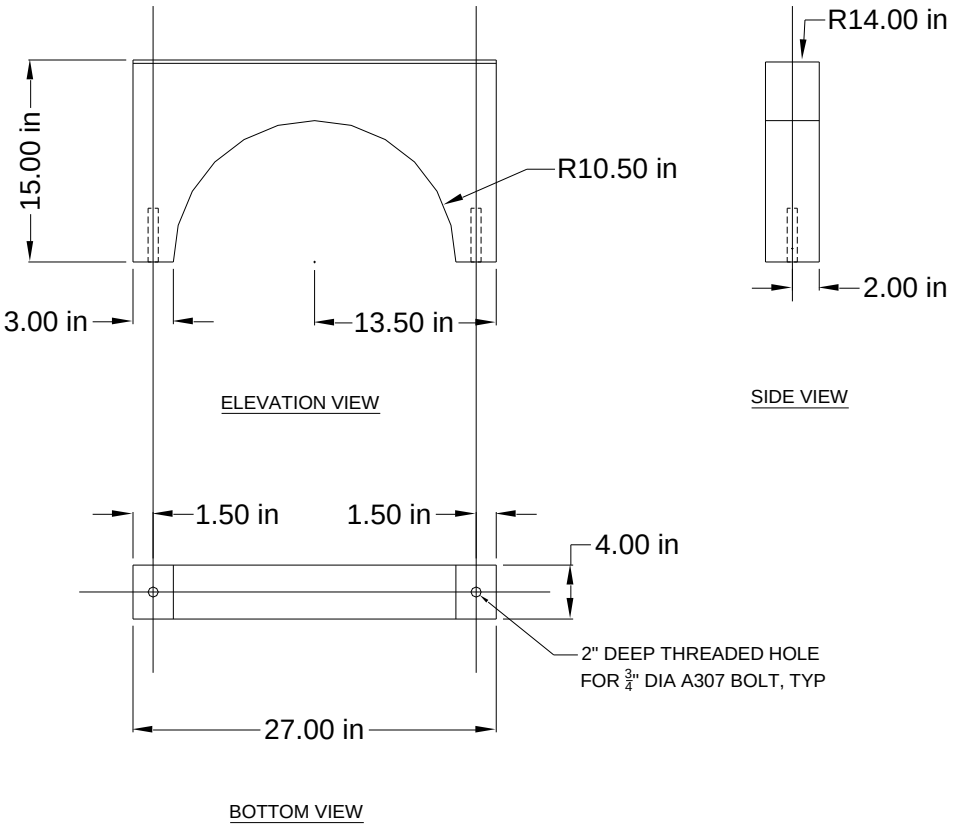

Figure B-3: Load cradle

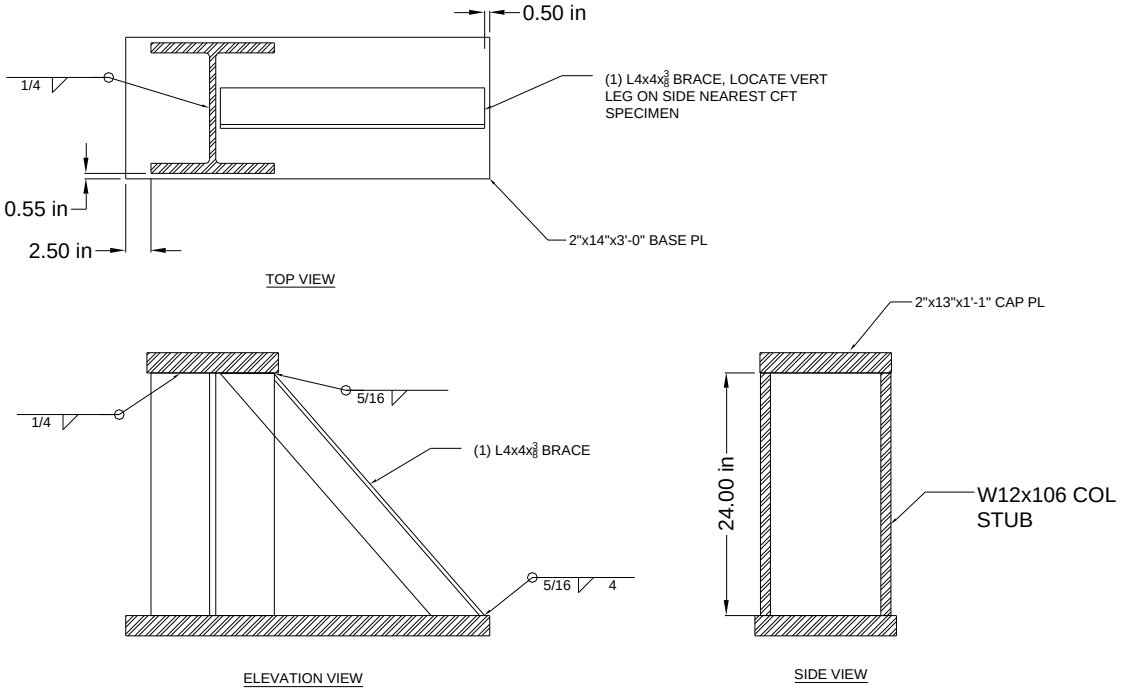

Figure B-4: Steel base

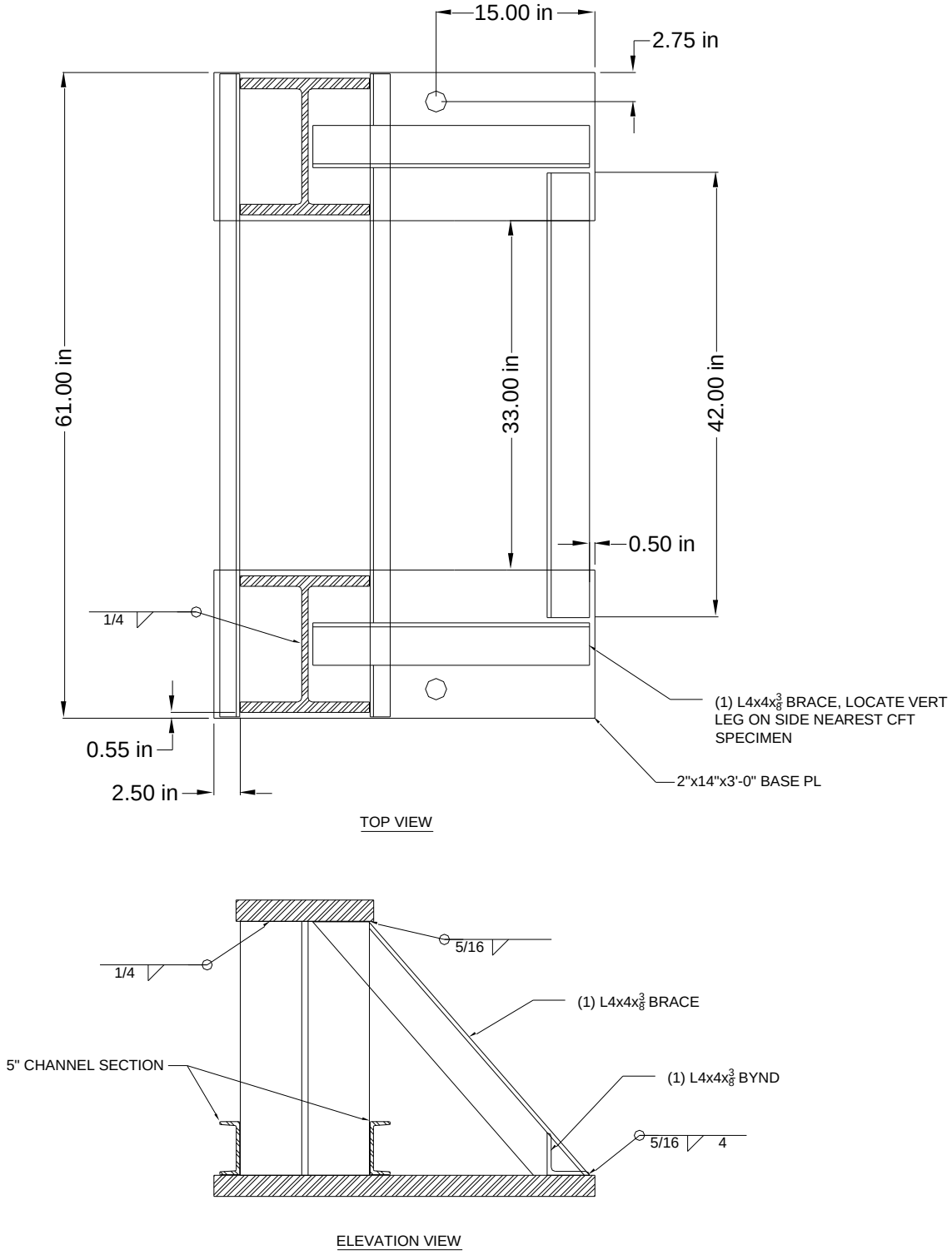

Figure B-5: Steel base assembly

Instrumentation Photos

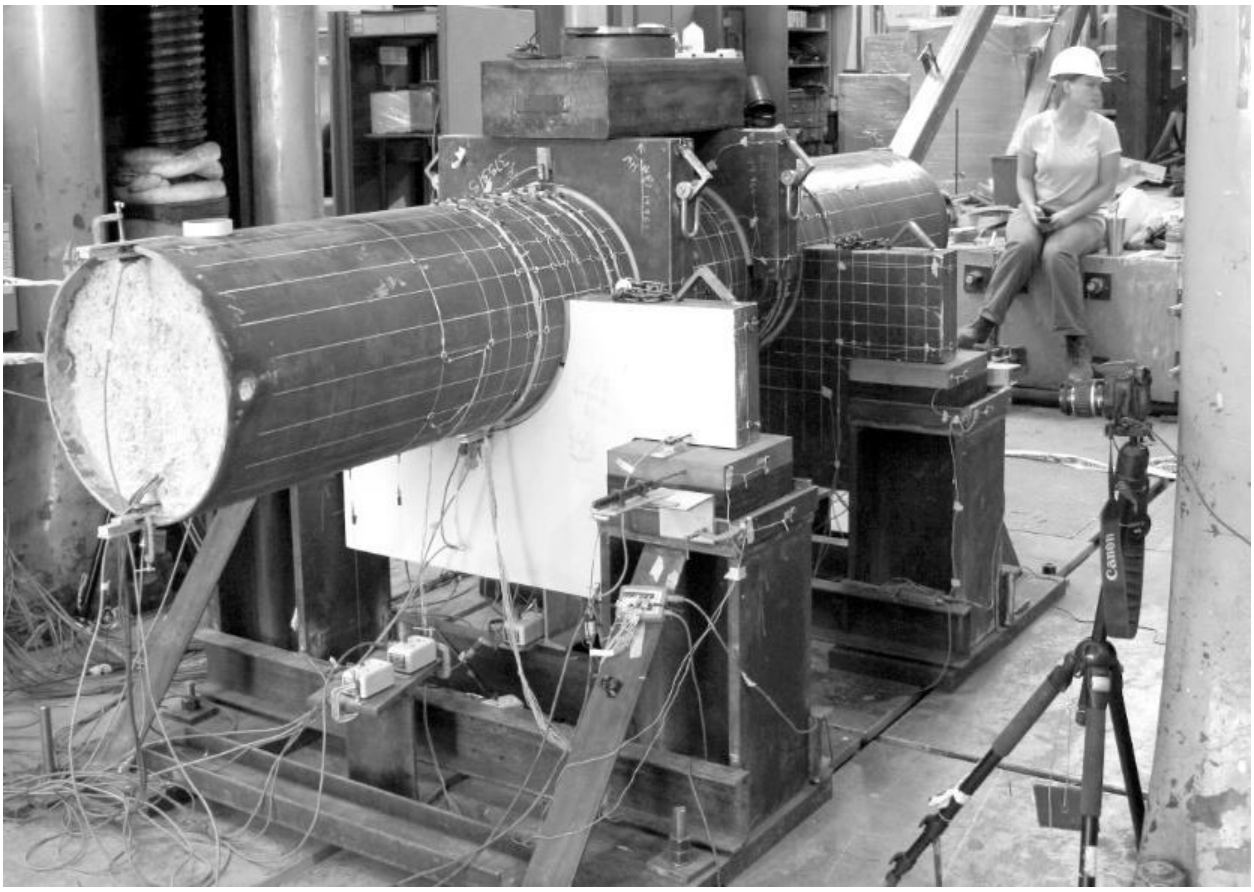

Figure B-6: General view

Figure B-7: Gridding process

Figure B-8: North Optotrak camera

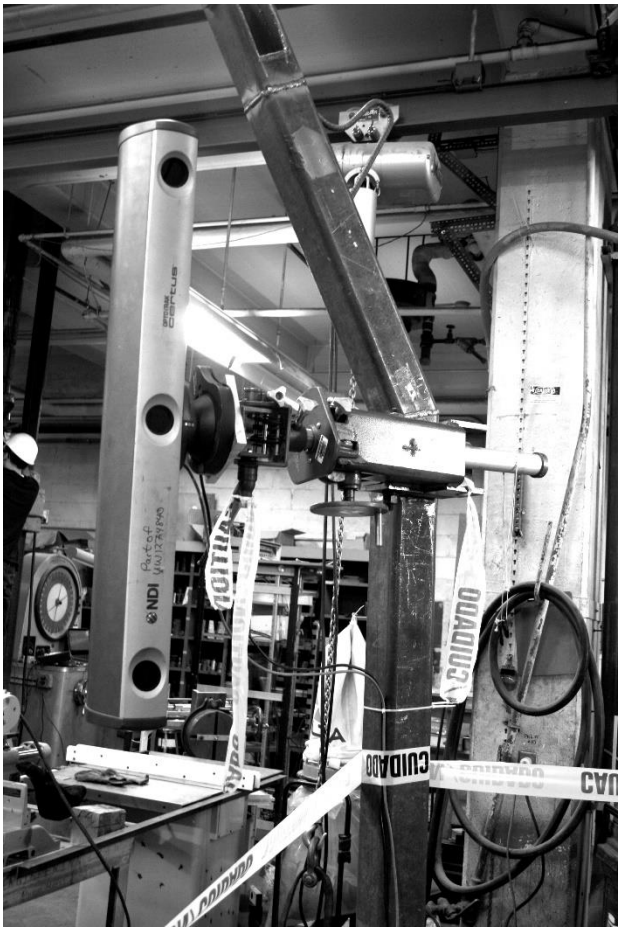

Figure B-9: South Optotrak camera

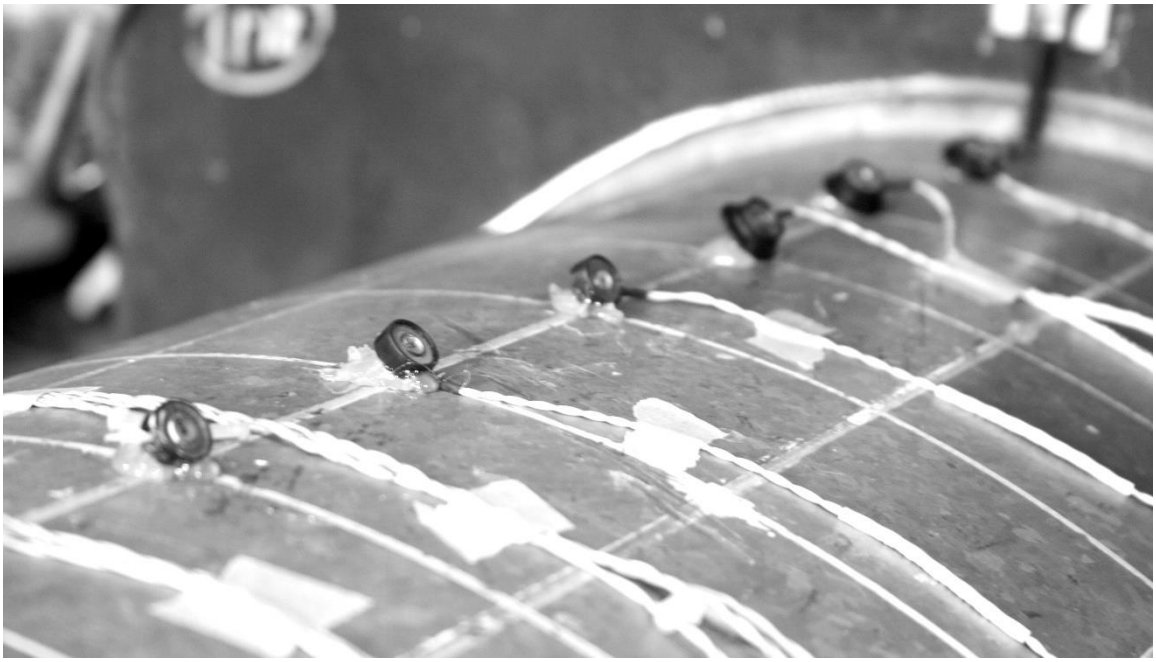

Figure B-10: Optotrak targets

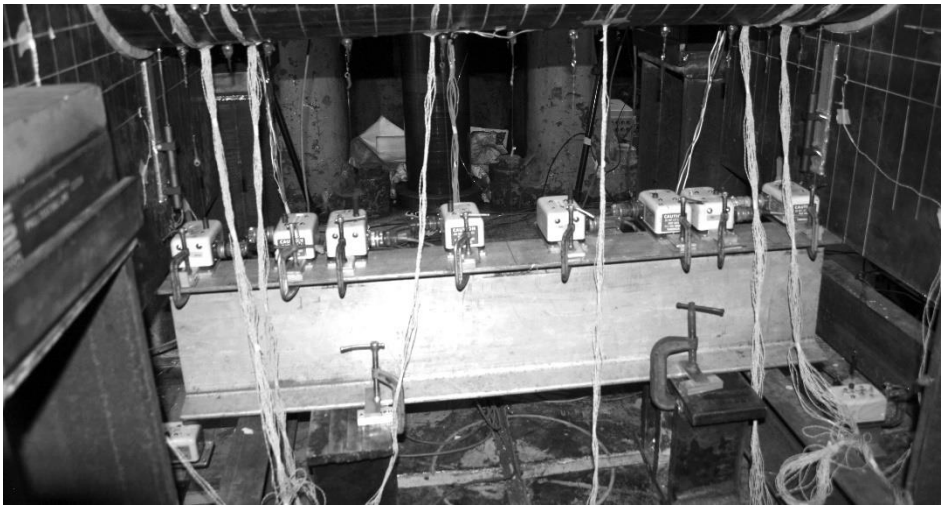

Figure B-11: String pots—west

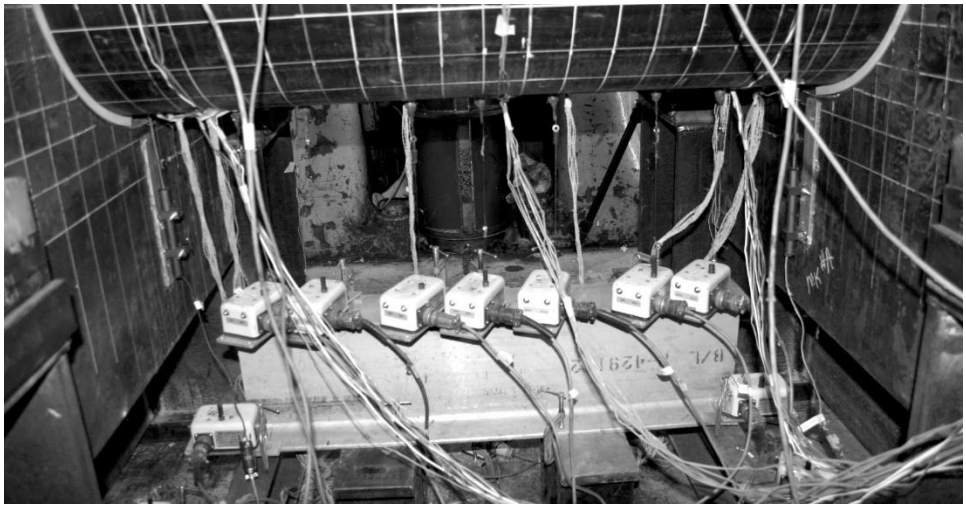

Figure B-12: String pots—east

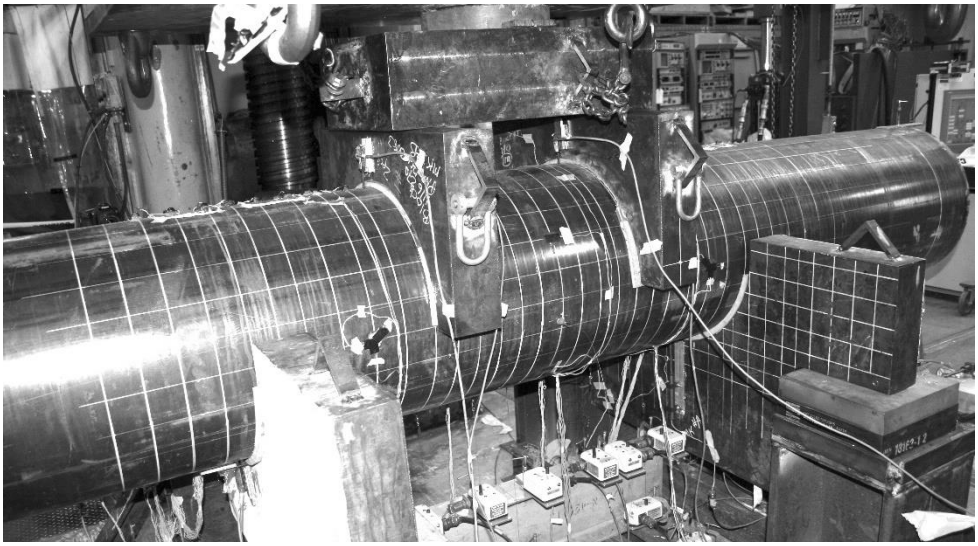

Figure B-13: General view

Figure B-14: South support

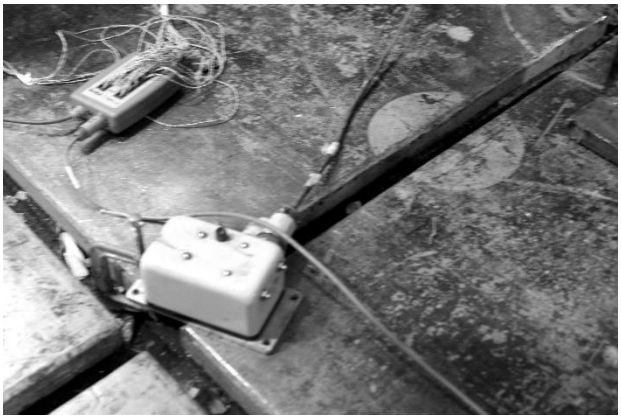

Figure B-15: String pot

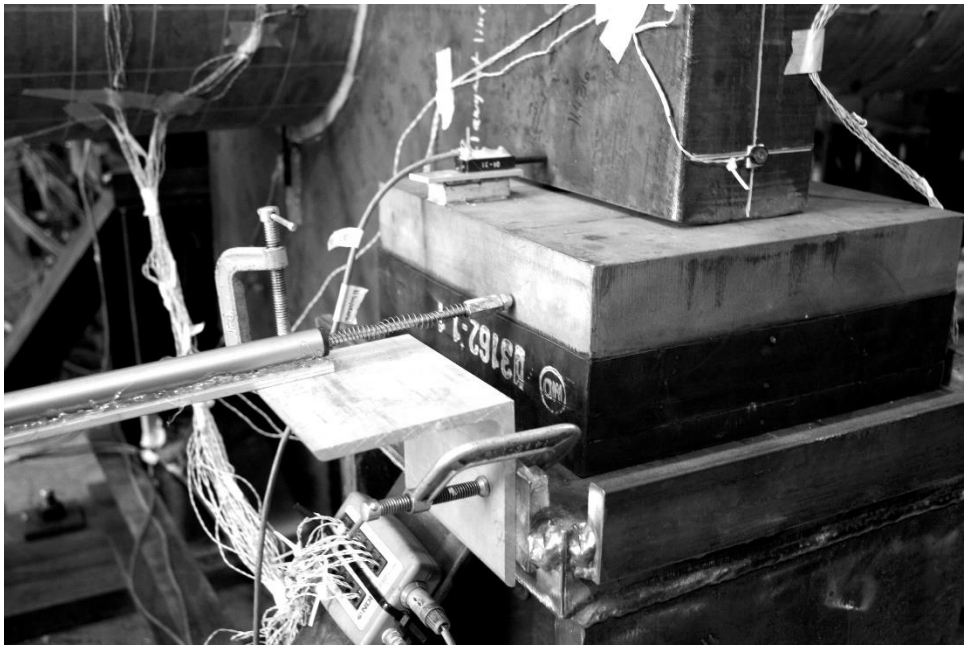

Figure B-16: Elastomeric bearing

Figure B-17: Support LDT

Figure B-18: Support Duncan pots

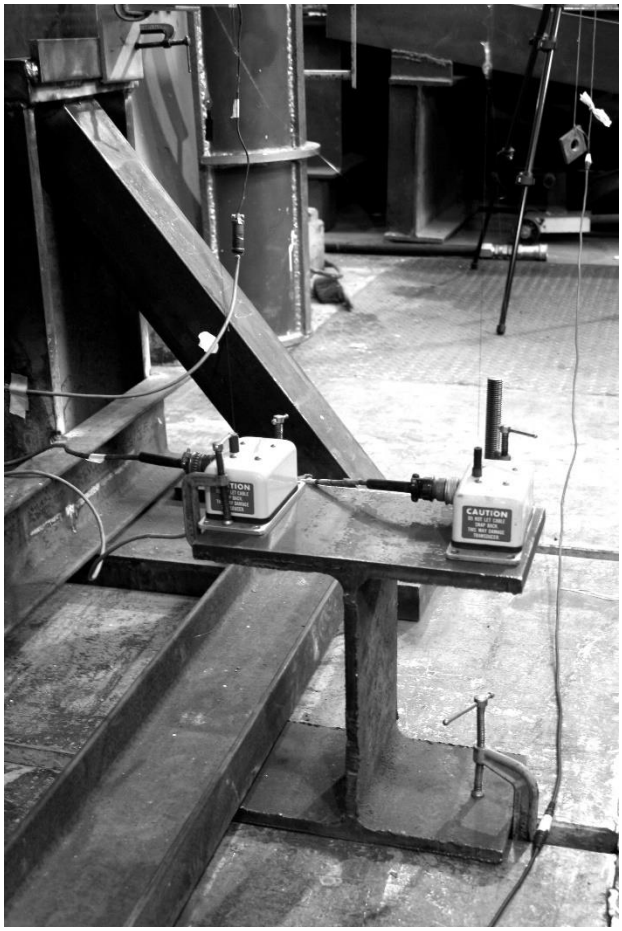

Figure B-19: South string pots

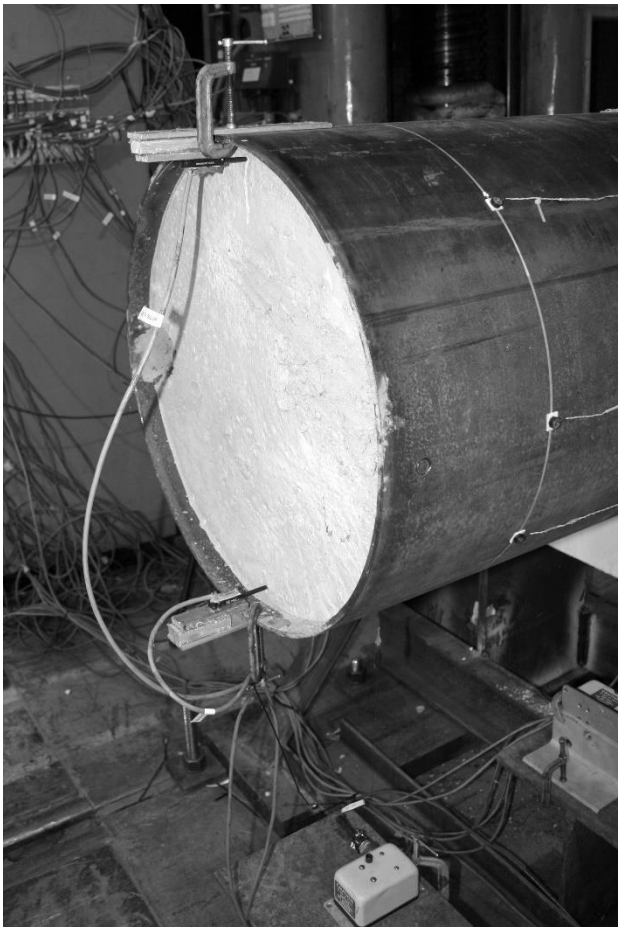

Figure B-20: Slip Duncan pots

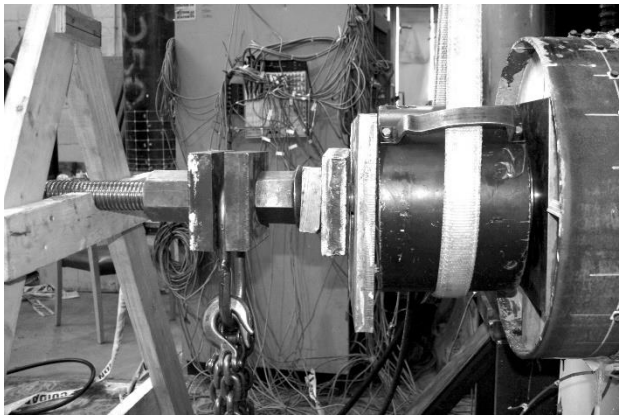

Figure B-21: North PT ram

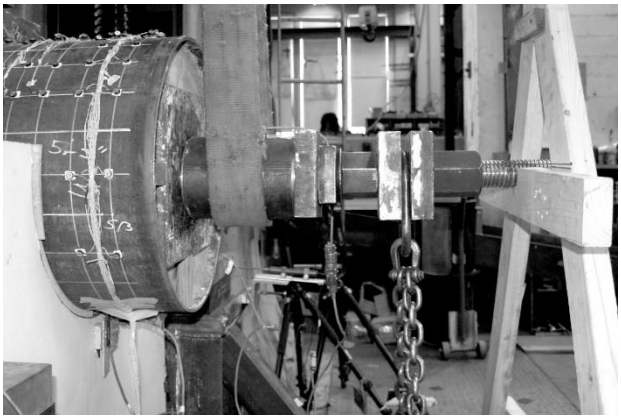

Figure B-22: South PT load cell

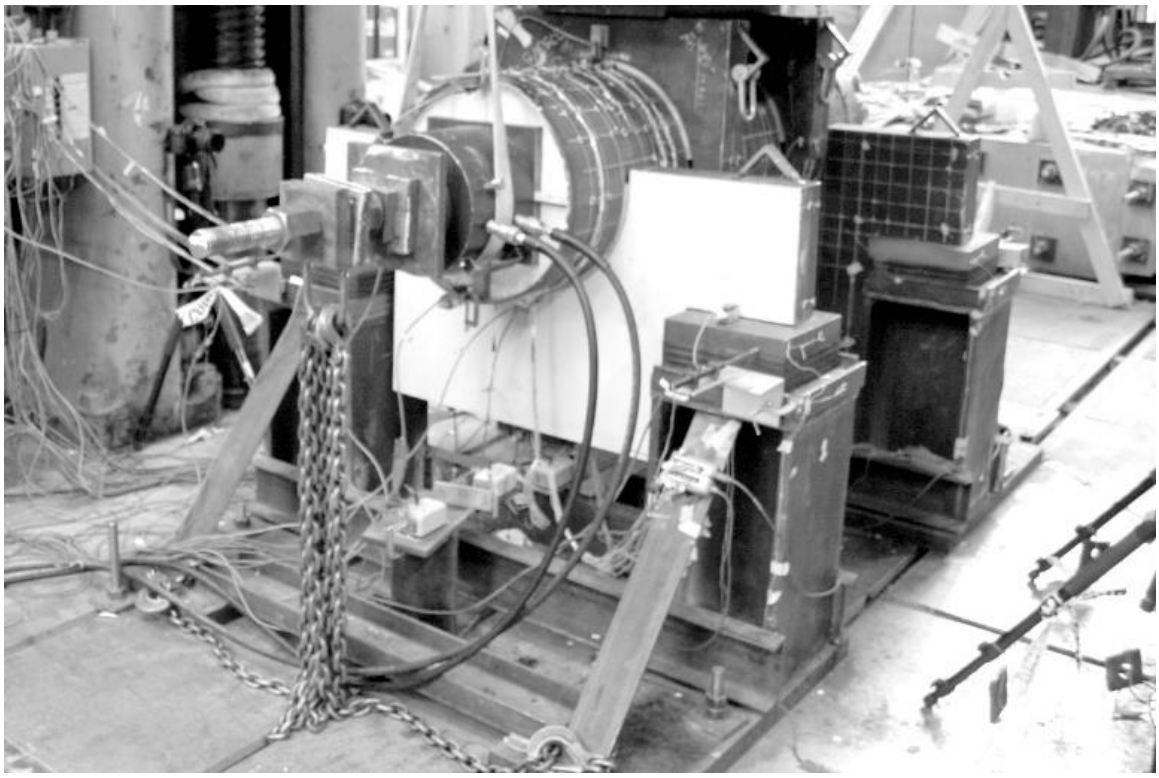

Figure B-23: Specimen 13 north end

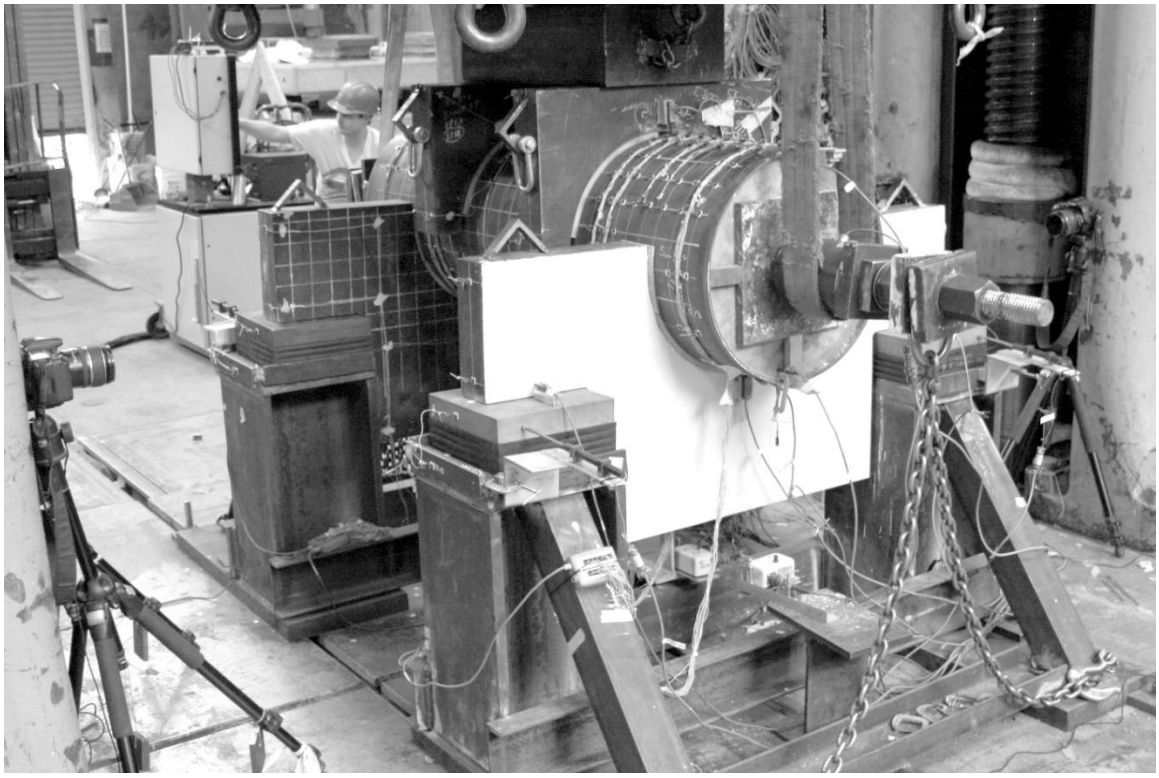

Figure B-24: Specimen 13 south end

APPENDIX C: Optotrak Displacement Correction Procedure

In order to isolate the CFT deformation from the total deformation, including that of the apparatus, the raw Optotrak displacements were corrected using the following procedure.

- Optotrak targets at mid-span and at each of the load cradles were identified for each specimen.
- Targets on the elastomeric bearings and on the steel base were identified at each end to remove the deformation of the elastomeric bearings.
- Targets on the CFT above the support cradles and on the support cradles were identified to remove the deformation of the cotton duck bearing pads.
- The displacement at each target was calculated with respect to its original position.
- The relative displacement of each elastomeric bearing and cotton duck bearing pad was calculated and subtracted from the raw displacement at mid-span and at the load cradles.

Table C.1 shows the targets used in this procedure for each specimen. The Optotrak data was not used for Specimen 15 as the system did not record during the test. It appears that one of the Optotrak cameras was bumped and slightly moved after alignment and calibration for Specimen 12 so the data is inconsistent for more rigorous strain analyses. Sunlight interfered with some of the readings during the test for Specimen 20, so alternate targets were used as needed.

Table C.1: Target legend for displacement calculation procedure

Specimen	Mid-span	North Load	South Load	North Support	North Elast.	North Cradle	North CFT	South Support	South Elast.	South Cradle	South CFT
1	69	62	78	16	15	13	12	132	131	129	128
2, 4, 6, 7, 8, 9, 11, 12, 13, 16, 21	73	67	79	23	24	25	28	115	116	118	119
3, 5, 10	73	67	79	23	24	25	28	23	116	118	119
14, 15	73	64	80	26	27	29	30	111	112	114	115
17, 18, 19	73	67	79	23	24	26	27	115	116	118	119
20	74	64	80	26	27	29	30	111	112	114	115
22	66	59	78	N/A	10	11	12	N/A	134	133	132

The Matlab code for this procedure follows.

```
Duck_Opt{1} = displacement_duck(Data_S1.Optotrak,O{1},a(1));
Elast_Opt{1} = displacement_elast(Data_S1.Optotrak,O{1},a(1));
[D_Opt_mid{1}, Span{1}] = displacement_mid(Data_S1.Optotrak,O{1};...
                          a(1),Duck_Opt{1},Elast_Opt{1});
D_Opt_N{1} = displacement_nor(Data_S1.Optotrak,O{1},a(1),...
                          Duck_Opt{1},Elast_Opt{1});
D_Opt_S{1} = displacement_sou(Data_S1.Optotrak,O{1},a(1),...
                          Duck_Opt{1},Elast_Opt{1});
```

Matlab functions:

```
function [ D ] = displacement_duck( Optotrak, Pts, ~)
% Optotrak target order is
% [    1       2       3         4        5        6       7       8        9      10       11  ]
% [ center North+10 South+10 N_support N_elast N_cradle N_tube S_support S_elast S_cradle S_tube]

headers = fieldnames(Optotrak);
steps = length(Optotrak.(headers{1}));
D = zeros(steps,2);

for j = 1:steps
    D(j,1) = min(25.4*0.375,(Optotrak.(headers{3*Pts(6)+1})(j)-...
Optotrak.(headers{3*Pts(6)+1})(1))-(Optotrak.(headers{3*Pts(7)+1})(j)-...
Optotrak.(headers{3*Pts(7)+1})(1)));
    D(j,2) = min(25.4*0.375,(Optotrak.(headers{3*Pts(10)+1})(j)-...
Optotrak.(headers{3*Pts(10)+1})(1))-(Optotrak.(headers{3*Pts(11)+1})(j)-...
Optotrak.(headers{3*Pts(11)+1})(1)));
end

D = 1 / 25.4 * D;
end
```

```
function [ D ] = displacement_elast( Optotrak, Pts, ~)
% Optotrak target order is
% [    1       2       3         4        5        6       7       8        9      10       11  ]
% [ center North+10 South+10 N_support N_elast N_cradle N_tube S_support S_elast S_cradle S_tube]

headers = fieldnames(Optotrak);
steps = length(Optotrak.(headers{1}));
D = zeros(steps,2);

for j = 1:steps
    D(j,1) = (Optotrak.(headers{3*Pts(4)+1})(j)-...
Optotrak.(headers{3*Pts(4)+1})(1))-(Optotrak.(headers{3*Pts(5)+1})(j)-...
Optotrak.(headers{3*Pts(5)+1})(1));
    D(j,2) = (Optotrak.(headers{3*Pts(8)+1})(j)-...
Optotrak.(headers{3*Pts(8)+1})(1))-(Optotrak.(headers{3*Pts(9)+1})(j)-...
Optotrak.(headers{3*Pts(9)+1})(1));
end

D = 1 / 25.4 * D;
end
```

```
function [ D, span ] = displacement_mid( Optotrak, Pts, a, CD, ED)
% Optotrak target order is
% [    1       2       3         4        5        6       7       8        9      10       11  ]
% [ center North+10 South+10 N_support N_elast N_cradle N_tube S_support S_elast S_cradle S_tube]

headers = fieldnames(Optotrak);
steps = length(Optotrak.(headers{1}));
D = zeros(steps,3);
span = zeros(steps,3);       % column 1 is from bearing to bearing, column 2 is the
north shear span, column 3 is the south shear span
a = a*25.4;
b = (Optotrak.(headers{3*Pts(2)-1})(1) - Optotrak.(headers{3*Pts(5)-1})(1));
c = (Optotrak.(headers{3*Pts(9)-1})(1) - Optotrak.(headers{3*Pts(3)-1})(1));
d = (Optotrak.(headers{3*Pts(9)-1})(1) - Optotrak.(headers{3*Pts(5)-1})(1));

for j = 1:steps
    D(j,1) = Optotrak.(headers{3*Pts(1)-1})(j) - ...
Optotrak.(headers{3*Pts(1)-1})(1);
    D(j,2) = Optotrak.(headers{3*Pts(1)})(j) - ...
Optotrak.(headers{3*Pts(1)})(1);
    span(j,1) = (Optotrak.(headers{3*Pts(9)-1})(j) - ...
Optotrak.(headers{3*Pts(5)-1})(j)) - d + (2*a + 25.4*20);
    span(j,2) = (Optotrak.(headers{3*Pts(2)-1})(j) - ...
Optotrak.(headers{3*Pts(5)-1})(j)) - b + a;
    span(j,3) = (Optotrak.(headers{3*Pts(9)-1})(j) - ...
Optotrak.(headers{3*Pts(3)-1})(j)) - c + a;
    X = [0 span(j,1)];
    V = Optotrak.(headers{3*Pts(1)+1})(j) - ...
Optotrak.(headers{3*Pts(1)+1})(1);
    Ex = [ED(j,1) ED(j,2)]*25.4;
    E = interp1(X, Ex, span(j,1)/2-D(j,1));
    duck_x = [CD(j,1) CD(j,2)]*25.4;
    duck = interp1(X, duck_x, span(j,1)/2-D(j,1));
    D(j,3) = (V + duck + E)* -1;
end

D = 1 / 25.4 * D;
span = 1 / 25.4 * span;
end
```

```
function [ D ] = displacement_nor( Optotrak, Pts, A, CD, ED)
% Optotrak target order is
% [    1       2       3         4        5        6       7       8        9      10       11  ]
% [ center North+10 South+10 N_support N_elast N_cradle N_tube S_support S_elast S_cradle S_tube]

headers = fieldnames(Optotrak);
steps = length(Optotrak.(headers{1}));
D = zeros(steps,3);
A =  A*25.4;
b = (Optotrak.(headers{3*Pts(2)-1})(1) - Optotrak.(headers{3*Pts(5)-1})(1));
d = (Optotrak.(headers{3*Pts(9)-1})(1) - Optotrak.(headers{3*Pts(5)-1})(1));

for j = 1:steps
    D(j,1) = Optotrak.(headers{3*Pts(2)-1})(j) - ...
Optotrak.(headers{3*Pts(2)- 1})(1);
```

```
    D(j,2) = Optotrak.(headers{3*Pts(2)})(j) - ...
Optotrak.(headers{3*Pts(2)})(1);
    span = Optotrak.(headers{3*Pts(9)-1})(j) - ...
Optotrak.(headers{3*Pts(5)-1})(j) - d + (2*A + 25.4*20);
    X = [0 span];
    a = Optotrak.(headers{3*Pts(2)-1})(j) - ...
Optotrak.(headers{3*Pts(5)-1})(j) - b + A;
    V = Optotrak.(headers{3*Pts(2)+1})(j) - ...
Optotrak.(headers{3*Pts(2)+1})(1);
    Ex = [ED(j,1) ED(j,2)]*25.4;
    E = interp1(X, Ex, a);
    duck_x = [CD(j,1) CD(j,2)]*25.4;
    duck = interp1(X, duck_x, a);
    D(j,3) = (V + duck + E)*-1;
end

D = 1 / 25.4 * D;
end
```

```
function [ D ] = displacement_sou( Optotrak, Pts, A, CD, ED)
% Optotrak target order is
% [    1       2       3        4        5        6       7       8        9      10       11  ]
% [ center North+10 South+10 N_support N_elast N_cradle N_tube S_support S_elast S_cradle S_tube]

headers = fieldnames(Optotrak);
steps = length(Optotrak.(headers{1}));
D = zeros(steps,3);
A =  A*25.4;
c = (Optotrak.(headers{3*Pts(9)-1})(1) - Optotrak.(headers{3*Pts(3)-1})(1));
d = (Optotrak.(headers{3*Pts(9)-1})(1) - Optotrak.(headers{3*Pts(5)-1})(1));

for j = 1:steps
    D(j,1) = Optotrak.(headers{3*Pts(3)-1})(j) - ...
Optotrak.(headers{3*Pts(3)-1})(1);
    D(j,2) = Optotrak.(headers{3*Pts(3)})(j) - ...
Optotrak.(headers{3*Pts(3)})(1);
    span = Optotrak.(headers{3*Pts(9)-1})(j) - ...
Optotrak.(headers{3*Pts(5)-1})(j) - d + (2*A + 25.4*20);
    X = [0 span];
    a = Optotrak.(headers{3*Pts(9)-1})(j) - ...
Optotrak.(headers{3*Pts(3)-1})(j) - c + A;
    V = Optotrak.(headers{3*Pts(3)+1})(j) - ...
Optotrak.(headers{3*Pts(3)+1})(1);
    Ex = [ED(j,1) ED(j,2)]*25.4;
    E = interp1(X, Ex, a);
    duck_x = [CD(j,1) CD(j,2)]*25.4;
    duck = interp1(X, duck_x, a);
    D(j,3) = (V + duck + E)*-1;
end

D = 1 / 25.4 * D;
end
```

APPENDIX D: Steel Strain Gauge Data

Three plots of normalized-moment versus steel strain at the CFT surface are included for each specimen. The first plot shows the strain gauges at mid-span, the second shows the strain gauge rosettes on the east and west sides of the south shear span, and the third shows the rosettes on the east and west sides of the north shear span. The light gray vertical lines show the uniaxial yield strain calculated from the tension tests.

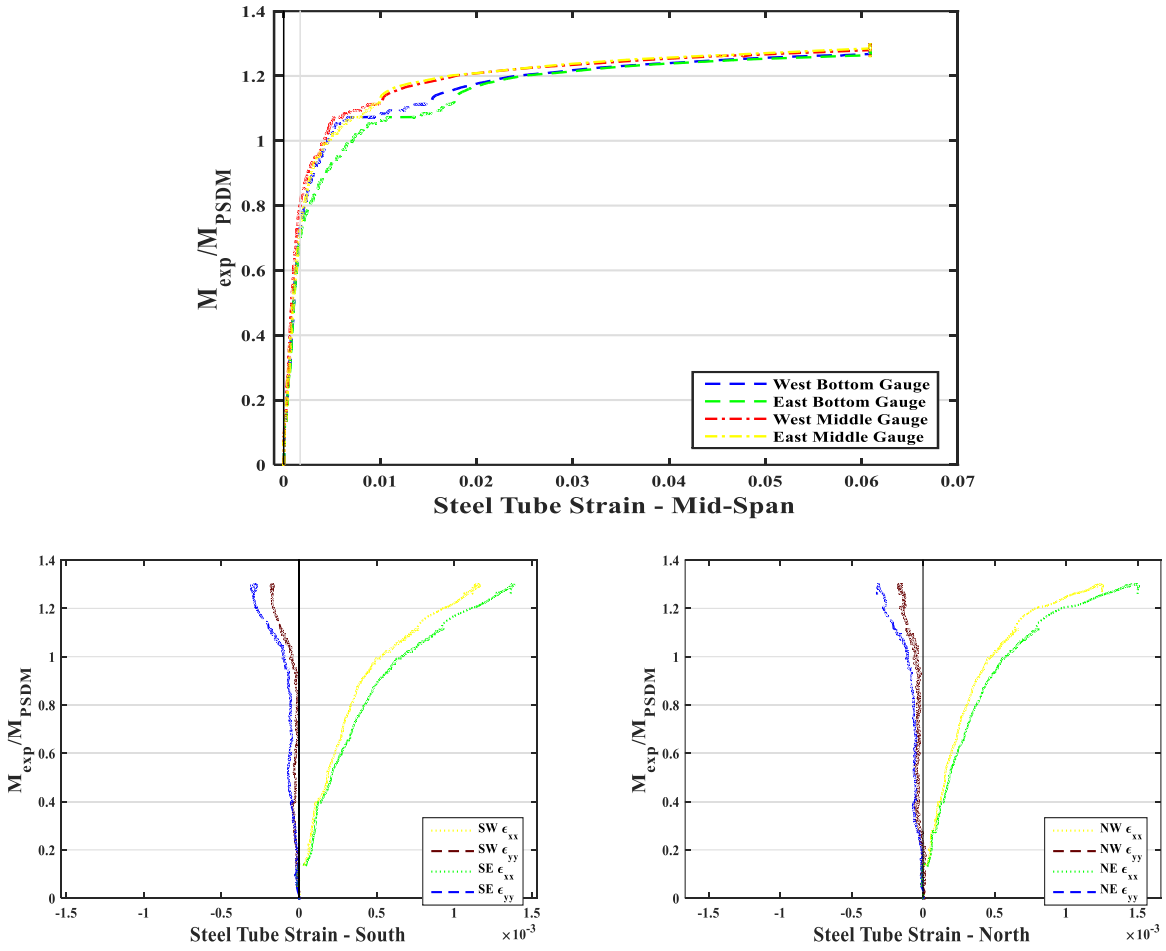

Steel strain gauge plots—Specimen 1

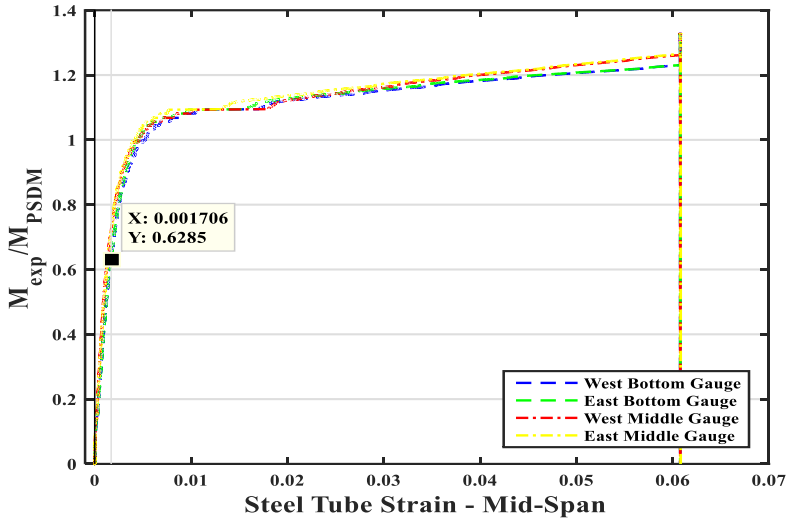

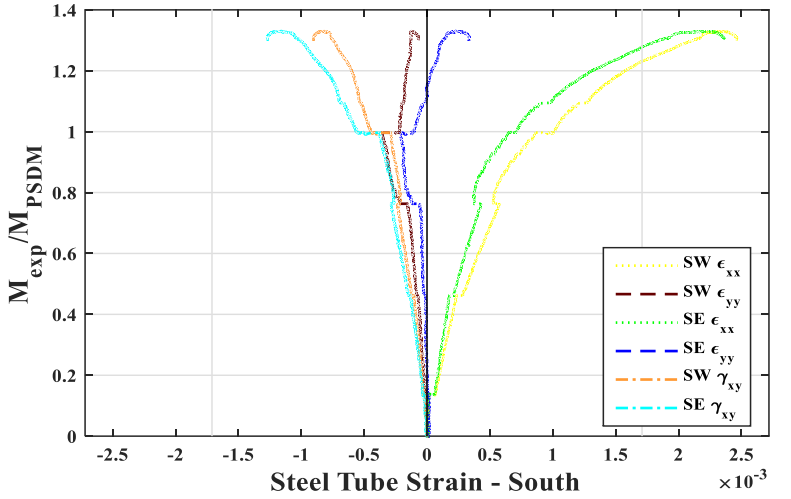

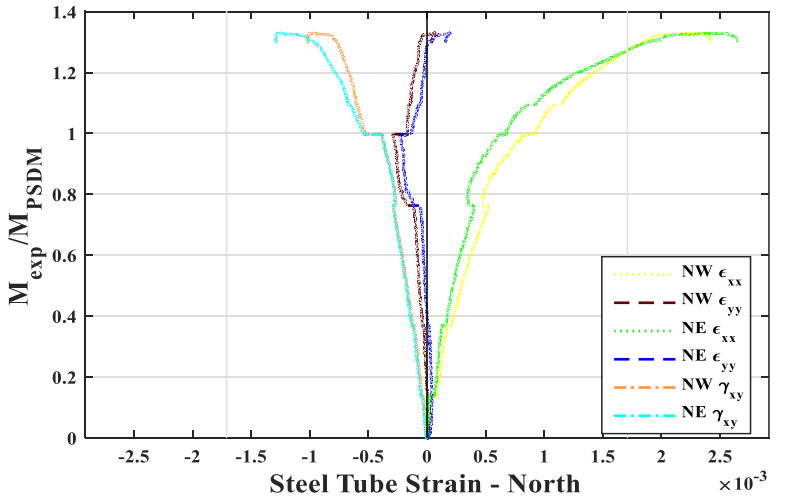

Steel strain gauge plots—Specimen 2

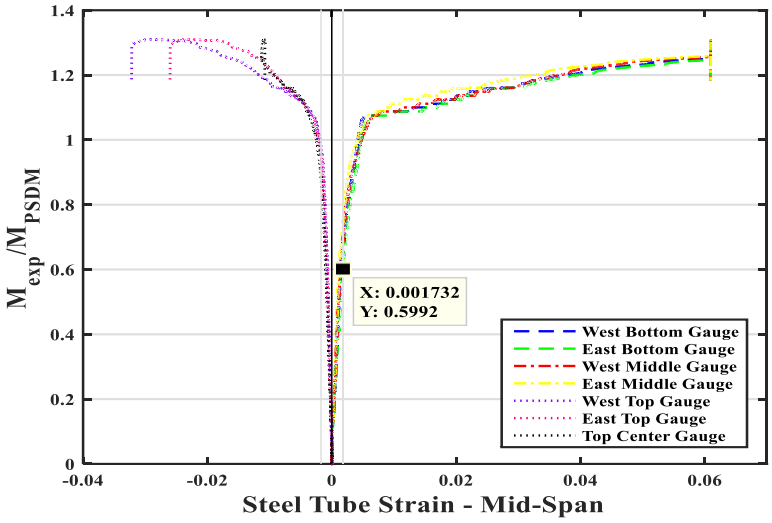

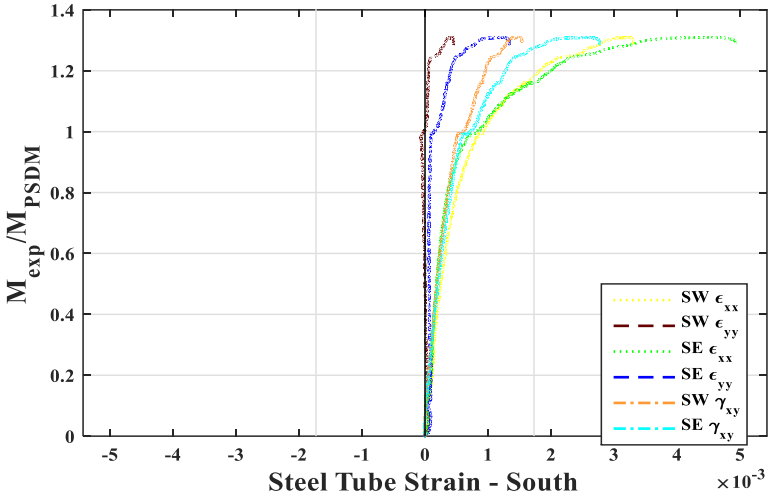

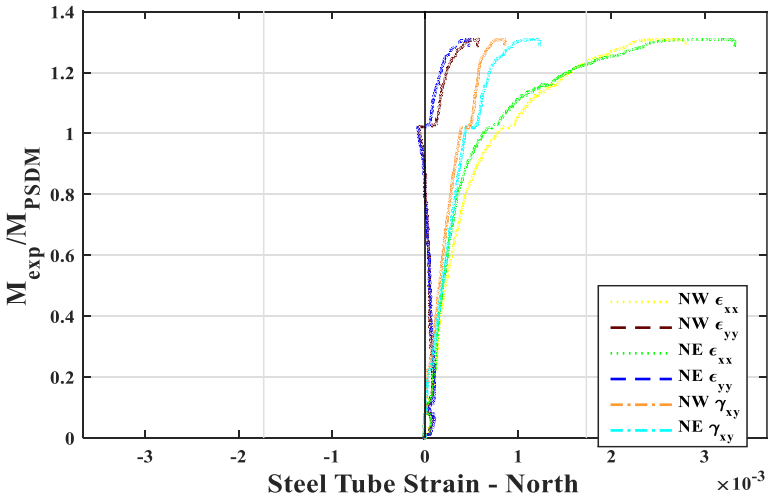

Steel strain gauge plots—Specimen 3

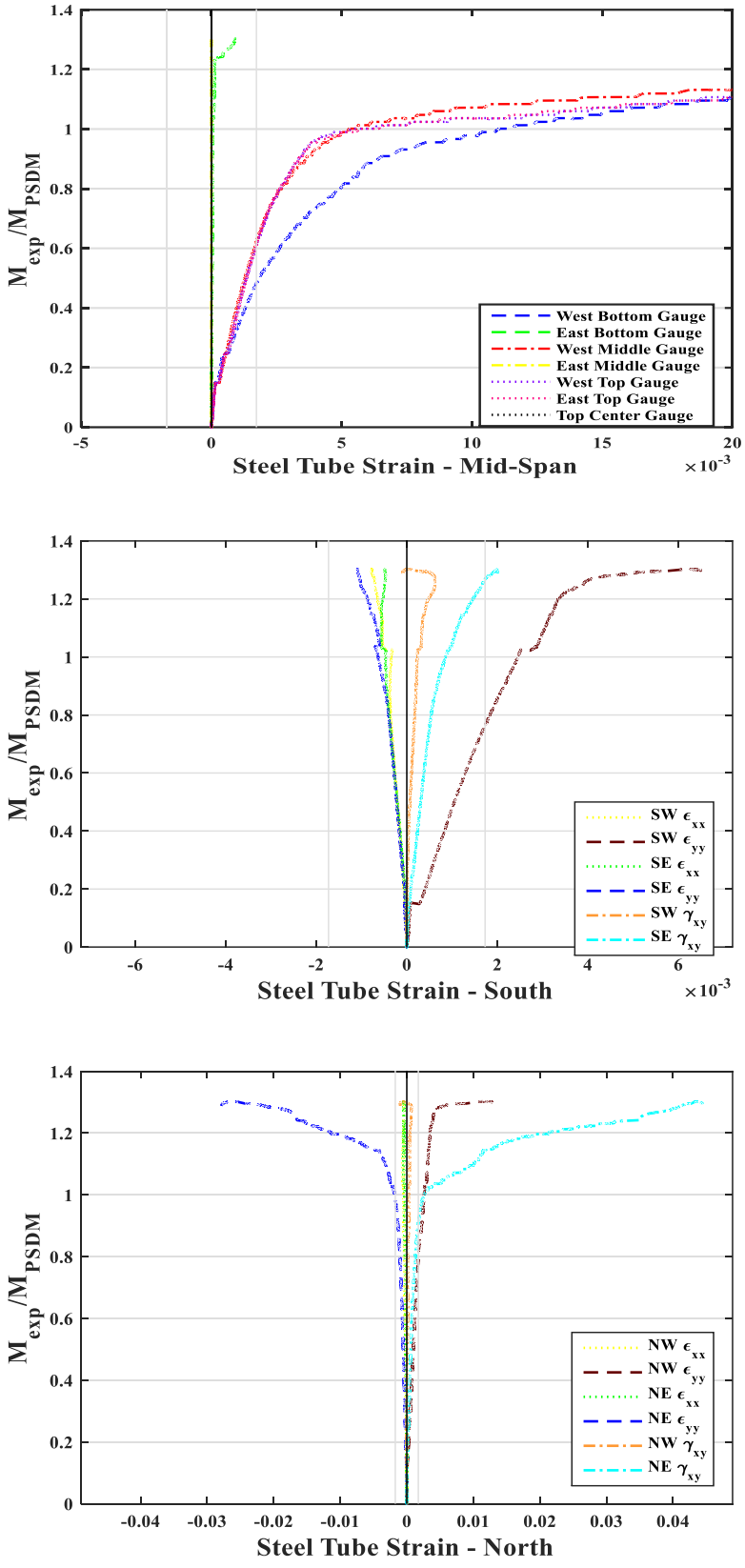

Steel strain gauge plots—Specimen 4

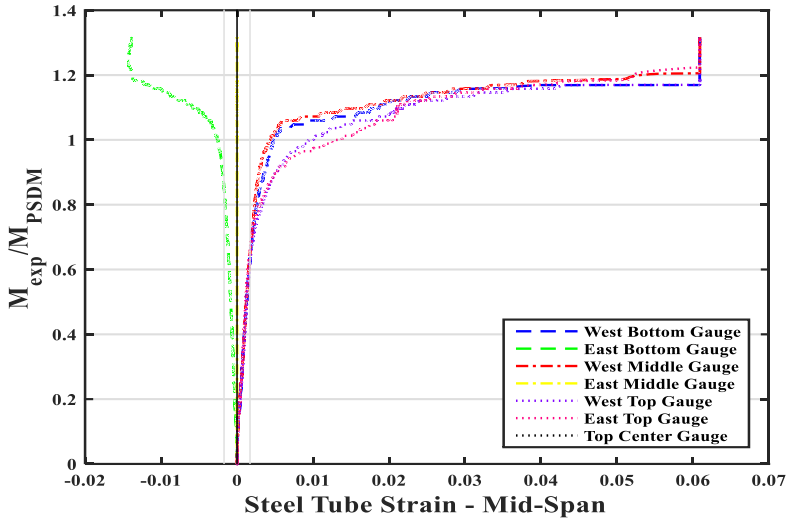

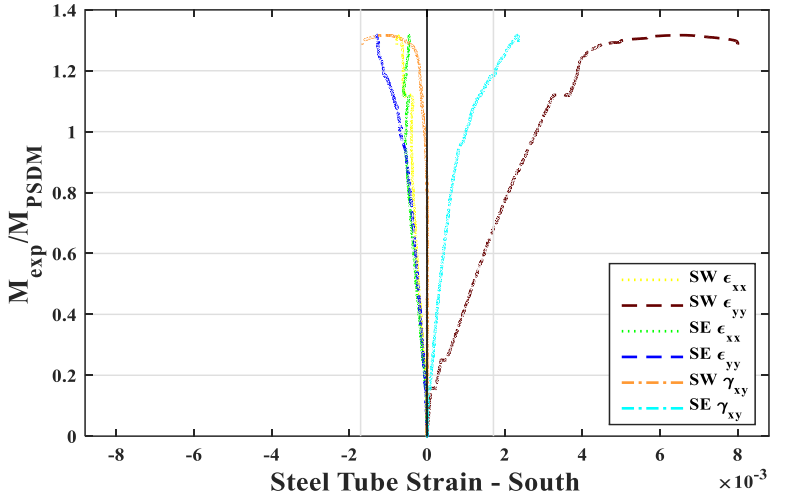

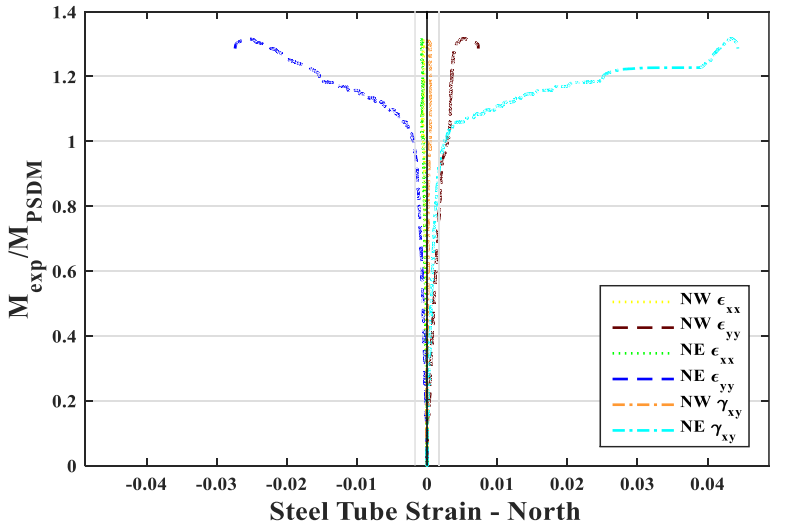

Steel strain gauge plots—Specimen 5

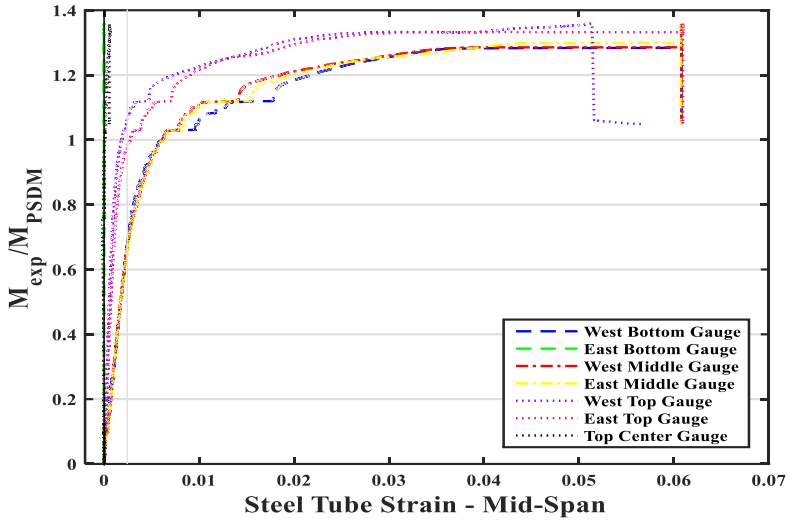

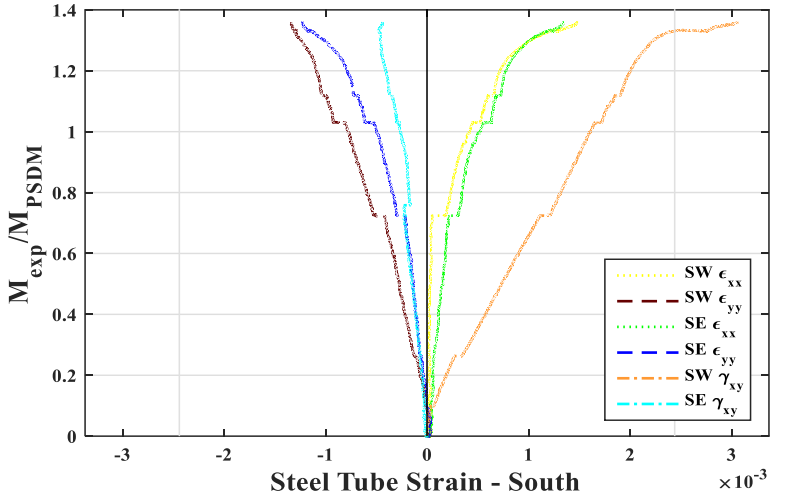

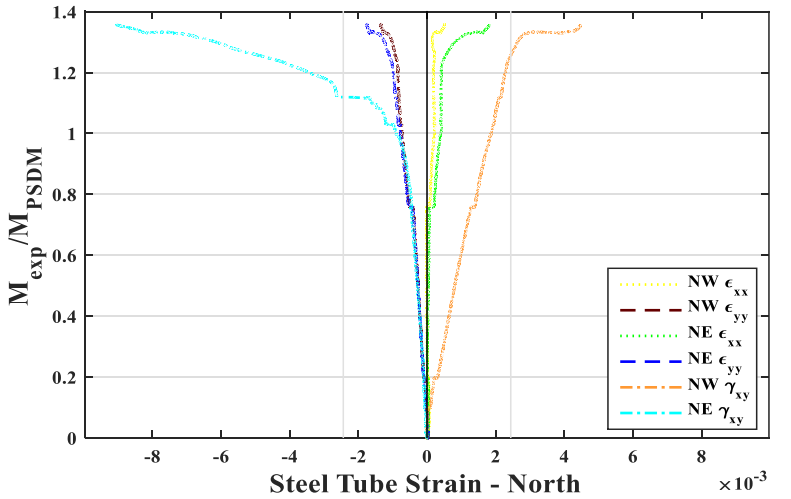

Steel strain gauge plots—Specimen 6

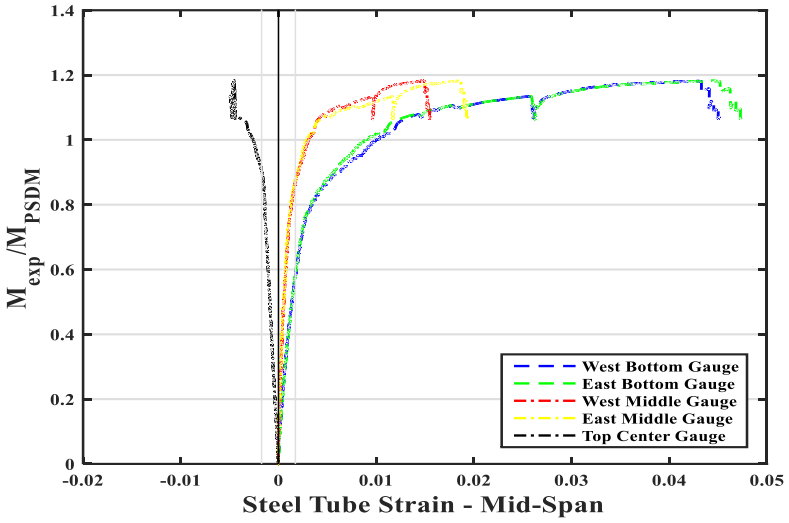

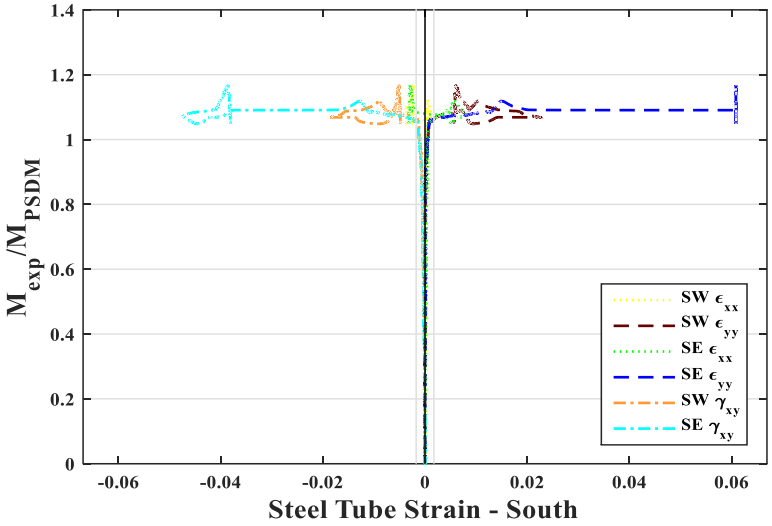

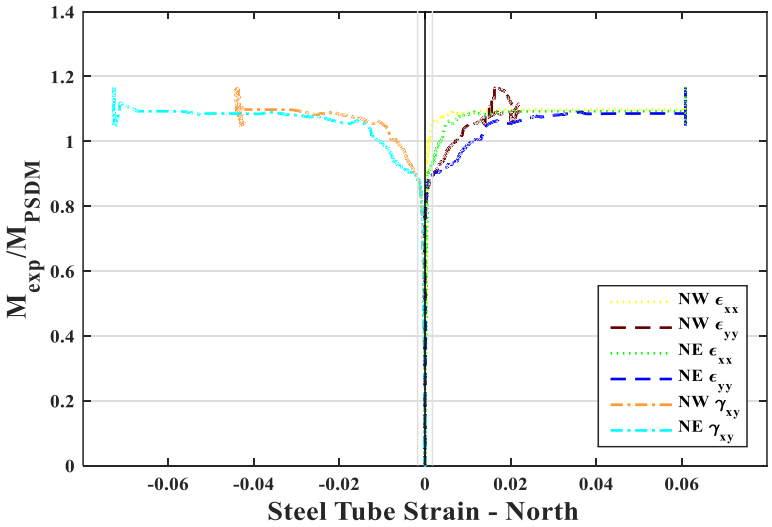

Steel strain gauge plots—Specimen 7

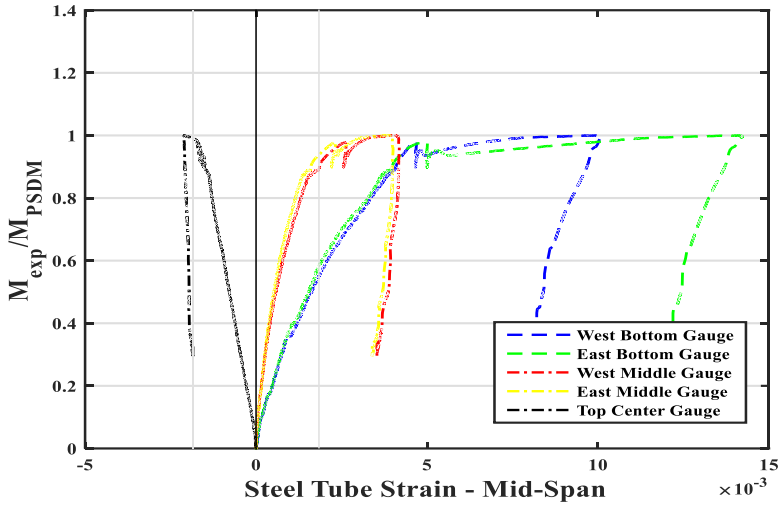

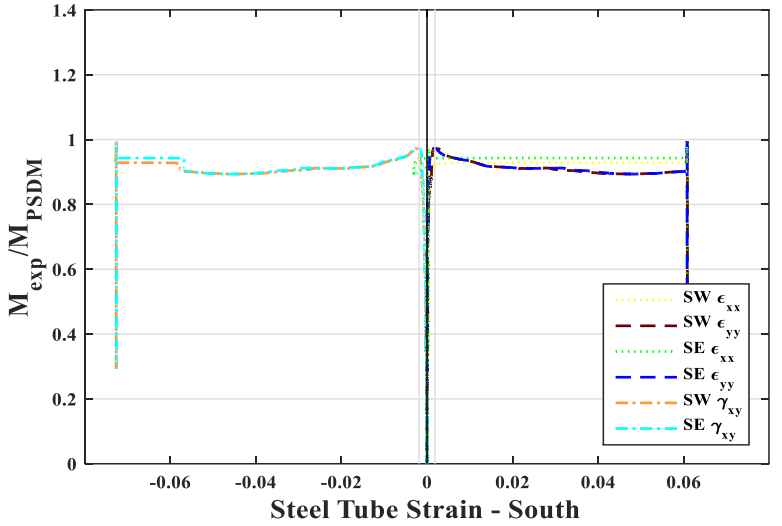

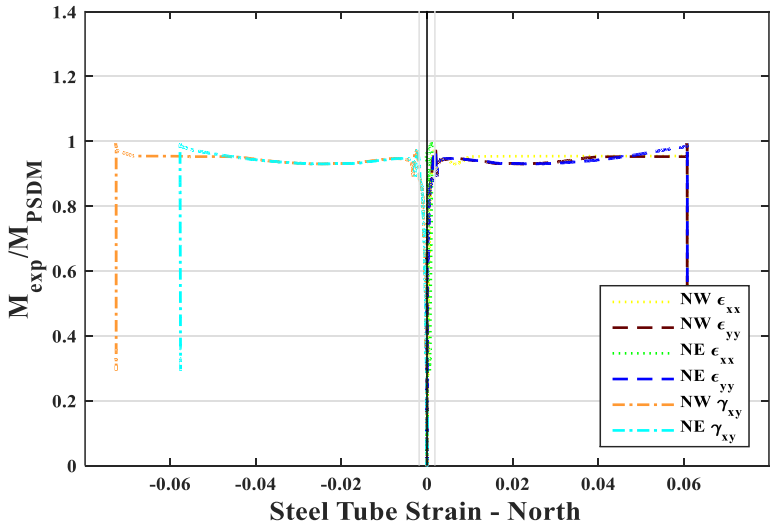

Steel strain gauge plots—Specimen 8

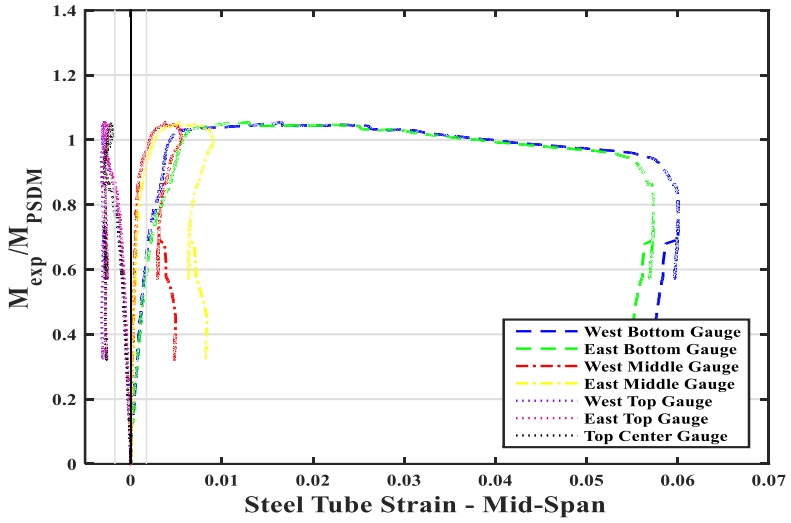

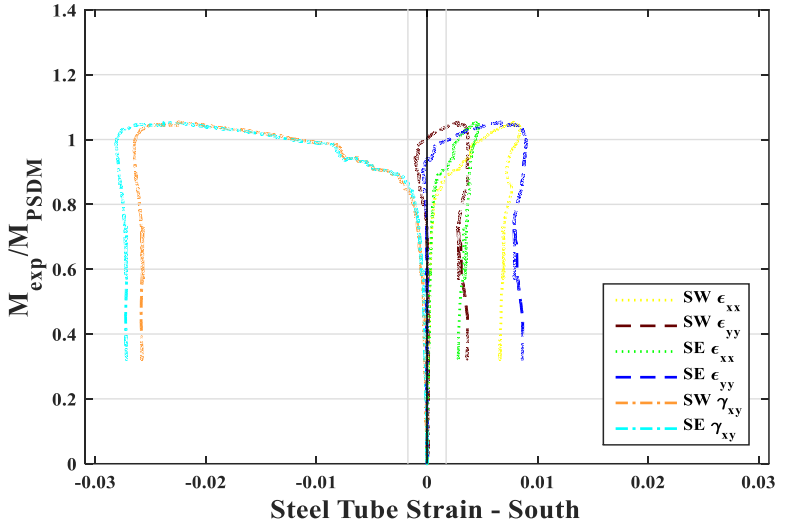

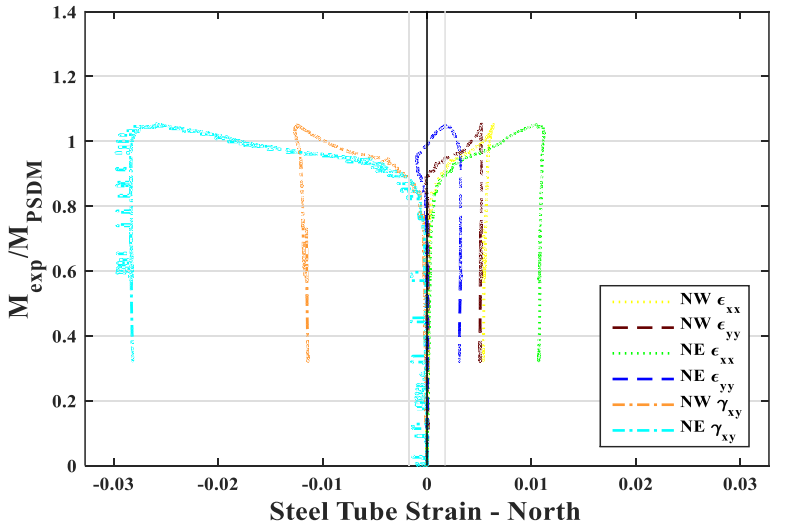

Steel strain gauge plots—Specimen 9

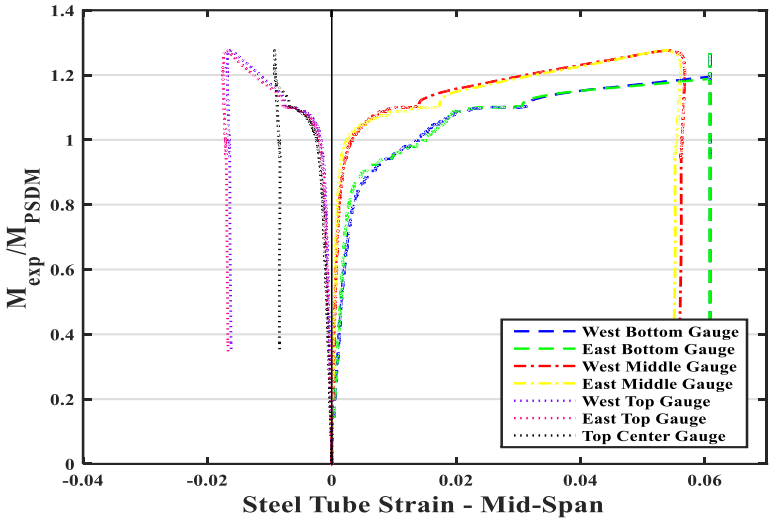

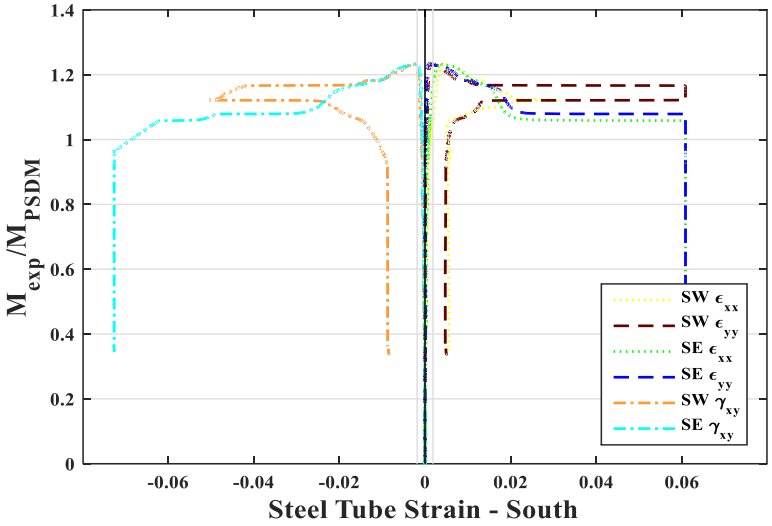

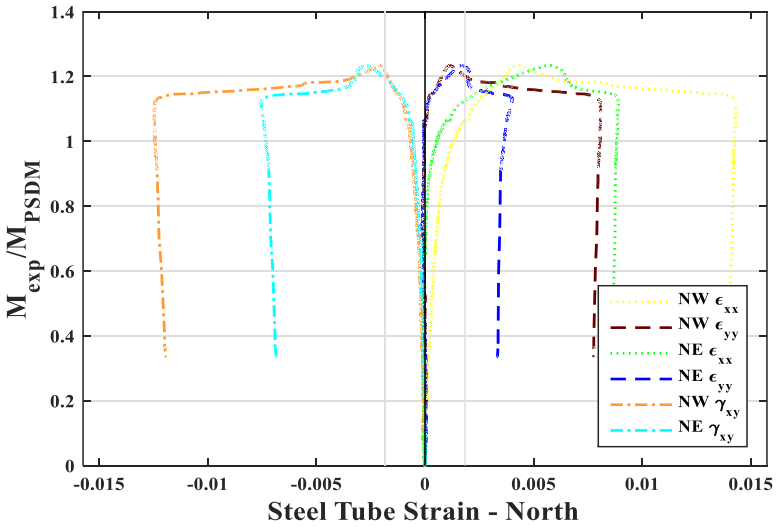

Steel strain gauge plots—Specimen 10

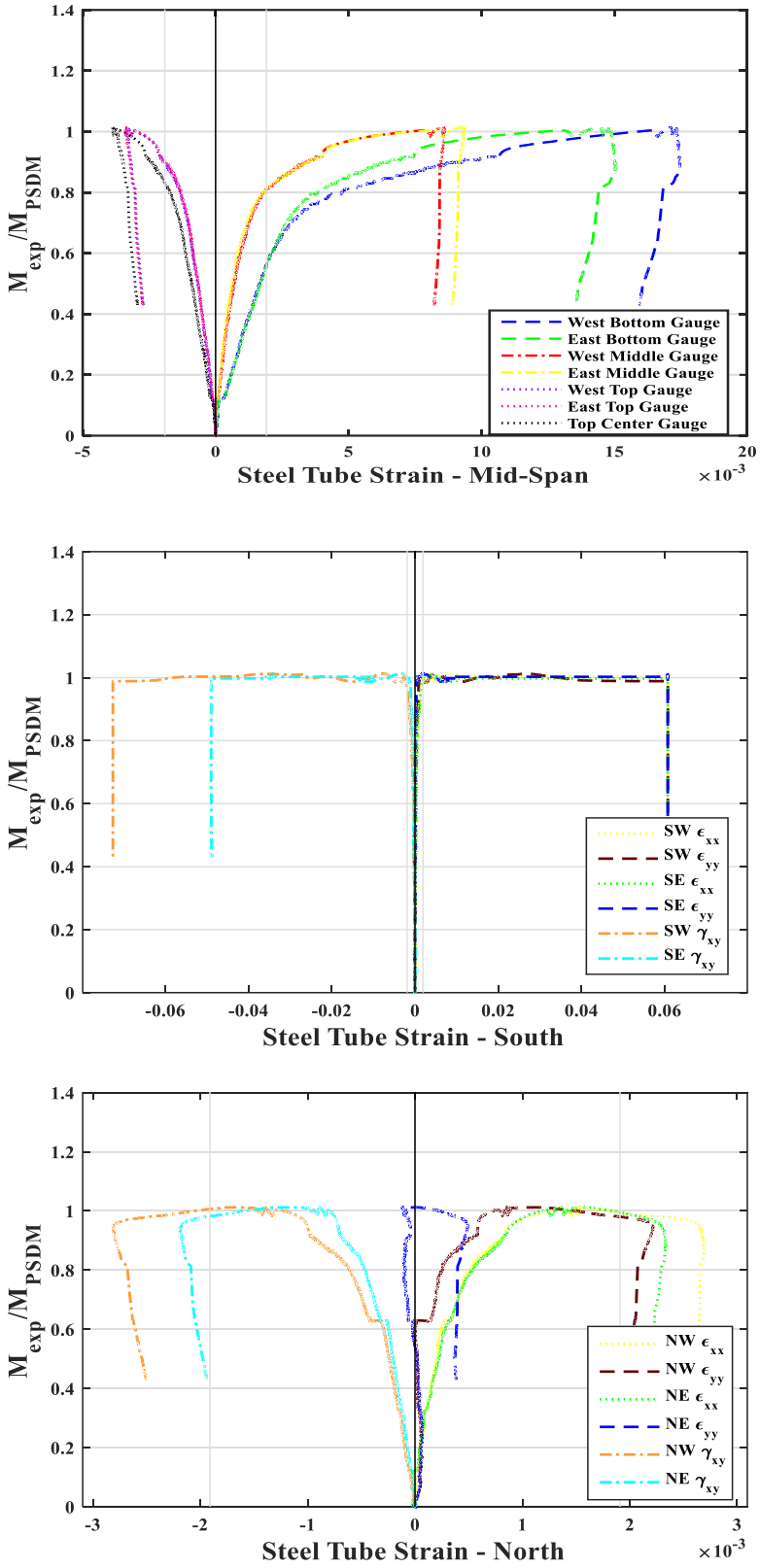

Steel strain gauge plots—Specimen 11

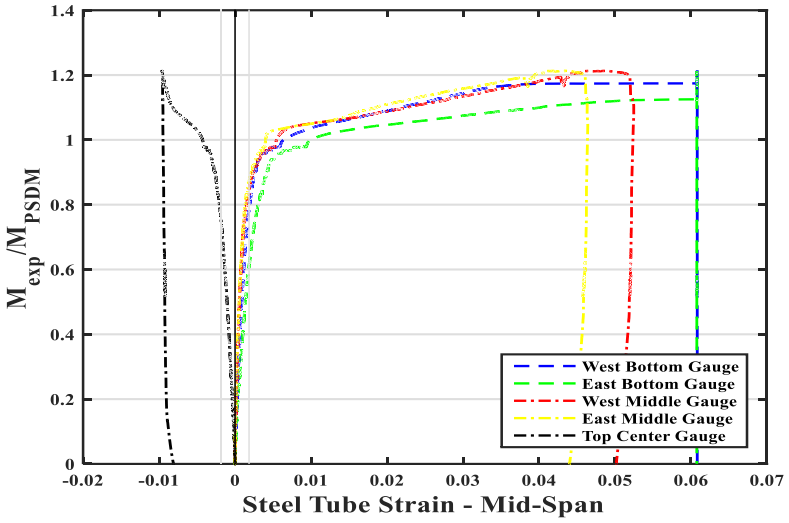

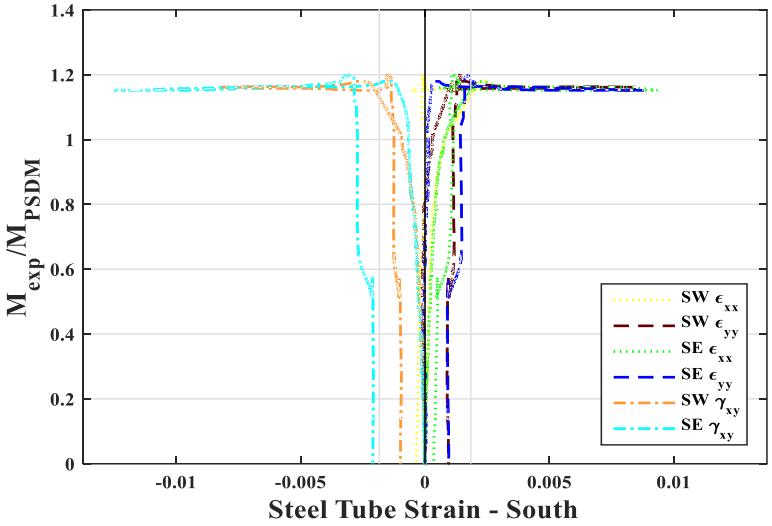

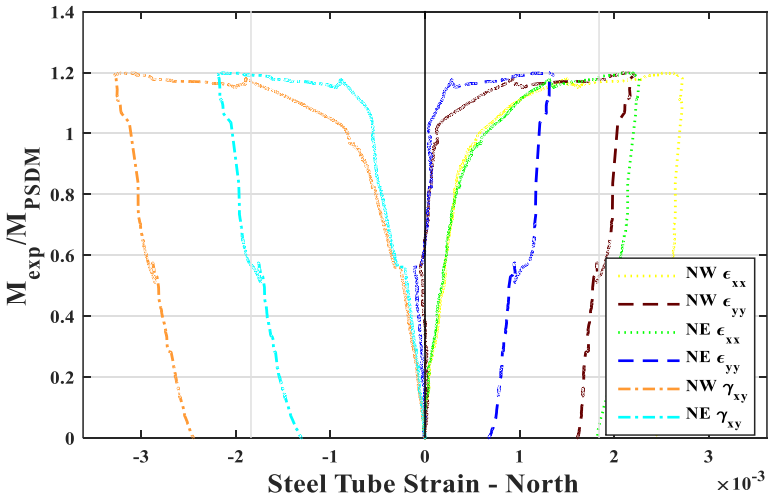

Steel strain gauge plots—Specimen 12

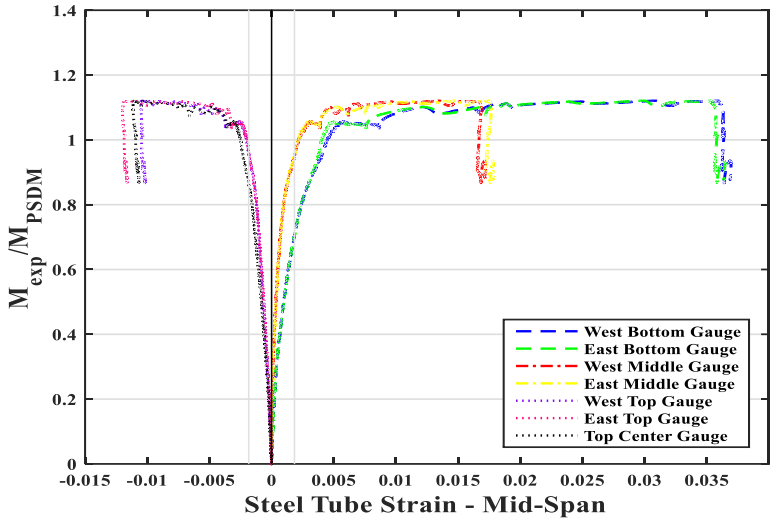

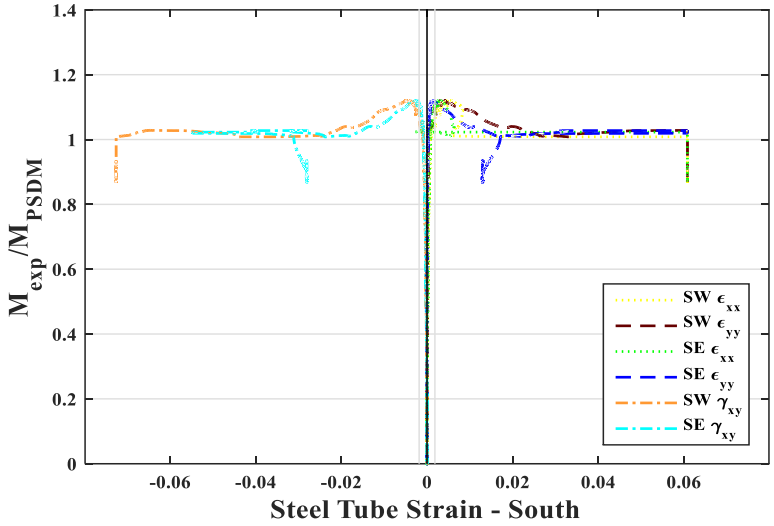

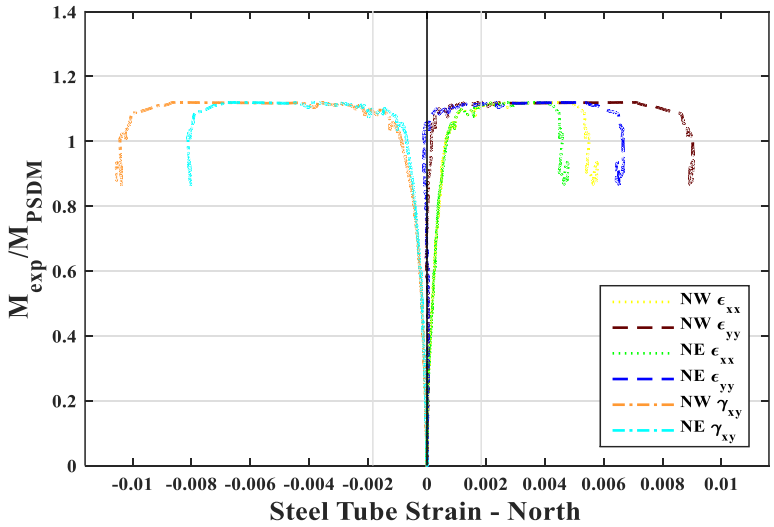

Steel strain gauge plots—Specimen 13

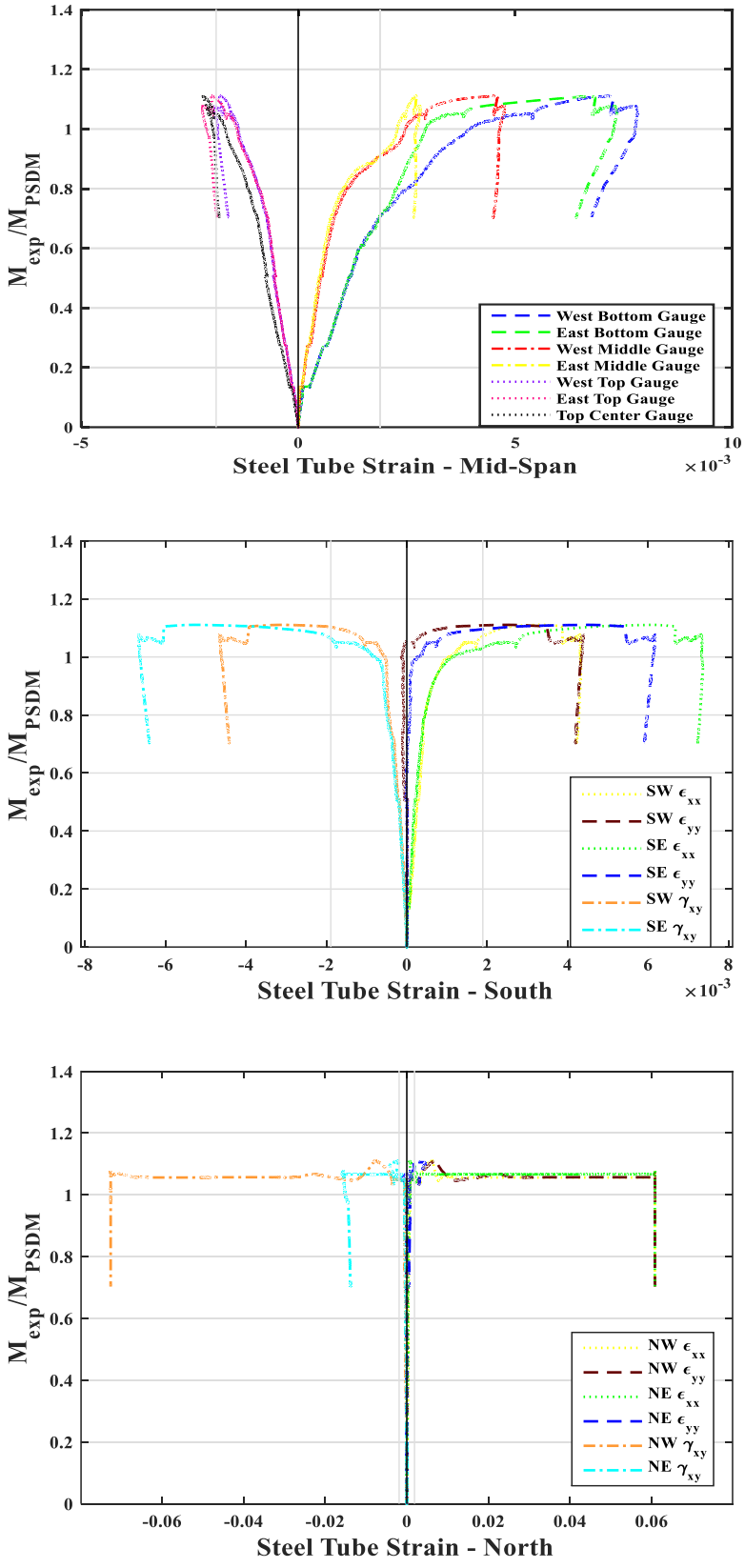

Steel strain gauge plots—Specimen 14

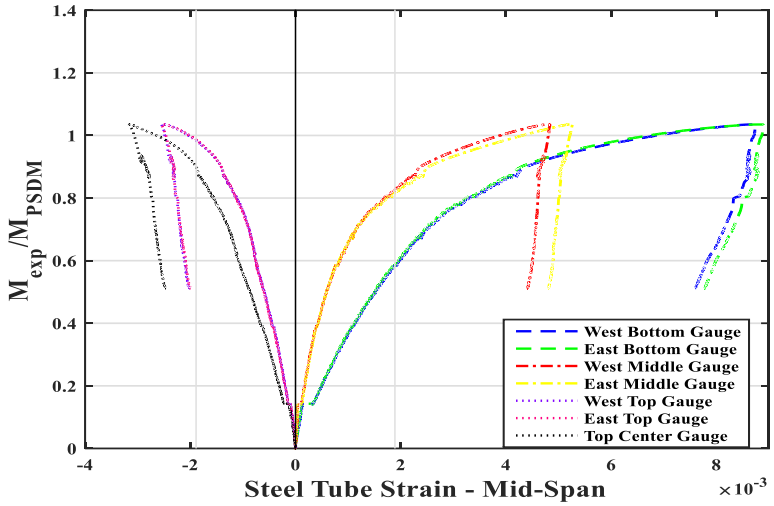

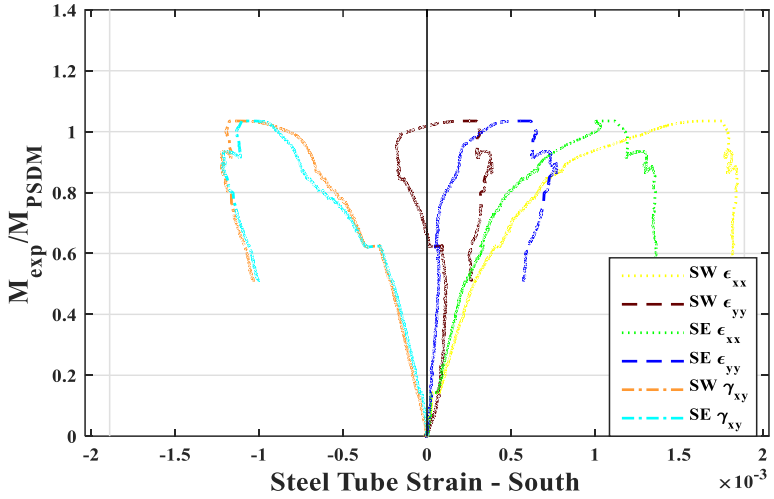

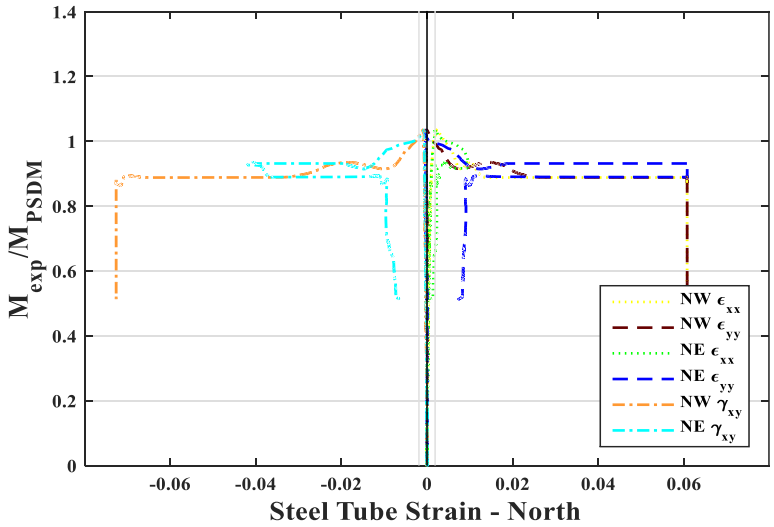

Steel strain gauge plots—Specimen 15

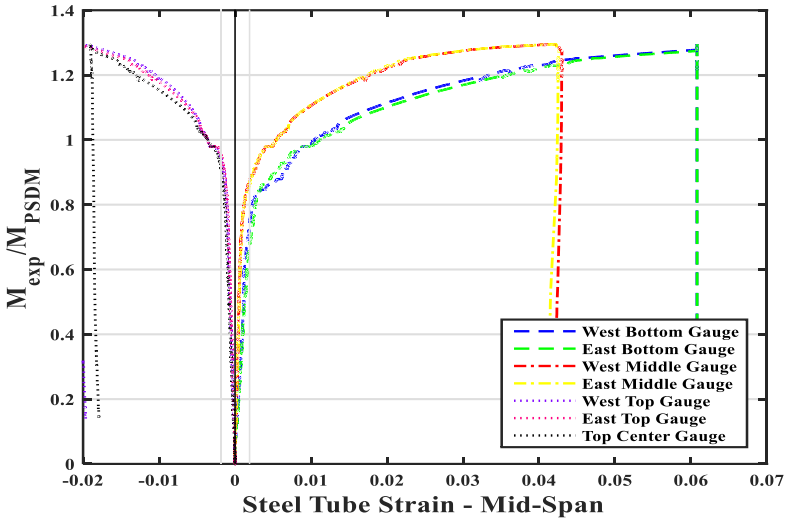

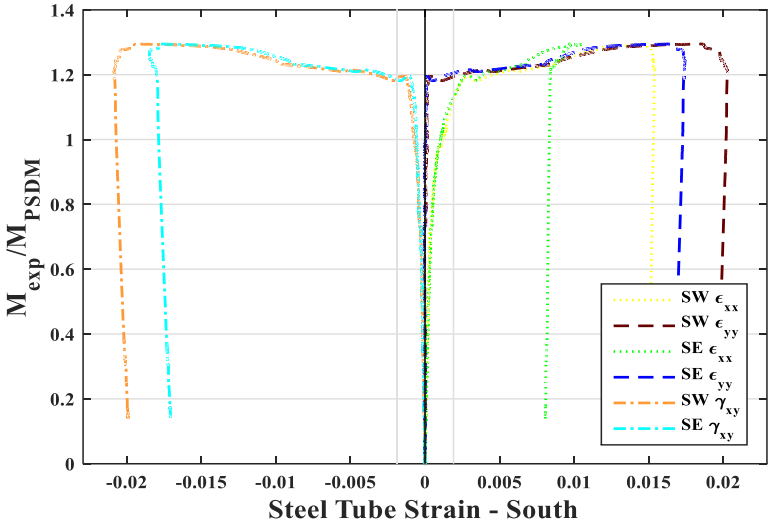

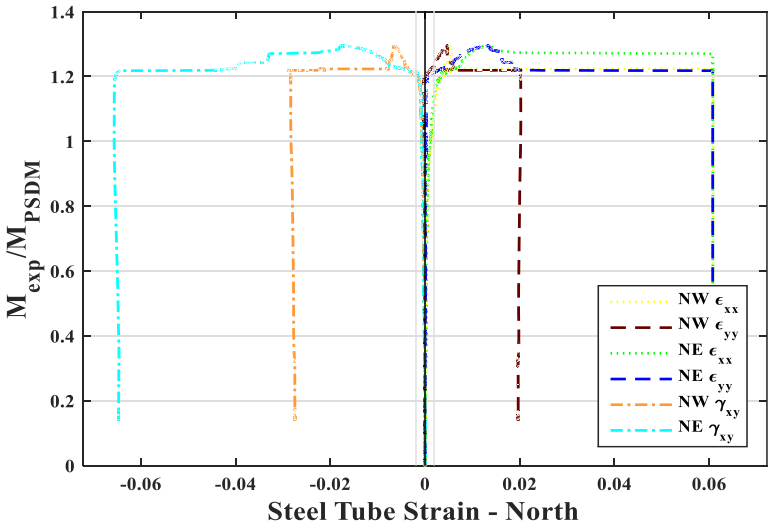

Steel strain gauge plots—Specimen 16

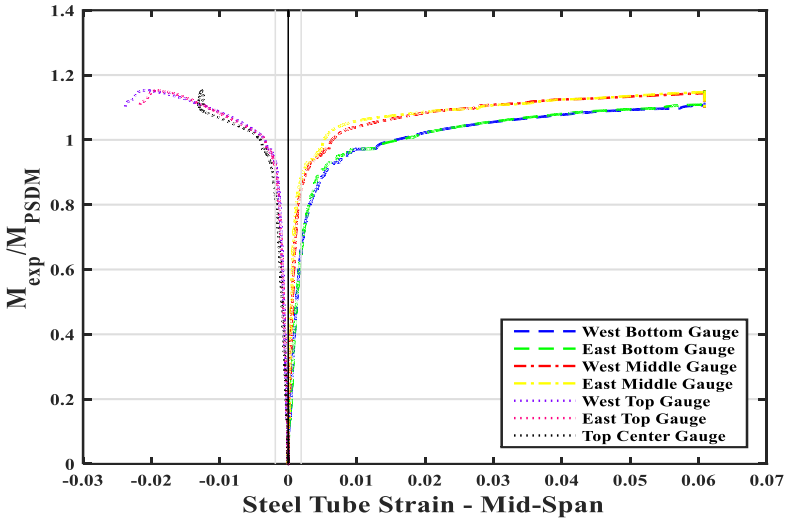

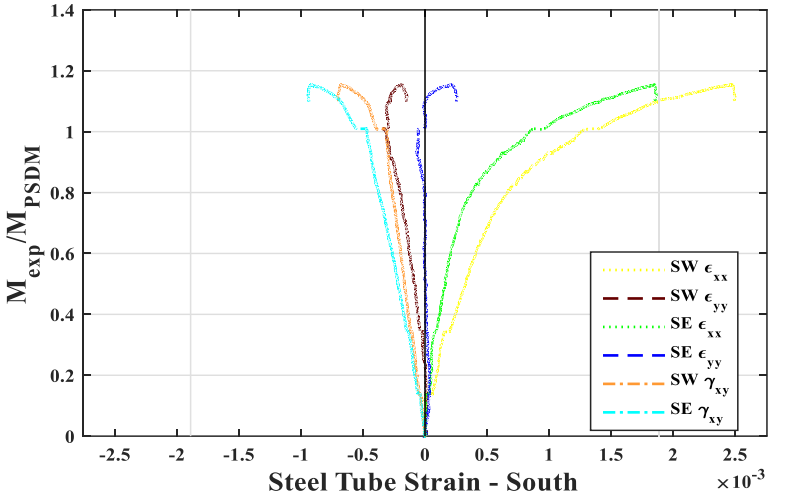

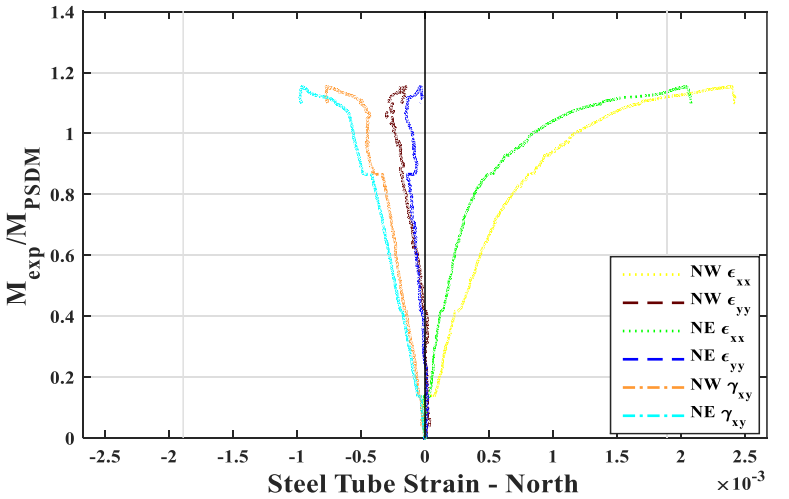

Steel strain gauge plots—Specimen 17

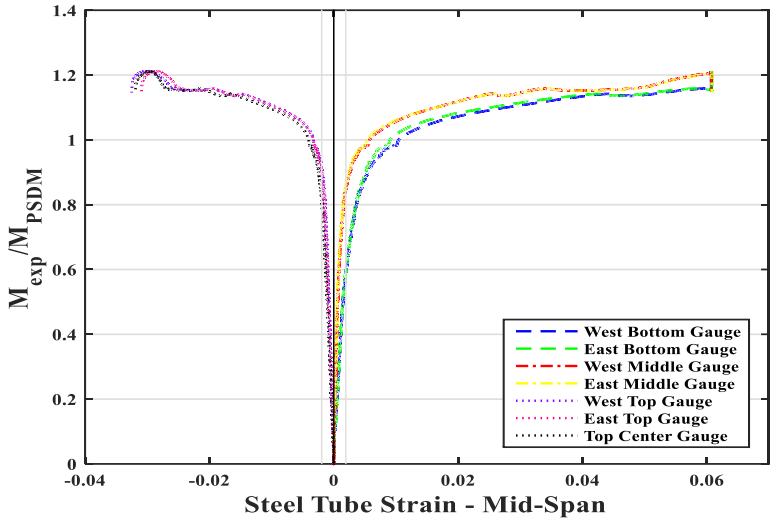

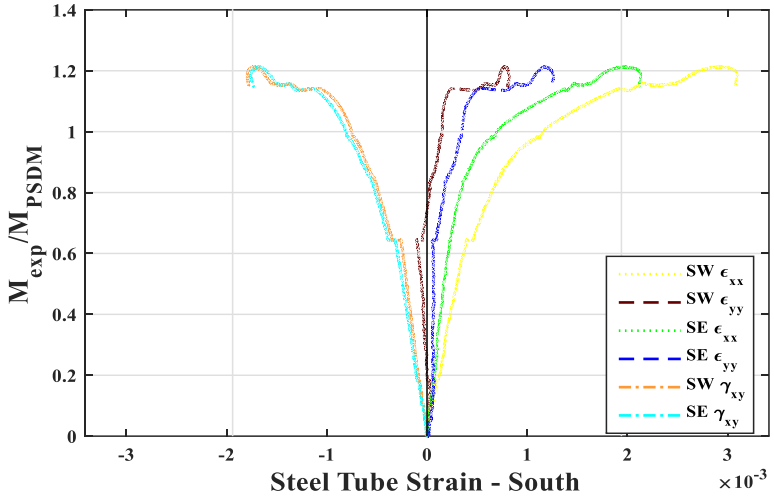

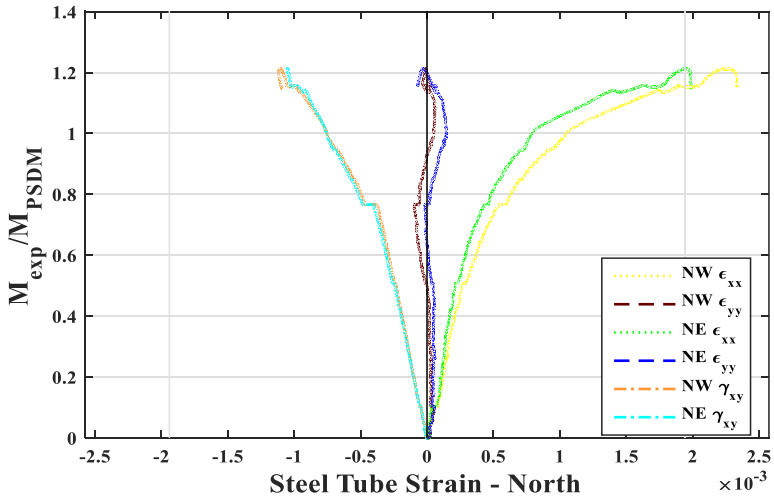

Steel strain gauge plots—Specimen 18

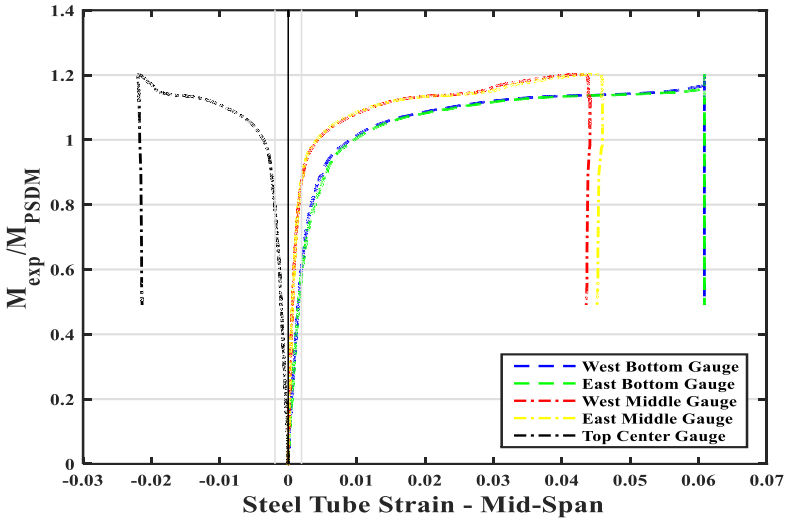

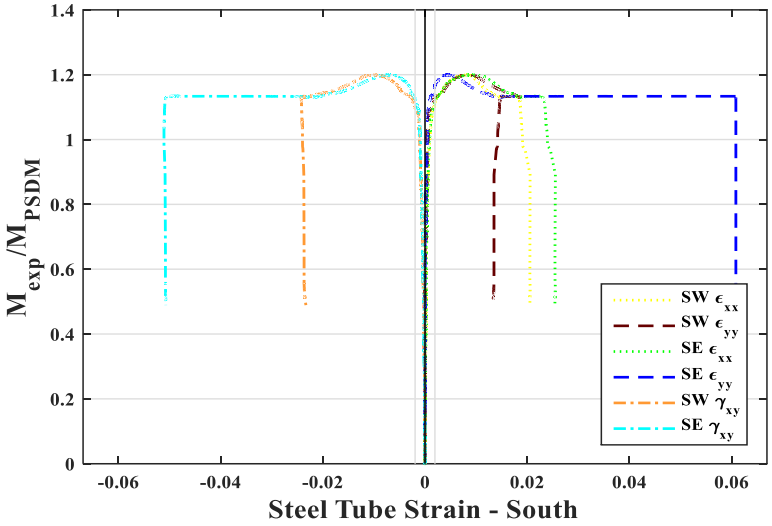

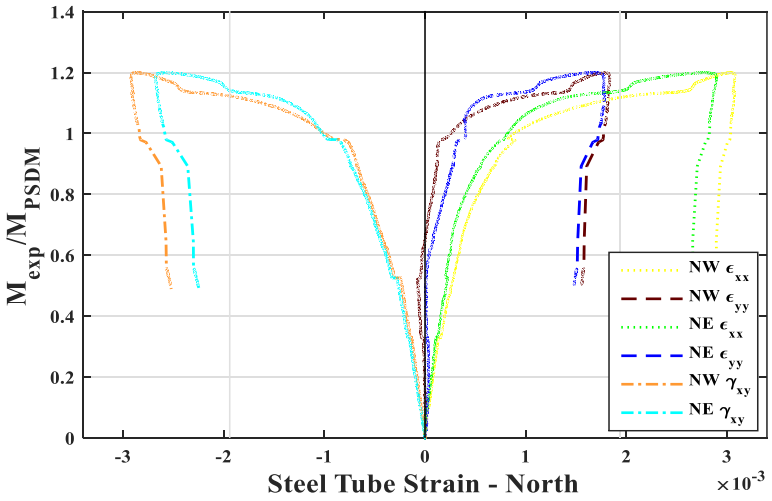

Steel strain gauge plots—Specimen 19

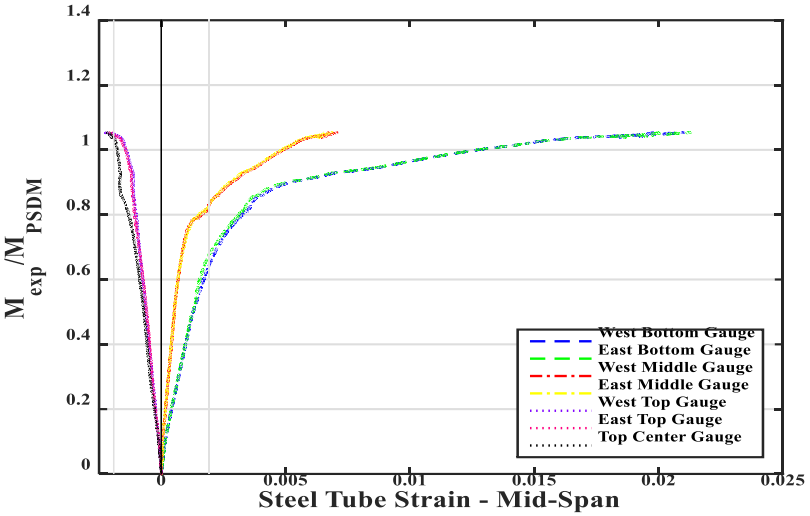

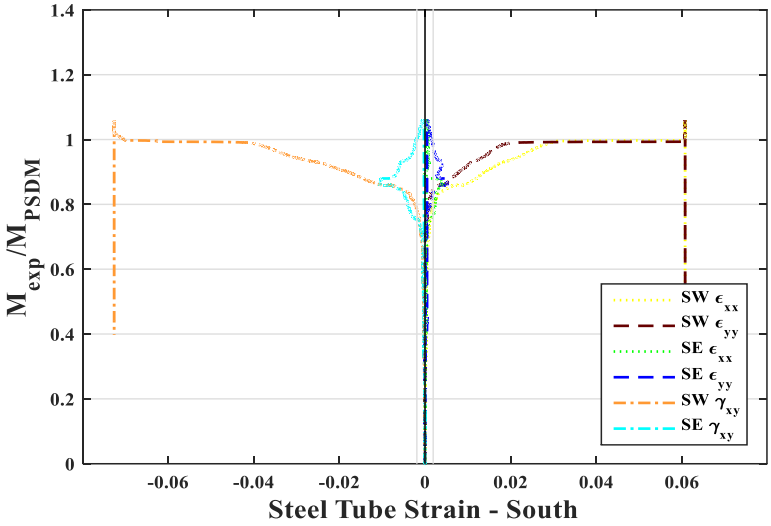

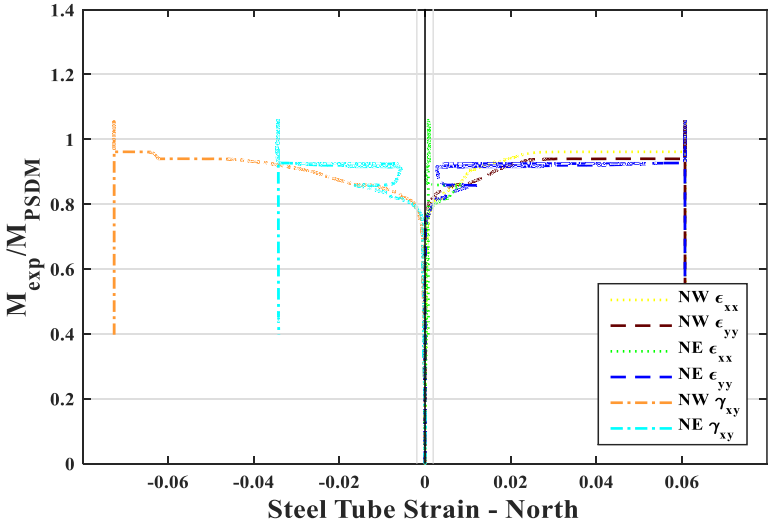

Steel strain gauge plots—Specimen 20

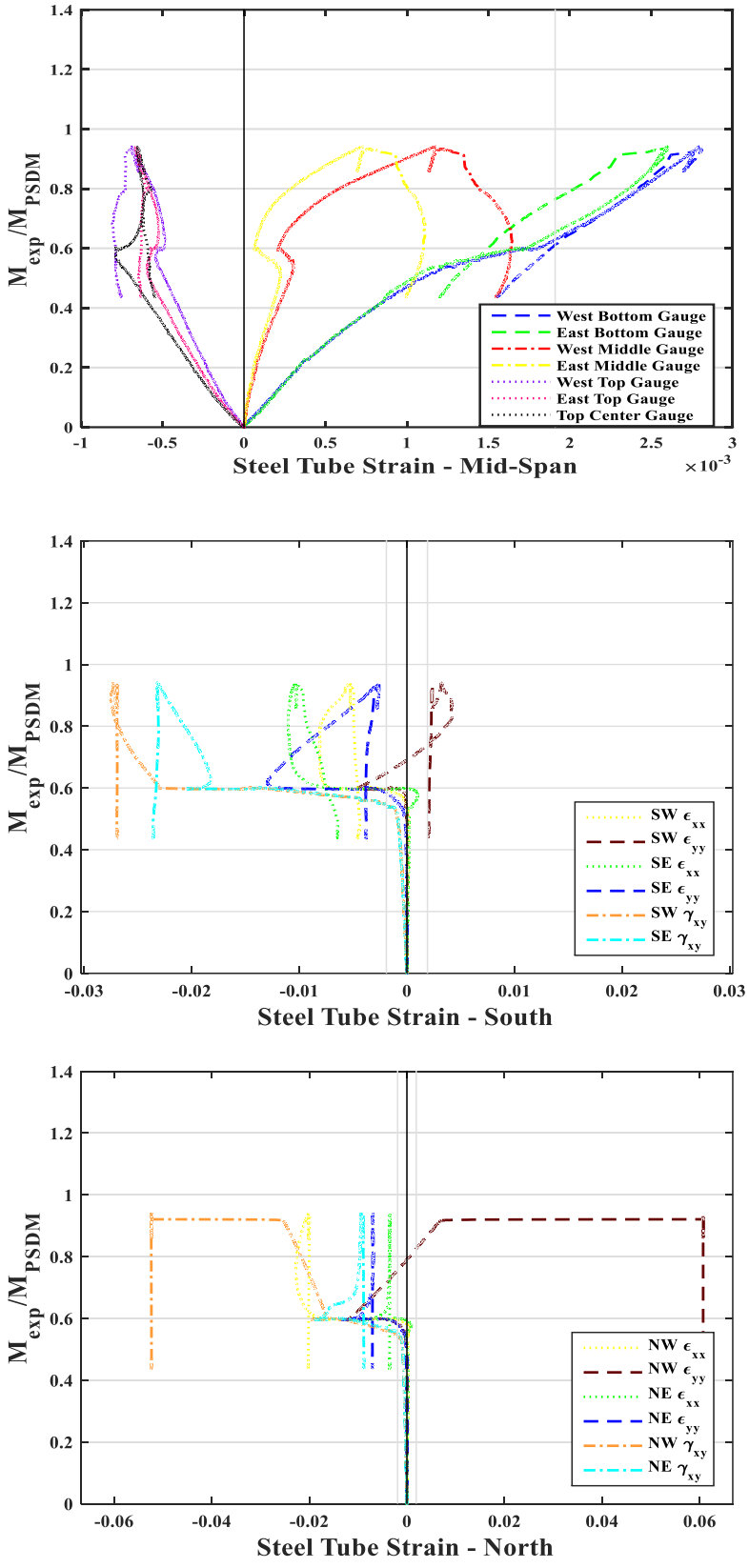

Steel strain gauge plots—Specimen 21

APPENDIX E: Concrete Strain Gauge Data

Two plots are included for each of the specimens outfitted with Geokon internal vibrating wire strain gauges. The first plots the applied shear force versus the strain reading at each of the gauges. The second plots the same but with is zoomed in on the pre-cracked behavior. Table 3.7 shows the layout of the strain gauges.

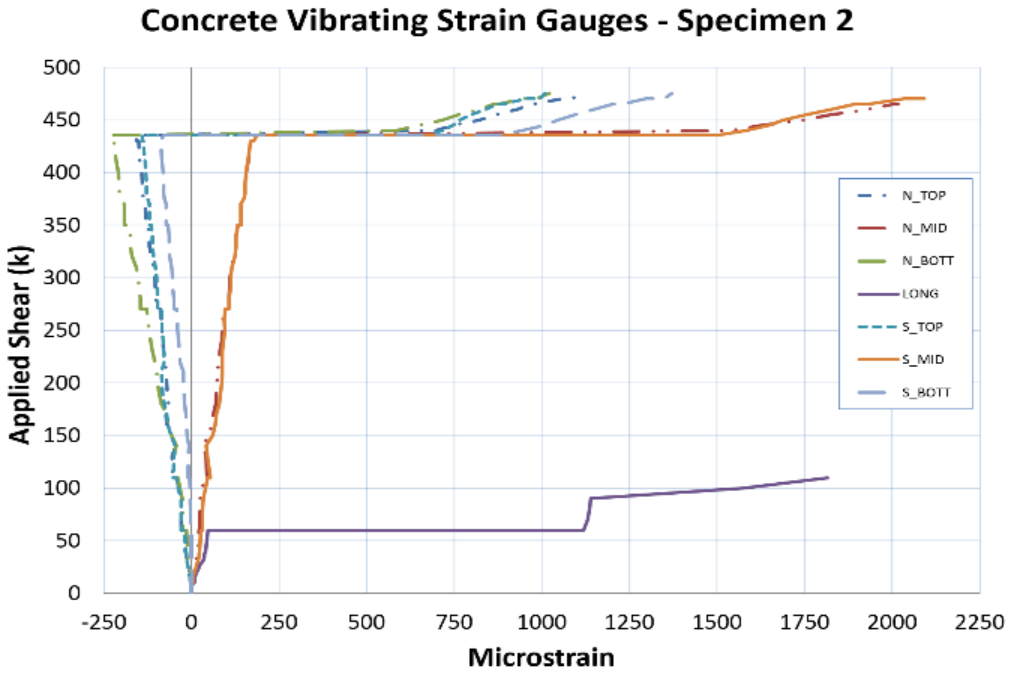

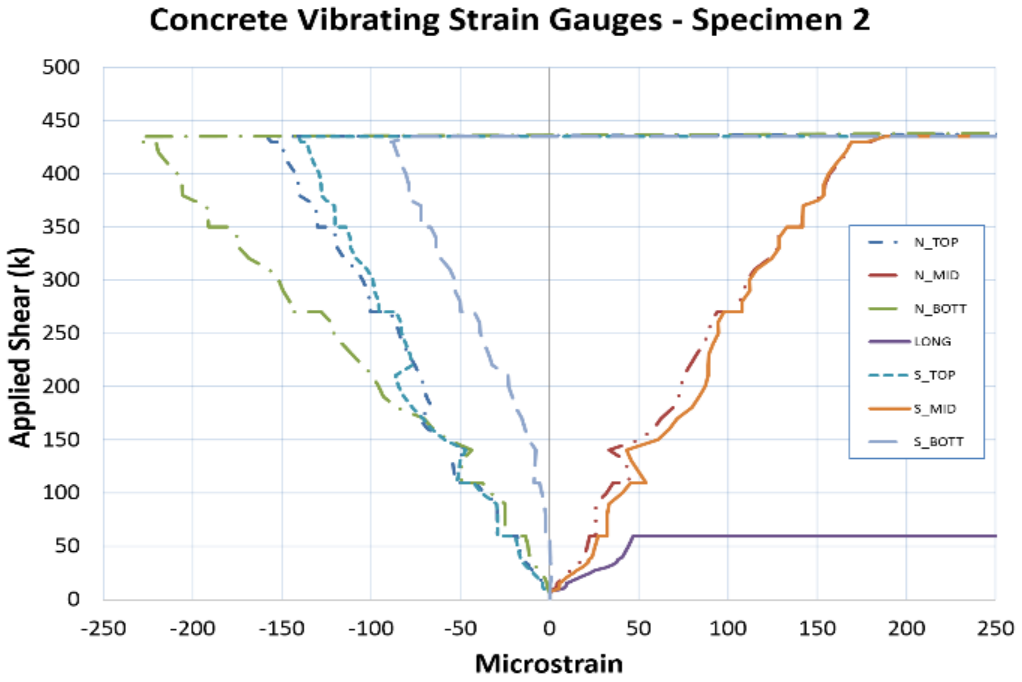

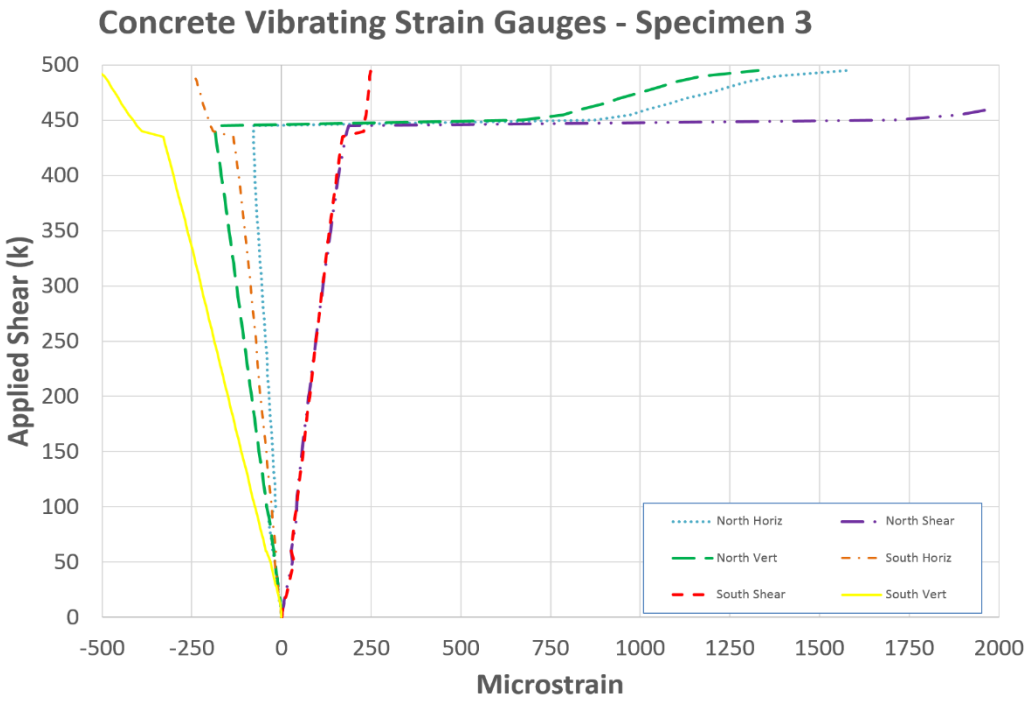
Concrete Vibrating Strain Gauges - Specimen 3
Applied Shear (k)
500
450
400
350
300
250
200
150
100
50
0
-500
-250
0
250
500
750
1000
1250
1500
1750
2000
Microstrain
North Horiz
North Shear
North Vert
South Horiz
South Shear
South Vert

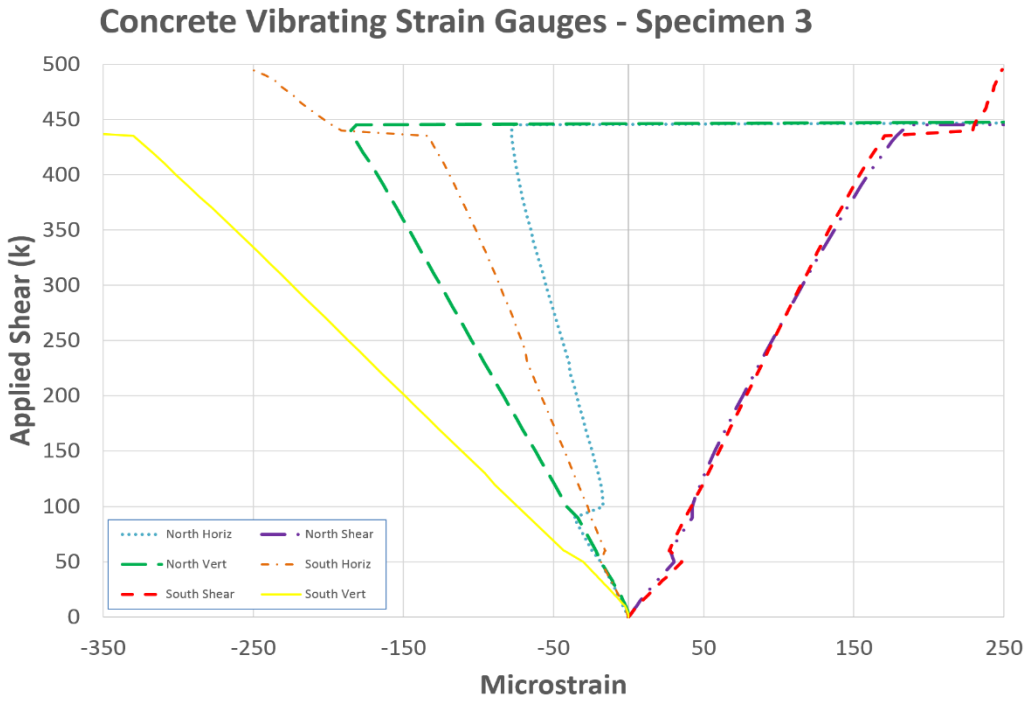
Concrete Vibrating Strain Gauges - Specimen 3
Applied Shear (k)
500
450
400
350
300
250
200
150
100
50
0
-350
-250
-150
-50
50
150
250
Microstrain
North Horiz
North Shear
North Vert
South Horiz
South Shear
South Vert

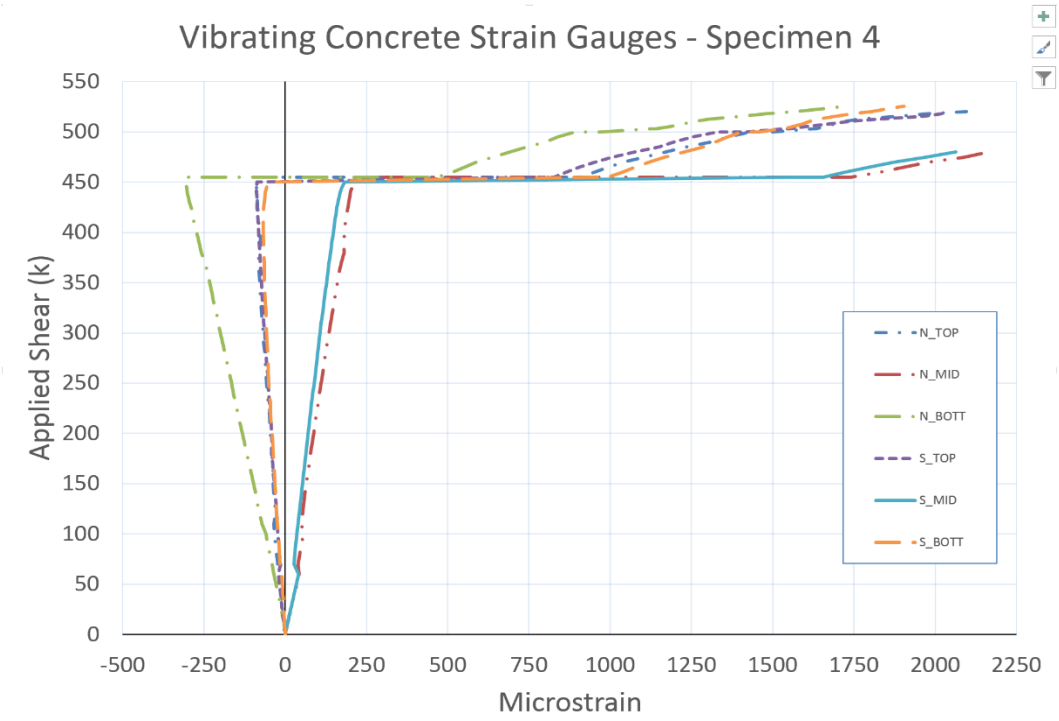
Vibrating Concrete Strain Gauges - Specimen 4
Applied Shear (k)
550
500
450
400
350
300
250
200
150
100
50
0
-500
-250
0
250
500
750
1000
1250
1500
1750
2000
2250
Microstrain
N_TOP
N_MID
N_BOTT
S_TOP
S_MID
S_BOTT

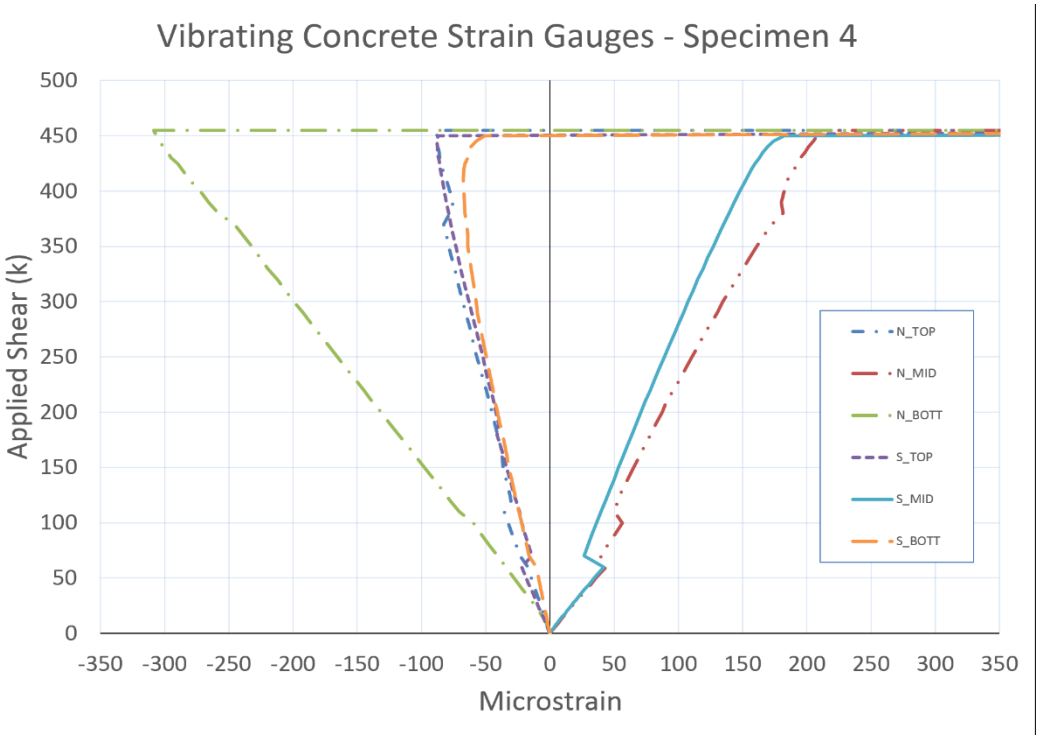
Vibrating Concrete Strain Gauges - Specimen 4
Applied Shear (k)
500
450
400
350
300
250
200
150
100
50
0
-350
-300
-250
-200
-150
-100
-50
0
50
100
150
200
250
300
350
Microstrain
N_TOP
N_MID
N_BOTT
S_TOP
S_MID
S_BOTT

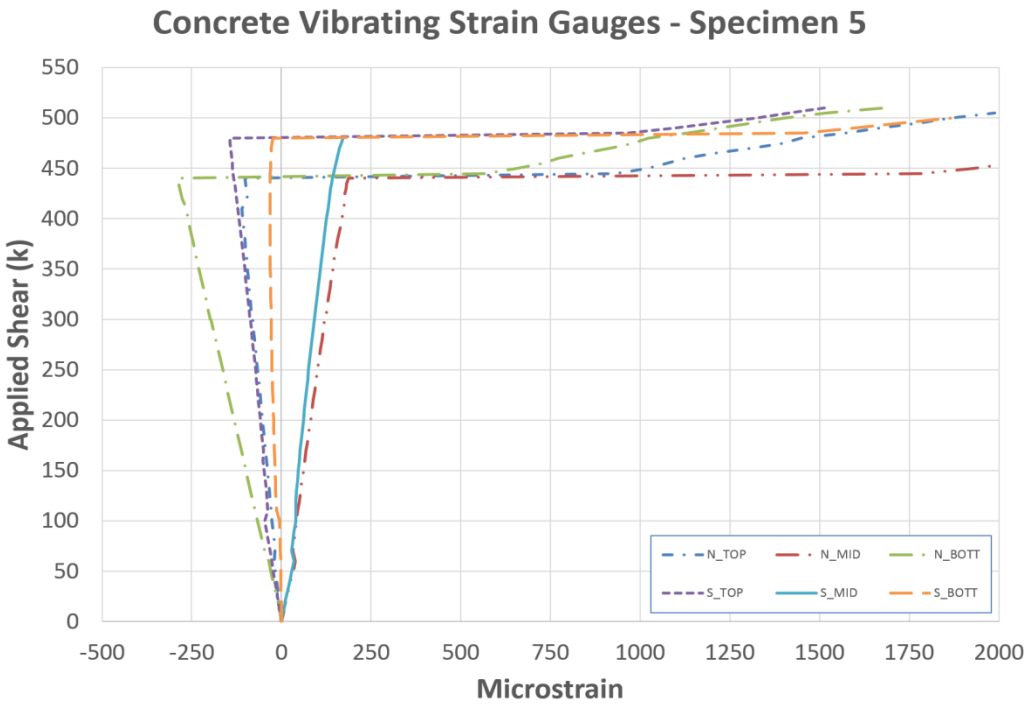
Concrete Vibrating Strain Gauges - Specimen 5
Applied Shear (k)
550
500
450
400
350
300
250
200
150
100
50
0
-500
-250
0
250
500
750
1000
1250
1500
1750
2000
Microstrain
N_TOP
N_MID
N_BOTT
S_TOP
S_MID
S_BOTT

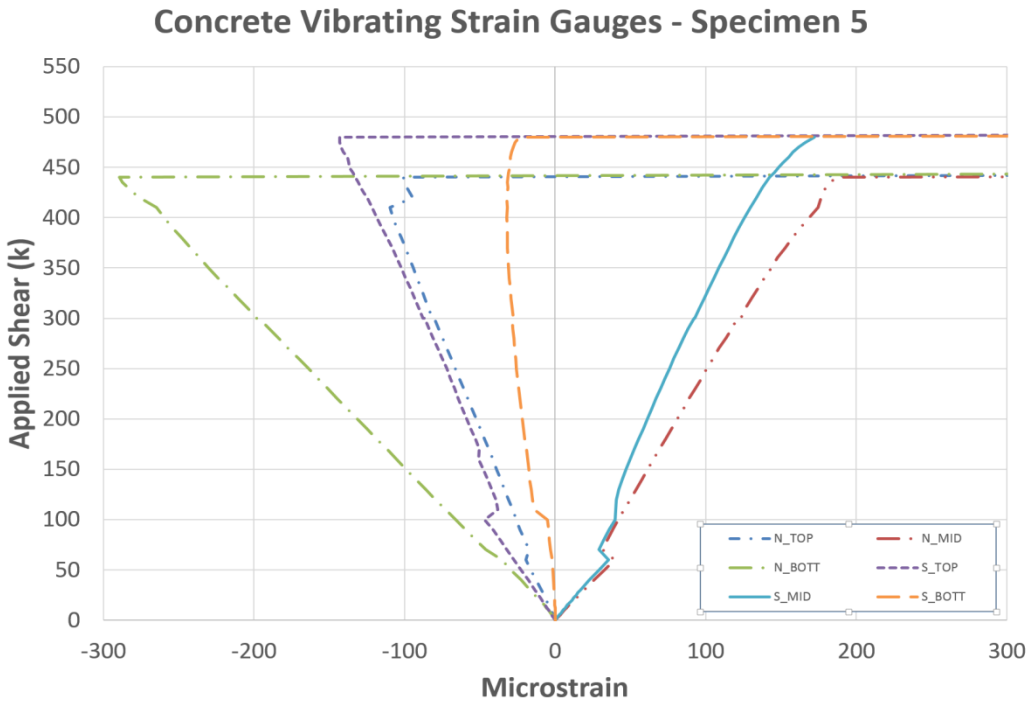
Concrete Vibrating Strain Gauges - Specimen 5
Applied Shear (k)
550
500
450
400
350
300
250
200
150
100
50
0
-300
-200
-100
0
100
200
300
Microstrain
N_TOP
N_MID
N_BOTT
S_TOP
S_MID
S_BOTT

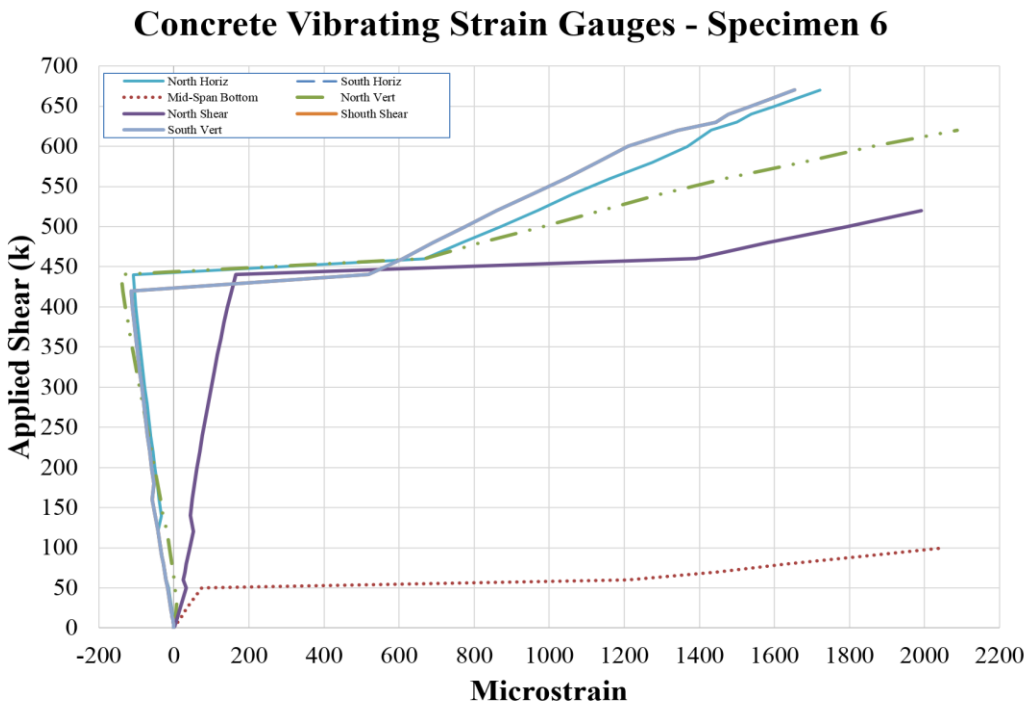
Concrete Vibrating Strain Gauges - Specimen 6
North Horiz
South Horiz
Mid-Span Bottom
North Vert
North Shear
Shouth Shear
South Vert
Applied Shear (k)
Microstrain
700
650
600
550
500
450
400
350
300
250
200
150
100
50
0
-200
0
200
400
600
800
1000
1200
1400
1600
1800
2000
2200

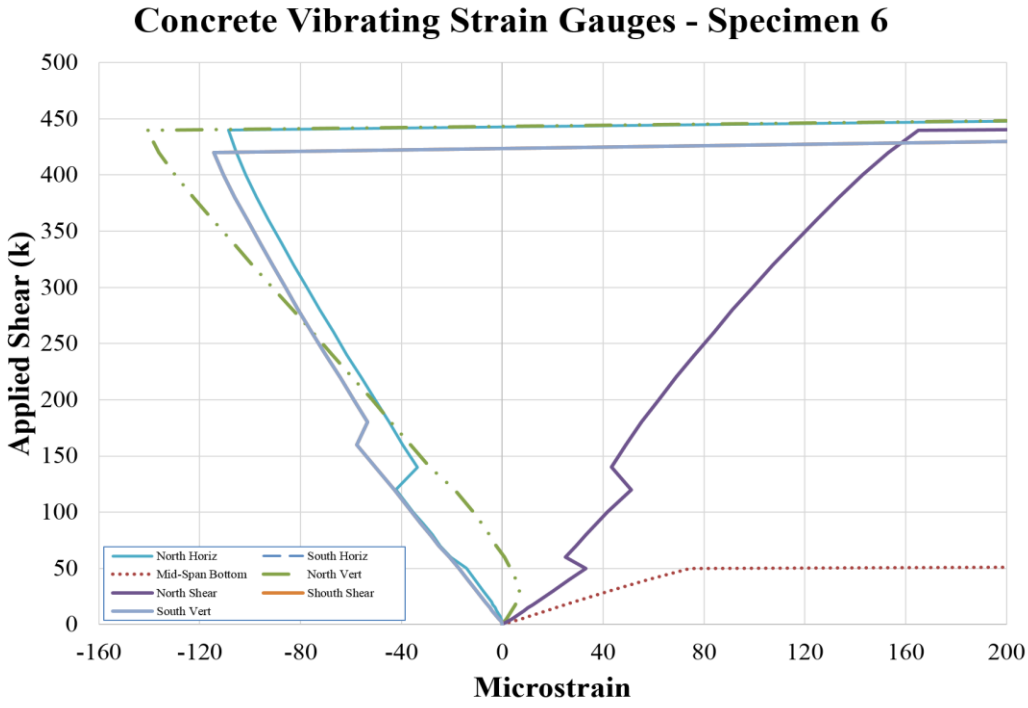
Concrete Vibrating Strain Gauges - Specimen 6
North Horiz
South Horiz
Mid-Span Bottom
North Vert
North Shear
Shouth Shear
South Vert
Applied Shear (k)
Microstrain
500
450
400
350
300
250
200
150
100
50
0
-160
-120
-80
-40
0
40
80
120
160
200

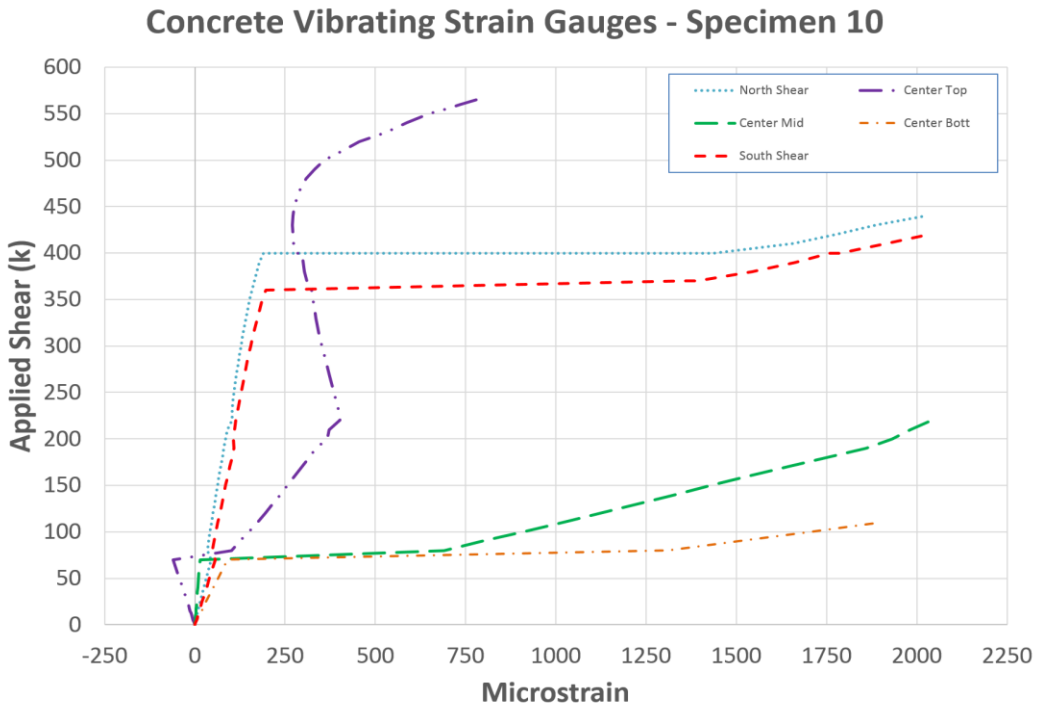
Concrete Vibrating Strain Gauges - Specimen 10
North Shear
Center Top
Center Mid
Center Bott
South Shear
Applied Shear (k)
600
550
500
450
400
350
300
250
200
150
100
50
0
-250
0
250
500
750
1000
1250
1500
1750
2000
2250
Microstrain

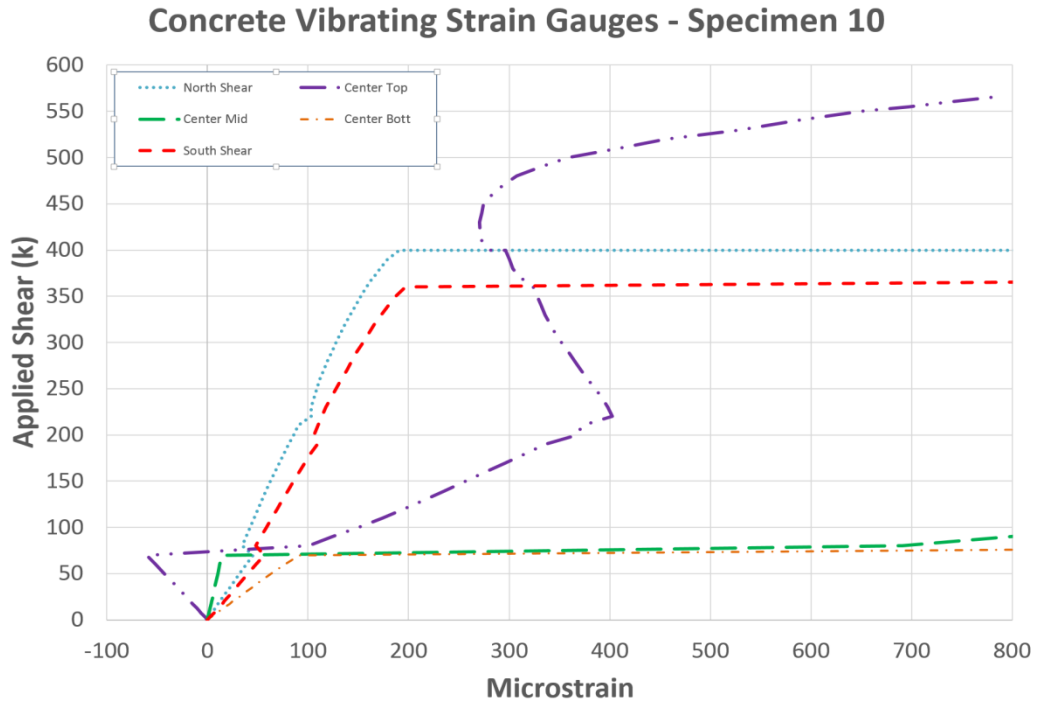
Concrete Vibrating Strain Gauges - Specimen 10
North Shear
Center Top
Center Mid
Center Bott
South Shear
Applied Shear (k)
600
550
500
450
400
350
300
250
200
150
100
50
0
-100
0
100
200
300
400
500
600
700
800
Microstrain

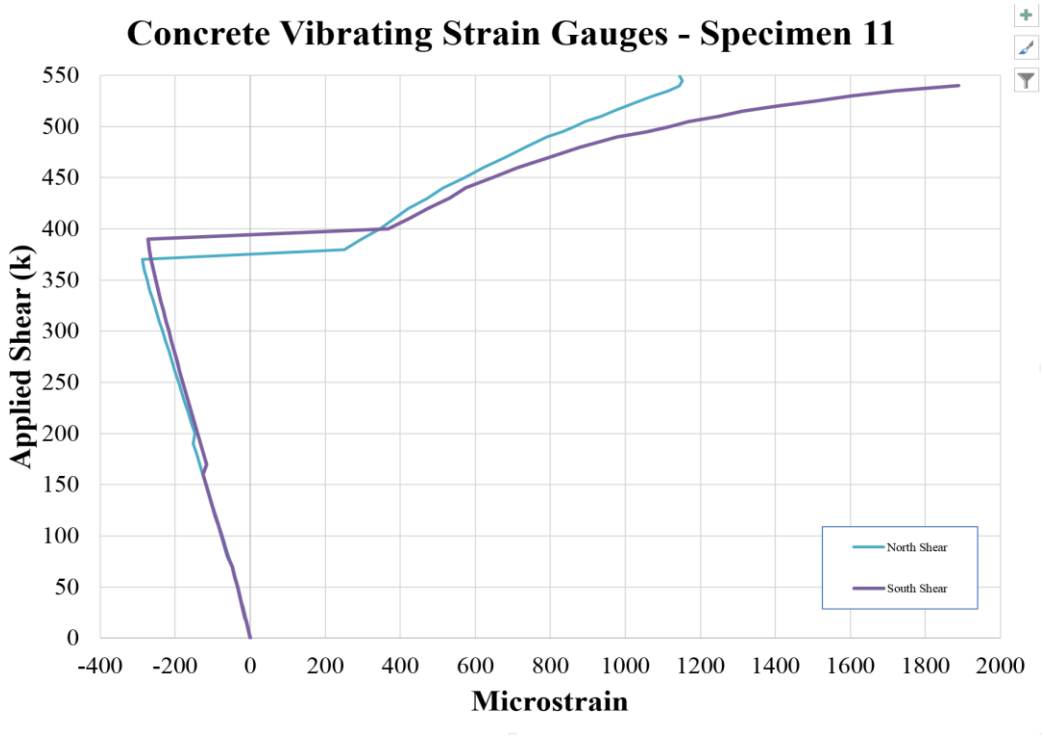
Concrete Vibrating Strain Gauges - Specimen 11
Applied Shear (k)
550
500
450
400
350
300
250
200
150
100
50
0
-400
-200
0
200
400
600
800
1000
1200
1400
1600
1800
2000
Microstrain
North Shear
South Shear

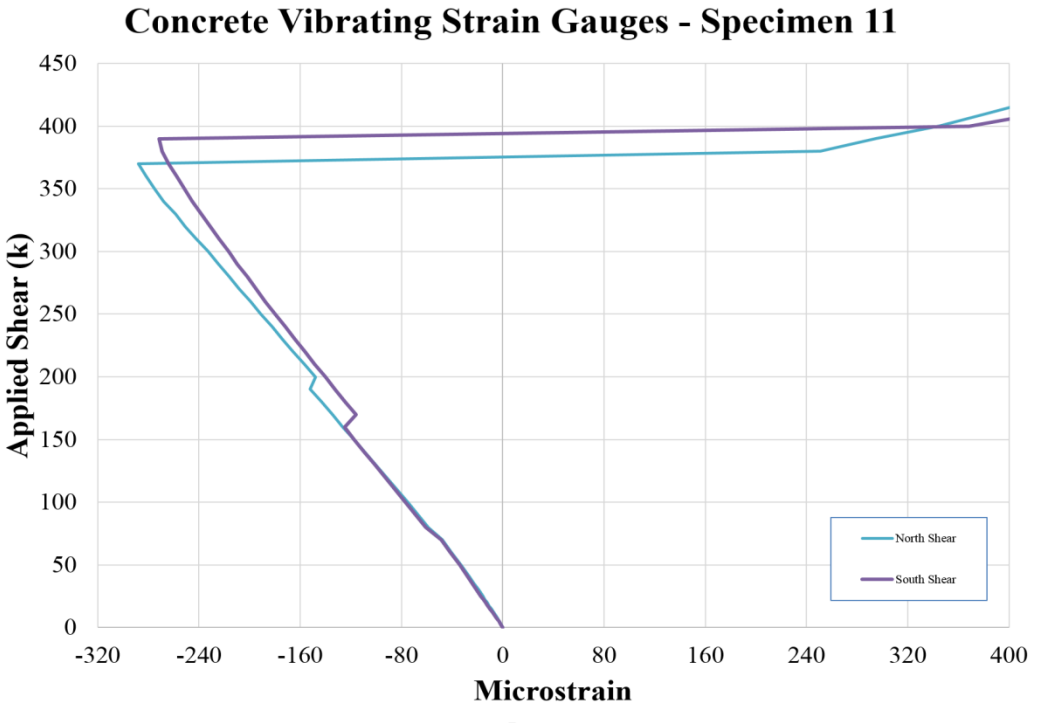
Concrete Vibrating Strain Gauges - Specimen 11
Applied Shear (k)
450
400
350
300
250
200
150
100
50
0
-320
-240
-160
-80
0
80
160
240
320
400
Microstrain
North Shear
South Shear

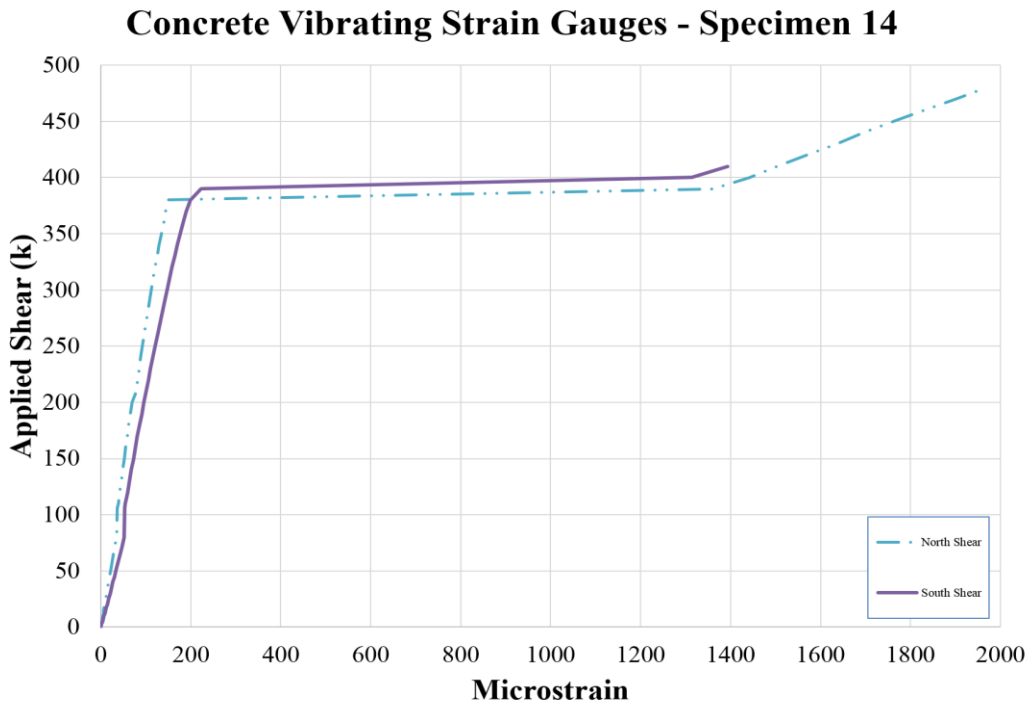
Concrete Vibrating Strain Gauges - Specimen 14
Applied Shear (k)
500
450
400
350
300
250
200
150
100
50
0
0
200
400
600
800
1000
1200
1400
1600
1800
2000
Microstrain
North Shear
South Shear

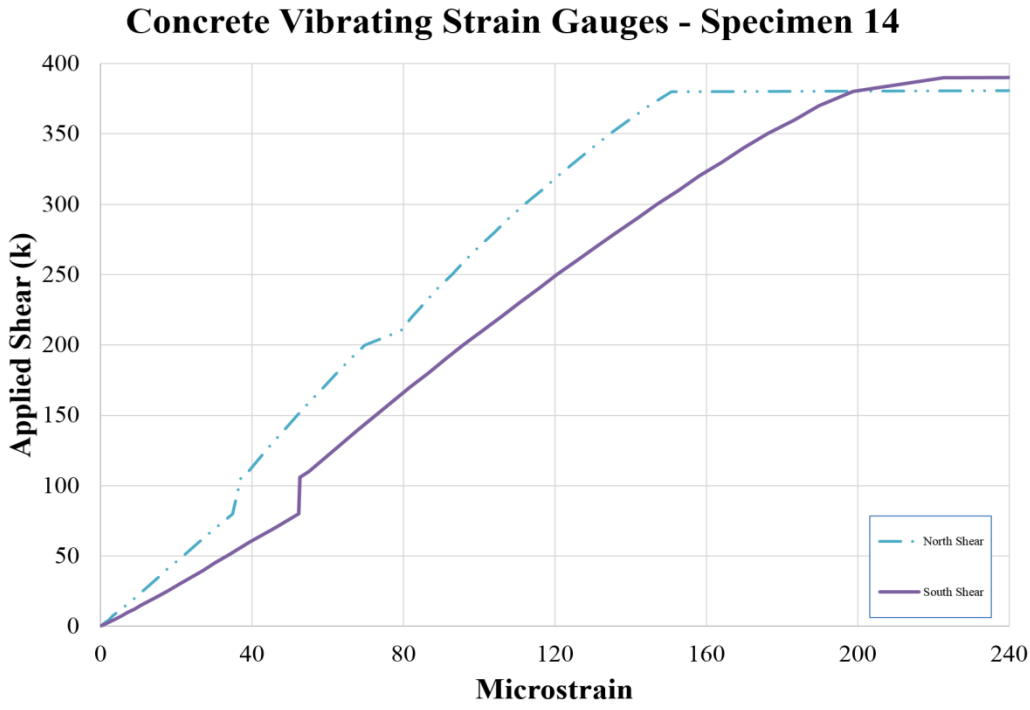
Concrete Vibrating Strain Gauges - Specimen 14
Applied Shear (k)
400
350
300
250
200
150
100
50
0
0
40
80
120
160
200
240
Microstrain
North Shear
South Shear

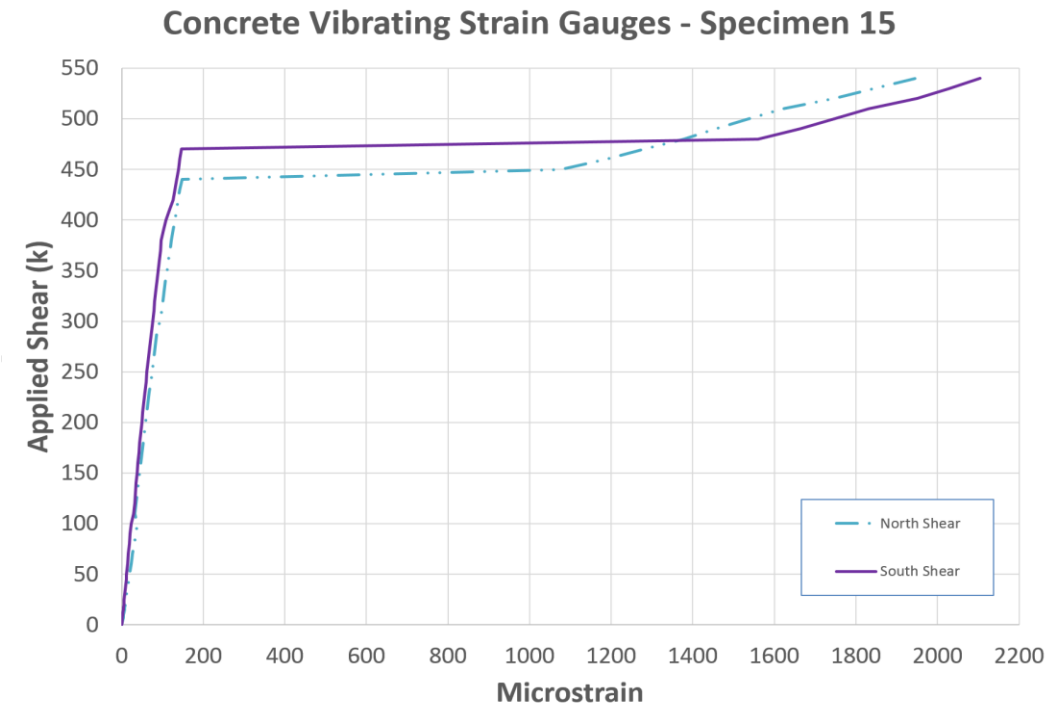
Concrete Vibrating Strain Gauges - Specimen 15
Applied Shear (k)
550
500
450
400
350
300
250
200
150
100
50
0
0
200
400
600
800
1000
1200
1400
1600
1800
2000
2200
Microstrain
North Shear
South Shear

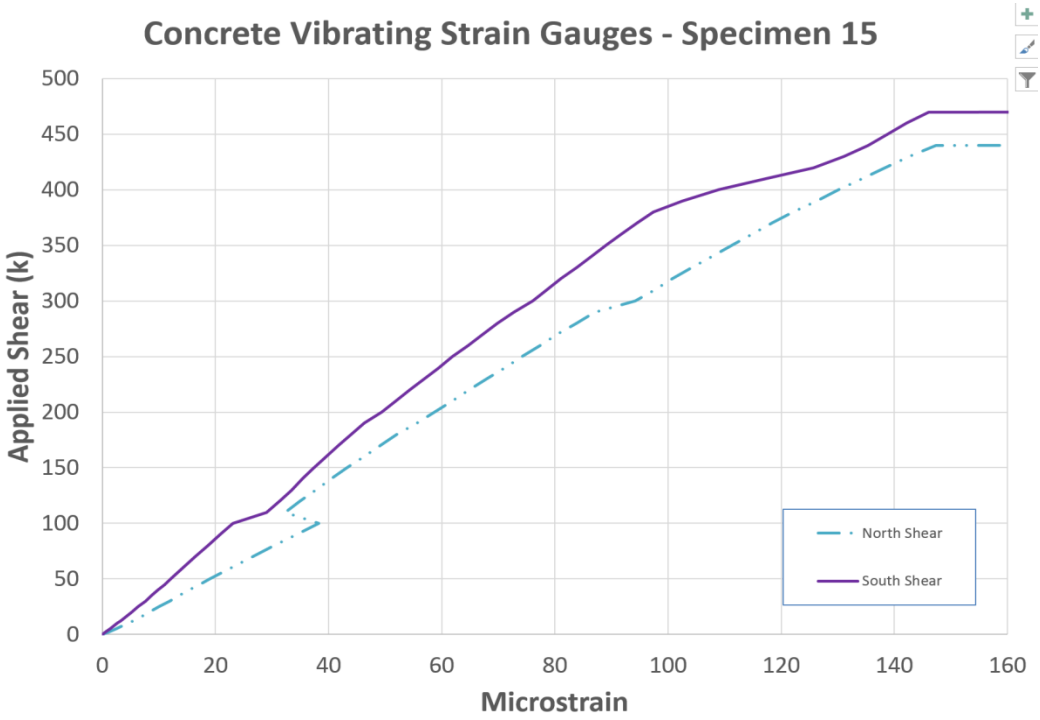
Concrete Vibrating Strain Gauges - Specimen 15
Applied Shear (k)
500
450
400
350
300
250
200
150
100
50
0
0
20
40
60
80
100
120
140
160
Microstrain
North Shear
South Shear

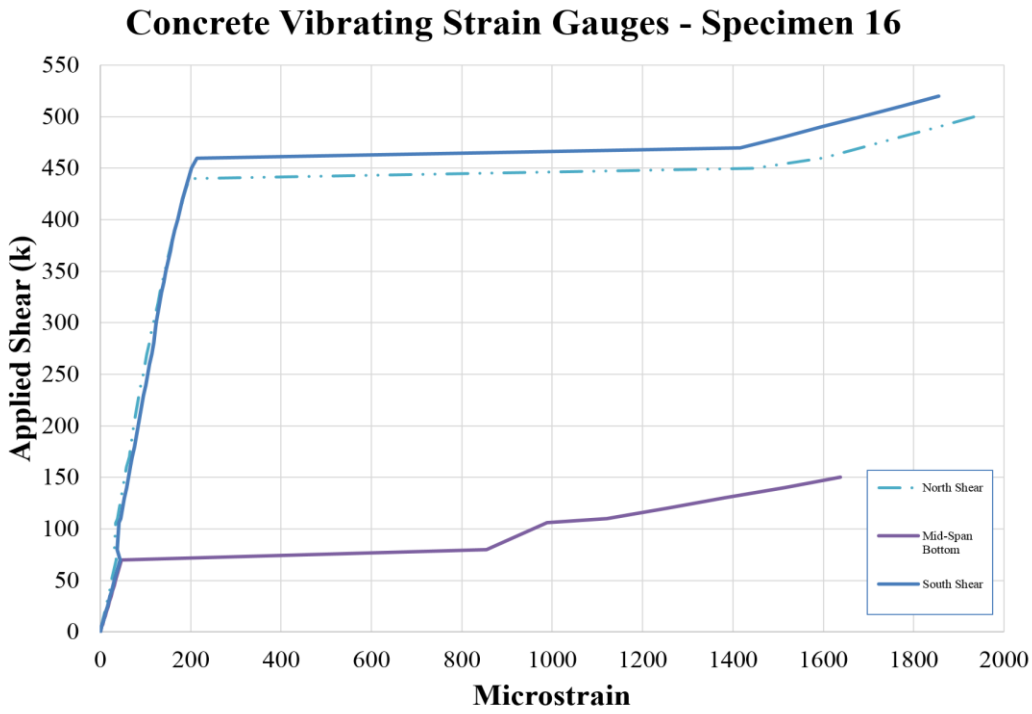
Concrete Vibrating Strain Gauges - Specimen 16
Applied Shear (k)
550
500
450
400
350
300
250
200
150
100
50
0
0
200
400
600
800
1000
1200
1400
1600
1800
2000
Microstrain
North Shear
Mid-Span Bottom
South Shear

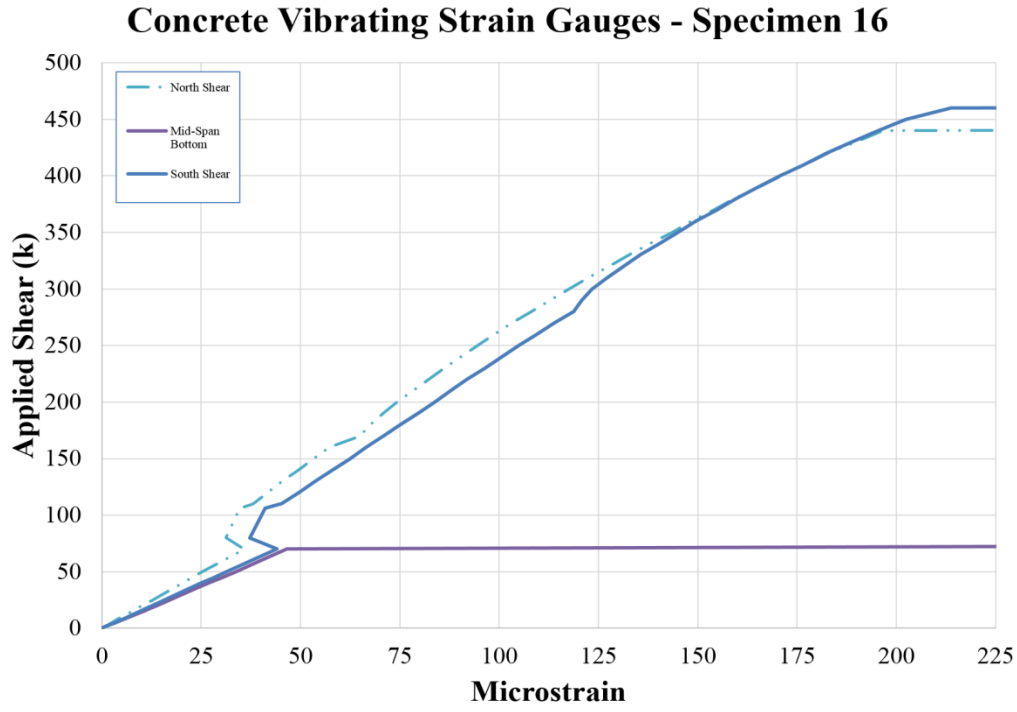
Concrete Vibrating Strain Gauges - Specimen 16
Applied Shear (k)
500
450
400
350
300
250
200
150
100
50
0
0
25
50
75
100
125
150
175
200
225
Microstrain
North Shear
Mid-Span Bottom
South Shear

APPENDIX F: Steel Tensile Stress-Strain Plots

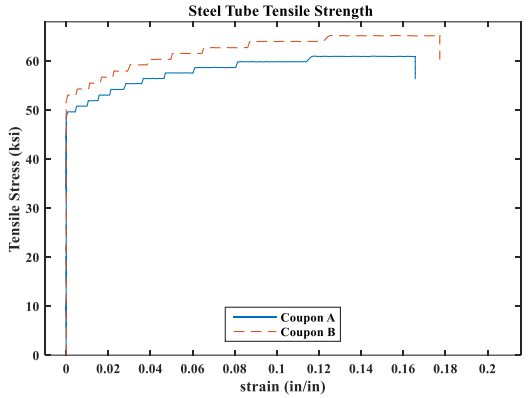

Figure F-1: Steel SS-1

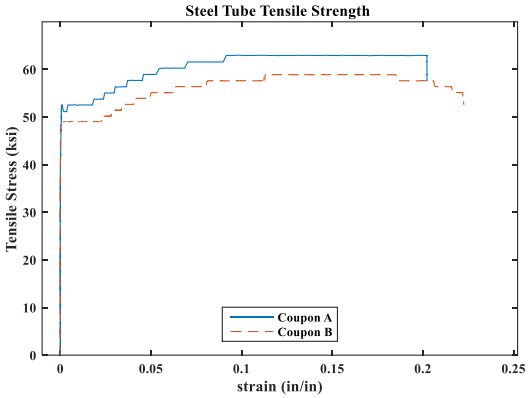

Figure F-2: Steel SS-2

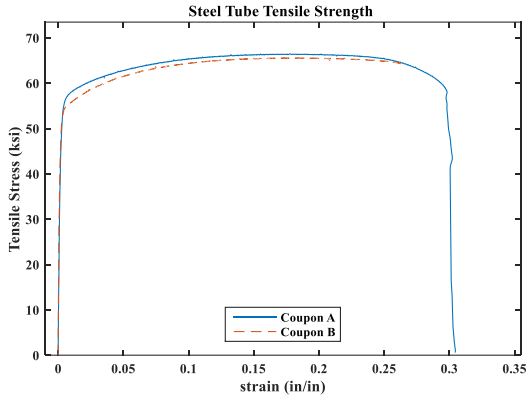

Figure F-3: Steel SS-3

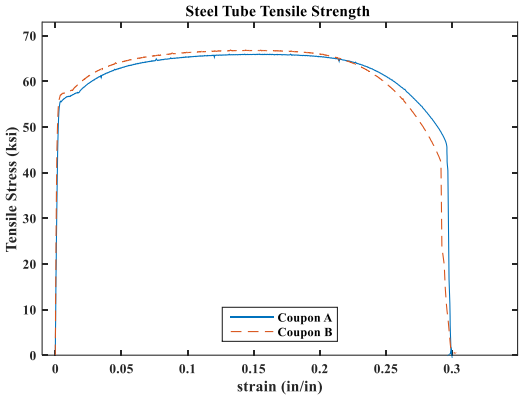

Figure F-4: Steel SS-4

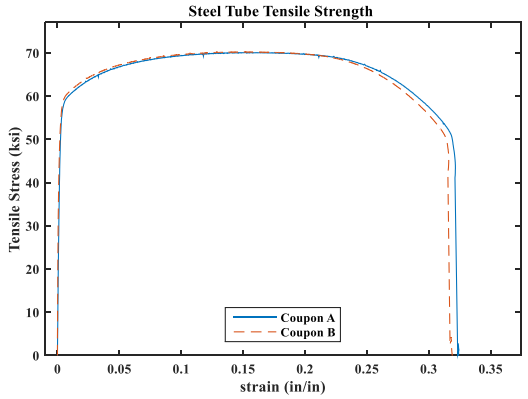

Figure F-5: Steel SS-5

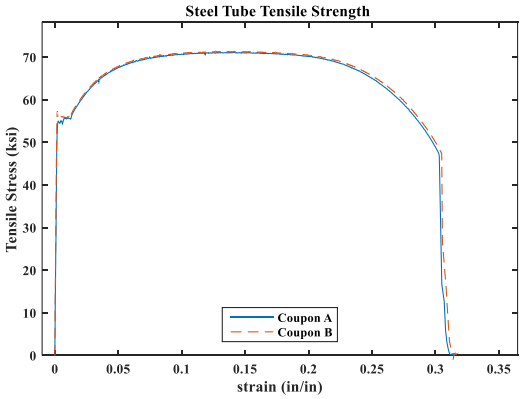

Figure F-6: Steel SS-6

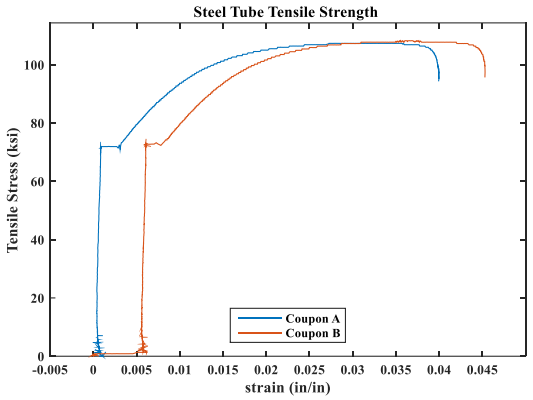

Figure F-7: Specimen 7 rebar

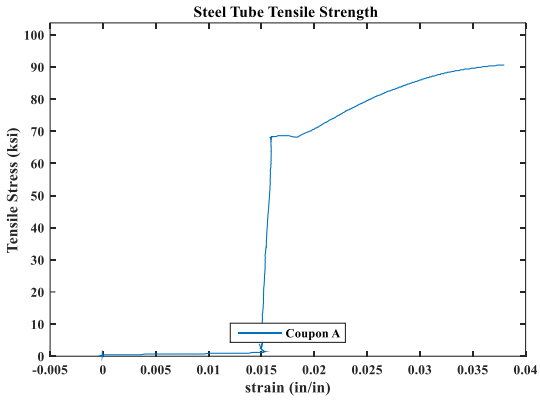

Figure F-8: Specimen 8 rebar

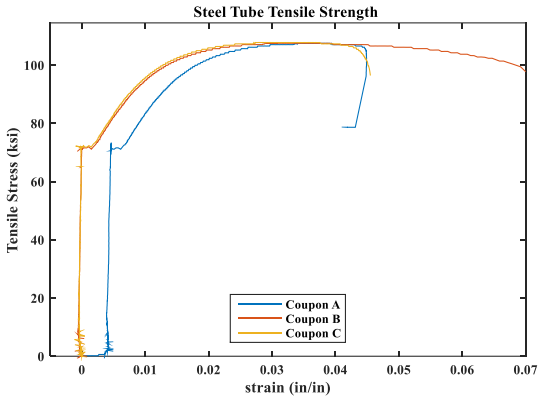

Figure F-9: Specimen 12 rebar

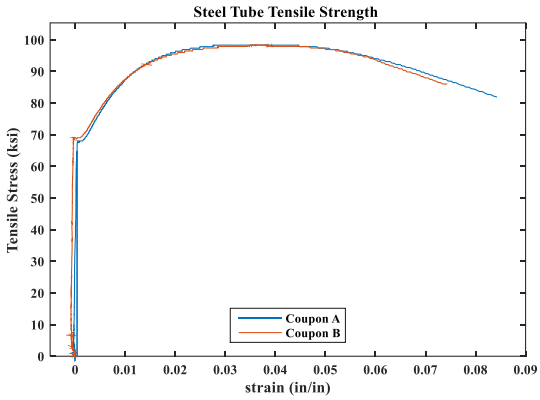

Figure F-10: Specimen 19 rebar

APPENDIX G: Concrete Mixes

Mix ID: 563375 Specified compressive strength: 6000 psi

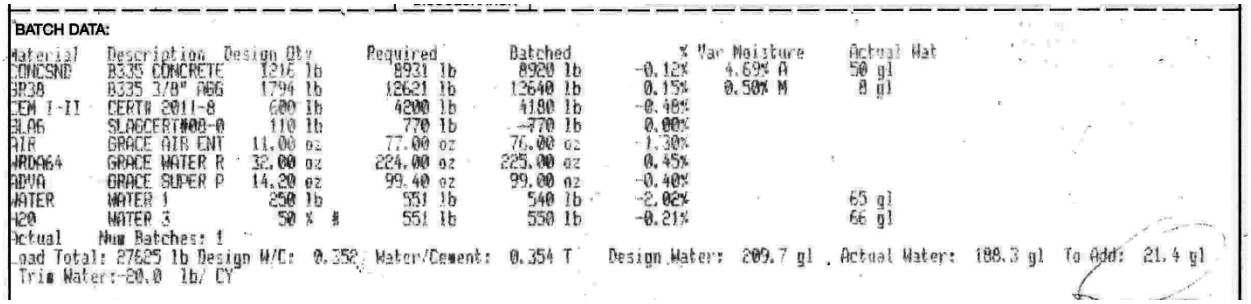

BATCH DATA:

Material	Description	Design Qty	Required	Batched	% Var	Moisture	Actual Wat
CONCSND	B335 CONCRETE	1216 lb	8931 lb	8920 lb	-0.12%	4.69% A	50 gl
GR38	B335 3/8" AGG	1794 lb	12621 lb	12640 lb	0.15%	0.50% M	8 gl
CEM I-II	CERT# 2011-8	600 lb	4200 lb	4180 lb	-0.48%		
SLAG	SLAGCERT#08-0	110 lb	770 lb	770 lb	0.00%		
AIR	GRACE AIR ENT	11.00 oz	77.00 oz	76.00 oz	-1.30%		
WRDA64	GRACE WATER R	32.00 oz	224.00 oz	225.00 oz	0.45%		
ADVA	GRACE SUPER P	14.20 oz	99.40 oz	99.00 oz	-0.40%		
WATER	WATER 1	250 lb	551 lb	540 lb	-2.02%		65 gl
H20	WATER 3	50 % #	551 lb	550 lb	-0.21%		66 gl

Actual Num Batches: 1

Load Total: 27625 lb Design W/C: 0.352 Water/Cement: 0.354 T Design Water: 209.7 gl Actual Water: 188.3 gl To Add: 21.4 gl

Trim Water:-20.0 lb/ CY

Mix ID: 880378X Specified compressive strength: 12000 psi

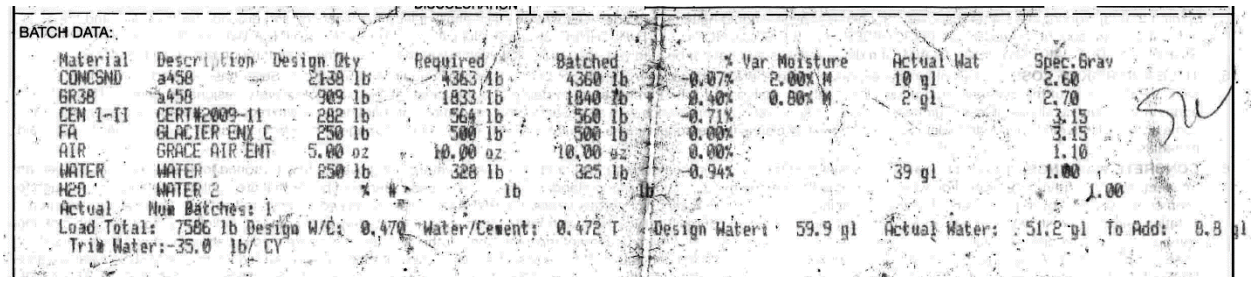

BATCH DATA:

Material	Description	Design Qty	Required	Batched	% Var	Moisture	Actual Wat	Spec.Grav
CONCSND	a450	2438 lb	4363 lb	4360 lb	-0.07%	2.00% M	10 gl	2.60
GR38	a450	909 lb	1833 lb	1840 lb	0.40%	0.80% M	2 gl	2.70
CEM I-II	CERT#2009-11	282 lb	564 lb	560 lb	-0.71%			3.15
FA	GLACIER ENV C	250 lb	500 lb	500 lb	0.00%			3.15
AIR	GRACE AIR ENT	5.00 oz	10.00 oz	10.00 oz	0.00%			1.10
WATER	WATER	250 lb	328 lb	325 lb	-0.94%		39 gl	1.00
H20	WATER 2	% #	lb	lb				1.00

Actual Num Batches: 1

Load Total: 7586 lb Design W/C: 0.470 Water/Cement: 0.472 T Design Water: 59.9 gl Actual Water: 51.2 gl To Add: 8.8 gl

Trim Water:-35.0 lb/ CY

Mix ID: 3051 Specified compressive strength: 2500 psi

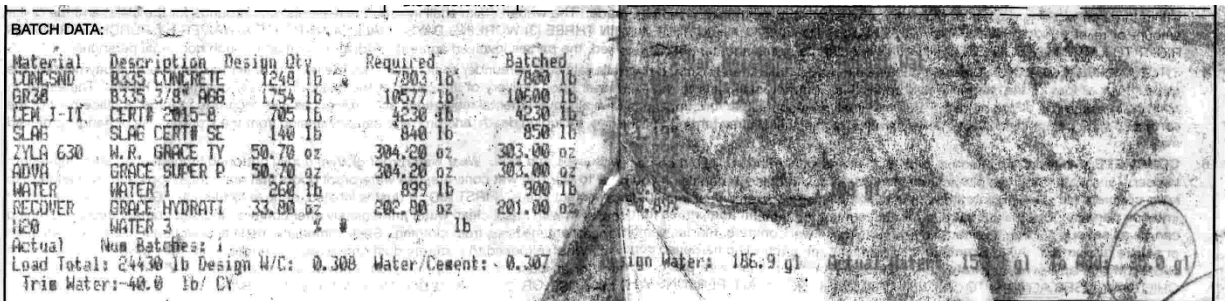

BATCH DATA:

Material	Description	Design Qty	Required	Batched
CONCSND	B335 CONCRETE	1248 lb	7803 lb	7800 lb
GR38	B335 3/8" AGG	1754 lb	10577 lb	10600 lb
CEM I-II	CERT# 2015-8	705 lb	4230 lb	4230 lb
SLAG	SLAG CERT# SE	140 lb	840 lb	850 lb
ZYLA 630	W.R. GRACE TY	50.70 oz	304.20 oz	303.00 oz
ADVA	GRACE SUPER P	50.70 oz	304.20 oz	303.00 oz
WATER	WATER 1	260 lb	899 lb	900 lb
RECOVER	GRACE HYDRATI	33.80 oz	202.80 oz	201.00 oz
H20	WATER 3	% #	lb	

Actual Num Batches: 1

Load Total: 24430 lb Design W/C: 0.308 Water/Cement: 0.307 Design Water: 186.9 gl

Trim Water:-40.0 lb/ CY

APPENDIX H: Elastomeric Bearing Force-Displacement Plots

Three sets of four reinforced elastomeric bearings were used during the testing program. One set was fabricated by the D.S. Brown Company (DSB) while the other two sets were fabricated by the Scougal Rubber Corporation (SR). Compression tests of the elastomeric bearings were performed on the 300-kip Baldwin hydraulic testing machine in the Structures Laboratory after the completion of the testing program. The force displacement plots are included in this Appendix. A preliminary compression test was performed on four of the bearings, two each from DSB and SR set 1. These are labeled Bearings A, B, C, and D in the plots below. Bearings A and B had already been used for five CFT tests while Bearings C and D were previously unused. The only known correlation is that Bearing C is DSB Bearing 1.

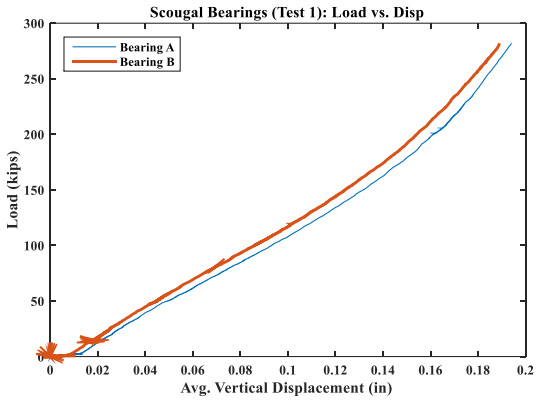

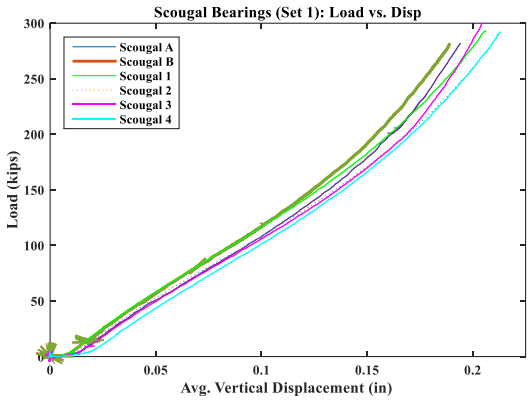

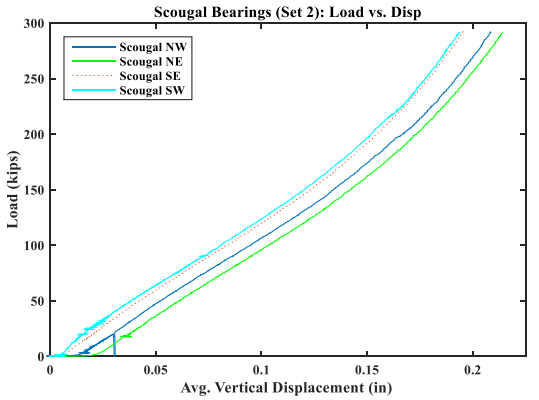

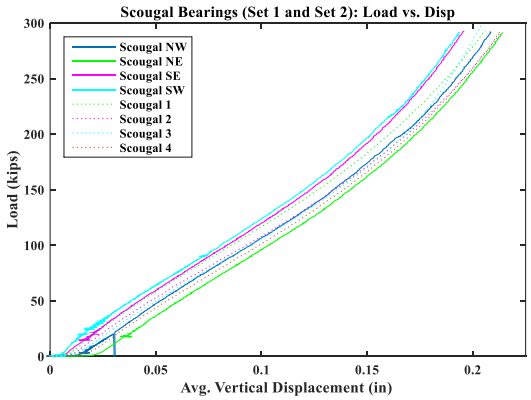

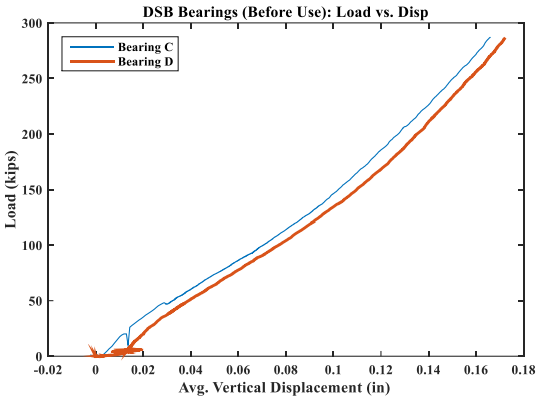
DSB Bearings (Before Use): Load vs. Disp
Bearing C
Bearing D
Load (kips)
Avg. Vertical Displacement (in)

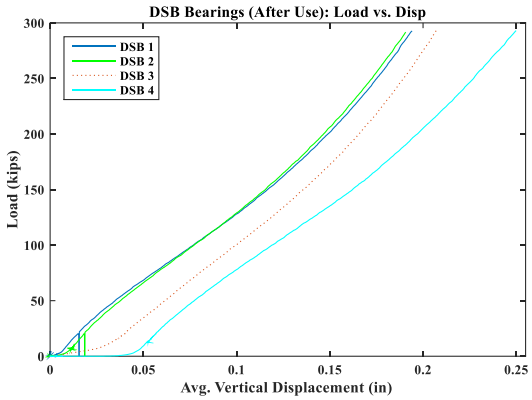
DSB Bearings (After Use): Load vs. Disp
DSB 1
DSB 2
DSB 3
DSB 4
Load (kips)
Avg. Vertical Displacement (in)

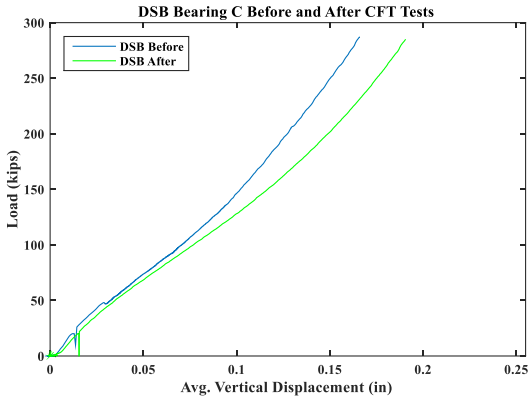
DSB Bearing C Before and After CFT Tests
DSB Before
DSB After
Load (kips)
Avg. Vertical Displacement (in)

APPENDIX I: Concrete Slip Plots

The relative displacement between the concrete fill and the steel tube was measured at the top and bottom of the CFTs at each end. The slip measurements are plotted against normalized moment and WSDOT normalized shear for each specimen without filtering or adjustment.

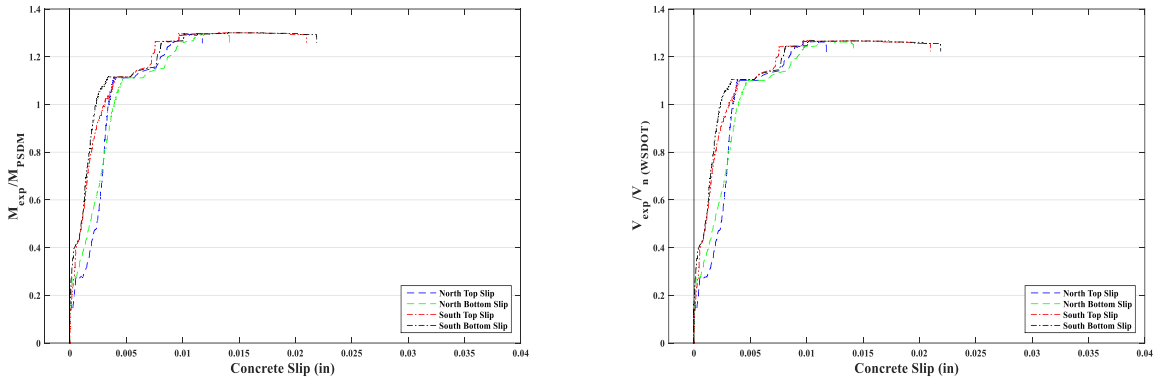

Concrete slip plots—Specimen 1

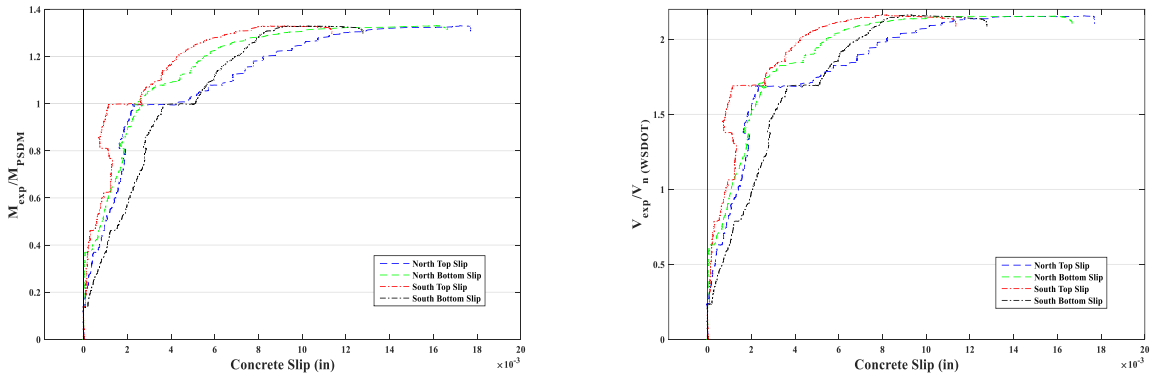

Concrete slip plots—Specimen 2

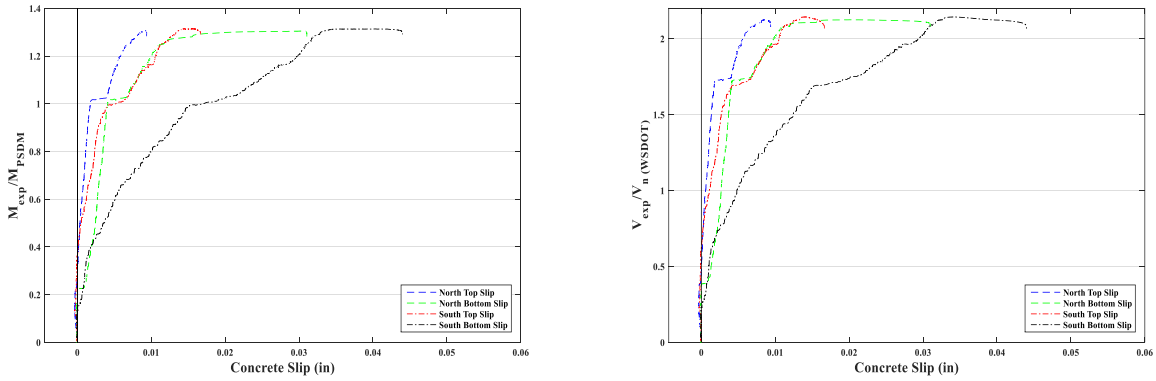

Concrete slip plots—Specimen 3

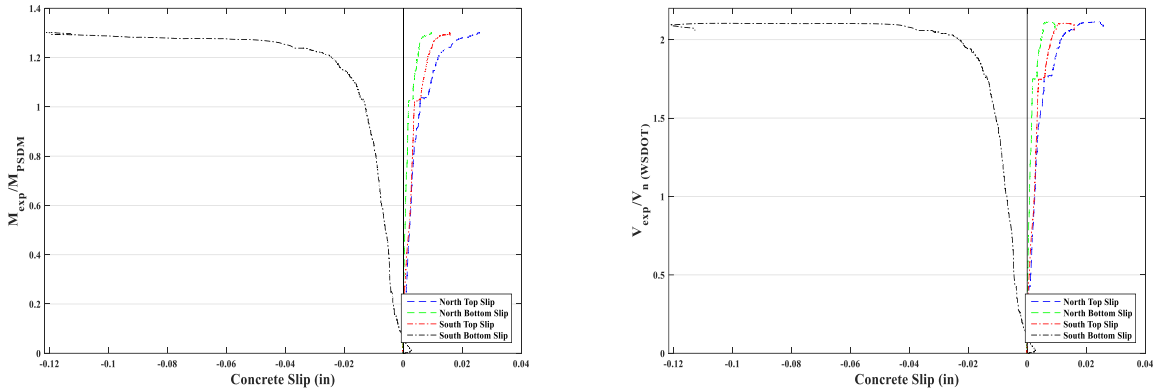

Concrete slip plots—Specimen 4

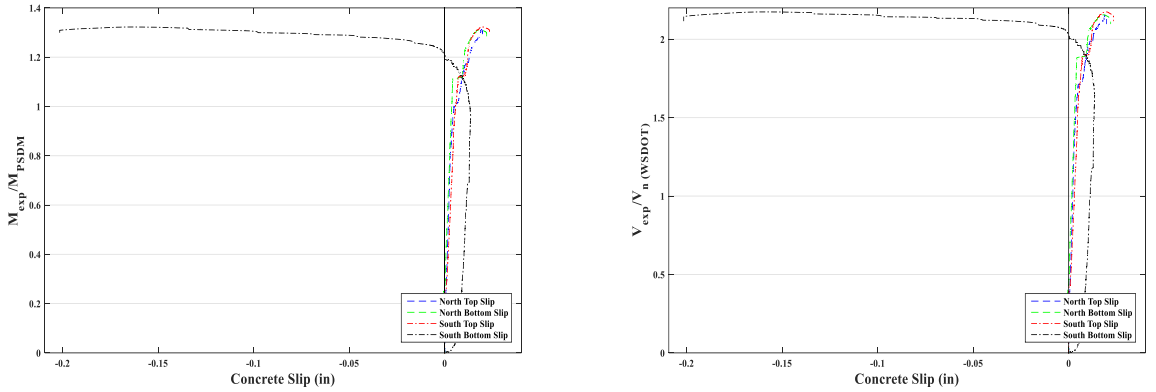

Concrete slip plots—Specimen 5

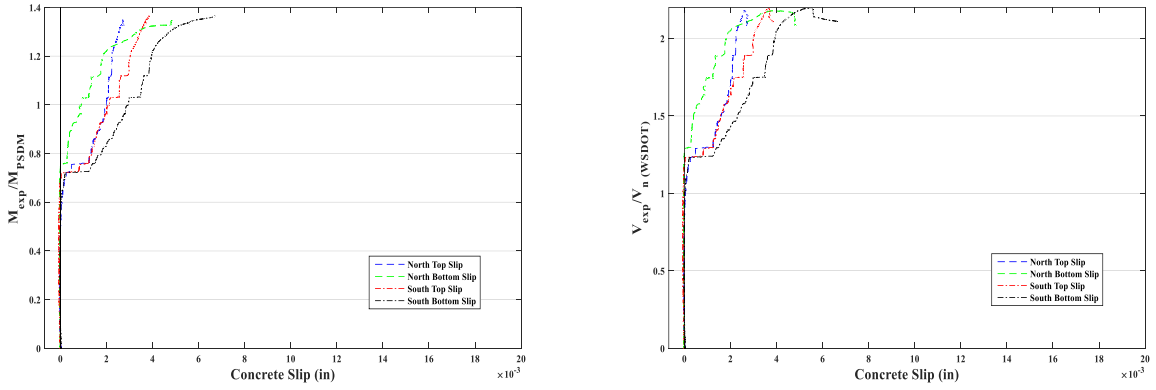

Concrete slip plots—Specimen 6

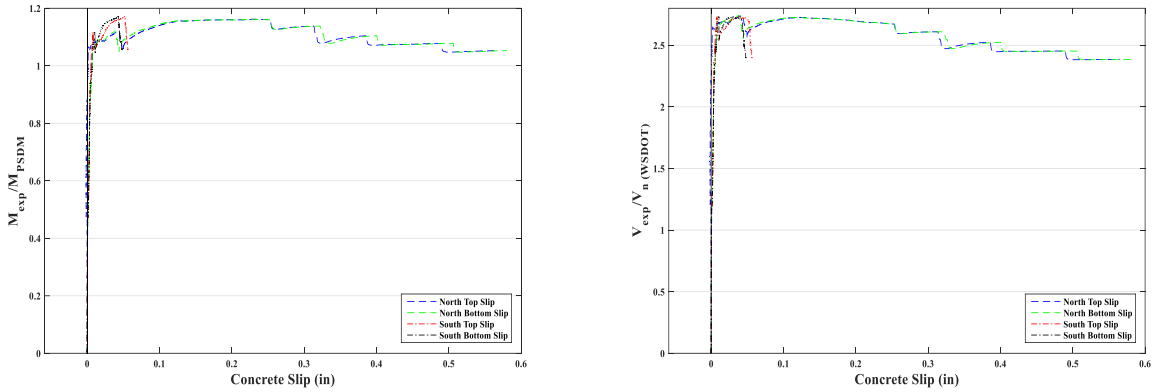

Concrete slip plots—Specimen 7

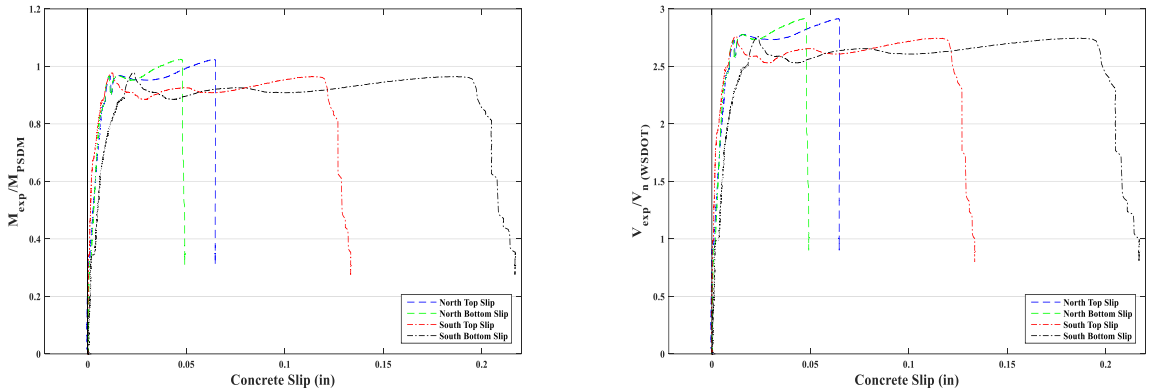

Concrete slip plots—Specimen 8

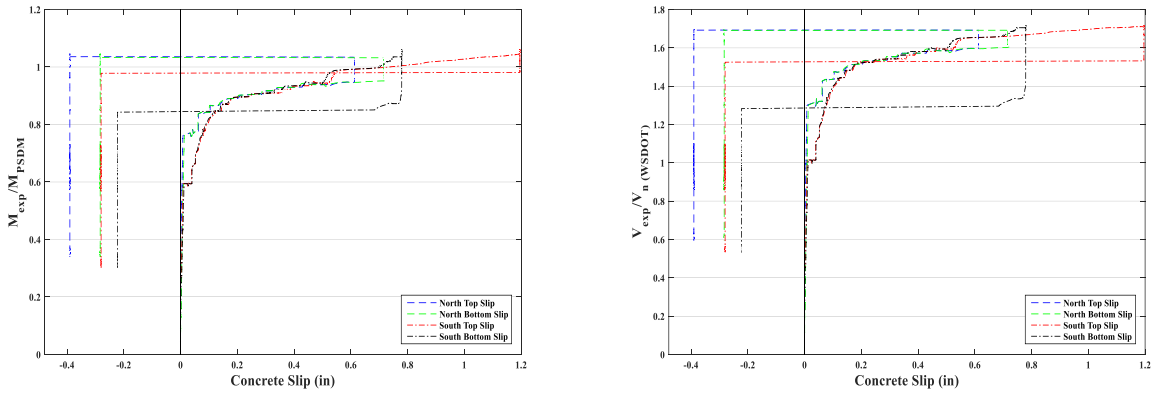

Concrete slip plots—Specimen 9

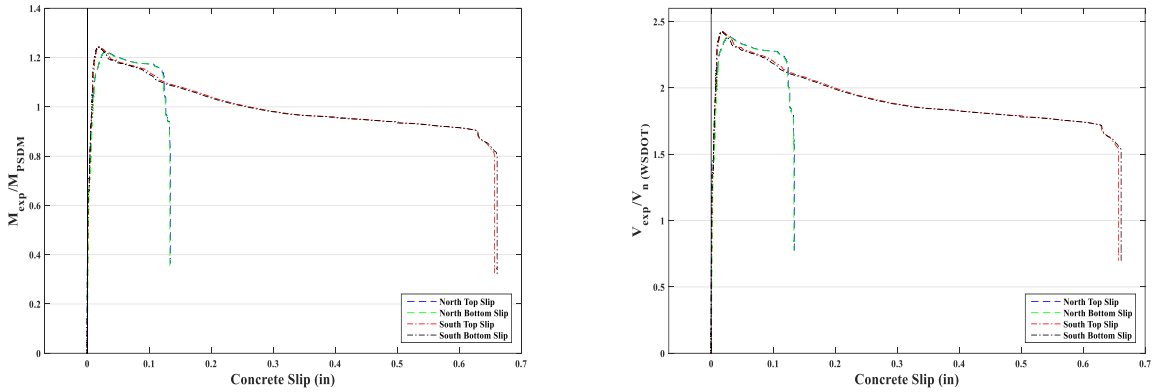

Concrete slip plots—Specimen 10

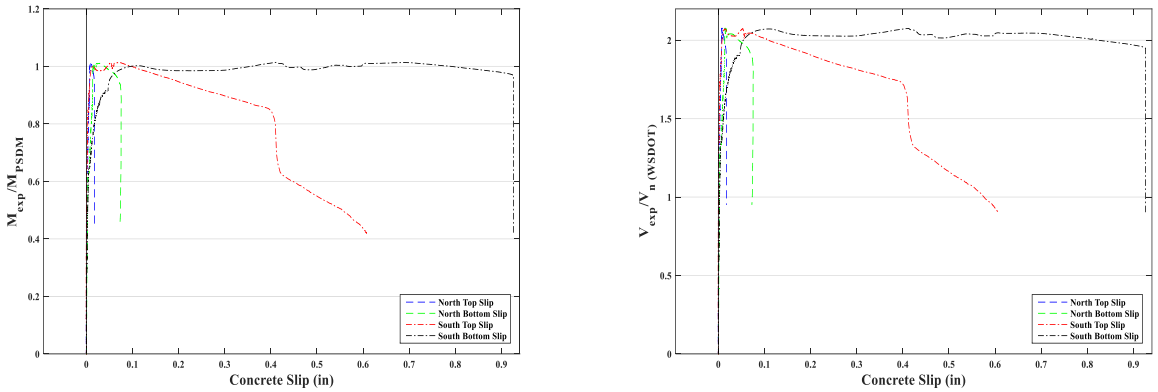

Concrete slip plots—Specimen 11

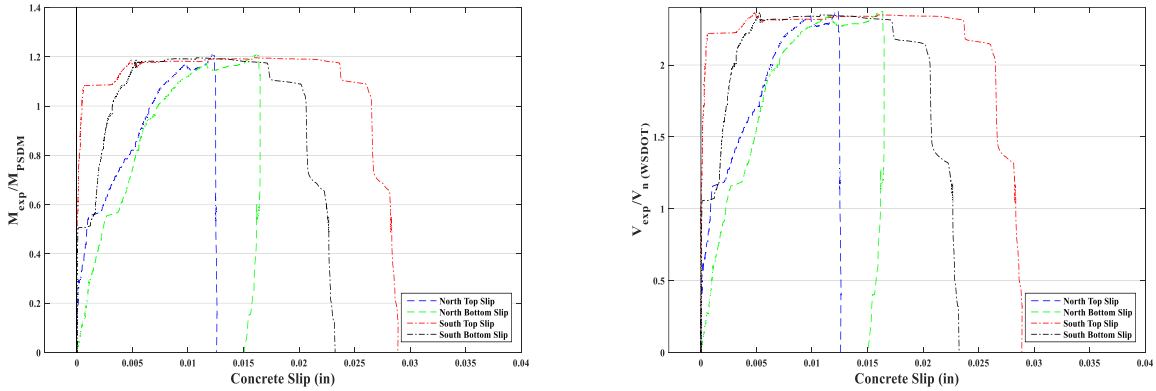

Concrete slip plots—Specimen 12

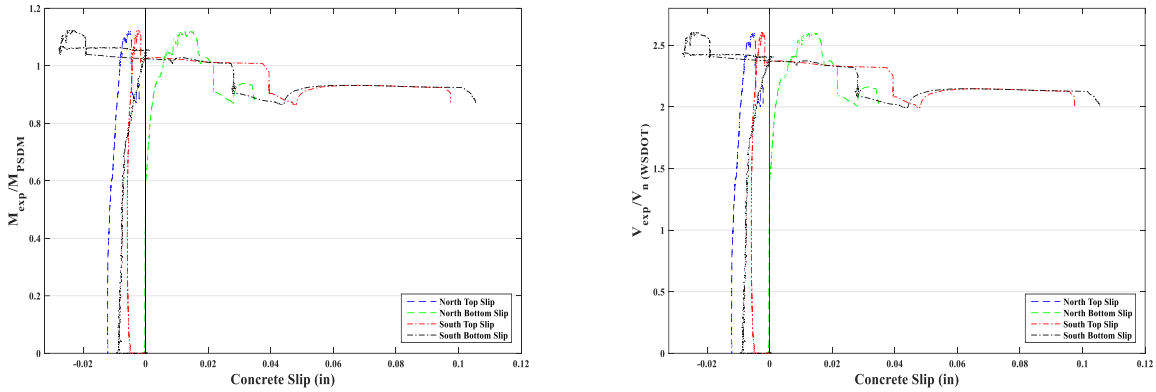

Concrete slip plots—Specimen 13

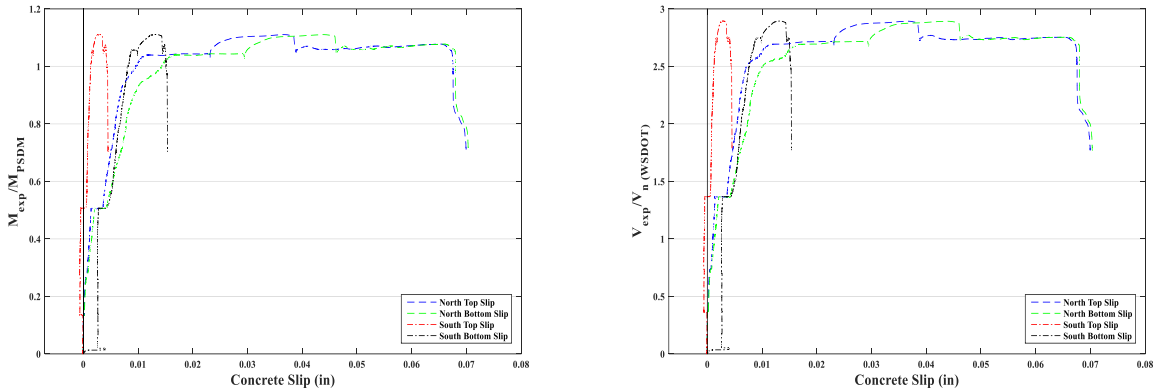

Concrete slip plots—Specimen 14

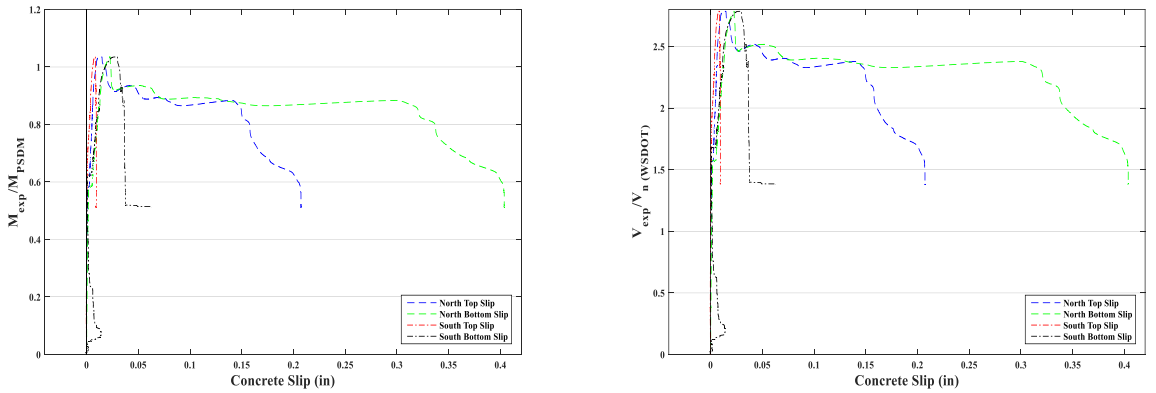

Concrete slip plots—Specimen 15

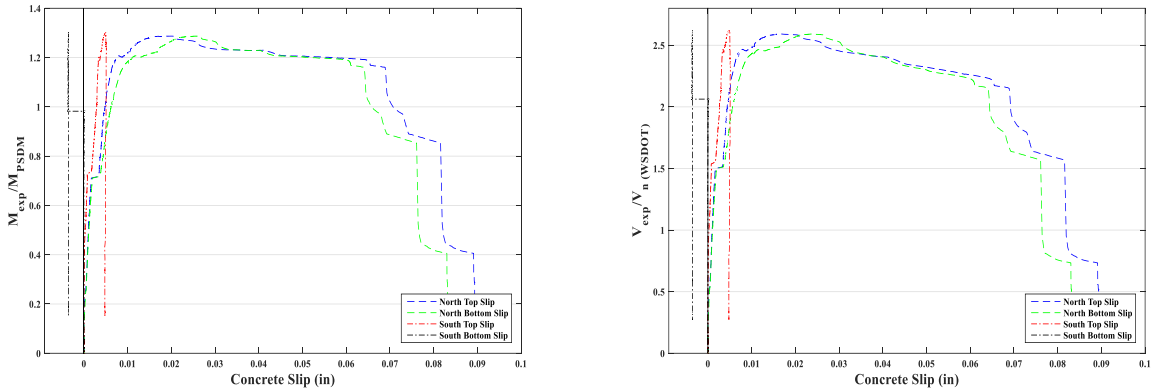

Concrete slip plots—Specimen 16

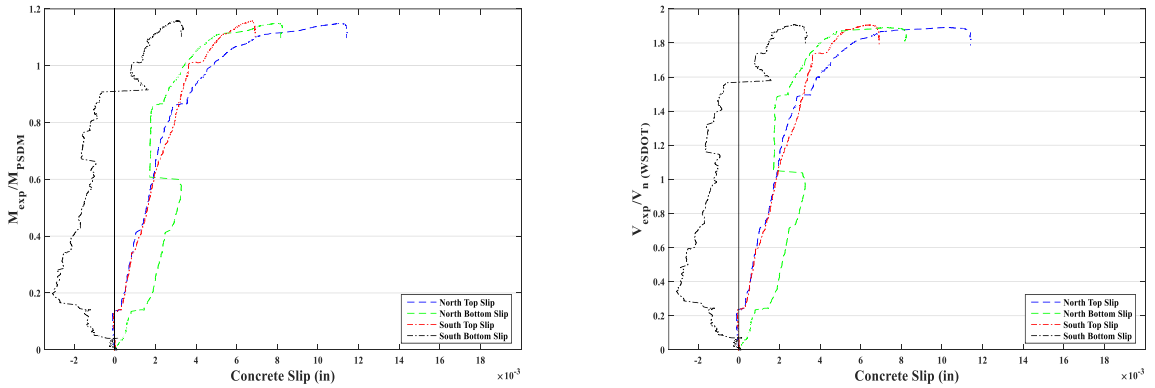

Concrete slip plots—Specimen 17

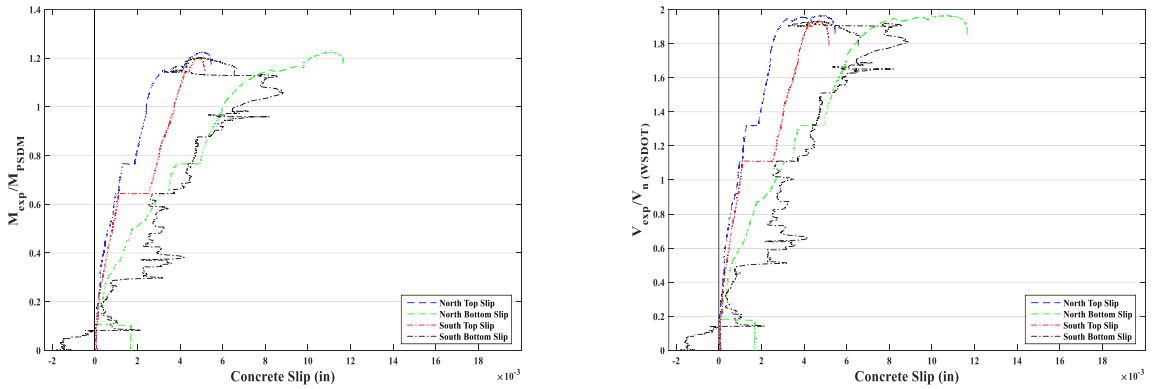

Concrete slip plots—Specimen 18

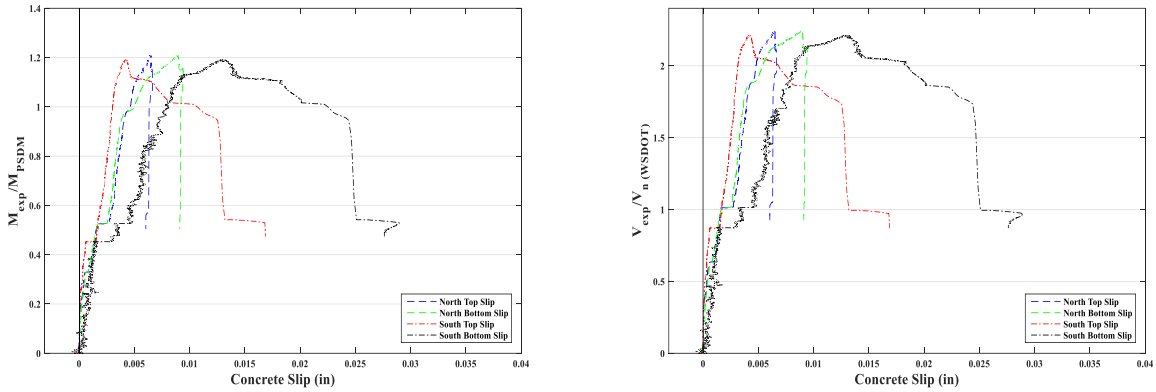

Concrete slip plots—Specimen 19

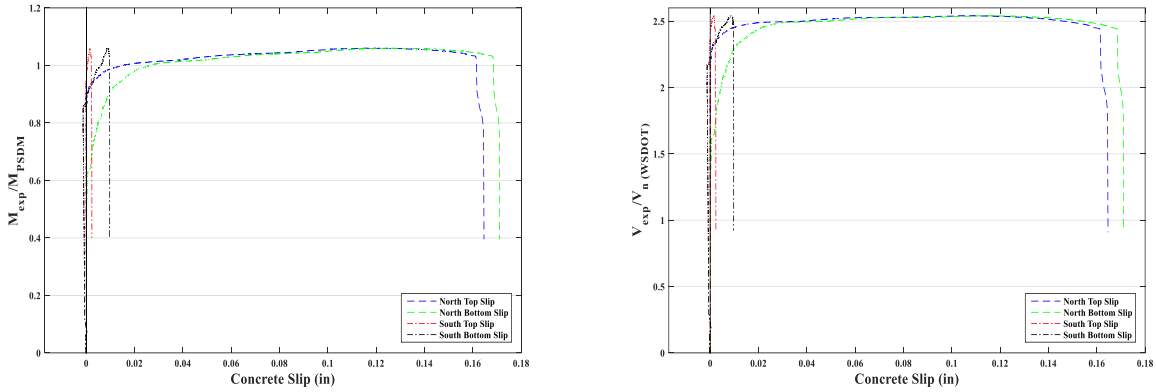

Concrete slip plots—Specimen 20

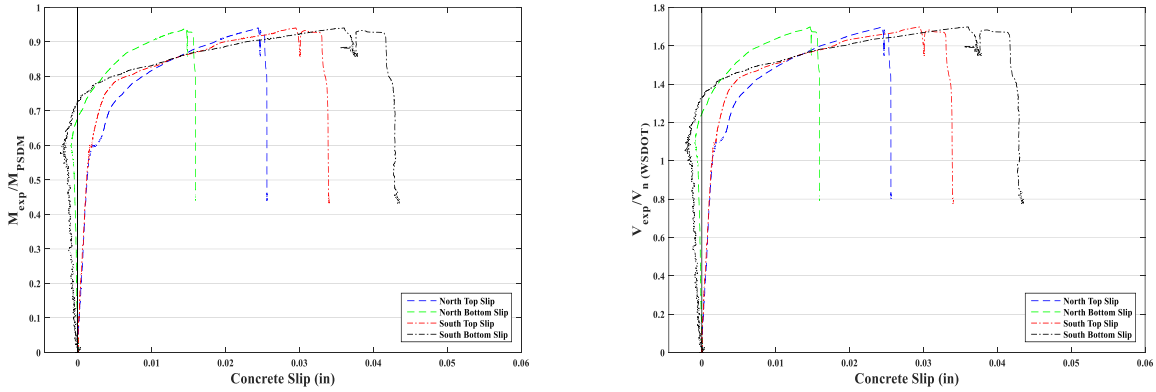

Concrete slip plots—Specimen 21